

FEBRUARY 2024

AJNR

VOLUME 45 • PP 127–248

# AJNR

## AMERICAN JOURNAL OF NEURORADIOLOGY

Official Journal ASNR • ASFNR • ASHNR • ASPNR • ASSR  
FEBRUARY 2024 | VOLUME 45 | NUMBER 2 | WWW.AJNR.ORG

THE JOURNAL OF DIAGNOSTIC AND INTERVENTIONAL NEURORADIOLOGY

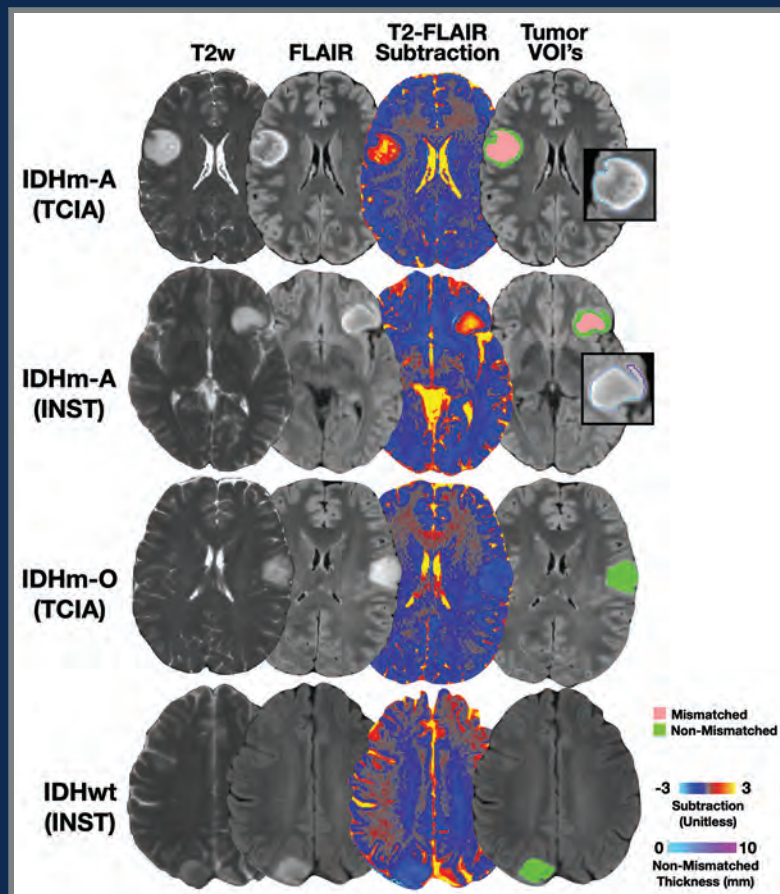
5th WHO Classification of genetic tumor syndromes and their imaging

Impaired glymphatic clearance in IIH

Clinical and imaging features of MOGAD

AI's potential role in radiology reports

Flat panel perfusion imaging provides relevant information after endovascular therapy



# FRED™ X™

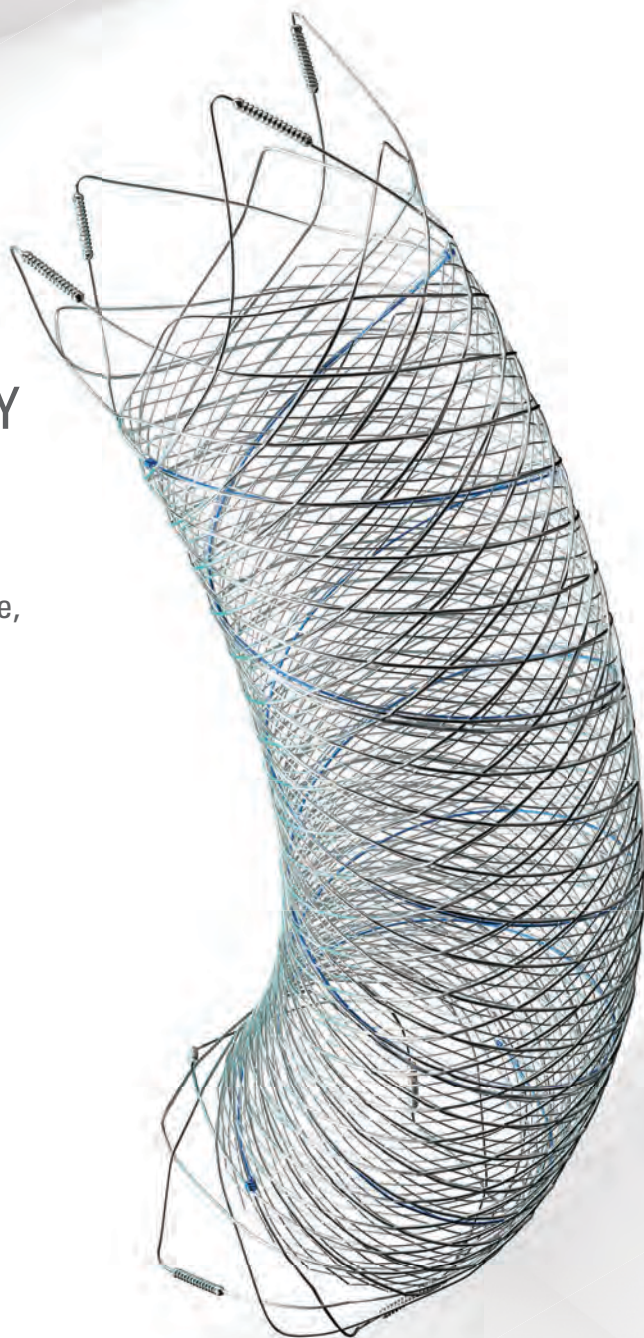
## Flow Diverter Stent

## THE NEXT ADVANCEMENT IN FLOW DIVERSION TECHNOLOGY

The FRED™ X Flow Diverter features the same precise placement and immediate opening of the FRED™ Device, now with X Technology. X Technology is a covalently bonded, nanoscale surface treatment, designed to:

- **REDUCE MATERIAL THROMBOGENICITY<sup>1</sup>**
- **MAINTAIN NATURAL VESSEL HEALING RESPONSE<sup>2,3,4</sup>**
- **IMPROVE DEVICE DELIVERABILITY AND RESHEATHING<sup>1</sup>**

The only FDA PMA approved portfolio with a 0.021" delivery system for smaller device sizes, and no distal lead wire.



For more information, contact your local MicroVention sales representative or visit our website. [www.microvention.com](http://www.microvention.com)



<sup>\*</sup> Data is derived from in vivo and ex vitro testing and may not be representative of clinical performance.

<sup>1</sup> Data on file

<sup>2</sup> Tanaka M et al. Design of biocompatible and biodegradable polymers based on intermediate water concept. Polymer Journal. 2015;47:114-121.

<sup>3</sup> Tanaka M et al. Blood compatible aspects of poly(2-methoxyethylacrylate) (PMEA) – relationship between protein adsorption and platelet adhesion on PMEA surface. Biomaterials. 2000;21:1471-1481.

<sup>4</sup> Schiel L et al. X Coating™: A new biopassive polymer coating. Canadian Perfusion Canadienne. June 2001;11(2):9.

**Indications for Use:** The FRED X System is indicated for use in the internal carotid artery from the petrous segment to the terminus for the endovascular treatment of adult patients (22 years of age or older) with wide-necked (neck width 4 mm or dome-to-neck ratio < 2) saccular or fusiform intracranial aneurysms arising from a parent vessel with a diameter 2.0 mm and 5.0 mm.

**Rx Only:** Federal (United States) law restricts this device to sale by or on the order of a physician. For Healthcare professionals intended use only.

MICROVENTION, FRED and HEADWAY are registered trademarks of MicroVention, Inc. in the United States and other jurisdictions. Stylized X is a trademark of MicroVention, Inc. © 2022 MicroVention, Inc. MM1222 US 03/22

# WEB™ 17

Aneurysm Embolization System

# LOWER PROFILE



## NEW SIZES



## MORE ACCESS OPTIONS



#### INDICATIONS FOR USE:

The WEB Aneurysm Embolization System is intended for the endovascular embolization of ruptured and unruptured intracranial aneurysms and other neurovascular abnormalities such as arteriovenous fistulae (AVF). The WEB Aneurysm Embolization System is also intended for vascular occlusion of blood vessels within the neurovascular system to permanently obstruct blood flow to an aneurysm or other vascular malformation.

#### POTENTIAL COMPLICATIONS:

Potential complications include but are not limited to the following: hematoma at the site of entry, aneurysm rupture, emboli, vessel perforation, parent artery occlusion, hemorrhage, ischemia, vasospasm, clot formation, device migration or misplacement, premature or difficult device detachment, non-detachment, incomplete aneurysm filling, revascularization, post-embolization syndrome, and neurological deficits including stroke and death. For complete indications, potential complications, warnings, precautions, and instructions, see instructions for use (IFU provided with the device).

VIA 21, 27, 33 - The VIA Microcatheter is intended for the introduction of interventional devices (such as the WEB device/stents/flow diverters) and infusion of diagnostic agents (such as contrast media) into the neuro, peripheral, and coronary vasculature.

VIA 17, 17 Preshaped - The VIA Microcatheter is intended for the introduction of interventional devices (such as the WEB device/stents/flow diverters) and infusion of diagnostic agents (such as contrast media) into the neuro, peripheral, and coronary vasculature.

The VIA Microcatheter is contraindicated for use with liquid embolic materials, such as n-butyl 2-cyanoacrylate or ethylene vinyl alcohol & DMSO (dimethyl sulfoxide).

The device should only be used by physicians who have undergone training in all aspects of the WEB Aneurysm Embolization System procedure as prescribed by the manufacturer.

RX Only: Federal law restricts this device to sale by or on the order of a physician.

For healthcare professional intended use only.



MicroVention Worldwide  
Innovator Center PH +1.714.247.8000

35 Enterprise  
Aliso Viejo, CA 92656 USA  
MicroVention UK Limited  
MicroVention Europe, S.A.R.L.  
MicroVention Deutschland GmbH  
Website  
PH +44 (0) 191 258 6777  
PH +33 (1) 39 21 77 46  
PH +49 211 210 798-0  
microvention.com



WEB™ and VIA™ are registered trademarks  
of Sequent Medical, Inc. in the United States.

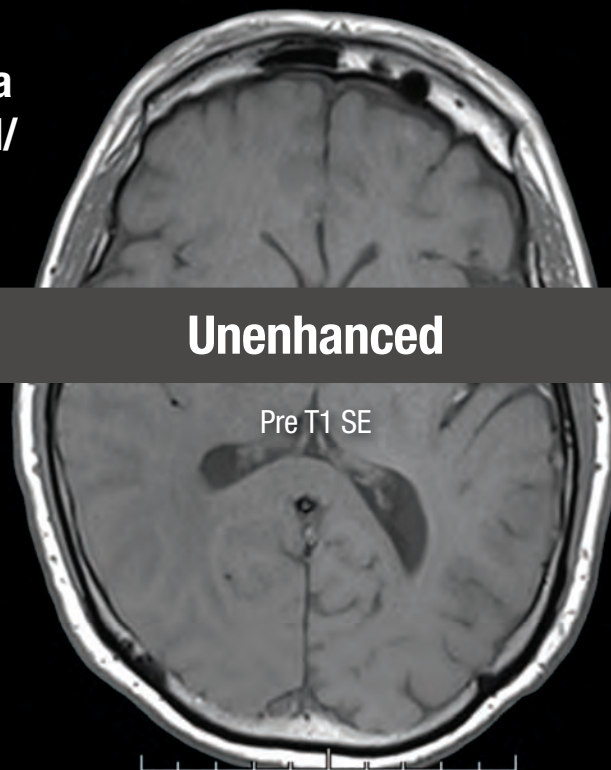
©2021 MicroVention, Inc. MM1184 WW 11/2021

# THIS IS HALF Gd\*

**\*Effective contrast enhancement at half the gadolinium dose (0.05 mmol/kg) vs a macrocyclic GBCA at a dose of 0.1 mmol/kg in approved indications in the U.S.<sup>1-6†</sup>**

  
**Vueway®**  
[gadopichlenol] injection  
485.1 mg/mL

**NO COMPROMISE IN MRI FROM BRACCO,  
YOUR TRUSTED PARTNER**



†Phase III CNS Study Design (Study GDX-44-010): Intra-individual, crossover comparison of 0.05 mmol/kg VUEWAY (gadopichlenol) injection vs. 0.1 mmol/kg Gadavist® in MRI of the CNS. Patients with known or suspected CNS lesions. Three primary visualization endpoints (lesion border delineation, lesion internal morphology, degree of contrast enhancement). The CNS study included 256 patients with known or highly suspected CNS lesion(s) with a mean age of 57 years (range: 18-84 years), and 53% female patients.

Please see Brief Summary of Prescribing Information including Boxed Warning on adjacent page.

## **VUEWAY® (gadopichlenol) solution for injection**

### **Indications**

VUEWAY injection is indicated in adults and children aged 2 years and older for use with magnetic resonance imaging (MRI) to detect and visualize lesions with abnormal vascularity in:

- the central nervous system (brain, spine and surrounding tissues),
- the body (head and neck, thorax, abdomen, pelvis, and musculoskeletal system).

### **IMPORTANT SAFETY INFORMATION**

#### **WARNING: NEPHROGENIC SYSTEMIC FIBROSIS (NSF)**

**Gadolinium-based contrast agents (GBCAs) increase the risk for NSF among patients with impaired elimination of the drugs. Avoid use of GBCAs in these patients unless the diagnostic information is essential and not available with non-contrasted MRI or other modalities. NSF may result in fatal or debilitating fibrosis affecting the skin, muscle and internal organs.**

- The risk for NSF appears highest among patients with:
  - Chronic, severe kidney disease (GFR < 30 mL/min/1.73 m<sup>2</sup>), or
  - Acute kidney injury.

- Screen patients for acute kidney injury and other conditions that may reduce renal function. For patients at risk for chronically reduced renal function (e.g. age > 60 years, hypertension, diabetes), estimate the glomerular filtration rate (GFR) through laboratory testing.
- For patients at highest risk for NSF, do not exceed the recommended VUEWAY dose and allow a sufficient period of time for elimination of the drug from the body prior to any re-administration.

### **Contraindications**

VUEWAY injection is contraindicated in patients with history of hypersensitivity reactions to VUEWAY.

### **Warnings**

Risk of **nephrogenic systemic fibrosis** is increased in patients using GBCA agents that have impaired elimination of the drugs, with the highest risk in patients with chronic, severe kidney disease as well as patients with acute kidney injury. Avoid use of GBCAs among these patients unless the diagnostic information is essential and not available with non-contrast MRI or other modalities.

**Hypersensitivity reactions**, including serious hypersensitivity reactions, could occur during use or shortly following VUEWAY administration. Assess all patients for any history of a reaction to contrast media, bronchial asthma and/or allergic disorders, administer VUEWAY only in

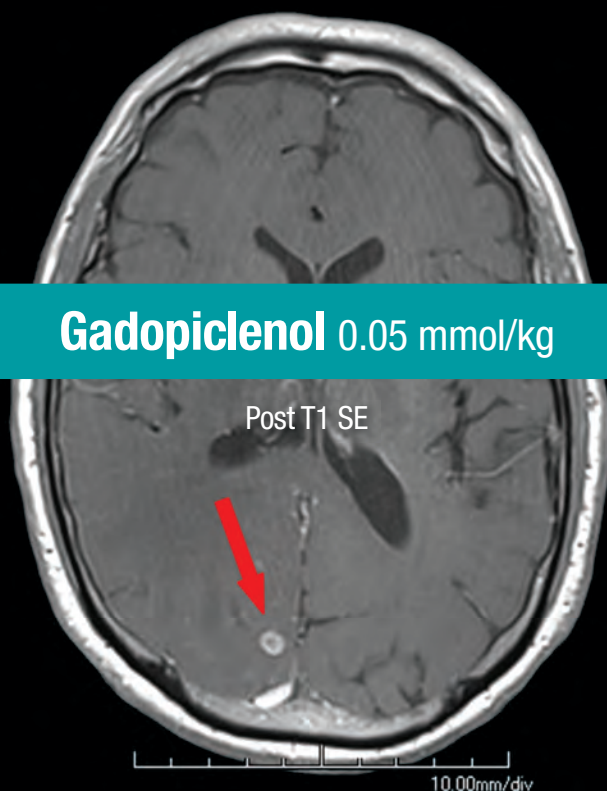


LIFE FROM INSIDE

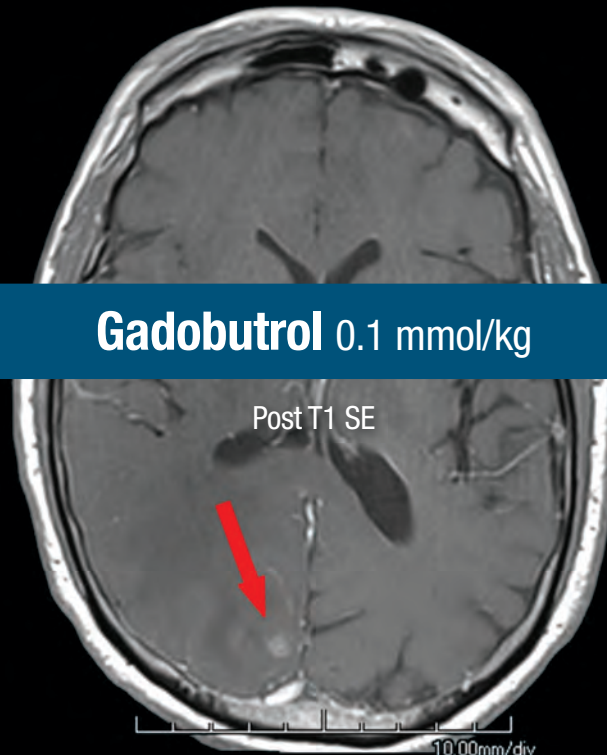
65-year-old man – 3.0 T Siemens  
Brain metastasis from lung adenocarcinoma<sup>7</sup>

SE = Spin Echo. These are representative images from reference studies; individual results may vary.

**Gadopichlenol** 0.05 mmol/kg



**Gadobutrol** 0.1 mmol/kg



situations where trained personnel and therapies are promptly available for the treatment of hypersensitivity reactions, and observe patients for signs and symptoms of hypersensitivity reactions after administration.

**Gadolinium retention** can be for months or years in several organs after administration. The highest concentrations (nanomoles per gram of tissue) have been identified in the bone, followed by other organs (brain, skin, kidney, liver and spleen). Minimize repetitive GBCA imaging studies, particularly closely spaced studies, when possible.

**Acute kidney injury** requiring dialysis has occurred with the use of GBCAs in patients with chronically reduced renal function. The risk of acute kidney injury may increase with increasing dose of the contrast agent.

Ensure catheter and venous patency before injecting as **extravasation** may occur, and cause tissue irritation.

VUEWAY may **impair the visualization of lesions** seen on non-contrast MRI. Therefore, caution should be exercised when VUEWAY MRI scans are interpreted without a companion non-contrast MRI scan.

The most common adverse reactions (incidence  $\geq 0.5\%$ ) are injection site pain (0.7%), and headache (0.7%).

**You are encouraged to report negative side effects of prescription drugs to the FDA. Visit [www.fda.gov/medwatch](http://www.fda.gov/medwatch) or call 1-800-FDA-1088.**

**Please see BRIEF SUMMARY of Prescribing Information for VUEWAY, including BOXED WARNING on Nephrogenic Systemic Fibrosis.**

Manufactured for Bracco Diagnostics Inc. by Liebel-Flarsheim Company LLC - Raleigh, NC, USA 27616.

VUEWAY is a trademark of Bracco Imaging S.p.A.

All other trademarks and registered trademarks are the property of their respective owners.

**References:** 1. VUEWAY® (gadopichlenol) solution for injection, 485.1 mg/mL Full Prescribing Information and Patient Medication Guide. Monroe Twp., NJ: Bracco Diagnostics Inc.; September 2022. 2. Robic C, Port M, Rousseaux O, et al. Physicochemical and pharmacokinetic profiles of gadopichlenol: a new macrocyclic gadolinium chelate with high T1 relaxivity. *Invest Radiol.* 2019 Aug;54:475-484. 3. GADAVIST® (gadobutrol) Injection. Full Prescribing Information. Bayer HealthCare Pharmaceuticals Inc. Whippany, NJ; April 2022. 4. DOTAREM® (gadoterate meglumine) Injection. Full Prescribing Information. Guerbet LLC. Princeton, NJ; April 2022. 5. CLARISCAN™ (gadoterate meglumine) injection for intravenous use. Full Prescribing Information. GE Healthcare. Chicago, IL; February 2020. 6. ProHance® (Gadoteridol) Injection, 279.3 mg/mL Full Prescribing Information and Patient Medication Guide. Monroe Twp., NJ: Bracco Diagnostics Inc.; June 2022. 7. Loevner LA, Kolumban B, Hutóczki G, et al. Efficacy and safety of gadopichlenol for contrast-enhanced MRI of the central nervous system: the PICTURE randomized clinical trial. *Invest Radiol.* 2023 May;58(5):307-313.

Bracco Diagnostics Inc.  
259 Prospect Plains Road, Building H  
Monroe Township, NJ 08831 USA  
Phone: 609-514-2200  
Toll-Free: 1-877-272-2269 (U.S. only)  
Fax: 609-514-2446

© 2023 Bracco Diagnostics Inc.  
All Rights Reserved. US-VW-2300022 08/23



VISIT  
[VUEWAY.COM](http://VUEWAY.COM)  
FOR MORE  
INFORMATION

# Vueway™

(gadopiclenol) injection, for intravenous use

**BRIEF SUMMARY:** Please see package insert of full prescribing information.

## WARNING: NEPHROGENIC SYSTEMIC FIBROSIS (NSF)

Gadolinium-based contrast agents (GBCAs) increase the risk for NSF among patients with impaired elimination of the drugs. Avoid use of GBCAs in these patients unless the diagnostic information is essential and not available with non-contrast MRI or other modalities. NSF may result in fatal or debilitating fibrosis affecting the skin, muscle and internal organs.

- The risk for NSF appears highest among patients with:
  - Chronic, severe kidney disease (GFR < 30 mL/min/1.73 m<sup>2</sup>), or
  - Acute kidney injury.
- Screen patients for acute kidney injury and other conditions that may reduce renal function. For patients at risk for chronically reduced renal function (e.g. age > 60 years, hypertension, diabetes), estimate the glomerular filtration rate (GFR) through laboratory testing.
- For patients at highest risk for NSF, do not exceed the recommended Vueway dose and allow a sufficient period of time for elimination of the drug from the body prior to any re-administration [see Warnings and Precautions (5.1) in the full Prescribing Information].

## INDICATIONS AND USAGE

Vueway™ (gadopiclenol) is a gadolinium-based contrast agent indicated in adult and pediatric patients aged 2 years and older for use with magnetic resonance imaging (MRI) to detect and visualize lesions with abnormal vascularity in:

- the central nervous system (brain, spine, and associated tissues),
- the body (head and neck, thorax, abdomen, pelvis, and musculoskeletal system).

## CONTRAINDICATIONS

Vueway is contraindicated in patients with history of hypersensitivity reactions to gadopichol.

## WARNINGS AND PRECAUTIONS

**Nephrogenic Systemic Fibrosis** Gadolinium-based contrast agents (GBCAs) increase the risk for nephrogenic systemic fibrosis (NSF) among patients with impaired elimination of the drugs. Avoid use of GBCAs among these patients unless the diagnostic information is essential and not available with non-contrast MRI or other modalities. The GBCA-associated NSF risk appears highest for patients with chronic, severe kidney disease (GFR < 30 mL/min/1.73 m<sup>2</sup>) as well as patients with acute kidney injury. The risk appears lower for patients with chronic, moderate kidney disease (GFR 30-59 mL/min/1.73 m<sup>2</sup>) and little, if any, for patients with chronic, mild kidney disease (GFR 60-89 mL/min/1.73 m<sup>2</sup>). NSF may result in fatal or debilitating fibrosis affecting the skin, muscle, and internal organs. Report any diagnosis of NSF following Vueway administration to Bracco Diagnostics Inc. (1-800-257-5181) or FDA (1-800-FDA-1088 or [www.fda.gov/medwatch](http://www.fda.gov/medwatch)).

Screen patients for acute kidney injury and other conditions that may reduce renal function. Features of acute kidney injury consist of rapid (over hours to days) and usually reversible decrease in kidney function, commonly in the setting of surgery, severe infection, injury or drug-induced kidney toxicity. Serum creatinine levels and estimated GFR may not reliably assess renal function in the setting of acute kidney injury. For patients at risk for chronically reduced renal function (e.g., age > 60 years, diabetes mellitus or chronic hypertension), estimate the GFR through laboratory testing.

Among the factors that may increase the risk for NSF are repeated or higher than recommended doses of a GBCA and the degree of renal impairment at the time of exposure. Record the specific GBCA and the dose administered to a patient. For patients at highest risk for NSF, do not exceed the recommended Vueway dose and allow a sufficient period of time for elimination of the drug prior to re-administration. For patients receiving hemodialysis, physicians may consider the prompt initiation of hemodialysis following the administration of a GBCA in order to enhance the contrast agent's elimination [see Use in Specific Populations (8.6) and Clinical Pharmacology (12.3) in the full Prescribing Information]. The usefulness of hemodialysis in the prevention of NSF is unknown.

**Hypersensitivity Reactions** With GBCAs, serious hypersensitivity reactions have occurred. In most cases, initial symptoms occurred within minutes of GBCA administration and resolved with prompt emergency treatment.

- Before Vueway administration, assess all patients for any history of a reaction to contrast media, bronchial asthma and/or allergic disorders. These patients may have an increased risk for a hypersensitivity reaction to Vueway.
- Vueway is contraindicated in patients with history of hypersensitivity reactions to Vueway [see Contraindications (4) in the full Prescribing Information].
- Administer Vueway only in situations where trained personnel and therapies are promptly available for the treatment of hypersensitivity reactions, including personnel trained in resuscitation.
- During and following Vueway administration, observe patients for signs and symptoms of hypersensitivity reactions.

**Gadolinium Retention** Gadolinium is retained for months or years in several organs. The highest concentrations (nanomoles per gram of tissue) have been identified in the bone, followed by other organs (e.g. brain, skin, kidney, liver, and spleen). The duration of retention also varies by tissue and is longest in bone. Linear GBCAs cause more retention than macrocyclic GBCAs. At equivalent doses, gadolinium retention varies among the linear agents with gadodiamide causing greater retention than other linear agents such as gadoxetate disodium, and gadobenate dimeglumine. Retention is lowest and similar

among the macrocyclic GBCAs such as gadoterate meglumine, gadobutrol, gadoteridol, and gadopichol.

Consequences of gadolinium retention in the brain have not been established. Pathologic and clinical consequences of GBCA administration and retention in skin and other organs have been established in patients with impaired renal function [see Warnings and Precautions (5.1) in the full Prescribing Information]. There are rare reports of pathologic skin changes in patients with normal renal function. Adverse events involving multiple organ systems have been reported in patients with normal renal function without an established causal link to gadolinium.

While clinical consequences of gadolinium retention have not been established in patients with normal renal function, certain patients might be at higher risk. These include patients requiring multiple lifetime doses, pregnant and pediatric patients, and patients with inflammatory conditions. Consider the retention characteristics of the agent when choosing a GBCA for these patients. Minimize repetitive GBCA imaging studies, particularly closely spaced studies, when possible.

**Acute Kidney Injury** In patients with chronically reduced renal function, acute kidney injury requiring dialysis has occurred with the use of GBCAs. The risk of acute kidney injury may increase with increasing dose of the contrast agent. Do not exceed the recommended dose.

**Extravasation and Injection Site Reactions** Injection site reactions such as injection site pain have been reported in the clinical studies with Vueway [see Adverse Reactions (6.1) in the full Prescribing Information]. Extravasation during Vueway administration may result in tissue irritation [see Nonclinical Toxicology (13.2) in the full Prescribing Information]. Ensure catheter and venous patency before the injection of Vueway.

**Interference with Visualization of Lesions Visible with Non-Contrast MRI** As with any GBCA, Vueway may impair the visualization of lesions seen on non-contrast MRI. Therefore, caution should be exercised when Vueway MRI scans are interpreted without a companion non-contrast MRI scan.

## ADVERSE REACTIONS

The following serious adverse reactions are discussed elsewhere in labeling:

- Nephrogenic Systemic Fibrosis [see Warnings and Precautions (5.1) in the full Prescribing Information]
- Hypersensitivity Reactions [see Contraindications (4) and Warnings and Precautions (5.2) in the full Prescribing Information]

**Clinical Trials Experience** Because clinical trials are conducted under widely varying conditions, adverse reaction rates observed in the clinical trials of a drug cannot be directly compared to rates in the clinical trials of another drug and may not reflect the rates observed in clinical practice.

The safety of Vueway was evaluated in 1,047 patients who received Vueway at doses ranging from 0.025 mmol/kg (one half the recommended dose) to 0.3 mmol/kg (six times the recommended dose). A total of 708 patients received the recommended dose of 0.05 mmol/kg. Among patients who received the recommended dose, the average age was 51 years (range 2 years to 88 years) and 56% were female. The ethnic distribution was 79% White, 10% Asian, 7% American Indian or Alaska native, 2% Black, and 2% patients of other or unspecified ethnic groups.

Overall, approximately 4.7% of subjects receiving the labeled dose reported one or more adverse reactions.

Table 1 lists adverse reactions that occurred in > 0.2% of patients who received 0.05 mmol/kg Vueway.

TABLE 1. ADVERSE REACTIONS REPORTED IN > 0.2% OF PATIENTS RECEIVING VUEWAY IN CLINICAL TRIALS	
Adverse Reaction	Vueway 0.05 mmol/kg (n=708) (%)
Injection site pain	0.7
Headache	0.7
Nausea	0.4
Injection site warmth	0.4
Injection site coldness	0.3
Dizziness	0.3
Local swelling	0.3

Adverse reactions that occurred with a frequency < 0.2% in patients who received 0.05 mmol/kg Vueway included: maculopapular rash, vomiting, worsened renal impairment, feeling hot, pyrexia, oral paresthesia, dysgeusia, diarrhea, pruritus, allergic dermatitis, erythema, injection site paresthesia, Cystatin C increase, and blood creatinine increase.

## Adverse Reactions in Pediatric Patients

One study with a single dose of Vueway (0.05 mmol/kg) was conducted in 80 pediatric patients aged 2 years to 17 years, including 60 patients who underwent a central nervous system (CNS) MRI and 20 patients who underwent a body MRI. One adverse reaction (maculopapular rash of moderate severity) in one patient (1.3%) was reported in the CNS cohort.

## USE IN SPECIFIC POPULATIONS

**Pregnancy Risk Summary** There are no available data on Vueway use in pregnant women to evaluate for a drug-associated risk of major birth defects, miscarriage or other adverse maternal or fetal outcomes. GBCAs cross the human placenta and result in fetal exposure and gadolinium retention. The available human data on GBCA exposure during pregnancy and adverse fetal outcomes are limited and inconclusive (see Data). In animal reproduction studies, there were no adverse developmental effects observed in rats or rabbits with intravenous administration of Vueway during organogenesis (see Data). Because of the potential risks of gadolinium to the fetus, use Vueway only if imaging is essential during pregnancy and cannot be delayed. The estimated background risk of major birth defects and miscarriage for the indicated population(s) are unknown. All pregnancies have a background risk of birth defect, loss, or other adverse outcomes. In the U.S. general population, the estimated background risk of major birth defects and miscarriage in clinically recognized pregnancies is 2% to 4% and 15% to 20% respectively. Data Human Data Contrast enhancement is visualized in the placenta and fetal tissues after maternal GBCA administration. Cohort studies and case reports on exposure to GBCAs during pregnancy have not reported a clear association between GBCAs and adverse effects in the exposed neonates. However, a retrospective cohort study comparing pregnant women who had a GBCA MRI to pregnant women who did not have an MRI reported a higher occurrence of stillbirths and neonatal deaths in the group receiving GBCA MRI. Limitations of this study include a lack of comparison with non-contrast MRI and lack of information about the maternal indication for MRI. Overall, these data preclude

a reliable evaluation of the potential risk of adverse fetal outcomes with the use of GBCAs in pregnancy.

**Animal Data Gadolinium Retention:** GBCAs administered to pregnant non-human primates (0.1 mmol/kg on gestational days 85 and 135) result in measurable gadolinium concentration in the offspring in bone, brain, skin, liver, kidney, and spleen for at least 7 months. GBCAs administered to pregnant mice (2 mmol/kg daily on gestational days 16 through 19) result in measurable gadolinium concentrations in the pups in bone, brain, kidney, liver, blood, muscle, and spleen at one-month postnatal age.

**Reproductive Toxicology:** Animal reproduction studies conducted with gadopichol showed some signs of maternal toxicity in rats at 10 mmol/kg and rabbits at 5 mmol/kg (corresponding to 52 times and 57 times the recommended human dose, respectively). This maternal toxicity was characterized in both species by swelling, decreased activity, and lower gestation weight gain and food consumption.

No effect on embryo-fetal development was observed in rats at 10 mmol/kg (corresponding to 52 times the recommended human dose). In rabbits, a lower mean fetal body weight was observed at 5 mmol/kg (corresponding to 57 times the recommended human dose) and this was attributed as a consequence of the lower gestation weight gain.

**Lactation Risk Summary** There are no data on the presence of gadopichol in human milk, the effects on the breastfed infant, or the effects on milk production. However, published lactation data on other GBCAs indicate that 0.01% to 0.04% of the maternal gadolinium dose is excreted in breast milk. Additionally, there is limited GBCA gastrointestinal absorption in the breast-fed infant. Gadopichol is present in rat milk. When a drug is present in animal milk, it is likely that the drug will be present in human milk (see Data). The developmental and health benefits of breastfeeding should be considered along with the mother's clinical need for Vueway and any potential adverse effects on the breastfed infant from Vueway or from the underlying maternal condition. Data In lactating rats receiving single intravenous injection of [<sup>153</sup>Gd]-gadopiclenol, 0.3% and 0.2% of the total administered radioactivity was transferred to the pups via maternal milk at 6 hours and 24 hours after administration, respectively. Furthermore, in nursing rat pups, oral absorption of gadopichol was 3.6%.

**Pediatric Use** The safety and effectiveness of Vueway for use with MRI to detect and visualize lesions with abnormal vascularity in the CNS (brain, spine, and associated tissues), and the body (head and neck, thorax, abdomen, pelvis, and musculoskeletal system) have been established in pediatric patients aged 2 years and older.

Use of Vueway in this age group is supported by evidence from adequate and well-controlled studies in adults with additional pharmacokinetic and safety data from an open-label, uncontrolled, multicenter, single dose study of Vueway (0.05 mmol/kg) in 80 pediatric patients aged 2 to 17 years. The 80 patients consisted of 60 patients who underwent a CNS MRI and 20 patients who underwent a body MRI [see Adverse Reactions (6.1) and Clinical Pharmacology (12.3) in the full Prescribing Information].

The safety and effectiveness of Vueway have not been established in pediatric patients younger than 2 years of age.

**Geriatric Use** Of the total number of Vueway-treated patients in clinical studies, 270 (26%) patients were 65 years of age and over, while 62 (6%) patients were 75 years of age and over. No overall differences in safety or efficacy were observed between these subjects and younger subjects.

This drug is known to be substantially excreted by the kidney, and the risk of adverse reactions to this drug may be greater in patients with impaired renal function. Because elderly patients are more likely to have decreased renal function, it may be useful to monitor renal function.

**Renal Impairment** In patients with renal impairment, the exposure of gadopichol is increased compared to patients with normal renal function. This may increase the risk of adverse reactions such as nephrogenic systemic fibrosis (NSF). Avoid use of GBCAs among these patients unless the diagnostic information is essential and not available with non-contrast MRI or other modalities. No dose adjustment of Vueway is recommended for patients with renal impairment. Vueway can be removed from the body by hemodialysis [see Warnings and Precautions (5.1, 5.3, 5.4) and Clinical Pharmacology (12.3) in the full Prescribing Information].

## OVERDOSAGE

Among subjects who received a single 0.3 mmol/kg intravenous dose of gadopichol (6 times the recommended dose of Vueway), headache and nausea were the most frequently reported adverse reactions. Gadopichol can be removed from the body by hemodialysis [see Clinical Pharmacology (12.3) in the full Prescribing Information].

**PATIENT COUNSELING INFORMATION** Advise the patient to read the FDA-approved patient labeling (Medication Guide).

**Nephrogenic Systemic Fibrosis** Inform the patient that Vueway may increase the risk for NSF among patients with impaired elimination of the drugs and that NSF may result in fatal or debilitating fibrosis affecting the skin, muscle and internal organs.

Instruct the patients to contact their physician if they develop signs or symptoms of NSF following Vueway administration, such as burning, itching, swelling, scaling, hardening and tightening of the skin; red or dark patches on the skin; stiffness in joints with trouble moving, bending or straightening the arms, hands, legs or feet; pain in the hip bones or ribs; or muscle weakness [see Warnings and Precautions (5.1) in the full Prescribing Information].

**Gadolinium Retention** Advise patients that gadolinium is retained for months or years in brain, bone, skin, and other organs following Vueway administration even in patients with normal renal function. The clinical consequences of retention are unknown. Retention depends on multiple factors and is greater following administration of linear GBCAs than following administration of macrocyclic GBCAs [see Warnings and Precautions (5.3) in the full Prescribing Information].

**Injection Site Reactions** Inform the patient that Vueway may cause reactions along the venous injection site, such as mild and transient burning or pain or feeling of warmth or coldness at the injection site [see Warnings and Precautions (5.5) in the full Prescribing Information].

**Pregnancy** Advise pregnant women of the potential risk of fetal exposure to Vueway [see Use in Specific Populations (8.1) in the full Prescribing Information].

## Rx only

US Patent No. 10,973,934  
Manufactured for Bracco Diagnostics Inc. by Liebel-Flarsheim Company LLC - Raleigh, NC, USA 27616.  
Toll Free: 1-877-272-2269 (U.S. only)  
Revised November 2022

# AJNR

## AMERICAN JOURNAL OF NEURORADIOLOGY

FEBRUARY 2024  
VOLUME 45  
NUMBER 2  
WWW.AJNR.ORG

Publication Preview at [www.ajnr.org](http://www.ajnr.org) features articles released in advance of print.  
Visit [www.ajnrblog.org](http://www.ajnrblog.org) to comment on AJNR content and chat with colleagues.

### EDITORIAL

- 127 **Striking a Balance: Global Perspectives on Neuroradiology Workload and Quality of Service** *Max Wintermark, et al.*

### REVIEW ARTICLE



- 128 **Newly Recognized Genetic Tumor Syndromes of the CNS in the 5th WHO Classification: Imaging Overview with Genetic Updates**  
*Amit Agarwal, et al.*

**BRAIN TUMOR  
IMAGING**

### STATE OF PRACTICE

- 139 **Recommended Resting-State fMRI Acquisition and Preprocessing Steps for Preoperative Mapping of Language and Motor and Visual Areas in Adult and Pediatric Patients with Brain Tumors and Epilepsy**  
*V.A. Kumar, et al.*

**NEUROIMAGING  
PHYSICS/FUNCTIONAL  
NEUROIMAGING/  
CT AND MRI  
TECHNOLOGY**

### GENERAL CONTENTS



- 149 **Diffusion-Weighted Imaging Reveals Impaired Glymphatic Clearance in Idiopathic Intracranial Hypertension** *Derrek Schartz, et al.*

**NEUROIMAGING  
PHYSICS/FUNCTIONAL  
NEUROIMAGING/  
CT AND MRI  
TECHNOLOGY**



- 155 **Assessment of Collateral Flow in Patients with Carotid Stenosis Using Random Vessel-Encoded Arterial Spin-Labeling: Comparison with Digital Subtraction Angiography** *Shanshan Lu, et al.*

**NEUROVASCULAR/  
STROKE IMAGING**



- 163 **Value of Immediate Flat Panel Perfusion Imaging after Endovascular Therapy (AFTERMATH): A Proof of Concept Study** *Adnan Mujanovic, et al.*

**NEUROVASCULAR/  
STROKE IMAGING**



- 171 **Transarterial Embolization of Anterior Cranial Fossa Dural AVFs as a First-Line Approach: A Single-Center Study** *Carl A. J. Puylaert, et al.*

**NEUROINTERVENTION**



- 176 **Safety and Efficacy of Low-Profile Braided Stents versus Flow Diverters in the Reconstructive Technique in the Treatment of Patients with Vertebrobasilar Dolichoectasia Aneurysms: A Cohort of 47 Patients with Long-Term Follow-Up** *Zhe Ji, et al.*

**NEUROINTERVENTION**



- 183 **Discrimination of Hemorrhage and Contrast Media in a Head Phantom on Photon-Counting Detector CT Data** *Franka Risch, et al.*

**NEUROINTERVENTION**

AJNR (Am J Neuroradiol ISSN 0195–6108) is a journal published monthly, owned and published by the American Society of Neuroradiology (ASNR), 820 Jorie Boulevard, Oak Brook, IL 60523. Annual dues for the ASNR include approximately 19% for a journal subscription. The journal is printed by Intellicor Communications, 330 Eden Road, Lancaster, PA 17601; Periodicals postage paid at Oak Brook, IL and additional mailing offices. Printed in the U.S.A. POSTMASTER: Please send address changes to American Journal of Neuroradiology, P.O. Box 3000, Denville, NJ 07834, U.S.A. Subscription rates: nonmember \$475 (\$560 foreign) print and online, \$320 online only; institutions \$550 (\$625 foreign) print and basic online, \$1080 (\$1160 foreign) print and extended online, \$380 online only (basic), \$825 online only (extended); single copies are \$35 each (\$40 foreign). Indexed by PubMed/MEDLINE, BIOSIS Previews, Current Contents (Clinical Medicine and Life Sciences), EMBASE, Google Scholar, HighWire Press, Q-Sensei, RefSeek, Science Citation Index, SCI Expanded, ReadCube, and Semantic Scholar. Copyright © American Society of Neuroradiology.

- ★ 188 **Quantification of T2-FLAIR Mismatch in Nonenhancing Diffuse Gliomas Using Digital Subtraction** *Nicholas S. Cho, et al.*
- 198 **Comparison of HASTE versus EPI-Based DWI for Retinoblastoma and Correlation with Prognostic Histopathologic Parameters** *Manish Sharma, et al.*
- 205 **MRI-Based Brain Volume Scoring in Cerebral Malaria Is Externally Valid and Applicable to Lower-Resolution Images** *Manu S. Goyal, et al.*
- 🔑 211 **Incidental Thalamic Lesions Identified on Brain MRI in Pediatric and Young Adult Patients: Imaging Features and Natural History** *Vinicius de Padua V. Alves, et al.*
- 218 **A Prospective Multi-Institutional Study Comparing the Brain Development in the Third Trimester between Opioid-Exposed and Nonexposed Fetuses Using Advanced Fetal MR Imaging Techniques** *Hyuk Jin Yun, et al.*
- 224 **White Matter Injury on Early-versus-Term-Equivalent Age Brain MRI in Infants Born Preterm** *Sriya Roychaudhuri, et al.*
- 📖 229 **Clinical and Imaging Findings in Children with Myelin Oligodendrocyte Glycoprotein Antibody Associated Disease (MOGAD): From Presentation to Relapse** *Elizabeth George, et al.*
- 🔑 236 **A Radiomic “Warning Sign” of Progression on Brain MRI in Individuals with MS** *Brendan S. Kelly, et al.*
- ★ 🔑 244 **AI-Assisted Summarization of Radiologic Reports: Evaluating GPT3davinci, BARTcnn, LongT5booksum, LEDbooksum, LEDlegal, and LEDclinical** *Aichi Chien, et al.*

**BRAIN TUMOR  
IMAGING**

**HEAD AND NECK  
IMAGING**

**PEDIATRIC  
NEUROIMAGING**

**PEDIATRIC  
NEUROIMAGING**

**PEDIATRIC  
NEUROIMAGING**

**PEDIATRIC  
NEUROIMAGING**

**PEDIATRIC  
NEUROIMAGING**

**ARTIFICIAL  
INTELLIGENCE**

**ARTIFICIAL  
INTELLIGENCE**

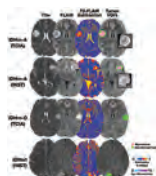
## ONLINE FEATURES

### LETTER

- E2 **Setting the Bar: The Japanese College of Radiology’s Perspective on Safeguarding Quality in the Interpretation of Cross-Sectional Studies per Day** *Satoru Takahashi, et al.*

## BOOK REVIEWS *R.M. Quencer, Section Editor*

Please visit [www.ajnrblog.org](http://www.ajnrblog.org) to read and comment on Book Reviews.



T2-FLAIR mismatch sign is a highly specific imaging biomarker of isocitrate dehydrogenase (IDH)-mutant, negative 1p/19q codeletion astrocytomas. Cho et al, quantified the degree of T2-FLAIR mismatch on segmented nonenhancing diffuse gliomas to assess improvements in diagnostic performance and investigate subregion characteristics within these lesions. Thresholds of  $\geq 42\%$  T2-FLAIR mismatch volume classified IDH-mutant astrocytoma with a specificity/sensitivity of 100%/19.6% (The Cancer Imaging Archive-TCIA) and 100%/31.6% (institutional-INST).



Indicates Editor's Choices selection



Indicates Fellows' Journal Club selection



Indicates open access to non-subscribers at [www.ajnr.org](http://www.ajnr.org)



Indicates article with supplemental online data



Indicates article with supplemental online video



Evidence-Based Medicine Level 1



Evidence-Based Medicine Level 2

I am a global citizen.  
I am patient-centered care.  
I am an academic neuroradiologist.  
I am a researcher.  
I am a life-long learner.  
I am determined.  
I am curious.  
I am a collaborative team player.  
I am a volunteer.  
**I am ASNR.**

Don't miss out on the tools, resources and relationships you've come to rely on. Log in and renew your ASNR membership today! [www.asnr.org](http://www.asnr.org)

### EDITOR-IN-CHIEF

#### Max Wintermark, MD, MAS, FASFN, FICIS

*Frank T. McGraw Memorial Chair in the Study of Cancer  
Professor and Chair of Neuroradiology  
The University of Texas MD Anderson Center*

### DEPUTY EDITOR

#### Lubdhra M. Shah, MD, MS

Professor of Radiology and Director of Spine Imaging  
Department of Radiology and Imaging Sciences  
University of Utah

### SPECIAL ADVISORS TO THE EDITOR-IN-CHIEF

#### Mauricio Castillo, MD, FACR

MA Mauro Distinguished Professor of Radiology  
University of North Carolina-Chapel Hill

#### Robert Quencer, MD

Professor Emeritus  
Department of Radiology  
University of Miami

### ARTIFICIAL INTELLIGENCE

#### Senior Editor

#### Reza Forghani, MD, PhD

Professor of Radiology & Artificial Intelligence  
Vice Chair of AI  
Director, Radiomics & Augmented Intelligence Laboratory (RAIL)  
Department of Radiology  
University of Florida College of Medicine

#### Associate Editors

#### Andreas Rauschecker, MD, PhD

Assistant Professor-in-Residence  
Co-Executive Director and Clinical Director,  
Center for Intelligent Imaging (ci<sup>2</sup>)  
Department of Radiology & Biomedical Imaging  
University of California, San Francisco

#### Sam (Seyedmehdi) Payabvash, MD

Assistant Professor of Radiology  
Yale School of Medicine  
Connecticut

### BRAIN TUMOR IMAGING

#### Senior Editor

#### Ben Ellingson, PhD

Professor and Director of MRI Research  
Director, UCLA Brain Tumor Imaging Laboratory  
Department of Radiological Sciences  
David Geffen School of Medicine  
University of California, Los Angeles

#### Associate Editors

#### Ali Nabavizadeh, MD

Assistant Professor of Radiology  
Division of Neuroradiology  
University of Pennsylvania

#### Mark S. Shiroishi, MD, MS, FASFN

Assistant Professor, Division of Neuroradiology,  
Department of Radiology  
Director of Neuro-Oncology Imaging - USC Brain Tumor Center  
Chief of Pediatric Neuroradiology - Los Angeles General Medical Center  
Affiliated Faculty - USC Imaging Genetics Center  
Mark and Mary Stevens Neuroimaging and Informatics Institute  
Keck School of Medicine of USC  
University of Southern California

### EMERGENCY NEURORADIOLOGY

#### Senior Editor

#### Karen Buch, MD

Assistant Professor of Radiology  
Massachusetts General Hospital

#### Associate Editors

#### Melissa A. Davis, MD, MBA

Vice Chair of Medical Informatics  
Associate Professor  
Department of Radiology and Biomedical Imaging  
Yale School of Medicine  
Connecticut

#### Jason Talbott, MD, PhD

Associate Professor, Neuroradiology Section  
Department of Radiology and Biomedical Imaging  
University of California, San Francisco and  
Zuckerberg San Francisco General Hospital

### HEAD AND NECK IMAGING

#### Senior Editor

#### Amy Juliano, MD

Associate Professor of Radiology  
Massachusetts Eye and Ear  
Harvard Medical School

#### Associate Editors

#### Burce Ozgen, MD

Clinical Professor of Radiology  
University of Illinois at Chicago

#### David Zander, MD

Assistant Professor, Radiology  
University of Colorado School of Medicine

### HEALTH POLICIES/QUALITY IMPROVEMENT/ EVIDENCE-BASED NEUROIMAGING

#### Senior Editor

#### Nadja Kadom, MD, FACR, FAAP

Professor, Department of Radiology and Imaging Sciences  
Emory University School of Medicine  
Pediatric Neuroradiologist, Department of Radiology  
Children's Healthcare of Atlanta

### Associate Editors

#### Melissa M. Chen, MD

Associate Professor,  
Department of Neuroradiology, Division of Diagnostic Imaging  
The University of Texas MD Anderson Center

#### Ajay Malhotra, MBBS, MD, MMM

Professor of Radiology and Biomedical Imaging and Neurosurgery  
Yale School of Medicine  
Connecticut

### MOLECULAR NEUROIMAGING/NUCLEAR MEDICINE

#### Senior Editor

#### Ana M. Franceschi, MD, PhD

Associate Professor of Radiology  
Donald and Barbara Zucker School of Medicine at Hofstra/Northwell  
The Feinstein Institutes for Medical Research  
Neuro-PET Imaging  
Lenox Hill Hospital  
New York

#### Associate Editors

#### Nadya Pyatigorskaya, MD, PhD

Neuroradiology Department, Pitié-Salpêtrière Hospital  
Researcher, Brain Institute (ICM)  
France

#### Marc Daniel Benayoun, PhD, MD

Assistant Professor of Radiology  
Co-Section Head of Nuclear Medicine  
Medical Director of Nuclear Medicine and PET  
Vice Chair of Radiation Drug Research Committee  
Atrium Wake Forest Health  
North Carolina

### NEURODEGENERATIVE DISORDER IMAGING

#### Senior Editor

#### Gloria Chiang, MD

Associate Professor, Co-Director of the Brain Health Imaging Institute  
Department of Radiology  
Weill Cornell Medicine/NewYork-Presbyterian Hospital

#### Associate Editors

#### Fang Frank Yu, MD

Assistant Professor of Radiology  
Division of Neuroradiology, Department of Radiology  
Advanced Imaging Research Center  
University of Texas Southwestern Medical Center

**Priya Rajagopalan, MBBS, MPH**

Assistant Professor of Radiology, Division of Neuroradiology  
Associate Program Director, Neuroradiology Fellowship  
Medical Director, Center for Image Acquisition Mark and Mary Stevens Neuroimaging and Informatics Institute  
Keck School of Medicine, University of Southern California

**NEUROIMAGING PHYSICS/FUNCTIONAL NEUROIMAGING/CT AND MRI TECHNOLOGY****Senior Editor****Hongyu An, DSc**

Professor, Mallinckrodt Institute of Radiology  
Neurology, Biomedical Engineering, Electrical and Systems Engineering, Division of Biology and Biomedical Sciences  
Director, Biomedical Magnetic Resonance Center  
Associate Director, Center for Clinical Imaging Research  
Washington University in St. Louis

**Associate Editors****Timothy J. Carroll, PhD**

Professor, Department of Radiology  
University of Chicago

**Hugo de Jong, PhD**

Professor of Medical Physics Radiology and Nuclear Medicine  
UMC Utrecht  
the Netherlands

**NEUROINTERVENTION****Senior Editor****Steven Hetts, MD, FACR**

Co-Chief, NeuroEndovascular Surgery Service Line  
Chief of Interventional Neuroradiology, Mission Bay Hospitals  
Professor of Radiology, Biomedical Imaging, and Neurological Surgery  
University of California, San Francisco

**Associate Editors****Kristine Blackham, MD**

Associate Professor  
Diagnostic and Interventional Neuroradiology  
Clinic for Radiology and Nuclear Medicine  
University Hospital of Basel

**Maksim Shapiro, MD**

Clinical Associate Professor  
Departments of Radiology, Neurosurgery, and Neurology  
Division of Neurointerventional Radiology  
NYU Langone Health and Bellevue NYCH + Hospitals  
New York

**NEUROPSYCHIATRIC IMAGING****Senior Editor****Jody Tanabe, MD**

Professor  
Chief of Neuroradiology  
University of Colorado-Anschutz Medical Campus

**Associate Editors****John-Paul J. Yu, MD, PhD**

Assistant Professor of Radiology, Psychiatry, and Biomedical Engineering  
University of Wisconsin School of Medicine and Public Health

**J. Eric Schmitt, MD, PhD**

Assistant Professor of Radiology and Psychiatry  
Division of Neuroradiology  
Perelman School of Medicine, University of Pennsylvania

**NEUROVASCULAR/STROKE IMAGING****Senior Editor****Ajay Gupta, MD, MS**

Alexander R. Margulis, MD, Distinguished  
Professor in Radiology  
Weill Cornell Medical College  
New York

**Associate Editors****Shalini Amukotuwa, MB BS, PhD, FRANZCR**

Head of Neuroradiology and Director of MRI, Monash Health  
Associate Professor of Radiology, Monash University  
Australia

**Mahmud Mossa-Basha, MD**

Professor of Radiology, Neurology and Electrical Engineering  
Vice Chair of Clinical Research and Clinical Transformation  
Co-Director of the Research Vascular Imaging Lab  
University of Washington School of Medicine

**PEDIATRIC NEUROIMAGING****Senior Editor****Caroline D. Robson, MBChB**

Division Chief & Endowed Chair, Neuroradiology  
Director, Head & Neck Imaging  
Department of Radiology  
Department of Otolaryngology  
Boston Children's Hospital  
Harvard Medical School

**Associate Editors****Anna Trofimova, MD, PhD**

Assistant Professor, Radiology and Imaging Sciences, Emory University  
Pediatric Neuroradiologist, Children's Healthcare of Atlanta

**Matthew Whitehead, MD**

Department of Radiology, Division of Neuroradiology  
Children's Hospital of Philadelphia  
Associate Professor of Radiology  
Perelman School of Medicine, University of Pennsylvania

**SPINE IMAGING AND SPINE IMAGE-GUIDED INTERVENTIONS****Senior Editor****J. Levi Chazen, MD**

Associate Professor, Neuroradiology  
Director, Spine Imaging  
Hospital for Special Surgery  
Weill Cornell Medicine  
New York

**Associate Editors****Jennifer McCarty, MD**

UTHealth Houston

**Vinil Shah, MD**

Associate Professor of Radiology Neuroradiology  
Division Chief  
University of California, San Francisco

**ULTRA-HIGH-FIELD MRI/IMAGING OF EPILEPSY/DEMYELINATING DISEASES/INFLAMMATION/INFECTION****Senior Editor****Erik Middlebrooks, MD**

Professor of Radiology  
Mayo Clinic Florida

**Associate Editors****Susie Y. Huang, MD, PhD**

Associate Professor of Radiology, Harvard Medical School  
Associate Chair, Faculty Affairs, Department of Radiology  
Director of Translational Neuro MR Imaging & Connectomics, Athinoula A. Martinos Center for Biomedical Imaging  
Massachusetts General Hospital

**Girish Bathla, MD, FRCR**

Associate Professor, Neuroradiology  
Mayo Clinic  
Minnesota

**OUTREACH AND EDUCATION****Senior Editor****Lea Alhilali, MD**

Radiology Partners, HonorHealth Research Institute  
Arizona

**DIGITAL MEDIA AND ENGAGEMENT****Senior Editor****Kevin Hsu, MD**

Clinical Assistant Professor  
Department of Radiology  
NYU Grossman School of Medicine  
New York

**Case Collection Editors****Matylda Machnowska, BMedSc, MD, FRCSC, ABR**

Assistant Professor of Radiology, University of Toronto  
Neuroradiologist, Sunnybrook Health Sciences Centre

**Anvita Pauranik, MD**

Clinical Assistant Professor of Radiology  
BC Children's Hospital  
University of British Columbia

**Sandy Cheng-Yu Chen, MD**

Chair, Translational Imaging Research Center  
Taipei Medical University Hospital  
Vice President of Taipei Medical University

**Social Media Editor****Kimberly Seifert, MD, MS**

Stanford University  
California

**Assistant Social Media Editors****Ani Hoxha, MD**

Mother Theresa UHC  
Albania

**Maxwell Opoku, MD**

Novosibirsk State Research University  
Russia

#### Podcast Editor

##### **Kevin Hiatt, MD**

Assistant Professor, Radiology  
Wake Forest University School of Medicine  
North Carolina

#### Deputy Podcast Editor

##### **George K. Vilanilam, MD**

PGY5 Resident Physician, Department of Radiology  
University of Arkansas for Medical Sciences

#### STATISTICS

##### Senior Editor

##### **Bryan A. Comstock, MS**

Senior Biostatistician, Department of Biostatistics  
University of Washington

#### EDITORIAL FELLOWS

##### **Alexandre Boutet, MD, PhD**

Neuroradiologist  
Joint Department of Medical Imaging  
University of Toronto

##### **Nicholas S. Cho, MD/PhD Candidate**

University of California, Los Angeles

##### **Burak Berksu Ozkara, MD**

Research Fellow  
Department of Neuroradiology  
The University of Texas MD Anderson Center

#### BOOK REVIEW EDITOR

##### **Robert Quencer, MD**

Professor Emeritus  
Department of Radiology  
University of Miami

---

*Founding Editor*  
**Juan M. Taveras**

*Editors Emeriti*  
Mauricio Castillo, Robert I. Grossman,  
Michael S. Huckman, Robert M. Quencer,  
Jeffrey S. Ross

---

*Managing Editor*  
**Karen Halm**  
*Assistant Managing Editor*  
**Laura Wilhelm**  
*Executive Director, ASNR*  
**Mary Beth Hepp**



# The ASNR Career Center

The Go-To Job Site for Neuroradiology Employers and Job Seekers

## ***For Job Seekers***

- Access to an expanded network of jobs via the National Healthcare Career Network
- Confidential resume posting
- Professional online profile

## ***For Employers***

- Employer resources to help you recruit top talent
- Multiple pricing options, including free Fellowship listings
- Resume search

Start here: [careers.asnr.org](https://careers.asnr.org)

JOIN US!

ASNR24

LAS VEGAS  
MAY 18-22, 2024

CELEBRATING NEURORADIOLOGISTS



Join us at ASNR24 where we plan on **Celebrating Neuroradiologists** and showcasing and celebrating our field's many accomplishments. Both in-person and on-demand registration options are available, allowing you to attend the Annual Meeting the way that works best for you!

Register today at [www.asnr.org/annualmeeting](http://www.asnr.org/annualmeeting)!

---

#### ASNR24 will feature:

- Symposium on *Neuroradiology: The New Frontier*, including sessions on VR/AI, photon counting, psychiatric disease, brain tumor imaging, health policy issues and genetic therapies for neurologic diseases.
- Sessions feature emerging topics, neuroradiology essentials, policy and practice updates, and discussions with international and industry colleagues. Many sessions this year will also feature case presentations, panel discussions, and audience response polling.
- Approximately 200 podium presentations and 500 ePosters and Educational Exhibits on the latest advancements in research, technology, policy and practice innovations for neuroradiology.
- Social and fun community connection experiences, including the Presidential Gala, Happy Hour with Partners and a Pool Party.
- Special sessions and social events for community and specialty groups, including Spine, Head and Neck, Healthcare, Pediatrics, Functional, AI, Interventional, Young Professionals, New Retirees, Fellowship Directors, International Affiliates, and many more.

#### ASNR24 Host Hotel and Conference Location

Caesars Palace  
3570 S Las Vegas Blvd.  
Las Vegas, NV 89109

Play, dine and unwind like royalty at Caesars Palace Las Vegas, the remarkable, palatial center-Strip resort. After a day of learning and networking, enjoy being just steps away from a variety of activities, ranging from world-class shopping and dining to outdoor adventures and shows. For ease and convenience, book in the ASNR hotel room block.



#### Accreditation Statement

The American Society of Neuroradiology is accredited by the Accreditation Council for Continuing Medical Education (ACCME) to provide continuing medical education for physicians and takes responsibility for the content, quality and scientific integrity of this CME activity.

The American Society of Neuroradiology designates this live activity for a maximum of 27.25 AMA PRA Category 1 Credits™. Physicians should claim only the credit commensurate with the extent of their participation in the activity. The American Society of Neuroradiology designates this enduring material for a maximum of 62.25 AMA PRA Category 1 Credits™. Physicians should claim only the credit commensurate with the extent of their participation in the activity.

---

Visit [www.asnr.org/annualmeeting](http://www.asnr.org/annualmeeting) for complete details and to register.

# Striking a Balance: Global Perspectives on Neuroradiology Workload and Quality of Service

Max Wintermark, Kei Yamada, Tchoyoson Lim, Roy Riascos, Carlos Torres, and Tarek Yousry

The recent editorial in the American Journal of Neuroradiology (*AJNR*), titled “Realistic Productivity in Academic Neuroradiology: A National Survey of Neuroradiology Division Chiefs”<sup>1</sup> prompts critical reflection on the correlation among workload, diagnostic errors, and the need for guidelines in academic neuroradiology in the United States. This discussion gains further depth when considering international perspectives, notably the recent position statement by the Japanese College of Radiology (JCR).<sup>2</sup>

The JCR, representing a large proportion of Japan's radiologists, acknowledges the unique challenges faced by its members, including a 4-fold increase in workload. In response, the JCR issued a position statement in 2022 recommending that radiologists' reports be limited to less than 4 cross-sectional studies (encompassing not only neuroradiologic studies but all CT, MR imaging, and PET/CT across all organ systems) per hour of uninterrupted reading time. This recommendation aligns closely with the median of 32 cross-sectional studies proposed by the neuroradiology section chiefs in the United States, and 40 studies proposed in a study of the impact of shift volume on neuroradiology diagnostic errors.<sup>3</sup> These thresholds prioritize patient safety and the quality of radiology services.

The landscape for assessing the neuroradiology workload and quality of service across the globe is very heterogeneous, making comparisons difficult. Significant differences in wealth across Africa, the Americas, Asia, Europe, and Oceania have a critical impact on the distribution of resources and the provision of imaging services. In addition to economic factors, the medical infrastructure and balance between public and private services are very diverse with a wide spectrum of radiology

practices ranging from well-organized neuroradiology services, with established fellowships and strong national society presence, to those lacking formal structures and organizations. In many countries, neuroradiology studies are actually interpreted by general radiologists.

The role of radiologists goes beyond image interpretation to include choosing imaging modalities, managing protocols, and communicating effectively as valuable members of clinical teams along with referring physicians. These activities, though vital for patient safety, are time-consuming and need to be factored into workload considerations.

The juxtaposition of the US survey and the Japanese position statement underscores the need for international guidelines for neuroradiology workload. Establishing a safe number of interpreted cross-sectional studies per time unit is crucial for maintaining the quality of radiology services worldwide. Such guidelines should account for local practices, case complexity, and the broader responsibilities of neuroradiologists.

The dialogue initiated in the *AJNR* in the July 2023 issue represents a hopeful first step toward redefining neuroradiology workload standards. As we navigate the delicate balance between productivity and patient safety, it becomes imperative to develop international guidelines that encompass the diverse practices and challenges faced by neuroradiologists globally. In doing so, we can foster a worldwide commitment to excellence in neuroradiology while ensuring the well-being of both patients and practitioners.

## REFERENCES

1. Wintermark M, Gupta V, Hess C, et al. **Realistic productivity in academic neuroradiology: a national survey of neuroradiology division chiefs.** *AJNR Am J Neuroradiol* 2023;44:759–61 CrossRef Medline
2. Takahashi S, Yamada K. **Setting the bar: the Japanese College of Radiology's perspective on safeguarding quality in the interpretation of cross-sectional studies per day.** *AJNR Am J Neuroradiol* CrossRef
3. Ivanovic V, Broadhead K, Chang YM, et al. **Shift volume directly impacts neuroradiology error rate at a large academic medical center: the case for volume limits.** *AJNR Am J Neuroradiol* CrossRef

# Newly Recognized Genetic Tumor Syndromes of the CNS in the 5th WHO Classification: Imaging Overview with Genetic Updates

 Amit Agarwal,  Girish Bathla,  Neetu Soni,  Amit Desai,  Pranav Ajmera,  Dinesh Rao,  Vivek Gupta, and  Prasanna Vibhute



## ABSTRACT

**SUMMARY:** The nervous system is commonly involved in a wide range of genetic tumor-predisposition syndromes. The classification of genetic tumor syndromes has evolved during the past years; however, it has now become clear that these syndromes can be categorized into a relatively small number of major mechanisms, which form the basis of the new 5th edition of the World Health Organization book (beta online version) on genetic tumor syndromes. For the first time, the World Health Organization has also included a separate chapter on genetic tumor syndromes in the latest edition of all the multisystem tumor series, including the 5th edition of CNS tumors. Our understanding of these syndromes has evolved rapidly since the previous edition (4th edition, 2016) with recognition of 8 new syndromes, including the following: Elongator protein complex–medulloblastoma syndrome, *BRCA1*–associated protein 1 tumor-predisposition syndrome, *DICER1* syndrome, familial paraganglioma syndrome, melanoma-astrocytoma syndrome, Carney complex, Fanconi anemia, and familial retinoblastoma. This review provides a description of these new CNS tumor syndromes with a focus on imaging and genetic characteristics.

**ABBREVIATIONS:** *BAP1* = *BRCA1*–associated protein 1; CNC = Carney complex; *ELP1* = Elongator protein complex; FA = Fanconi anemia; HNPG = head and neck paraganglioma; HNSCC = head and neck squamous cell carcinoma; MAS = melanoma-astrocytoma syndrome; MMNST = malignant melanotic nerve sheath tumor; NF = neurofibromatosis; NGS = next generation sequencing; PG = paraganglioma; PPB = pleuropulmonary blastoma; *SDH* = succinate dehydrogenase; *SHH* = sonic hedgehog; WHO = World Health Organization

The World Health Organization (WHO) series of books (WHO Blue Books) and their Web site (<https://tumourclassification.iarc.who.int>) provide a routinely updated classification of multi-system tumors for standardizing diagnostic practices across the globe. This series is written by a wide group of multidisciplinary authors and editors, including radiologists who are experts in their respective fields, with the aim of providing the most updated nomenclature of tumors. During the past decade, there has been a rapid increase in our understanding of the variation in human genome sequences and identification of molecular information in tumor pathogenesis. This increase has led to better definitions of tumors that are difficult to classify on the basis of histomorphology and immunohistochemistry alone, and it also adds prognostic and therapeutic value. The diagnosis and management of tumors increasingly depend on their genetic causative mechanism, which


ranges from simple sequence variants (mutations) to more profound genetic alterations such as translocations and gene fusions. As a result, the WHO, for the first time in 2022, released a dedicated book on genetic tumor syndromes, which forms the 14th and final volume of the 5th edition series on tumors. Besides the dedicated book, a new or updated chapter on genetic tumor syndromes has been added to the 5th edition of each organ system, including CNS tumors and head and neck tumors.<sup>1</sup>


The nervous system is frequently implicated in a wide range of hereditary tumor-predisposition syndromes with 10 syndromes described in the 4th edition (2016), including neurofibromatosis (NF), Von Hippel-Lindau disease, tuberous sclerosis, and Li-Fraumeni syndrome. Our understanding of these syndromes has evolved rapidly since the previous edition, with recognition of 8 new syndromes including the following: Elongator protein complex (*ELP1*)–medulloblastoma syndrome, *BRCA1*–associated protein 1 (*BAP1*) tumor-predisposition syndrome, *DICER1* syndrome, familial paraganglioma syndrome, melanoma-astrocytoma syndrome (MAS), Carney complex (CNC), Fanconi anemia (FA), and familial retinoblastoma (Online Supplemental Data). The previous (4th) edition syndromes are preserved in the new (5th) edition except for Turcot syndrome, which has been removed, and its 2 subtypes (constitutional mismatch repair deficiency syndrome and familial adenomatous polyposis 1) are now

Received July 11, 2023; accepted after revision September 14.

From the Departments of Radiology (A.A., G.B., N.S., P.A.), and Neuroradiology (A.D., D.R., V.G., P.V.), Mayo Clinic, Jacksonville, Florida.

Please address correspondence to Amit Agarwal, MD, Department of Radiology, 4500 San Pablo Rd, Mayo Clinic, Jacksonville, FL 32224; e-mail: [agarwal.amit@mayo.edu](mailto:agarwal.amit@mayo.edu); @amitagarwalmd

 Indicates open access to non-subscribers at [www.ajnr.org](http://www.ajnr.org)

 Indicates article with online supplemental data.

<http://dx.doi.org/10.3174/ajnr.A8039>

**Newly recognized CNS genetic tumor syndromes in the 5th WHO classification with updates on genetic pathway**

WHO Classification, 4th Edition 2016	WHO Classification, 5th Edition 2022		
Familial Tumor Syndromes (Chapter 16)	Genetic Tumor Syndromes Involving the CNS (Chapter 14)		
	New Syndromes	Genetic Pathway	Most Common Nervous System Tumors
NF type 1	<i>ELP1</i> -medulloblastoma	Growth factor receptor	Medulloblastoma
NF type 2	<i>BAP1</i> tumor predisposition	Ubiquitin protein	Meningioma
Schwannomatosis	<i>DICER1</i> syndrome	microRNA regulation	Metastasis (from pulmonary blastoma)
Von Hippel-Lindau syndrome	CNC	<i>PKA</i> signaling pathway	Malignant melanotic Nerve sheath tumor
Tuberous sclerosis	Melanoma-astrocytoma	Cell cycle and apoptosis	Glioma
Li-Fraumeni syndrome	Familial paraganglioma	Oxidative stress (Krebs)	Paraganglioma
Cowden syndrome	FA	DNA repair and genomic stability	Medulloblastoma
Turcot syndrome	Familial retinoblastoma	Cell cycle and apoptosis	Retinoblastoma
Constitutional mismatch repair deficiency syndrome	All entities from 4th edition kept in the new edition, except Turcot syndrome Constitutional mismatch repair deficiency (previously subtype under Turcot syndrome) Familial adenomatous polyposis 1 (previously subtype under Turcot syndrome)		
Familial adenomatous polyposis 1			
Nevoid basal cell carcinoma syndrome			
Rhabdoid tumor syndrome			

identified as distinct entities. This change highlights the gradual shift from arbitrary and eponymic naming of the syndromes to a more gene-based system. Thus, a total of 19 CNS genetic tumor syndromes are now identified (Table), with the understanding that this is an evolving field and many changes may occur in the future.

There is more emphasis on the genetic pathogenesis of the previous and new entities in the 5th edition. Many of these syndromes are also described in other organ system books, with, however, greater emphasis on the nervous system in the book on CNS tumors.<sup>1,2</sup> Also, many of the tumors can be seen in different tumor syndromes; for example, melanocytic nerve sheath tumors can be seen in MAS and CNC. Some of the newly recognized syndromes are well-known entities, (eg, FA); however, their involvement in CNS tumor predisposition has been better defined lately, necessitating inclusion in the chapter on CNS genetic tumor syndromes. Conventionally, the diagnosis of these syndromes relied on clinical features and family history; however, with the recent advancement in molecular genetics, the pathologist or geneticist might be the first to identify the syndrome. Radiologists are a vital part of the multidisciplinary team for these complex tumor syndromes and should be abreast of the changes in nomenclature. For example, it is important for the radiologist to know that most *ELP1*-related medulloblastomas are desmoplastic/nodular subtype and occur along the lateral cerebellar convexity with a low chance of recurrence postsurgery.<sup>3</sup> These disorders are often highly complex, and patients are typically best served in specialized centers with broad multidisciplinary expertise.

In this article, we discuss the pathologic and imaging findings of the new tumor syndromes and highlight the inheritance pattern, because screening imaging examinations are increasingly being performed on the family members of these patients. Because genetic tumor syndromes are rare overall, the role of imaging-based artificial intelligence models in their prediction is still uncertain. However, some early studies have shown that there may be some benefit to the incorporation of radiomic data. Noortman et al,<sup>4</sup> showed that PET-based radiomics moderately improved the distinction of cluster 1 and 2 paragangliomas

(PGs) and from sporadic paragangliomas. Similarly, a recent meta-analysis noted that radiomics-based models showed robust performance in predicting medulloblastoma subgroups.<sup>5</sup> Machine learning-based studies have previously shown promise in the identification of underlying genetic alterations in other tumors such as glioblastomas.<sup>6</sup> The role of artificial intelligence-based studies in differentiating syndromic-versus-nonsyndromic tumors should be further explored in larger pooled cohorts.<sup>4,5</sup>

### Genetics and Signaling Pathway

Alteration in the sequence of the human genome is the basis of heritable (constitutional) disorders further triggered by environmental factors. During the past few years, it has become clear that most genetic tumor syndromes are caused by a specific signaling pathway triggered by the genetic mutations and epigenetic factors. Figure 1 highlights the chromosomal distribution of genes involved in the old and new CNS genetic tumor syndromes, except for the succinate dehydrogenase (*SDH*) gene implicated in familial paraganglioma, which is located along the inner membrane of the mitochondria. The Table highlights the protein-signaling pathway for the new genetic syndromes. The growth factor receptor and the related signaling pathway are the major categories with the highest number of CNS and non-CNS tumor entities. These include NF, *ELP1*-related medulloblastoma syndrome, and nevoid basal cell carcinoma syndrome, among others. Some categories like the ubiquitin protein pathway have only the single entity of *BAP1*-related tumor predisposition syndrome. These changes in the signaling pathway and the altered protein product form the basis of molecularly targeted therapies and immunotherapy, an example being targeting the sonic hedgehog (*SHH*) signaling pathway through *SHH* inhibitors in medulloblastomas.<sup>7</sup>

The molecular and genetic information has facilitated the concept of “integrated diagnosis” to summarize all the information of a given tumor. This is a layered/tiered approach to the pathology report with a 4-line format, including integrated diagnosis, histologic diagnosis, WHO grade, and molecular information.

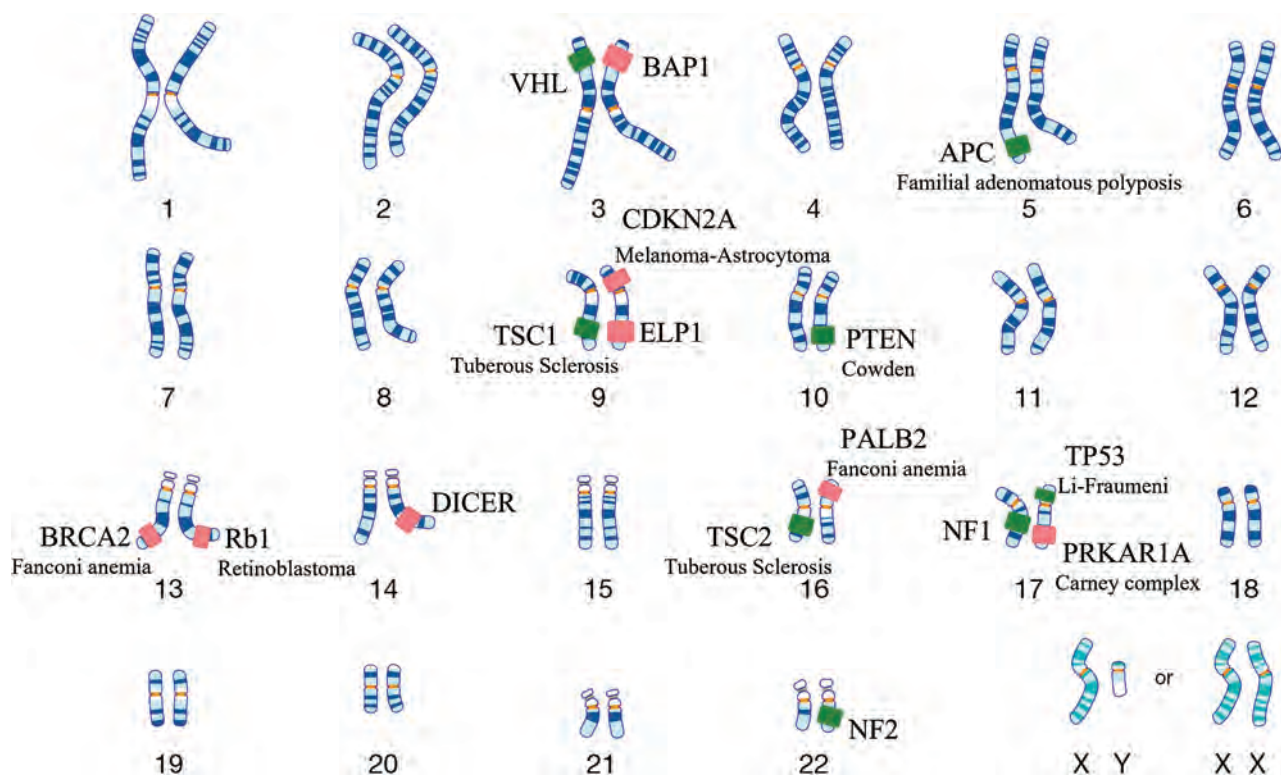


**FIG 1.** This diagram highlights the chromosomal distribution of genes involved in the old (green boxes) and newly recognized (red boxes) CNS genetic tumor syndromes, with representation of 7 of the 8 new entities. The *SDH* gene implicated in familial paraganglioma is located along the inner membrane of mitochondria and is not depicted here. *VHL* indicates Von Hippel-Lindau syndrome.

For example, the integrated diagnosis for an *ELP1*-related medulloblastoma (Fig 2) would be reported as following: medulloblastoma desmoplastic/nodular morphology (histologic), WHO grade 4 (grade), with *SHH* activation (*TP53* wild-type) and *ELP1* germline mutation (molecular and genetic information). Molecular testing is a key component to the integrated diagnosis and overall characterization of many tumors, with a variety of techniques that can be used in a step-wise approach, including immunohistochemistry, fluorescence in situ hybridization, polymerase chain reaction, and next generation sequencing (NGS). Immunohistochemistry is a robust and economical test (<24 hours to complete) that is an excellent first-line method for determining the molecular subgroups. These are very efficient tests that detect the mutant protein (*IDH*, *BRAF*, *H3*) and serve as surrogate markers for genes encoding those proteins.

Given all the genetic information now available, the WHO decided to rename the chapter from “Familial Tumor Syndrome” (4th edition) to “Genetic Tumor Predisposition Syndromes” (5th edition), stressing that many individuals might have the mutation and have a predisposition but may not develop these tumors. Many syndromes resulting in a predisposition to leukemia or lymphoma have been covered under “Hematolymphoid Neoplasia Genetic Predisposition Syndromes” and are not discussed in the chapter on CNS genetic tumor syndromes.<sup>2</sup>

#### Newly Recognized Genetic Tumor Syndromes

***ELP1*-Medulloblastoma Syndrome.** Medulloblastoma is the second most frequent malignant CNS tumor in children, and apart

from sporadic occurrence, it can be associated with multiple cancer-predisposition syndromes like Turcot, Li-Fraumeni, and Gorlin syndromes. A mutation in a cancer-predisposition gene is estimated to be present in >40% of *SHH*-activated medulloblastomas, most commonly (14%) caused by biallelic alterations of *ELP1*.<sup>8</sup> *ELP1*-medulloblastoma syndrome is an autosomal dominant disorder caused by pathogenic germline variants in the *ELP1* gene (9q31.3). This is a tumor-suppressor gene that encodes for the protein *ELP1*, which is a part of the 6-subunit Elongator protein complex. This plays a key role in transcription of proteins that affect the structural framework (cytoskeleton) of the cell for a variety of cells including neurogenesis. This is a newly recognized genetic tumor syndrome in the WHO 5th edition of CNS tumors and is characterized by an increased risk of *SHH*-activated *TP53* wild-type (grade 4) medulloblastomas during childhood. The median age at diagnosis is 6 years (range, 2–19 years), often with a family history positive for medulloblastomas.<sup>1,8</sup> On histopathology, the desmoplastic/nodular pattern is most common (76%), followed by classic (18%) and large-cell/anaplastic (6%) morphology (Online Supplemental Data).<sup>3,8</sup> The imaging features of the *SHH* subgroup are similar to those of the sporadic tumors and depend on the histologic subtype with the desmoplastic/nodular lesions located along the lateral cerebellar convexities and the less common, classic, or large-cell/anaplastic, variants located along the midline (Fig 2 and the Online Supplemental Data).

All the histologic subtypes are well-circumscribed and hyperintense on T2-weighted images. The enhancement is usually solid and intense, except the classic variant in which it can range from minimal and patchy to marked.<sup>9</sup> *ELP1*

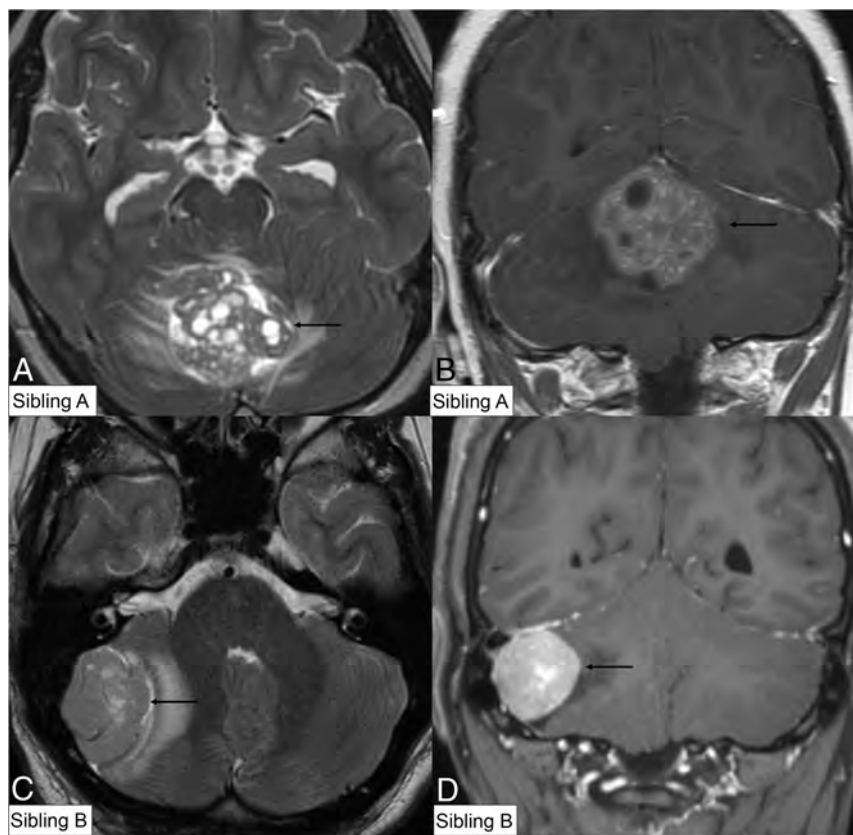


**FIG 2.** *ELPI*-related medulloblastomas in siblings. A 6-year-old boy (sibling A) with MR imaging revealing a heterogeneously T2 hyperintense (A, axial T2 TSE) mass with cystic changes and heterogeneous enhancement (B, coronal postcontrast). Histopathology with immunohistochemistry revealed a large-cell anaplastic-pattern WHO grade 4, *SHH*-activated (*TP53* wild-type) medulloblastoma. The patient's older brother, an 18-year-old boy (sibling B), was diagnosed with a similar tumor 7 years later. MR imaging revealed a right lateral cerebellar T2 hyperintense mass (C, axial T2 TSE) with solid contrast enhancement (D, coronal postcontrast). Pathology revealed an *SHH*-activated (*TP53* wild-type) medulloblastoma with desmoplastic/nodular morphology. A neuro-oncology genetic panel (utilizing NGS technique) in both siblings showed biallelic inactivation of *ELPI* due to somatic loss of chromosome arm 9q along with homozygous deletion of the tumor-suppressor gene *PTCH1*, confirming an *ELPI* germline mutation. Both siblings remain disease-free (9 years postsurgery for sibling A, and 1 year for sibling B) (Online Supplemental Data).

immunohistochemistry is a highly specific biomarker for identifying these medulloblastomas and is increasingly becoming a part of the neuropathologist's panel to screen for tumor predisposition syndromes in children with medulloblastomas. Medulloblastomas have the potential for leptomeningeal spread, locally, or along the spinal axis and rarely extend outside the CNS. Leptomeningeal spread is usually along the cerebellar or cord surface, attached to the pia mater. Early studies indicate a favorable prognosis for *ELPI*-medulloblastomas with the 5-year overall survival rate of around 92%. Surveillance protocols have been established for many known syndromes like Gorlin syndromes and include annual MR imaging until 8 years of age; however, no formal protocol has yet been proposed for *ELPI*-medulloblastomas.<sup>8,10</sup>

#### ***BAP1* Tumor-Predisposition Syndrome**

*BAP1* tumor-predisposition syndrome is an autosomal dominant disorder caused by pathogenic germline variants in the *BAP1*

tumor-suppressor gene (3p21.1). This syndrome is characterized by a predisposition to tumors of multiple organ systems including the eye, pleura, peritoneum, kidneys, liver, and meninges. Uveal melanoma and mesothelioma are the most common tumors in this syndrome, seen in around 36% and 25% of patients, respectively.<sup>11</sup> Other tumors in descending order of frequency include cutaneous melanoma, renal cell carcinoma, and basal cell carcinoma (Online Supplemental Data). Meningioma is the most common CNS tumor of this syndrome, seen in around 9% of patients (Fig 3).<sup>12</sup> While most meningiomas are sporadic, many tumor-predisposition syndromes are increasingly being identified, including well-known conditions like NF-2 (or secondary to newly described entities like *SMARCB1*, *SMARCE1* mutation, and *BAP1* syndrome).<sup>13</sup> Recent studies have shown that the patterns of mutations in many meningiomas are strongly associated with a distinct location and histologic subtypes; for example, anterior skull base meningiomas often have mutations in *SMO*, whereas posterior fossa and convexity meningiomas often have mutations in *NF2*.

Meningiomas with rhabdoid features represent a highly aggressive grade 3 malignancy with high rates of recurrence and mortality. Initial studies have shown that rhabdoid meningiomas often have *BAP1* mutations, are clinically aggressive, and are more likely to recur, compared with *BAP1*-

retained similar grade meningiomas.<sup>12,14</sup> Recent advancements in the molecular-genetic taxonomy of meningiomas help in the identification of patients with inherited forms of meningiomas, with assessment of mutations, like *SMARCB1* and *BAP1*, increasingly being performed at specialized centers, especially in cases of multiple meningiomas or younger age of onset. The *BAP1* mutation can be easily assessed using simple and inexpensive immunohistochemical testing for *BAP1* protein expression (Online Supplemental Data).<sup>1,13</sup> Patients with *BAP1* tumor-predisposition syndrome present with a younger age of onset compared with the sporadic counterpart for the same tumor type, with frequent occurrence of multiple cancers. For example, mesotheliomas with loss of *BAP1* occur around 20 years earlier and are frequently peritoneal, rather than pleural, with a substantially different clinical course. The lifetime risk of developing cancer in this syndrome is as high as 80%–100%, with many patients developing multiple tumors.<sup>11,15</sup> Most families with this germline mutation have at least 2 types of tumors in first- or second-degree relatives.

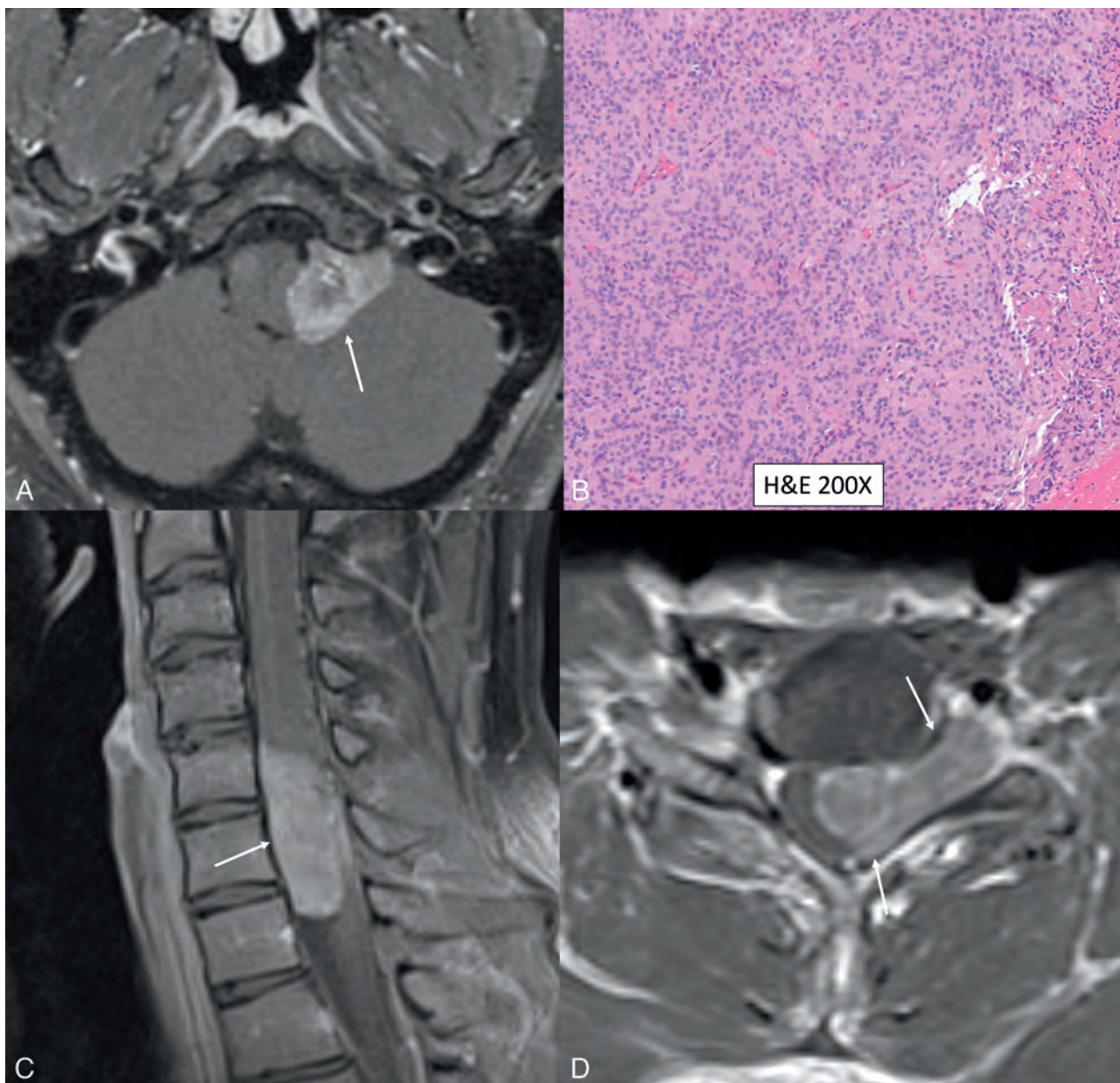


**FIG 3.** Rhabdoid intracranial and spinal meningiomas with loss of *BAP1* expression. Left lateral cerebellomedullary cistern enhancing mass (A, axial postcontrast T1, *white arrow*) in a 36-year-old man, extending into the hypoglossal canal, revealing atypical meningioma (CNS WHO grade 2) on histology, with rhabdoid features (B) and loss of *BAP1* expression on immunohistochemistry (Online Supplemental Data). Coronal (C) and axial (D) contrast-enhanced MR images in a different patient depict an extramedullary cervical mass extending along the left neural foramen (*arrows*). Histopathology (not shown) revealed rhabdoid meningioma with loss of *BAP1* expression.

Genetic counseling should be offered to patients with a history of  $\geq 2$  *BAP1*-related tumors or 1 tumor and a family history of similar tumors. Promising therapeutic avenues are being explored to specifically target *BAP1*-deficient tumor cells that are highly sensitive to novel therapies like inhibitors of enhancer of zeste homolog 2 (*EZH2*).<sup>16</sup>

#### **DICER1 Syndrome**

*DICER1* syndrome is an autosomal dominant tumor predisposition syndrome caused by heterozygous germline loss-of-function mutation in the *DICER1* gene (14q32.13), modifying the protein-coding genes by modulating microRNAs. This feature confers a

lifetime risk of a variety of neoplastic and dysplastic lesions, classically associated with pleuropulmonary blastoma (PPB), a rare malignant tumor of the lung, seen primarily in children younger than of 6 years of age.<sup>1,17</sup> Type I PPB is a purely cystic mass, occurring before 2 years of age. Type II is a solid-cystic tumor, while type III is purely solid; both types present from approximately 2 to 6 years of age and are malignant. Type III (solid) is the most aggressive with the highest mortality (up to 60%). Finally, “type I regressed” (Ir) is a cystic tumor lacking malignant cells and represents regressed type I PPB with no potential for malignancy.<sup>18</sup> *DICER1* syndrome occurs in children and young adults, with the most frequent phenotypes including PPB,

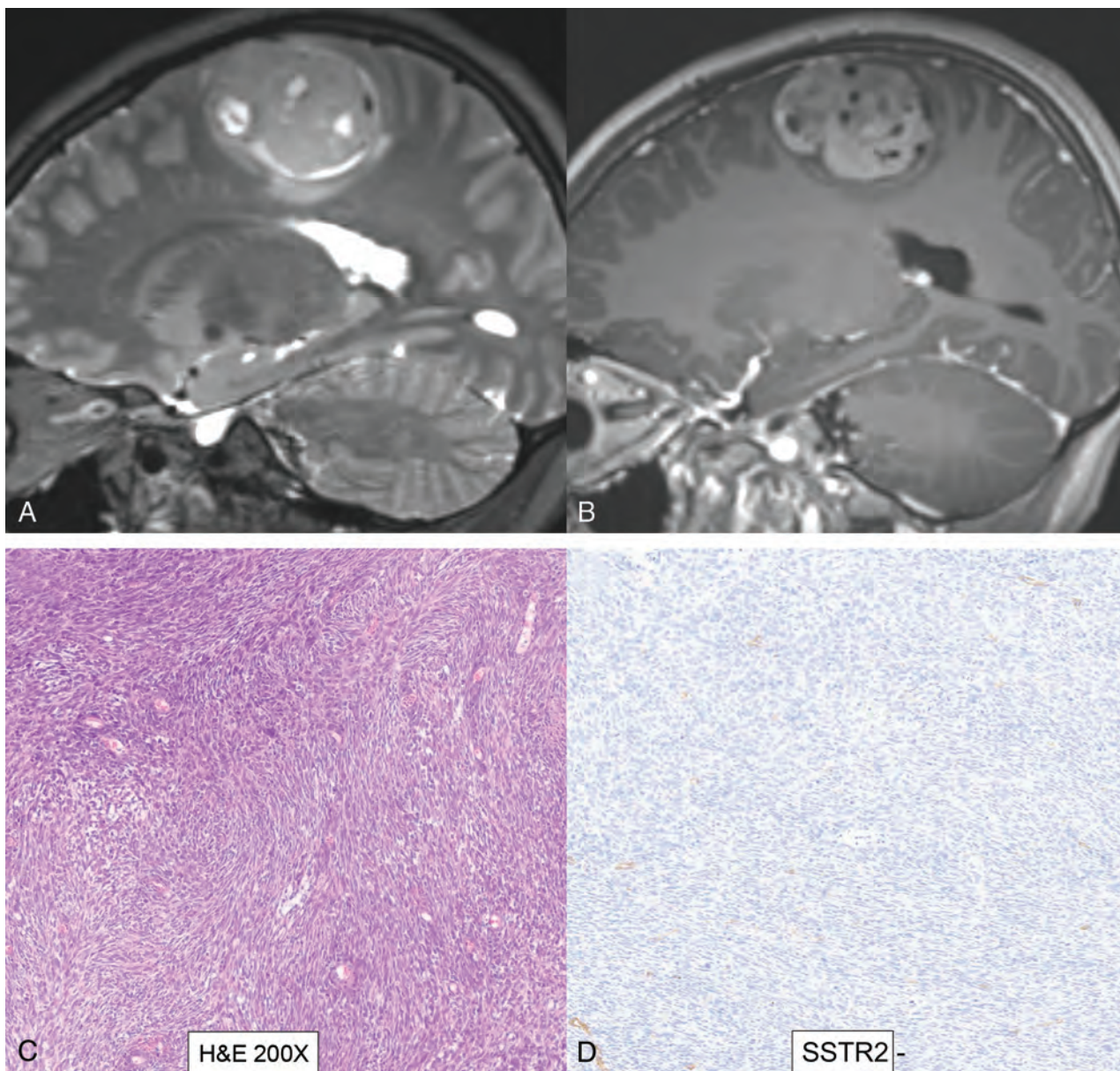


**FIG 4.** *DICER1*-mutant intracranial sarcoma. Sagittal T2 (A) and postcontrast (B) MR images in a 16-year-old adolescent girl reveal a dural-based left parasagittal T2-hyperintense enhancing mass, presumed to be a meningioma on imaging. Histopathology, however, revealed spindle and pleomorphic cells (C), and immunohistochemistry tests were negative for *GFAP*, *OLIG2*, *SSTR2* (D), *STAT6*, S-100, and *SOX10*, arguing against glial, meningothelial, or melanocytic tumors. A Somatic Disease/Germline Comparator Exome sequencing panel revealed a pathogenic germline *DICER1* mutation. Overall, the histomorphologic and immunophenotypic findings supported a sarcomatoid neoplasm. The additional presence of pathogenic *DICER1* mutations was diagnostic of primary intracranial sarcoma, *DICER1*-mutant. Because the prognosis for patients with *DICER1*-mutant primary intracranial sarcoma remains unknown due to limited clinical data, a CNS WHO grade designation was not rendered, according to the 2021 WHO Classification of Tumors of the Central Nervous System.

multinodular goiter, cystic nephroma, and Sertoli-Leydig ovarian neoplasms (Online Supplemental Data).<sup>17</sup>

The most common CNS manifestation of *DICER1* syndrome is brain parenchymal metastasis (from PPB) with the CNS being the most common site of distal metastasis. Surveillance MR imaging of the brain is recommended for up to 3 years after the diagnosis of aggressive forms of PPB (types II solid-cystic and III solid), because most of the brain metastases occur within 2 years of diagnosis. A few cases of spinal cord and leptomeningeal metastasis have also been reported.<sup>1,19</sup> The primary CNS tumor

manifestations of this syndrome include pineoblastoma, pituitary blastoma, embryonal tumor with multilayered rosettes, and *DICER1*-mutant primary intracranial sarcoma (Fig 4), which are indistinguishable on imaging and pathology from their sporadic counterparts. Although PPBs are the most common tumors in *DICER1* syndrome, pituitary blastoma is most pathognomonic of this syndrome, with all reported cases to date arising in the setting of this syndrome.<sup>20</sup>

Pineoblastoma is a rare primitive neuroectodermal grade 4 tumor, classically seen with *RB1* in familial retinoblastoma, that

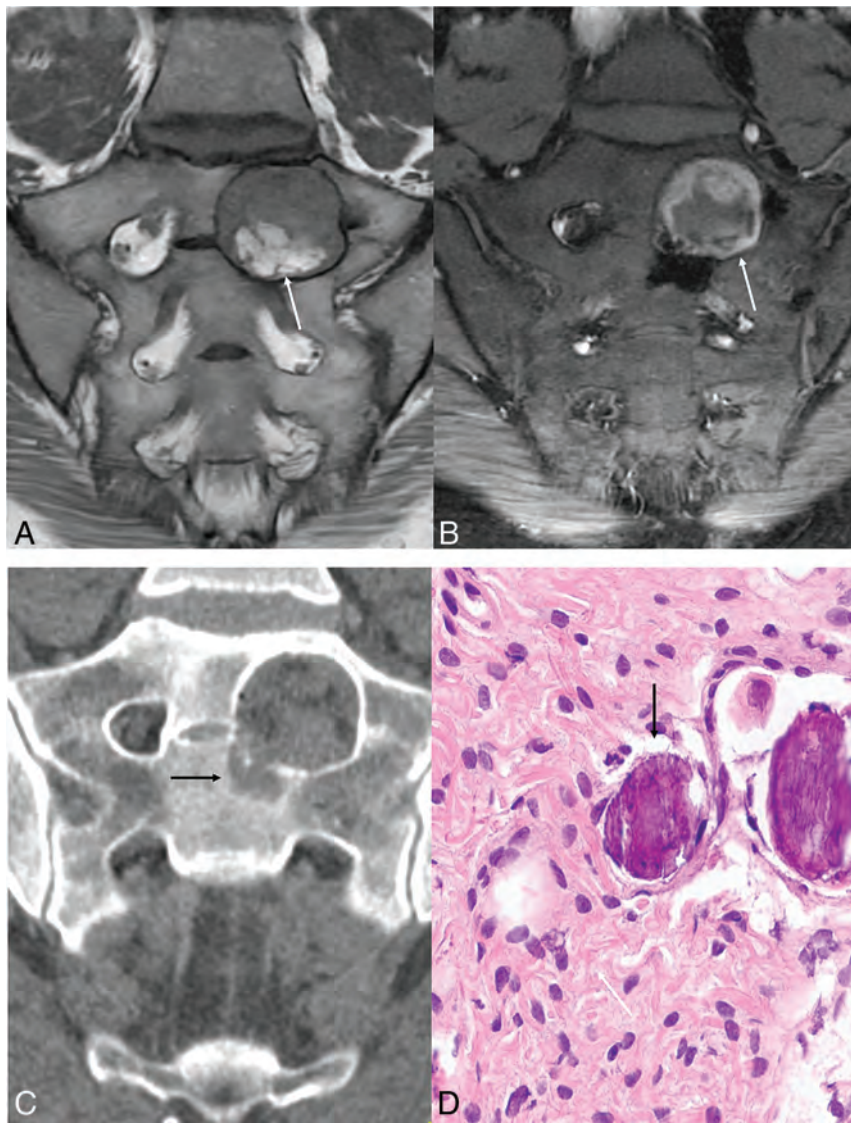


**FIG 5.** MMNST in a 26-year-old woman with CNC. Coronal MR images (A and B) reveal a mass along the left S1–S2 neural foramen with intrinsic T1-hyperintense content (A, T1-weighted, non-fat-saturated, arrow) with peripheral enhancement and a central nonenhancing component (B, postcontrast with fat saturation, arrow). Note marked expansion of the neural foramen and erosive osseous changes along the inferior edge on coronal CT (C, arrow). Histopathology reveals a spindle cell (D, white arrow) neoplasm with psammomatous bodies (D, black arrow). Immunohistochemistry was positive for *SOX10*, *S-100*, and *MelanA*, confirming the diagnosis of MMNST. Neoplastic cells showed complete loss of *PRKARIA*, confirming an association with CNC (Online Supplemental Data).

has also been associated with the *DICER1* mutation. Head and neck manifestations of this syndrome include nasal chondromesenchymal hamartoma, multinodular goiter, ciliary body medulloepithelioma, thyroblastomas, and thyroid carcinomas.<sup>1,2</sup> Multinodular goiter occurring in patients younger than 18 years of age should prompt *DICER1* testing, even in the absence of a family history or other syndromic tumors. Despite a higher risk of malignancy, most patients with the pathogenic germline *DICER1* variants live healthy lives with tumors seen in <20% patients by the age of 50 years.<sup>17</sup> Surveillance guidelines for these individuals include periodic chest radiographs and thyroid and pelvic sonography.<sup>21</sup>

## CNC

CNC is a rare autosomal dominant syndrome with almost 100% penetrance, caused, in most cases (>70%), by heterogeneous inactivating pathogenic variants in the *PRKARIA* gene (17q22-24). This regulates the cell signaling of the body, with protein kinase A (PKA) and subsequent loss of the tumor-suppressor function, resulting in overactivation of the cyclic adenosine monophosphate-protein kinase A (*cAMP*-PKA) pathway causing tumorigenesis.<sup>22</sup> CNC was initially described in 1985, with myxomas, spotty pigmentation, and endocrine overactivity being the dominant features and should not be confused with the Carney triad. Myxomas may involve the heart (22%–53%), skin and mucosa (10%–30%), or bilateral breasts (25% of women with CNC). Nodular vertebral lesions on MR imaging may be seen in up to 32% of patients.<sup>23</sup> These lesions are often multiple and can affect any part of the vertebral body. They show T1/T2 prolongation with postcontrast enhancement. Vertebral lesions are invariably nonaggressive on imaging and are presumed to represent osteochondromyxomas.<sup>23,24</sup>

The main nervous system manifestation is malignant melanotic nerve sheath tumor (MMNST), seen in 8%–10% of adults with the syndrome, often along the paraspinal sympathetic chain and the gastrointestinal tract, less commonly intracranial and dermal. Historically considered benign, these were reclassified as malignant tumors in the 2020 WHO Classification of Tumors as well as in the 2021 WHO Classification Tumors of the Central Nervous System. Psammomatous MMNST (which contains psammoma bodies) accounts for about one-half of all

MMNSTs, and approximately 50% of these are associated with CNC. A recent series noted a median age of 34.5 years (range, 25–54 years) at presentation.<sup>22,25</sup> Lesions may show calcifications on CT and demonstrate T1/T2 shortening on MR imaging due to the presence of melanin (Fig 5 and Online Supplemental Data).<sup>26</sup> CNC is also characterized by endocrinal neoplasms, most frequently being primary pigmented nodular adrenocortical disease, resulting in Cushing syndrome, seen in 26%–58% of patients with CNC. Somatotroph pituitary neuroendocrine tumor (adenoma) may occur in 10%–18% of adults. These tumors often secrete growth hormone and are generally diagnosed early, often at a microadenoma stage.<sup>22–25</sup>

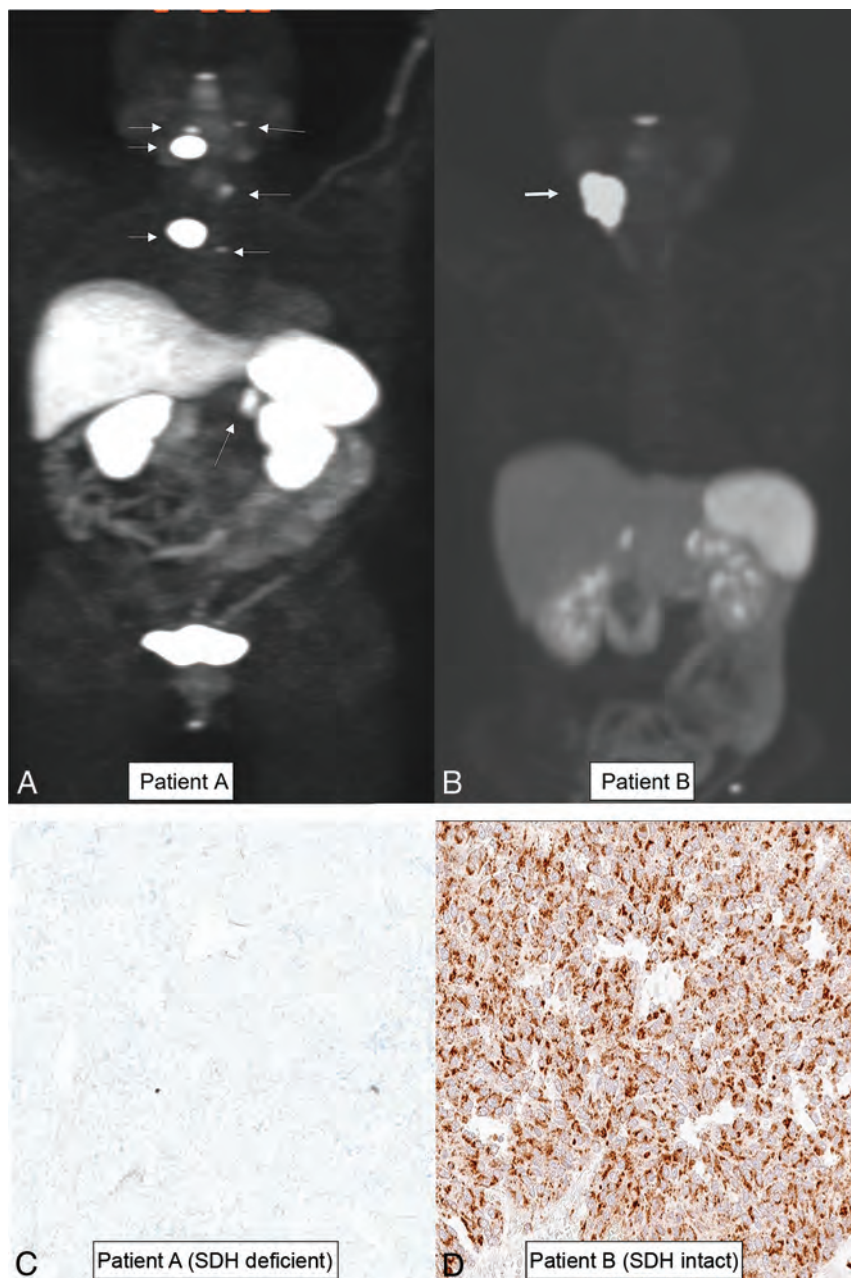


**FIG 6.** HNPGBs in 2 different patients, one with *SDH* mutation (patient A) and the other with normal *SDH* expression (patient B). Patient A has familial paraganglioma syndrome with multiple HNPGBs and a left adrenal pheochromocytoma (A, arrowheads) on a  $^{68}\text{Ga}$ -DOTATATE PET scan, with complete loss of *SDH* expression on immunohistochemistry (C). A solitary HNPGB along the right carotid artery is noted on a  $^{68}\text{Ga}$ -DOTATATE PET scan in patient B (B, arrow) with normal *SDH* expression on pathology (D).

## MAS

MAS is a rare autosomal dominant tumor-predisposition syndrome caused by a germline mutation of the *CDKN2A* tumor-suppressor gene (9p21.3), which codes for cell-cycle regulators and the apoptosis pathway (*P16INK4A* and *P14ARF*). MAS is characterized by an increased risk of multiple tumors, including cutaneous melanoma, astrocytoma, nerve sheath tumors, pancreatic cancer, and squamous cell carcinoma of the oropharynx.<sup>27</sup> In 1993, Kaufman et al<sup>28</sup> identified familial MAS in a 3-generation family with members having melanomas or astrocytomas.

Subsequent studies have found more families with similar syndromes, linking an increased risk of dysplastic nevi, cutaneous melanoma, and nervous system tumors, especially astrocytomas. MAS is considered a glioma-predisposition syndrome with diverse histologic and genetic features. Dysplastic nevi and melanomas associated with MAS are predominantly cutaneous, rather than mucosal, acral, or uveal. Astrocytomas associated with MAS include pleomorphic xanthoastrocytoma (Online Supplemental Data) and diffuse astrocytic gliomas, ranging from low-grade diffuse astrocytomas to high-grade (glioblastoma), which are typically located in the cerebral hemispheres or cerebellum.<sup>27</sup> Patients can present with numerous glial neoplasms, with reported cases of simultaneous development of pleomorphic xanthoastrocytoma, diffuse astrocytoma, and paraspinal nerve sheath tumors.<sup>29</sup> These tumors cannot be differentiated from their sporadic counterparts on the basis of histopathology, and detection of the *CDKN2A* mutation is required for diagnosis of the syndrome. Some cases with large deletions involving *CDKN2A* and *CKDN2B* have shown manifestations like neurofibromas, giant cell tumors of bone, and multiple primary cancers resembling NF1 or Li-Fraumeni syndrome. Clinical outcomes and standardized surveillance protocols for MAS-associated tumors are still being investigated. Regular dermatologic examinations, brain imaging, and genetic counseling are usually recommended for monitoring various cancers and guiding patients and their families.<sup>27-30</sup>

## Familial Paraganglioma Syndrome

Familial paraganglioma syndrome represents a group of inherited cancer syndromes characterized by the development

of PGs and pheochromocytomas. These are highly vascular neuroendocrine tumors arising from the extra-adrenal neural crest tissue or the adrenal medulla, respectively. Head and neck PGs (HNPGBs) develop within the parasympathetic chain, most commonly along the ninth and tenth cranial nerves (jugular foramen, carotid body), followed by the middle ear cavity. Nearly 95% of these are nonsecretory, contrary to secretory PGs, which mainly involve the adrenal medulla (pheochromocytomas). About 30%–40% of PGs in adults are hereditary, characterized

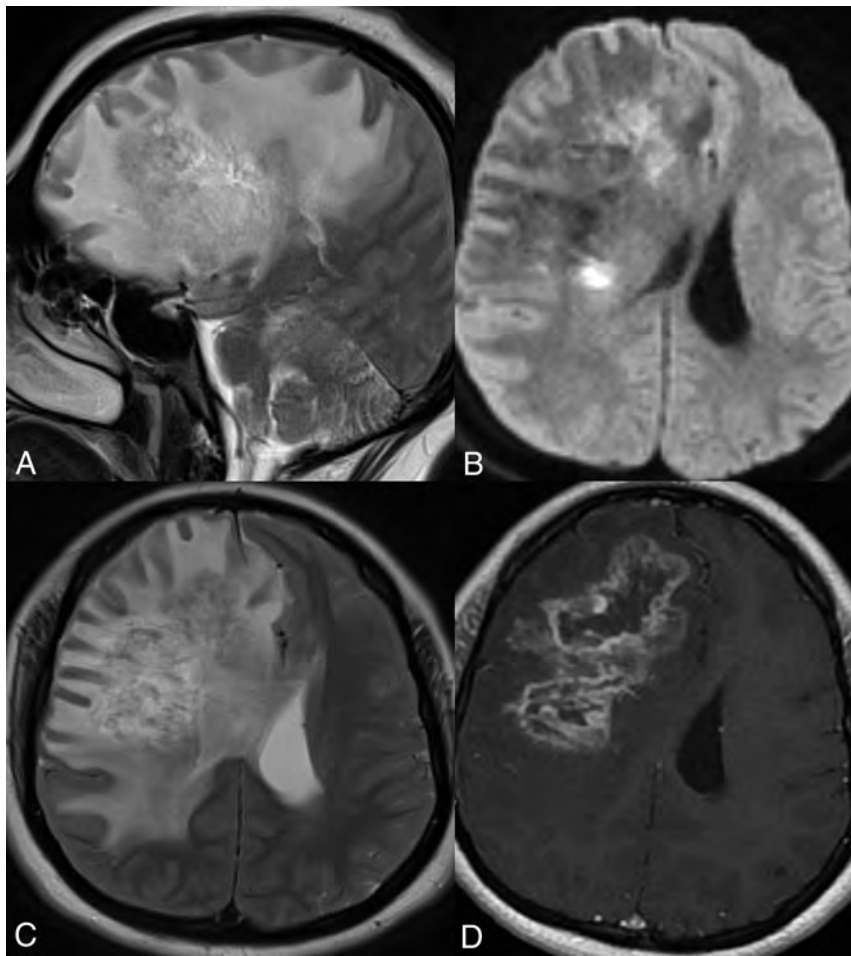


**FIG 7.** Cerebroretinal vasculopathy and leukoencephalopathy in a 20-year-old man with FA. MR imaging including a sagittal T2-weighted image (A), axial diffusion (B), T2 TSE (C), and postcontrast (D) images reveal a large area of white matter edema with heterogeneous enhancement and central necrosis in the right frontal lobe. The primary radiographic differential included a high-grade glial neoplasm, and a biopsy was performed. Histopathology revealed severe vasculopathy exhibiting vascular hyaline changes and perivascular and transmural chronic inflammation. The background white matter demonstrated extensive vacuolization and gliosis with necrosis surrounding the vessels. No evidence of JC virus or Epstein-Barr virus was identified by in situ hybridization, and no fungal organisms were detected. Follow-up MR imaging (Online Supplemental Data) after 6 months of immunosuppressive treatment showed marked reduction in the right frontal edema and enhancement, however, with new areas of edema and enhancement in the left parieto-occipital lobe. Advanced veno-occlusive retinopathy with neovascularization was noted on funduscopy (Online Supplemental Data).

by a younger age at presentation and a higher risk of multiplicity and metastatic spread, along with a higher incidence of extra-adrenal tumors.<sup>31</sup> Apart from the genetic mutations in Von Hippel-Lindau disease, multiple endocrine neoplasia type 2, and NF-1, nearly 10 separate genes have been implicated in this syndrome. Of these, the mitochondrial succinate dehydrogenase (SDH) complex subunit genes (*SDH A-D*) and 1 complex cofactor, *SDHAF2*, are collectively responsible for nearly one-half of all germline mutations. Inactivating mutations in any of the *SDH* genes result in the accumulation of succinate and the formation of reactive oxygen species (pseudohypoxia cluster). HNPGs are largely either sporadic or associated with germline *SDH* variants. Of these, carriers of *SDHD/SDHAF2* mutations have the highest risk of multifocal HNPGs.<sup>32,33</sup>

Overall, contrast-enhanced MR imaging has a sensitivity and specificity of nearly 95% and 99%, respectively, but CT has a better sensitivity to identify tumors of <1 cm and those in the jugulotympanic region.<sup>34</sup> MR imaging perfusion may help differentiate HNPGs from non-PG tumors such as schwannomas, with the former showing markedly higher vascularity and perfusion. *SDH*-intact (no mutation) tumors show higher mean and normalized ADC values (normalized mean ADC, 1.73 versus 1.31;  $P < .001$ ) compared with *SDH*-mutated tumors.<sup>35</sup> Gallium 68DOTATATE PET demonstrates high lesion detectability for *SDH*-mutated PGs and is generally considered first-line imaging for HNPGs, especially when suspecting metastatic or multifocal disease (Fig 6) or identifying peptide-receptor therapy candidates. This has emerged as the new standard of care for functional imaging of neuroendocrine tumors. It is highly sensitive for the detection of both solitary and metastatic PGs, substantially more so than <sup>123</sup>I metaiodobenzylguanidine scintigraphy, CT, or MR imaging, particularly for demonstrating metastatic bone disease.<sup>34,36</sup>

## FA

FA is a clinically heterogeneous multi-system disorder with an incidence of around 1 per 100,000 live births and is more common in Ashkenazi Jews, Afrikaners, and Spanish gypsies. The underlying etiology is the inability of the affected cells to repair DNA inter-strand crosslinks.<sup>37</sup> At least 22 genes have been implicated (*FANCA-FANCW*) with most inherited in an autosomal recessive pattern and a smaller minority being X-linked recessive (2%) or autosomal dominant (*RAD51*).<sup>38</sup> This syndrome is characterized by developmental abnormalities in the major organs, inherited bone marrow failure characterized by pancytopenia, and a high predisposition to cancer.<sup>1,37</sup> The median age at diagnosis is about 7 years, though earlier diagnosis is becoming common with higher disease awareness and prenatal screening. The most common neoplasms associated with this syndrome are myeloproliferative conditions, including myeloid leukemia, squamous cell carcinoma of the head and neck (HNSCC), Wilms tumor, and medulloblastoma. Leukemia, specifically acute myeloid leukemia, is the most common cancer in patients with FA. Overall, HNSCC is the most common solid tumor in patients

with FA, with the incidence being 500–700 times higher than in the general population. Patients with FA generally develop HNSCC at a younger age (20–50 years), usually with a more aggressive clinical course and advanced disease at presentation. HNSCC is the leading cause of death in patients with FA in adulthood. Thus, surveillance for HNSCC in FA is recommended starting at a young age and continuing through life.<sup>39</sup>

Medulloblastoma is the characteristic CNS tumor in FA secondary to biallelic germline mutations in *BRCA2* or *PALB2*.<sup>1,3,40</sup> A few cases of cerebroretinal vasculopathy and leukoencephalopathy have been reported in literature. These are characterized by recurrent space-occupying brain lesions that can mimic glial neoplasms along with retinal vasculopathy, with patients presenting in their early twenties (Fig 7 and Online Supplemental Data).<sup>41</sup> Rare cases of embryonal tumors and glioblastomas have also been reported with these mutations. These mutations are also associated with cancers of the breast, ovaries, and pancreas. Medulloblastomas arising in the setting of FA are usually the large-cell/anaplastic histologic type, with *SHH*-activated *TP53*-mutant being the most common molecular subtype. These medulloblastomas with germline *BRCA2* or *PALB2* mutations have a poor prognosis and a significantly higher risk of the patient developing metastases after treatment.<sup>40,42</sup> The poor prognosis is due to the aggressive biology of the tumor and because these patients cannot tolerate high-dose chemotherapy, given the underlying myelodysplastic condition. The essential diagnostic criterion for FA is positive findings on the diepoxybutane test, wherein chromosomal breakage is seen after exposure to diepoxybutane in leukocytes. Identification of pathogenic germline mutations in a *FANC* gene through NGS is, however, more sensitive and desirable.<sup>1,38</sup>

### Familial Retinoblastoma

Retinoblastoma is the most common intraocular malignancy in children with small, blue, round-cell morphology and a classic histologic pattern characterized by hyperchromatic small, round, blue cells arranged in sheets, nests, and trabeculae (rosettes). This CNS tumor can be secondary to a germline *RB1* mutation (heritable) or somatic mutation (*RB1* sporadic, *MYCN*-driven). *MYCN* oncogene–related retinoblastomas are the least common, are non-hereditary, and are almost always unilateral, with a very early age of presentation.<sup>43</sup> Familial retinoblastoma is secondary to a germline *RB1* mutation with bilateral ocular disease in 60% of patients along with synchronous or metachronous intracranial tumors (pineal or suprasellar). Histologic features of pineal and ocular tumors are identical in familial retinoblastoma. The combination of intraocular retinoblastoma (unilateral or bilateral) and a histologically similar-but-independent focus of brain tumor (pineal region or suprasellar) is called “trilateral retinoblastoma.” Children with familial retinoblastoma have a particularly high incidence of and earlier onset of trilateral retinoblastoma.<sup>44,45</sup> Most of these tumors are seen in children younger than 3 years of age, with familial tumors arising at an earlier age (younger than 1 year) compared with the sporadic counterpart.

These tumors arise from the inner or outer retinal layers, and can be endophytic or exophytic, causing vitreous invasion or retinal detachment, respectively. The most important predictive

factors for recurrence include the extent of retrolaminar optic nerve involvement and choroidal invasion (Online Supplemental Data).<sup>1</sup> Patients with familial retinoblastoma, whether treated by radiation or not, are at higher risk of subsequently developing sarcomas as a second neoplasm. With better understanding of tumor genetics, a clear association of the *RB1* gene in oncogenesis of osteosarcomas has been established.<sup>29,46</sup> Patients with familial retinoblastomas should be screened for osteosarcomas (10–20 years of age) and soft-tissue sarcomas (10–50 years).<sup>47</sup>

### CONCLUSIONS

Multiple new genetic tumor syndromes have been described in the new 5th edition of the WHO Classification of Tumors of the Central Nervous System, highlighting the rapid advances in our understanding of the molecular and genetic tumor markers, including the diversity of clinically relevant molecular types and subtypes. Recognition of these genetic tumor-predisposition syndromes is of great importance to patients and their families. Surveillance protocols for individuals affected by these syndromes are being established, with consensus from international experts. The radiologist plays a vital role in identification, surveillance, and follow-up of CNS tumors seen in these genetic syndromes and for screening examinations for family members. Radiologists should be aware of the tumors associated with these syndromes, the inheritance pattern, and the latest guidelines for screening of family members and can expect to see higher numbers of screening examinations in their practice.

Disclosure forms provided by the authors are available with the full text and PDF of this article at [www.ajnr.org](http://www.ajnr.org).

### REFERENCES

1. WHO Classification of Tumours Editorial Board. *Central Nervous System Tumors*. 5th ed. International Agency for Research on Cancer; 2022 (beta online version)
2. WHO Classification of Tumours Editorial Board. *Genetic Tumour Syndromes*. 5th ed. International Agency for Research on Cancer; 2021
3. Carta R, Del Baldo G, Miele E, et al. **Cancer predisposition syndromes and medulloblastoma in the molecular era.** *Front Oncol* 2020;10:566822 CrossRef Medline
4. Noortman WA, Vriens D, Geus LF, et al. **FDG-PET/CT radiomics for the identification of genetic clusters in pheochromocytomas and paragangliomas.** *Eur Radiol* 2022;32:7227–36 CrossRef Medline
5. Karabacak M, Ozkara BB, Ozturk A, et al. **Radiomics-based machine learning models for prediction of medulloblastoma subgroups: a systematic review and meta-analysis of the diagnostic test performance.** *Acta Radiol* 2023;64:1994–200 CrossRef Medline
6. Sohn B, An C, Kim D, et al. **Radiomics-based prediction of multiple gene alteration incorporating mutual genetic information in glioblastoma and grade 4 astrocytoma, IDH-mutant.** *J Neurooncol* 2021;155:267–76 CrossRef Medline
7. Rimkus TK, Carpenter RL, Qasem S, et al. **Targeting the sonic hedgehog signaling pathway: review of smoothened and GLI inhibitors.** *Cancers (Basel)* 2016;8:22 CrossRef Medline
8. Waszak SM, Robinson GW, Gudenas BL, et al. **Germline Elongator mutations in Sonic Hedgehog medulloblastoma.** *Nature* 2020;580:396–401 CrossRef Medline
9. Fruehwald-Pallamar J, Puchner SB, Rossi A, et al. **Magnetic resonance imaging spectrum of medulloblastoma.** *Neuroradiology* 2011;53:387–96 CrossRef Medline

10. Tauziède-Espariat A, Guerrini-Rousseau L, Perrier A, et al. **Immunohistochemistry as a tool to identify ELP1-associated medulloblastoma.** *Acta Neuropathol* 2022;143:523–25 CrossRef Medline
11. Walpole S, Pritchard AL, Cebulla CM, et al. **Comprehensive study of the clinical phenotype of germline BAP1 variant-carrying families worldwide.** *J Natl Cancer Inst* 2018;110:1328–41 CrossRef Medline
12. Shankar GM, Abedalthagafi M, Vaubel RA, et al. **Germline and somatic BAP1 mutations in high-grade rhabdoid meningiomas.** *Neuro Oncol* 2017;19:535–45 CrossRef Medline
13. Kerr K, Qualmann K, Esquenazi Y, et al. **Familial syndromes involving meningiomas provide mechanistic insight into sporadic disease.** *Neurosurgery* 2018;83:1107–18 CrossRef Medline
14. Shankar GM, Santagata S. **BAP1 mutations in high-grade meningioma: implications for patient care.** *Neuro Oncol* 2017;19:1447–56 CrossRef Medline
15. Rai K, Pilarski R, Cebulla CM, et al. **Comprehensive review of BAP1 tumor predisposition syndrome with report of two new cases.** *Clin Genet* 2016;89:285–94 CrossRef Medline
16. LaFave LM, Béguelin W, Koche R, et al. **Loss of BAP1 function leads to EZH2-dependent transformation.** *Nat Med* 2015;21:1344–49 CrossRef Medline
17. Caroleo AM, De Ioris MA, Boccuto L, et al. **DICER1 syndrome and cancer predisposition: from a rare pediatric tumor to lifetime risk.** *Front Oncol* 2020;10:614541 CrossRef Medline
18. Schultz KA, Yang J, Doros L, et al. **DICER1-pleuropulmonary blastoma familial tumor predisposition syndrome: a unique constellation of neoplastic conditions.** *Pathol Case Rev* 2014;19:90–100 CrossRef Medline
19. de Kock L, Priest JR, Foulkes WD, et al. **An update on the central nervous system manifestations of DICER1 syndrome.** *Acta Neuropathol* 2020;139:689–701 CrossRef Medline
20. de Kock L, Sabbaghian N, Plourde F, et al. **Pituitary blastoma: a pathognomonic feature of germ-line DICER1 mutations.** *Acta Neuropathol* 2014;128:111–22 CrossRef Medline
21. Schultz KA, Williams GM, Kamihara J, et al. **DICER1 and associated conditions: identification of at-risk individuals and recommended surveillance strategies.** *Clin Cancer Res* 2018;24:2251–61 CrossRef Medline
22. Bertherat J, Horvath A, Groussin L, et al. **Mutations in regulatory subunit type 1A of cyclic adenosine 5'-monophosphate-dependent protein kinase (PRKAR1A): phenotype analysis in 353 patients and 80 different genotypes.** *J Clin Endocrinol Metab* 2009;94:2085–91 CrossRef Medline
23. Espiard S, Vantyghem MC, Assié G, et al. **Frequency and incidence of Carney complex manifestations: a prospective multicenter study with a three-year follow-up.** *J Clin Endocrinol Metab* 2020;105:dgaa002 CrossRef Medline
24. Bové JV. **Osteochondromyxoma.** In: WHO Classification of Tumours Editorial Board. *Soft Tissue and Bone Tumours. Classification of Tumours Series.* Vol. 3. 5th ed. International Agency for Research on Cancer; 2020
25. Stratakis CA, Kirschner LS, Carney JA. **Clinical and molecular features of the Carney complex: diagnostic criteria and recommendations for patient evaluation.** *J Clin Endocrinol Metab* 2001;86:4041–46 CrossRef Medline
26. Yeom JA, Song YS, Lee IS, et al. **Malignant melanotic nerve sheath tumors in the spinal canal of psammomatous and non-psammomatous type.** *World J Clin Cases* 2022;10:8735–41 CrossRef Medline
27. Chan AK, Han SJ, Choy W, et al. **Familial melanoma-astrocytoma syndrome: synchronous diffuse astrocytoma and pleomorphic xanthoastrocytoma in a patient with germline CDKN2A/B deletion and a significant family history.** *Clin Neuropathol* 2017;36:213–21 CrossRef Medline
28. Kaufman DK, Kimmel DW, Parisi JE, et al. **A familial syndrome with cutaneous malignant melanoma and cerebral astrocytoma.** *Neurology* 1993;43:1728–31 CrossRef Medline
29. Sargen MR, Merrill SL, Chu EY, et al. **CDKN2A mutations with p14 loss predisposing to multiple nerve sheath tumours, melanoma, dysplastic naevi and internal malignancies: a case series and review of the literature.** *Br J Dermatol* 2016;175:785–89 CrossRef Medline
30. Baker MJ, Goldstein AM, Gordon PL, et al. **An interstitial deletion within 9p21.3 and extending beyond CDKN2A predisposes to melanoma, neural system tumours and possible haematological malignancies.** *J Med Genet* 2016;53:721–27 CrossRef Medline
31. Boedeker CC, Hensen EF, Neumann HP, et al. **Genetics of hereditary head and neck paragangliomas.** *Head Neck* 2014;36:907–16 CrossRef Medline
32. Turchini J, Cheung VK, Tischler AS, et al. **Pathology and genetics of pheochromocytoma and paraganglioma.** *Histopathology* 2018;72:97–105 CrossRef Medline
33. Fishbein L, Leshchiner I, Walter V, et al; Cancer Genome Atlas Research Network. **Comprehensive molecular characterization of pheochromocytoma and paraganglioma.** *Cancer Cell* 2017;31:181–93 CrossRef Medline
34. Lin EP, Chin BB, Fishbein L, et al. **Head and neck paragangliomas: an update on the molecular classification, state-of-the-art imaging, and management recommendations.** *Radiol Imaging Cancer* 2022;4:e210088 CrossRef Medline
35. Ota Y, Liao E, Capizzano AA, et al. **Diagnostic role of diffusion-weighted and dynamic contrast-enhanced perfusion MR imaging in paragangliomas and schwannomas in the head and neck.** *AJNR Am J Neuroradiol* 2021;42:1839–46 CrossRef Medline
36. Janssen I, Blanchet EM, Adams K, et al. **Superiority of [68Ga]-DOTATATE PET/CT to other functional imaging modalities in the localization of SDHB-associated metastatic pheochromocytoma and paraganglioma.** *Clin Cancer Res* 2015;21:3888–95 CrossRef Medline
37. Nalepa G, Clapp DW. **Fanconi anaemia and cancer: an intricate relationship.** *Nat Rev Cancer* 2018;18:168–85 CrossRef Medline
38. Ameziene N, May P, Haitjema A, et al. **A novel Fanconi anaemia subtype associated with a dominant-negative mutation in RAD51.** *Nat Commun* 2015;6:8829 CrossRef Medline
39. Kutler DI, Patel KR, Auerbach AD, et al. **Natural history and management of Fanconi anemia patients with head and neck cancer: a 10-year follow-up.** *Laryngoscope* 2016;126:870–79 CrossRef Medline
40. Miele E, Mastronuzzi A, Po A, et al. **Characterization of medulloblastoma in Fanconi anemia: a novel mutation in the BRCA2 gene and SHH molecular subgroup.** *Biomark Res* 2015;3:13 CrossRef Medline
41. Niedermayer I, Reiche W, Graf N, et al. **Cerebroretinal vasculopathy and leukoencephalopathy mimicking a brain tumor: report of two early-onset cases with Fanconi's anemia-like phenotypes suggesting an autosomal-recessive inheritance pattern.** *Clin Neuropathol* 2000;19:285–95 Medline
42. Dewire MD, Ellison DW, Patay Z, et al. **Fanconi anemia and biallelic BRCA2 mutation diagnosed in a young child with an embryonal CNS tumor.** *Pediatr Blood Cancer* 2009;53:1140–42 CrossRef Medline
43. Rushlow DE, Mol BM, Kennett JY, et al. **Characterisation of retinoblastomas without RB1 mutations: genomic, gene expression, and clinical studies.** *Lancet Oncol* 2013;14:327–34 CrossRef Medline
44. de Jong MC, Kors WA, de Graaf P, et al. **Trilateral retinoblastoma: a systematic review and meta-analysis.** *Lancet Oncol* 2014;15:1157–67 CrossRef Medline
45. Kivelä T. **Trilateral retinoblastoma: a meta-analysis of hereditary retinoblastoma associated with primary ectopic intracranial retinoblastoma.** *J Clin Oncol* 1999;17:1829–37 CrossRef Medline
46. Miller CW, Aslo A, Won A, et al. **Alterations of the p53, Rb and MDM2 genes in osteosarcoma.** *J Cancer Res Clin Oncol* 1996;122:559–65 CrossRef Medline
47. Fabius AW, Hoefen M, van Leeuwen FE, et al. **Subsequent malignant neoplasms in retinoblastoma survivors.** *Cancers (Basel)* 2021;13:1200 CrossRef Medline

# Recommended Resting-State fMRI Acquisition and Preprocessing Steps for Preoperative Mapping of Language and Motor and Visual Areas in Adult and Pediatric Patients with Brain Tumors and Epilepsy

V.A. Kumar, J. Lee, H.-L. Liu, J.W. Allen, C.G. Filippi, A.I. Holodny, K. Hsu, R. Jain, M.P. McAndrews, K.K. Peck, G. Shah, J.S. Shimony, S. Singh, M. Zeineh, J. Tanabe, B. Vachha, A. Vossough, K. Welker, C. Whitlow, M. Wintermark, G. Zaharchuk, and H.I. Sair

## ABSTRACT

Resting-state (rs) fMRI has been shown to be useful for preoperative mapping of functional areas in patients with brain tumors and epilepsy. However, its lack of standardization limits its widespread use and hinders multicenter collaboration. The American Society of Functional Neuroradiology, American Society of Pediatric Neuroradiology, and the American Society of Neuroradiology Functional and Diffusion MR Imaging Study Group recommend specific rs-fMRI acquisition approaches and preprocessing steps that will further support rs-fMRI for future clinical use. A task force with expertise in fMRI from multiple institutions provided recommendations on the rs-fMRI steps needed for mapping of language, motor, and visual areas in adult and pediatric patients with brain tumor and epilepsy. These were based on an extensive literature review and expert consensus.

Following rs-fMRI acquisition parameters are recommended: minimum 6-minute acquisition time; scan with eyes open with fixation; obtain rs-fMRI before both task-based fMRI and contrast administration; temporal resolution of  $\leq 2$  seconds; scanner field strength of 3T or higher. The following rs-fMRI preprocessing steps and parameters are recommended: motion correction (seed-based correlation analysis [SBC], independent component analysis [ICA]); despiking (SBC); volume censoring (SBC, ICA); nuisance regression of CSF and white matter signals (SBC); head motion regression (SBC, ICA); bandpass filtering (SBC, ICA); and spatial smoothing with a kernel size that is twice the effective voxel size (SBC, ICA).

The consensus recommendations put forth for rs-fMRI acquisition and preprocessing steps will aid in standardization of practice and guide rs-fMRI program development across institutions. Standardized rs-fMRI protocols and processing pipelines are essential for multicenter trials and to implement rs-fMRI as part of standard clinical practice.

**ABBREVIATIONS:** BOLD = blood oxygenation level–dependent; EC = eyes closed; EO-F = eyes open with fixation; EO = eyes open without fixation; FC = functional connectivity; GSR = global signal regression; ICA = independent component analysis; rs = resting-state; rs-FC = rs-functional connectivity; RSN = resting-state networks; SBC = seed-based correlation analysis; STC = slice timing correction; tb = task-based; TR = repetition time

Resting-state (rs) fMRI has been found promising for presurgical mapping of eloquent brain areas for brain tumor and epilepsy surgery.<sup>1</sup> For example, rs-fMRI is beneficial in localizing

language areas when task-based (tb) fMRI cannot be performed due to cognitive impairment or limited tb-fMRI.<sup>2</sup> However, more studies are needed to validate the clinical utility of rs-fMRI for preoperative localization of language in adults and pediatric patients.

Rs-fMRI can be performed while the patient is at rest, and it can be acquired without the need for highly trained personnel. However, rs-fMRI is more susceptible to head motion than tb-fMRI.<sup>3,4</sup> It is critical to specify rs-fMRI acquisition and preprocessing steps and parameters to isolate the blood oxygen level–dependent (BOLD) signal corresponding to networks of interest. Additionally, not all preprocessing steps may be needed because

Received July 23, 2023; accepted after revision October 12.

From the University of Texas MD Anderson Cancer Center (V.A.K., J.L., H.-L.L., M.W.), Houston, Texas; Emory University (J.W.A.), Atlanta, Georgia; Tufts University (C.G.F.), Boston, Massachusetts; Memorial Sloan Kettering Cancer Center (A.I.H., K.K.P.), New York, New York; New York University (K.H., R.J.), New York, New York; University of Toronto (M.P.M.), Toronto, Ontario, Canada; University of Michigan (G.S.), Ann Arbor, Michigan; Washington University School of Medicine (J.S.S.), St. Louis, Missouri; University of Texas Southwestern Medical Center (S.S.), Dallas, Texas; Stanford University (M.Z., G.Z.), Palo Alto, California; University of Colorado (J.T.), Aurora, Colorado; University of Massachusetts (B.V.), Worcester, Massachusetts; Children's Hospital of Philadelphia, University of Pennsylvania (A.V.), Philadelphia, Pennsylvania; Mayo Clinic (K.W.), Rochester, Minnesota; Wake Forest University (C.W.), Winston-Salem, North Carolina; and Johns Hopkins University (H.I.S.), Baltimore, Maryland.

From the American Society of Functional Neuroradiology (ASFN), American Society of Pediatric Neuroradiology (ASPN), American Society of Neuroradiology (ASNR) Clinical Translation of Functional and Diffusion MRI Study Group.

V.A. Kumar and J. Lee are co-first authors.

Please address correspondence to Vinodh A. Kumar, MD, The University of Texas MD Anderson Cancer Center, Department of Neuroradiology, 1400 Pressler St., Houston, TX, USA 77030; e-mail: vakumar@mdanderson.org; @VinceKumarMD

<http://dx.doi.org/10.3174/ajnr.A8067>

some potentially carry the risk of removing the intrinsic BOLD signal.<sup>3</sup>

Yet, there is no standardization of rs-fMRI acquisition and preprocessing steps across institutions, hindering data sharing, comparison of results, and scientific transparency. Therefore, an expert task force consisting of 16 neuroradiologists, 2 pediatric neuroradiologists, 2 imaging physicists, and 1 clinical neuropsychologist with expertise in fMRI was formed to provide recommendations for specific rs-fMRI acquisition and preprocessing steps based on literature review and expert consensus for presurgical mapping of language, motor, and visual areas in patients with brain tumor and epilepsy. This task force hopes to encourage multicenter studies to implement rs-fMRI for widespread clinical use. Unlike tb-fMRI,<sup>5</sup> our recommendations can be used for both adult and pediatric patients.

LITERATURE SEARCH STRATEGY AND REVIEW PROCESS

References were identified through a literature search on PubMed and the Web of Science using the following keywords: (functional connectivity OR resting state OR resting-state) AND (fMRI OR functional MR imaging OR functional MR imaging) AND (brain neoplasm OR brain tumor OR epilepsy) AND (motor OR sensorimotor OR language OR visual OR vision) in July 2022. Although in some publications, the terms are used interchangeably, for the purpose of this article, rs-fMRI refers to BOLD signal acquisition during rest and rs-functional connectivity (rs-FC) refers to postprocessed resting-state correlation results. Rs-FC data are often represented as resting-state networks (RSN) of closely connected areas across the brain (eg, language).

From the total of 1291 articles that were identified from the initial keyword search, 305 duplicate articles were removed. The

abstracts of the remaining 986 articles were evaluated and further subselected for the following criteria: rs-fMRI studies written in English that localized and/or lateralized individual language, motor, and/or visual areas in patients with brain tumor and/or epilepsy for preoperative planning from January 2008 until July 2022. Studies that used rs-fMRI to localize seizure-onset zones to examine connectome or local properties of the rs-fMRI signal with an amplitude of low-frequency fluctuation and regional homogeneity analysis without localizing functional areas were excluded. A total of 75 articles met the inclusion criteria.

All the acquisition and preprocessing steps that each article used were recorded. For articles that used >1 parameter for a step, they would be counted more than once for analysis. For example, if an article used 2 different temporal resolutions, this article would be counted as 2 different studies. Articles that used a near-equivalent number of patients with brain tumor and epilepsy would also be counted as 2 distinct studies. Additionally, when we recorded the number of studies that used specific preprocessing steps, they were separated on the basis of whether they used seed-based correlation analysis (SBC), independent component analysis (ICA), and/or other algorithms such as multilayer perceptron, cortical parcellation, or deep learning analysis. If articles used >1 type of algorithm, they would be included in the analysis more than once. Thus, a total of 86 studies were used for the literature review. In addition, for articles that did not report the length of the scan, this was calculated by multiplying the temporal resolution used by the number of volumes scanned.

Individuals with expertise in fMRI were invited to form a task force to reach expert consensus on the specific rs-fMRI acquisition and preprocessing steps for presurgical planning in patients with brain tumors and epilepsy (Tables 1 and 2). Across a total of 4 Webinar meetings, the task force members anonymously voted on every acquisition and preprocessing step after presentation of the literature review and after the ensuing group discussion. On the basis of a Delphi method, expert consensus was reached when ≥60% of the members recommended a specific acquisition/preprocessing step.<sup>6</sup> The parameters that were not recommended were deemed optional. Subsequently, 2 American Society of Pediatric Neuroradiology neuroradiologists with expertise in pediatric fMRI were invited to provide additional input as it related to pediatric rs-fMRI.

Table 1: Resting-state fMRI acquisition parameters

Acquisition Parameters	Recommended
Length of scan	Minimum of 6 minutes
Eye status	EO-F
Order of rs-fMRI vs tb-fMRI	rs-fMRI before tb-fMRI
TR	≤2 Seconds
Physiologic noise source monitoring	Optional
IV contrast administration	After rs-fMRI
Scanner field strength	3T or higher

Table 2: Resting-state fMRI preprocessing steps

Preprocessing Steps	Recommended
Motion correction	Yes, for SBC and ICA
STC	Optional for TR ≤2 Recommended for TR >2 for SBC and ICA
Elimination of systematic odd-even slice-intensity differences	Optional
Despiking	Yes, for SBC only
Volume censoring/scrubbing	Yes, for SBC and ICA
Linear detrending	Optional
Nuisance regression: CSF/white matter	Yes, for SBC only
Nuisance regression: head motion	Yes, for SBC and ICA
Nuisance regression: global signal	Optional
Temporal filtering	Yes, bandpass filtering for SBC and ICA
Spatial smoothing	Yes, with smoothing kernel at twice the voxel size for SBC and ICA

RECOMMENDATIONS OF ACQUISITION AND PREPROCESSING STEPS

Acquisition Steps

**Length of Scan:** Recommend Minimum of 6 Minutes. Because the scan acquisition time for rs-fMRI can influence the sensitivity, reliability, and stability for detecting rs-FC, determining the appropriate scan length is important. The task force recommends a minimum rs-fMRI scan time of 6 minutes for preoperative mapping of the motor, language, and visual areas in patients with brain tumor and epilepsy.

The reliability, consistency, and strength of rs-fMRI increases with scan duration. Birn et al<sup>7</sup> have shown that the reliability across the 153 rs-FCs increased with scan duration and demonstrated improvement in the intrasession reliability of rs-fMRI FC by 20% at 12 versus 6 minutes. An even greater improvement in intrasession reliability was noted at 6 minutes (intraclass correlation coefficient = 0.4) compared with 3 minutes (intraclass correlation coefficient = 0.2).<sup>7</sup> Stronger reliability of the functional connectivity (FC) was noted with increased scan acquisition, but this improvement plateaued at around 13 minutes.<sup>7</sup> However, these studies were conducted on healthy subjects.

For patients with neurologic deficits who need mapping of large cortical areas, shorter scan duration may be more clinically optimal.<sup>8</sup> In most preoperative MR imaging examinations, patients need to undergo scanning for extended periods of time to include anatomic registration images, tb-fMRI, DTI, and other clinical sequences, and lying still in a scanner will likely be tiring and uncomfortable, especially for patients who are claustrophobic.<sup>8</sup> Furthermore, longer scan times could increase the chance of excessive head motion and patients falling asleep. Six minutes of scanning time was shown to be sufficient for the correlation strengths within and between major RSNs to stabilize in healthy participants, with only minimal benefits beyond this duration.<sup>9</sup> Even shorter scan times, approximately 3–4 minutes, have been shown to reliably detect motor and language areas, using a high-speed multiband acquisition with a very short (eg, <500 ms) temporal resolution in patients with glioma.<sup>10</sup>

For the purposes of presurgical mapping of motor, language, and visual areas, we thus recommend a minimum of 6 minutes of scan time, acknowledging that more scan time may be needed to map other rs-fMRI networks. From our literature review, 79/86 (92%) studies reported the scan length per session that they used. The mean, mode, and median scan lengths per session were the following: 7, 6, and 6.1 minutes with the scan length ranging from 4.3 to 28 minutes. In addition to reporting the total length of the scan, we chose to report the scanning time by the length of scan per session: 67/79 (85%) studies had 1 rs-fMRI acquisition session, 9/79 (11%) studies had 2 rs-fMRI sessions, and 3/79 (4%) had 4 rs-fMRI sessions. Thus, on the basis of the literature review, most of the studies used only 1 rs-fMRI acquisition session.

**Eye Status: Recommend Eyes Open with Fixation.** Three eye status conditions during presurgical rs-fMRI were considered: eyes closed (EC), eyes open with fixation (EO-F), and eyes open without fixation (EO). The specific eye status condition can impact the strength, reliability, and consistency of rs-FC.<sup>11</sup> As discussed below, the task force recommends EO-F, typically to a crosshair. At institutions that cannot accommodate EO-F, the EC is considered acceptable for presurgical planning.

Patients closing their eyes during a rs-fMRI scan increases their risk of falling asleep.<sup>12,13</sup> Tagliazucchi et al<sup>13</sup> demonstrated in 71 healthy subjects with EC during a rs-fMRI scan that after 4 minutes of scanning, one-third of the participants fell asleep, and within 10 minutes, one-half were asleep. However, in EO-F, they stayed awake longer compared with either EC or EO.<sup>13</sup> Most importantly, Tagliazucchi et al showed changes in rs-FC in various brain areas, including the sensorimotor and visual areas,

during sleep compared with the awake state.<sup>13</sup> Furthermore, Wang et al<sup>14</sup> showed that being awake increased test-retest reliability across various RSNs, including the somatomotor and visual networks. Furthermore, Agcaoglu et al<sup>15</sup> noted that the EC condition likely led to subjects being drowsy and daydreaming, which led to more variability and no interactions with demographic covariates in contrast to the EO-F condition.

Conversely, the EC and EO states are considered true resting states and not as cognitively demanding as EO-F.<sup>16</sup> Additionally, multiple studies have shown that variability in the strength or reliability of the FC of sensorimotor<sup>15,17,18</sup> and visual<sup>11,16,17</sup> networks to other networks depends on the eye status condition. While this result would be a factor to consider if we were to quantify or analyze FC, for the purpose of preoperative mapping of cortical areas, ensuring that the patients are awake and minimizing movement should be emphasized. In this regard, both the EC and EO are less favorable because of potential excess eye movement during the scan compared with EO-F.<sup>11</sup> In EC, patients falling asleep could lead to excessive head motion.

From our literature review, 70/86 (81%) studies reported the eye status condition of their patients. Thirty-five of 70 (50%) studies had their patients close their eyes, 24/70 (34%) studies had patients fixate their eyes on a crosshair, 6/70 (8.6%) studies had patients open eyes without fixation, and 5/70 (7.1%) studies had sedated patients. More rs-fMRI studies using the eyes closed condition may be because it is logistically easier than displaying a crosshair.

**Order of rs-fMRI versus tb-fMRI: Recommend rs-fMRI before tb-fMRI.** The task force recommends that rs-fMRI be obtained before tb-fMRI when feasible. The FC of rs-areas can be influenced by tasks.<sup>19,20</sup> Wang et al<sup>19</sup> reported changes in the nodal degree and global efficiency across intra- and extra-default mode areas and FC during the posttask relative to pretask resting states in healthy participants. Tung et al<sup>20</sup> noted a transient (5 minute) effect of increased FC between the motor cortex in the post-motor task resting state compared with pretask.<sup>20</sup> This effect was not noted in the control group. Because tb-fMRI protocols can vary among patients and institutions, having patients undergo rs-fMRI and then tb-fMRI will allow better standardization for multicenter studies. Furthermore, because rs-fMRI is more sensitive to motion artifacts than tb-fMRI,<sup>4</sup> acquiring it near the start of the imaging session would reduce the chance of these artifacts. Nevertheless, if tb-fMRI needs to be obtained before rs-fMRI due to established institutional protocols and subject limitations, it is the opinion of the task force that rs-fMRI can still be analyzed. A compromise is that other structural imaging such as DTI can be performed between tb- and rs-fMRI acquisitions to minimize potential tb-fMRI influences on rs-fMRI FC.

From our literature review, 58/86 (67%) studies reported using both rs-fMRI and tb-fMRI paradigms. Twenty-six of 58 studies (45%) reported a specific order in which they performed both fMRI scans. Eighteen of 26 (69%) studies acquired rs-fMRI before tb-fMRI paradigms, whereas 8/26 (31%) studies performed tb-fMRI before rs-fMRI.

**Repetition time (TR): Recommend TR of ≤2 Seconds.** For rs-fMRI, using a single-shot EPI sequence is most common. TR

defines the repetition time or the rate of sampling of the low-frequency rs-BOLD signal fluctuation. The task force recommends a TR of  $\leq 2$  seconds.

An accelerated TR can improve the discrimination of different components with ICA because of the increase in temporal information.<sup>21</sup> The Human Connectome Project (<https://www.humanconnectome.org/>) used a TR of 0.7 seconds to scan 1200 controls, improving identification of resting-state signal fluctuations and increasing their ability to detect physiologic noise.<sup>22</sup> Voets et al<sup>23</sup> reported similar findings and compared the use of 3 different temporal sampling rates at 0.72, 1.56, and 3.5 seconds to localize the motor region in patients with gliomas. Using a TR of  $< 2$  seconds compared with 3.5 seconds resulted in greater success in localizing and spatially separating the motor region into its 3 functional zones.<sup>23</sup> Additionally, a long TR of  $> 4$ –5 seconds approaches the Nyquist limit frequency for typical BOLD frequencies ( $< 0.1$  Hz). Using simulated tb-fMRI, Parker et al<sup>24</sup> observed a decrease in *t*-statistics with longer TRs.<sup>24</sup> The gain in *t*-statistics due to the slice timing correction (STC) was negligible at a TR of  $< 2$  seconds compared with a TR of  $> 2$  sections (see STC correction below).

In modern scanners, multiband acquisition allows shorter TR while maintaining whole-brain coverage, which can increase rs-fMRI sensitivity<sup>21</sup> and statistical power. If one is not using simultaneous multislice scanning, shortening the TR will compromise the spatial resolution or section coverage.<sup>22</sup> Multislice scanning capability may not be readily available on clinical scanners at this time.

From our literature review, 85/86 (99%) studies reported the TR they used. The mean, mode, and median TRs were the following: 2.2, 2, and 2 seconds with the TR ranging from 0.14 to 5 seconds.

**Physiologic Noise-Source Monitoring: Optional.** Physiologic noise-source monitoring of cardiac and respiratory origins aims to remove low-frequency physiologic fluctuations unrelated to neuronal activity that could introduce artifacts and decrease the sensitivity of rs-fMRI.<sup>25</sup> The 2 main sources of physiologic fluctuations are heart-related variations, typically around 0.9–1.2 Hz, and respiratory variations, around 0.2–0.4 Hz,<sup>26</sup> which can be detected via photoplethysmography on the index finger and a pneumatic belt around the abdomen, respectively.<sup>27</sup> Cardiac pulsations can cause CSF and brain parenchymal movement, which can cause changes in the BOLD fMRI series, specifically in the vertebrobasilar system.<sup>26</sup> Respiratory movement can affect rs-fMRI.<sup>26</sup> The task force considers physiologic noise monitoring optional.

Although physiologic recording correction for physiologic variations is possible using retrospective correction techniques like RETROICOR,<sup>28</sup> the signal variation can also be minimized through a combination of appropriate data-preprocessing steps.<sup>9</sup> RETROICOR can suppress both cardiac and respiratory fluctuations by 68% and 50%, respectively.<sup>28</sup> Finite impulse response band-reject digital filters and retrospective gating in *k*-space using data-driven algorithms can also remove cardiac and respiratory fluctuations.<sup>26</sup> However, these steps require external physiologic monitoring, which would be additional steps that could unnecessarily lengthen the fMRI procedure in the clinic. In contrast, there are software solutions that do not require such external monitoring. For example, Behzadi et al<sup>29</sup> have shown that by using

anatomic component correction, cardiac and respiratory noise can be simultaneously removed by conducting white matter and CSF regression without external monitoring. Van Dijk et al<sup>9</sup> showed that regressing nuisance correlations from white matter, ventricular, and whole-brain signals can adequately remove artifacts from cardiorespiratory sources. Bandpass filtering out low-frequency fluctuations can also remove physiologic fluctuations. Separating noise components with independent component analysis could offer additional correction.<sup>30</sup>

Monitoring physiologic noise for removal may be helpful in patients anticipated to have excessive physiologic variation, such as pediatric patients or those with movement disorders. Notably, variations in respiration could be  $< 0.1$  Hz, which overlaps with BOLD signal fluctuations between 0.01 and 0.1 Hz,<sup>9,25</sup> precluding straightforward removal by bandpass filtering. However, even in the situation above, using a short TR, ICA, or a combination of various preprocessing techniques, such as nuisance regression<sup>9</sup> or global signal regression,<sup>31</sup> can reduce the noise contributions and make it feasible to detect the rs-BOLD signal relevant to preoperative mapping of rs-FC. In multislice fMRI data, physiologic noise sources at greater frequencies than the expected bandwidth of rs-fMRI BOLD fluctuations can, through undersampling, be aliased down into the target signal band.<sup>32</sup>

Two of 86 (2.3%) studies in our literature review externally monitored and adjusted for cardiac and respiratory sources of variation in the BOLD signal.

**Gadolinium-Based Contrast Agent Administration: Recommend rs-fMRI before Contrast Administration.** There is limited literature support for IV administration of gadolinium-based contrast agents before or after rs-fMRI. Clinical decisions on when to administer gadolinium-based contrast agent will typically depend on institutional policy, experience, and/or the purpose of the fMRI scan. In a tb-fMRI study, Naganawa et al<sup>33</sup> showed that administering gadolinium-based contrast agents decreased the sensitivity at which the primary motor cortex could be localized in 8 healthy participants who underwent a self-paced motor task compared with precontrast imaging.

The task force recommends obtaining the rs-fMRI scan before contrast administration. However, in cases in which a patient's standard-of-care imaging needs to be prioritized and information gleaned from rs-fMRI might be helpful, postcontrast rs-fMRI data could still be interpreted with caution. This suggestion is especially relevant in cases in which the patient may not be able to complete the entire scan.

**Scanner Field Strength: Recommend 3T or Higher.** Based on the literature review, the most common MR imaging field strength used for rs-fMRI is 3T. Scanners of all 3 field strengths (1.5T, 3T, and 7T) can be used for preoperative mapping of rs-areas. Scanners with higher field strengths produce higher SNRs, which can be used to achieve higher spatial resolution.<sup>34</sup> Additionally, the greater magnetic susceptibility effects at higher magnetic field strengths increase the expected BOLD signal change. Garcia-Eulate et al<sup>35</sup> showed that 3T MR imaging showed improved localization of the motor and somatosensory areas with rs-fMRI compared with 1.5T. Krasnow et al<sup>36</sup> also determined activation

in several regions such as the inferior frontal gyrus, orbitofrontal gyrus, and lingual gyrus with 3T, which could not be detected with 1.5T.

Compared with 3T, a 7T study has shown more precise mapping of RSNs,<sup>37</sup> and another study showed that the measured rs-fMRI signal increased almost 2-fold.<sup>38</sup> However, not only is 7T less widely available than 3T, it can introduce more physiologic, motion, and susceptibility artifacts.<sup>34</sup> If a patient has implants that are MR imaging-conditional at only 1.5T or metal objects that are expected to cause susceptibility artifacts near the functional areas of interest, then 1.5T may be preferable.

From our literature review, 85/86 (99%) studies that used rs-fMRI for presurgical mapping reported the scanner field strength used. Seventy-five of 85 (88%) studies acquired rs-fMRI with 3T scanners, 9/85 (11%) studies used 1.5T scanners, and 1/85 (1.2%) studies used a 7T scanner.

### **Preprocessing Steps**

**Motion Correction: Recommended for Both SBC and ICA.** Motion correction involves spatially realigning the dynamic volumes acquired during the rs-fMRI scan to a reference volume that is usually the first or the middle volume of the scan.<sup>39</sup> The task force recommends including motion correction as a preprocessing step for both SBC and ICA.

Head movement, even in the order of millimeters, can prevent accurate rs-fMRI estimates.<sup>3</sup> Head motion can cause a change in tissue composition within a voxel, which can, in turn, affect its net magnetization and introduce spin-history artifacts that could be difficult to distinguish from true rs-fMRI signal.<sup>3</sup> Head motion introduces distance-dependent bias,<sup>40</sup> in which movement can increase BOLD signal changes in certain regions of the brain but cause a decrease in others.<sup>41</sup> Finally, head motion can introduce BOLD signals that may not be distinguishable from neural activity,<sup>3</sup> contributing to false-positive connections. Especially with the high susceptibility to motion artifacts of rs-fMRI, motion correction is essential to improve its sensitivity<sup>3</sup> and specificity.<sup>42</sup>

Jo et al<sup>40</sup> showed a decrease in distance-dependent correlation bias after motion correction.<sup>40</sup> Maknojia et al<sup>3</sup> noted that motion correction was essential to isolate true rs-networks from noise, and Beall et al<sup>43</sup> showed a reduced image temporal standard deviation (SD) after motion correction. Additionally, motion parameters can be included in the general linear model for nuisance regression.<sup>44</sup> Oakes et al<sup>42</sup> did a comparative analysis of commonly used software programs such as Analysis of Functional Neuro Images (AFNI; <http://afni.nimh.nih.gov/afni>), SPM (<http://www.fil.ion.ucl.ac.uk/spm/software/spm12>), FSL (<http://www.fmrib.ox.ac.uk/fsl>), AIR,<sup>45,46</sup> and BrainVoyager (<https://www.brainvoyager.com/bv/doc/UsersGuide/BrainVoyager> UsersGuide.html) and concluded that all performed equivalently.

While motion correction can improve data quality, it cannot negate all the effects of head motion.<sup>27,47</sup> Head motion control should be emphasized to the patients being scanned. Additionally, other preprocessing techniques such as despiking, volume censoring, and/or head motion regression should additionally be considered.<sup>27</sup>

All the studies in our literature review, including those that used SBC, ICA, and other methods, conducted motion correction (100%, 86/86).

**STC: Optional at a TR of  $\leq 2$  Seconds; Recommended at a TR of  $> 2$  Seconds for Both SBC and ICA.** The majority of fMRI studies use a 2D multislice single-shot gradient-echo EPI sequence. Because the slices are acquired via a sequential or interleaved mode, each section is acquired at a different time within the TR.<sup>24</sup> These time differences cause temporal shifts in the data, which could result in a mismatch between the measured-versus-actual hemodynamic response.<sup>48</sup> STC accounts for such time differences by temporally realigning the individual slices to a reference section to correct for any phase shifts, to model the signal from the whole volume at the same time point.<sup>49</sup> The task force recommends STC at a TR of  $> 2$  seconds for both SBC and ICA. If the recommended TR parameter is followed at a TR of  $\leq 2$ , then STC would be an optional step.

At a TR of  $\leq 2$  seconds, STC will likely have minimal benefit in detecting activation in the RSNs compared with not applying the correction.<sup>49</sup> At this short TR, acquisition delays between slices are minimal. The Human Connectome Project rs-fMRI used a subsecond TR and did not use STC because of unavoidable errors from temporal interpolation that could obscure high-frequency signals.<sup>22</sup> Parker et al<sup>24</sup> have shown that STC at a TR of  $< 2$  seconds for tb-fMRI TRs of 0.5 and 1.1 seconds using FSL and SPM resulted in only minimal benefits of 2.2% and 5% compared with uncorrected data at TR = 2 seconds for which the benefit was 15.6%.<sup>24</sup> Poldrack et al<sup>50</sup> do not recommend using STC at a short TR because artifacts in the reference image could be propagated to other slices.

At a longer TR, STC can improve detection of both rs-FC and tb-fMRI activations by removing temporal sources of variance,<sup>22</sup> particularly in cases with medium-to-high motion.<sup>49</sup> Parker et al<sup>24</sup> demonstrated an improvement of 55.7% in global *t*-statistics at a TR of 5 seconds compared with or without STC. STC is especially important when mapping the dorsal areas such as the motor cortex.<sup>48</sup> STC at a TR of  $> 2$  can also be synergistic when combined with other preprocessing steps. Because movement introduces both spatial and temporal artifacts, a combination of STC and motion correction is needed to avoid the time-series consisting of temporally nonuniform samples.<sup>48</sup> Additionally, STC is necessary when using spatial smoothing because slices with large delays could introduce residual data when averaged with adjacent slices with smaller delays.<sup>24</sup>

From our literature review, 62/86 (72%) studies performed STC, among which 26 studies were scanned at a TR of  $\leq 2$  seconds and the other 36 were scanned at TR  $> 2$  seconds.

**Elimination of Systematic Odd-Even Section-Intensity Differences: Optional.** During interleaved section acquisition, odd-numbered and even-numbered slices are acquired with a relatively large time difference, which can be up to half the TR. The task force considers elimination of systematic odd-even section-intensity differences an optional preprocessing step.

On the basis of expert opinion, it is no longer necessary to eliminate odd-even section-intensity differences with newer model scanners. However, before the advent of such scanners, elimination of odd-even section-intensity differences was necessary to exclude crosstalk between interleaved section acquisitions.<sup>51</sup> Additionally, limited studies and rs-fMRI software tools use this preprocessing step.

From our literature review, 11/86 studies (13%) eliminated systematic odd-even section-intensity differences.

**Despiking: Recommended for SBC Only.** Despiking is a method to correct spikes representing artifacts induced by sudden motion or system instability in the fMRI time-series by truncating,<sup>40</sup> removing, or interpolating<sup>52</sup> signal of the independent voxels. Spikes are often defined as signals that exceed the median and/or mean of the rs-fMRI time-series by a set SD. The task force would recommend despiking for SBC only. On the basis of the literature, a maximum threshold of <5% would likely be acceptable. Patel et al<sup>52</sup> reported wavelet despiking at an average of 1.5% and excluded patients with spike percentages of >5% because they had moved excessively. Power et al<sup>53</sup> also used the despiking setting of 4% with the ArtRepair software ([https://www.nitrc.org/projects/art\\_repair/](https://www.nitrc.org/projects/art_repair/)).

Despiking can identify and remove a wide range of movement-induced artifacts across different frequencies that may not be typically removed by other preprocessing techniques, such as linear regression.<sup>52</sup> Even small movements of the head can introduce secondary sources of artifacts, including spin-history artifacts, which have failed to be effectively removed by nuisance regression and/or volume censoring.<sup>52</sup> However, despiking, specifically wavelet despiking, recently introduced by Patel et al<sup>52</sup> has proved effective in removing these types of motion artifacts from low-to-high frequencies. Patel et al showed that combining wavelet despiking with regression was superior in removing both linear and nonlinear sources of artifacts related to movement and retained less signal variance compared with nuisance regression alone. When combined with nuisance regression, it could identify correlation estimates at strengths similar to those of volume censoring.<sup>40</sup> However, compared with volume censoring, despiking removes voxels with motion artifacts without removing the entire volume of data.<sup>52</sup> Despiking is especially recommended in patients with potentially rapid head movements, such as patients with epilepsy and/or pediatric patients.<sup>52</sup>

On the other hand, despiking can potentially flag too many data points for correction. Replacing flagged data by interpolating adjacent data could add too many artificial signals. Removing too many data points could prohibit detection of functional correlations. Therefore, when using despiking, users need to avoid being too aggressive.

From our literature review, only 8/86 studies (9.3%) used despiking, because it is not available in many commonly used software packages. However, among the 8 studies that used it, 14% of the studies that employed SBC used despiking, whereas 5% of the studies that utilized ICA used despiking.

**Volume Censoring/Scrubbing: Recommended for Both SBC and ICA.** Volume censoring or scrubbing is frame wise removal of any volume with excessive movement or signal changes over a predetermined threshold.<sup>41</sup> Such volumes are identified by first calculating the frame wise displacement of the head position, which measures how much the head moved compared with previous time points and/or DVARS (D: temporal derivative of time courses, VARS: RMS variance over voxels), which measures the rate of change of BOLD signal across the entire brain at each frame of data.<sup>41</sup> If the frame wise displacement or DVARS of

specific volume exceeds a set threshold, that volume would be either dampened, removed,<sup>41</sup> or interpolated.<sup>27</sup> The task force would recommend volume censoring for both SBC and ICA.

The threshold will determine how much data will be removed. It will depend on various factors, such as the number of time points and the duration of the scan. The task force cannot recommend a specific threshold at this time. On the basis of the literature, Power et al<sup>41</sup> chose a value of 0.5 mm for frame wise displacement and a 0.5% change in BOLD signal for DVARS to represent the minimum threshold for movement in still adults. In healthy children, they reported approximately 25% of the rs-fMRI data being affected by motion artifacts. They required a minimum of at least 125 frames, around 5 minutes of data, to be kept after scrubbing, but they had no maximum threshold for how much data could be removed.<sup>41</sup>

Artifacts in rs-fMRI data can be caused by various sources.<sup>41</sup> Susceptibility artifacts can cause image distortions and signal dropouts.<sup>41</sup> Even a small head movement can cause a shift in the position of the brain in space, which can cause a large difference in the amplitude of the BOLD signal and subsequently changes in rs-FC.<sup>41</sup> Head movement can also cause short-range correlations to strengthen, whereas medium- to long-distance FC weakens them.<sup>40</sup> Volume censoring can correct for this bias.<sup>40</sup> Although volume censoring and despiking have similar goals in eliminating motion artifacts exceeding a threshold, volume censoring may be advantageous in patients with the potential for large movements,<sup>3</sup> removing entire frames of data instead of only affected voxels. Additionally, when slow, residual movements are spread over consecutive voxels, volume censoring may, in theory, perform better than despiking.

The disadvantage with volume censoring is that because entire frames of data are removed, more data are typically removed than in other preprocessing steps. Power et al<sup>41</sup> reported removing up to 39% of the data after volume censoring of 22 healthy children who underwent rs-fMRI. For cooperative patients with relatively little motion, volume censoring is expected to be beneficial; however, in patients who move excessively, volume censoring may be unfavorable.

From our literature review, 20/86 (23%) studies performed volume censoring.

**Linear Detrending: Optional.** Linear detrending removes linear BOLD signal drifts or trends typically caused by scanner instability, physiologic fluctuations, and/or head motion.<sup>54,55</sup> The task force considers linear detrending optional.

Typically, linear signal drifts are low-frequency in nature and can mostly be accounted for by using bandpass and/or high-pass filtering. However, if temporal filtering is not performed, linear detrending is necessary and can help account for scanner instabilities or residual slow head movement.

From our literature review, 41/86 (48%) studies performed linear detrending.

**Nuisance Regression: CSF/White Matter Regression—Recommended for SBC Only.** Nuisance signal regression removes temporal components in BOLD signal time courses that are correlated with head motion and CSF/white matter signal fluctuations to eliminate non-

neural contributions.<sup>29</sup> Currently, the main method for nuisance signal regression is a general linear model-based approach in which motion time curves and tissue-based signal time courses are regressed from the rs-fMRI data.<sup>56</sup> The task force would recommend nuisance regression of CSF/white matter signal time curves for SBC only.

Because most neuronal activation occurs in the gray matter, signal changes in the white matter and CSF would mostly be non-neural in origin, such as cardiac and respiratory fluctuations.<sup>29</sup> These can be estimated from various sources including anatomic data, ROIs with high temporal SDs, and noise components from ICA or principal component analysis.<sup>29,57</sup> Nuisance regression of CSF, white matter, and head motion can reduce temporal SDs<sup>29</sup> and improve the specificity at which FC can be estimated.<sup>56</sup> Muschelli et al<sup>56</sup> noted a decrease of motion artifacts, causing variability in FC while preserving the signal of interest with nuisance regression of CSF and white matter. While bandpass filtering without nuisance regression reduces BOLD signal fluctuations due to motion, it did not prevent the spread of motion-contaminated BOLD signal fluctuations.<sup>58</sup>

In cases of standard space transformation for individual patients, incorrect tissue segmentation or inclusion of nuisance signals that represent neural activity would reduce the performance of nuisance regression.<sup>29</sup> Furthermore, a portion of white matter or CSF can be misclassified by large brain tumors or other lesions, affecting the fidelity of the nuisance regressors. From our literature review, 51/86 (59%) studies performed nuisance regression of CSF and/or white matter. Forty-eight of 51 (94%) of these performed both white matter and CSF regression, while 3/51 (5.9%) performed regression for only CSF. Of these 51 studies, 79% of the studies used SBC compared with 33% of the studies that used ICA.

**Nuisance Regression: Head Motion Regression—Recommended for Both SBC and ICA.** Head motion regression is another type of nuisance regression in which translational and rotational motion estimates from image realignment are applied as the nuisance regressors.<sup>27</sup> The number of motion parameters ranges from 6 to 36,<sup>27,59</sup> with 6 being the most common.<sup>27</sup> The expert task force recommends head motion regression for both SBC and ICA.

Due to the complex effects of head motion, image spatial realignment is not enough to fully eliminate motion artifacts,<sup>56</sup> and additional correction is of benefit. Although volume registration works well for small movements, larger motion errors can arise during realignment.<sup>3</sup> Patients may move more than healthy adults.<sup>3</sup> Furthermore, head movement can warp the magnetization gradient,<sup>3</sup> possibly resulting in image distortions.

A possible problem with head motion regression is that in cases of extensive head motion, the realignment parameters may still not fully explain the motion-related signal changes.<sup>27</sup> Additionally, an excess of motion regressors could remove neuronal-related signal fluctuations,<sup>27</sup> especially in cases in which there is minimal head movement.<sup>3</sup> From our literature review, 45/86 (52%) studies conducted head motion regression.

**Nuisance Regression: Global Signal Regression Optional.** Global signal regression (GSR) is regressing out the average time-series

across the whole-brain volume. GSR is an effective though controversial means of reducing widely shared variance and thereby improving the spatial specificity of computed maps.<sup>60–62</sup> The task force considers GSR an optional preprocessing step.

Part of the global signal is of neural origin;<sup>63</sup> however, much of the global signal represents non-neural artifacts attributable to physical effects of head motion<sup>31,59,64,65</sup> and variations in the partial pressure of arterial carbon dioxide.<sup>66</sup> GSR can reduce signal variances due to head motion and physiologic fluctuations better than CSF and white matter regression and motion correction combined.<sup>31</sup> Without GSR, all parts of the brain appear to be strongly positively correlated.<sup>67–70</sup> GSR causes all subsequently computed correlation maps to be approximately zero-centered; in other words, positive and negative values are approximately balanced over the whole brain.<sup>60</sup> Thus, GSR negatively biases all computed correlations but preserves relative iso-correlation contours. This negative bias has caused some to criticize GSR because it induces artifactual anticorrelations<sup>71,72</sup> and removes neural components in the global signal, though an alternative counter view is that widely shared variance in the fMRI signal induces artifactual positive correlations. More recent objections to GSR suggest that it can distort quantitative FC differences across diagnostic groups.<sup>73,74</sup> A more recent consensus article attempts to reconcile these opposing viewpoints.<sup>75</sup>

From our literature review, 27/86 (31%) studies conducted GSR.

**Temporal Filtering: Recommended Bandpass Filtering for Both SBC and ICA.** Bandpass, low-pass, or high-pass temporal filtering has been commonly applied for rs-fMRI. This preprocessing step removes BOLD signal components with frequencies typically lower than 0.01 Hz and/or higher than 0.1 Hz. The task force recommends bandpass filtering the rs-fMRI data for both SBC and ICA. On the basis of the literature, 0.01–0.08 Hz was the most common bandpass filtering frequency range.

Filtering out any frequencies outside the typical rs-fMRI frequency range of 0.01–0.1 Hz is important to eliminate any residual noise from head motion, physiologic origins, and/or low-frequency drifts.<sup>76</sup> Bandpass filtering increased the signal-to-noise separation within well-known RSNs and increased the test-retest reliability of whole-brain connectivity in both healthy controls and subjects with mild Alzheimer disease.<sup>77</sup> Bandpass filtering is often combined with nuisance regression of CSF/WM, motion, and global signal.<sup>58</sup> In a study conducted by Risk et al,<sup>78</sup> the accumulation of spatially heterogeneous multiband noise, the physiologic noise from CSF pulsations, and the variance from intracranial brain motion increased the SD and resulted in reduced rs-FC estimates, even when using nuisance regression. However, when nuisance regression was combined with bandpass filtering, they obtained higher functional correlations at higher multiband factors.<sup>78</sup> Additionally, Van Dijk et al<sup>79</sup> demonstrated that linear trends were removed with bandpass filtering, while maintaining frequencies of <0.08 Hz. Overall, bandpass filtering allows removal of extremes of high and low BOLD signal frequencies and would, therefore, allow the best estimate of localization of RSNs. The upper and lower thresholds at which the BOLD signal is filtered usually depend on the institution.

A disadvantage of bandpass filtering is that neural signal above or below the thresholds could be lost.<sup>78</sup> Physiologic

fluctuations in BOLD signal existing from 0.01 to 0.1 Hz may still not be removed with bandpass filtering. For example, low-frequency fluctuations due to the heart rate can occur at 0.04 Hz, and small fluctuations in breathing, at 0.03 Hz.<sup>27</sup> While such physiologic fluctuations are non-neural in nature,<sup>27</sup> they will be reflected in the BOLD signal in white matter and CSF, which can be removed through nuisance regression.

Low-pass and high-pass filtering can also be used in rs-fMRI preprocessing. Low-pass filtering is advantageous because it can filter out non-neural signals that are typically above 0.1 Hz.<sup>27</sup> Because most physiologic noise typically presents at high frequencies,<sup>29</sup> low-pass filtering can effectively remove such sources of noise while retaining the rs-BOLD signal of interest. However, intrinsic brain signal could still exist beyond 0.1 Hz.<sup>27</sup> Studies that used high-pass filtering detected only frequencies above, usually, 0.01 Hz, because any frequencies below 0.01 Hz most likely do not represent true rs-fMRI signal but represent noise instead. High-pass filtering can be used as an alternative to linear detrending because it can remove linear drifts that occur at low frequencies, below 0.02 Hz. However, high-pass filtering cannot remove motion artifacts at frequencies above 0.01 Hz.

From our literature review, 75/86 (87%) studies applied a temporal filter to the rs-fMRI data. Forty-five of 75 (60%) studies applied bandpass filtering, 20/75 (27%) studies applied low-pass filtering, and 10/75 (13%) studies applied high-pass filtering.

**Spatial Smoothing: Recommended with a Kernel Size Twice the Voxel Size for Both SBC and ICA.** For spatial smoothing, the signal at each voxel is averaged across a range of neighboring voxels to reduce noise<sup>80</sup> and increases sensitivity.<sup>81</sup> The task force recommends spatial smoothing for both SBC and ICA with a kernel size approximately twice the acquired voxel size. Kokkonen et al<sup>82</sup> reported unsuccessful mapping of sensorimotor areas when using unsmoothed data. Huang et al<sup>83</sup> reported that a Gaussian kernel size of 6-mm full width at half maximum with approximately 3-mm isotropic voxels increased the SNR of BOLD to enable more reliable mapping of motor and language areas. Alakorkko et al<sup>80</sup> showed that spatial smoothing can increase the correlation strength of voxels across rs-FCs. With young children with smaller brain sizes, the operator could consider proportionally reducing the voxel size and number of slices.

A smoothing kernel that is too small may have little benefit, while a kernel that is too large could reduce spatial specificity.<sup>81</sup> A kernel size that is twice the voxel size of the functional images has been recommended<sup>84-86</sup> to ensure the validity of the random field theory-based multiple comparison correction.<sup>86</sup>

From our literature review, 78/86 (91%) studies performed spatial smoothing. The kernel size ranged from 1 to 10 mm full width at half maximum, with a mean, mode, and median of 6.1, 6, and 6 mm full width at half maximum, respectively. Seventy-four of 78 (95%) studies reported the kernel size they used. Thirty-eight of 74 (51%) studies used a kernel size that was twice the voxel size.

## CONCLUSIONS

The American Society of Functional Neuroradiology, the American Society of Pediatric Neuroradiology, and the American

Society of Neuroradiology Clinical Translation of Functional and Diffusion MR Imaging Study Group suggests the use of the proposed standardized rs-fMRI acquisition and preprocessing steps as initial guidelines for institutions using rs-fMRI for preoperative mapping of language, motor, and visual areas in patients with brain tumors and epilepsy. The recommendations provided are based on a comprehensive review of the literature and consensus opinion from experts in fMRI from institutions in the United States and Canada. These rs-fMRI guidelines may lead to the development of a standard rs-fMRI pipeline as well as commercial rs-fMRI processing software. The rs-fMRI guidelines will also encourage and standardize multicenter studies that will help validate rs-fMRI for widespread clinical use. Future studies are needed to define a specific order of the rs-fMRI preprocessing steps, because currently, there is insufficient literature support and not enough expert consensus to provide an order for all the steps. Further studies are also needed evaluating the interactions of different preprocessing steps based on their order of implementation. Finally, the task force would emphasize that while the recommended acquisition/preprocessing steps are preferred, the ones that were deemed optional are not necessarily precluded and may be beneficial depending on the circumstances.

Disclosure forms provided by the authors are available with the full text and PDF of this article at [www.ajnr.org](http://www.ajnr.org).

## REFERENCES

1. Leuthardt EC, Guzman G, Bandt SK, et al. **Integration of resting state functional MRI into clinical practice: a large single institution experience.** *PLoS One* 2018;13:e0198349 CrossRef Medline
2. Kumar VA, Heiba IM, Prabhu SS, et al. **The role of resting-state functional MRI for clinical preoperative language mapping.** *Cancer Imaging* 2020;20:47 CrossRef Medline
3. Maknojia S, Churchill NW, Schweizer TA, et al. **Resting state fMRI: going through the motions.** *Front Neurosci* 2019;13:825 CrossRef Medline
4. Huijbers W, Van Dijk KR, Boenniger MM, et al. **Less head motion during MRI under task than resting-state conditions.** *Neuroimage* 2017;147:111–20 CrossRef Medline
5. Black DF, Vachha B, Mian A, et al. **American Society of Functional Neuroradiology-recommended fMRI paradigm algorithms for presurgical language assessment.** *AJNR Am J Neuroradiol* 2017;38:E65–73 CrossRef Medline
6. Niederberger M, Spranger J. **Delphi technique in health sciences: a map.** *Front Public Health* 2020;8:457 CrossRef Medline
7. Birn RM, Molloy EK, Patriat R, et al. **The effect of scan length on the reliability of resting-state fMRI connectivity estimates.** *Neuroimage* 2013;83:550–58 CrossRef Medline
8. Abdul Wahab NS, Yahya N, Yusoff AN, et al. **Effects of different scan duration on brain effective connectivity among default mode network nodes.** *Diagnostics (Basel)* 2022;12:12 CrossRef Medline
9. Van Dijk KR, Hedden T, Venkataraman A, et al. **Intrinsic functional connectivity as a tool for human connectomics: theory, properties, and optimization.** *J Neurophysiol* 2010;103:297–321 CrossRef Medline
10. Vakamudi K, Posse S, Jung R, et al. **Real-time presurgical resting-state fMRI in patients with brain tumors: quality control and comparison with task-fMRI and intraoperative mapping.** *Hum Brain Mapp* 2020;41:797–814 CrossRef Medline
11. Patriat R, Molloy EK, Meier TB, et al. **The effect of resting condition on resting-state fMRI reliability and consistency: a comparison between resting with eyes open, closed, and fixated.** *Neuroimage* 2013;78:463–73 CrossRef Medline

12. Allen EA, Damaraju E, Eichele T, et al. **EEG signatures of dynamic functional network connectivity states.** *Brain Topogr* 2018;31:101–16 CrossRef Medline
13. Tagliazucchi E, Laufs H. **Decoding wakefulness levels from typical fMRI resting-state data reveals reliable drifts between wakefulness and sleep.** *Neuron* 2014;82:695–708 CrossRef Medline
14. Wang J, Han J, Nguyen VT, et al. **Improving the test-retest reliability of resting state fMRI by removing the impact of sleep.** *Front Neurosci* 2017;11:249 CrossRef Medline
15. Agcaoglu O, Wilson TW, Wang YP, et al. **Resting state connectivity differences in eyes open versus eyes closed conditions.** *Hum Brain Mapp* 2019;40:2488–98 CrossRef Medline
16. Zou Q, Miao X, Liu D, et al. **Reliability comparison of spontaneous brain activities between BOLD and CBF contrasts in eyes-open and eyes-closed resting states.** *Neuroimage* 2015;121:91–10 CrossRef Medline
17. Costumero V, Bueichekú E, Adrián-Ventura J, et al. **Opening or closing eyes at rest modulates the functional connectivity of V1 with default and salience networks.** *Sci Rep* 2020;10:9137 CrossRef Medline
18. Wei J, Chen T, Li C, et al. **Eyes-open and eyes-closed resting states with opposite brain activity in sensorimotor and occipital regions: multidimensional evidences from machine learning perspective.** *Front Hum Neurosci* 2018;12:422 CrossRef Medline
19. Wang Z, Liu J, Zhong N, et al. **Changes in the brain intrinsic organization in both on-task state and post-task resting state.** *Neuroimage* 2012;62:394–407 CrossRef Medline
20. Tung KC, Uh J, Mao D, et al. **Alterations in resting functional connectivity due to recent motor task.** *Neuroimage* 2013;78:316–24 CrossRef Medline
21. Feinberg DA, Moeller S, Smith SM, et al. **Multiplexed echo planar imaging for sub-second whole brain fMRI and fast diffusion imaging.** *PLoS One* 2010;5:e15710 CrossRef Medline
22. Smith SM, Beckmann CF, Andersson J, et al; WU-Minn HCP Consortium. **Resting-state fMRI in the Human Connectome Project.** *Neuroimage* 2013;80:144–68 CrossRef Medline
23. Voets NL, Plaha P, Parker Jones O, et al. **Presurgical localization of the primary sensorimotor cortex in gliomas: when is resting state fMRI beneficial and sufficient?** *Clin Neuroradiol* 2021;31:245–56 CrossRef Medline
24. Parker D, Liu X, Razlighi QR. **Optimal slice timing correction and its interaction with fMRI parameters and artifacts.** *Med Image Anal* 2017;35:434–45 CrossRef Medline
25. Birn RM, Diamond JB, Smith MA, et al. **Separating respiratory-variation-related fluctuations from neuronal-activity-related fluctuations in fMRI.** *Neuroimage* 2006;31:1536–48 CrossRef Medline
26. Lin FH, Nummenmaa A, Witzel T, et al. **Physiological noise reduction using volumetric functional magnetic resonance inverse imaging.** *Hum Brain Mapp* 2012;33:2815–30 CrossRef Medline
27. Caballero-Gaudes C, Reynolds RC. **Methods for cleaning the BOLD fMRI signal.** *Neuroimage* 2017;154:128–49 CrossRef Medline
28. Glover GH, Li TQ, Ress D. **Image-based method for retrospective correction of physiological motion effects in fMRI: RETROICOR.** *Magn Reson Med* 2000;44:162–67 CrossRef Medline
29. Behzadi Y, Restom K, Liu J, et al. **A component based noise correction method (CompCor) for BOLD and perfusion based fMRI.** *Neuroimage* 2007;37:90–101 CrossRef Medline
30. Golestani AM, Chen JJ. **Performance of temporal and spatial independent component analysis in identifying and removing low-frequency physiological and motion effects in resting-state fMRI.** *Front Neurosci* 2022;16:867243 CrossRef Medline
31. Power JD, Plitt M, Laumann TO, et al. **Sources and implications of whole-brain fMRI signals in humans.** *Neuroimage* 2017;146:609–25 CrossRef Medline
32. Frank LR, Buxton RB, Wong EC. **Estimation of respiration-induced noise fluctuations from undersampled multislice fMRI data.** *Magn Reson Med* 2001;45:635–44 CrossRef Medline
33. Naganawa S, Nishihashi T, Fukatsu H, et al. **Pre-surgical mapping of primary motor cortex by functional MRI at 3 T: effects of intravenous administration of Gd-DTPA.** *Eur Radiol* 2004;14:112–14 CrossRef Medline
34. Vachha B, Huang SY. **MRI with ultrahigh field strength and high-performance gradients: challenges and opportunities for clinical neuroimaging at 7 T and beyond.** *Eur Radiol Exp* 2021;5:35 CrossRef Medline
35. Garcia-Eulate R, Garcia-Garcia D, Dominguez PD, et al. **Functional bold MRI: advantages of the 3 T vs. the 1.5 T.** *Clin Imaging* 2011;35:236–41 CrossRef Medline
36. Krasnow B, Tamm L, Greicius MD, et al. **Comparison of fMRI activation at 3 and 1.5 T during perceptual, cognitive, and affective processing.** *Neuroimage* 2003;18:813–26 CrossRef Medline
37. Gorgolewski KJ, Mendes N, Wilfling D, et al. **A high resolution 7-Tesla resting-state fMRI test-retest dataset with cognitive and physiological measures.** *Sci Data* 2015;2:140054 CrossRef Medline
38. Bianciardi M, Fukunaga M, van Gelderen P, et al. **Sources of functional magnetic resonance imaging signal fluctuations in the human brain at rest: a 7 T study.** *Magn Reson Imaging* 2009;27:1019–29 CrossRef Medline
39. Jiang A, Kennedy DN, Baker JR, et al. **Motion detection and correction in functional MR imaging.** *Human Brain Mapping* 1995;3:224–35 CrossRef
40. Jo HJ, Gotts SJ, Reynolds RC, et al. **Effective preprocessing procedures virtually eliminate distance-dependent motion artifacts in resting state FMRI.** *J Appl Math* 2013;2013:10.1155/2013/935154 CrossRef Medline
41. Power JD, Barnes KA, Snyder AZ, et al. **Spurious but systematic correlations in functional connectivity MRI networks arise from subject motion.** *Neuroimage* 2012;59:2142–54 CrossRef Medline
42. Oakes TR, Johnstone T, Ores Walsh KS, et al. **Comparison of fMRI motion correction software tools.** *Neuroimage* 2005;28:529–43 CrossRef Medline
43. Beall EB, Lowe MJ. **SimPACE: generating simulated motion corrupted BOLD data with synthetic-navigated acquisition or the development and evaluation of SLOMOCO: a new, highly effective slice-wise motion correction.** *Neuroimage* 2014;101:21–34 CrossRef Medline
44. Johnstone T, Ores Walsh KS, Greischar LL, et al. **Motion correction and the use of motion covariates in multiple-subject fMRI analysis.** *Hum Brain Mapp* 2006;27:779–88 CrossRef Medline
45. Woods RP, Cherry SR, Mazziotta JC. **Rapid automated algorithm for aligning and reslicing PET images.** *J Comput Assist Tomogr* 1992;16:620–33 CrossRef Medline
46. Woods RP, Mazziotta JC, Cherry SR. **MRI-PET registration with automated algorithm.** *J Comput Assist Tomogr* 1993;17:536–46 CrossRef Medline
47. Friston KJ, Williams S, Howard R, et al. **Movement-related effects in fMRI time-series.** *Magn Reson Med* 1996;35:346–55 CrossRef Medline
48. Sladky R, Friston KJ, Tröstl J, et al. **Slice-timing effects and their correction in functional MRI.** *Neuroimage* 2011;58:588–94 CrossRef Medline
49. Parker DB, Razlighi QR. **The benefit of slice timing correction in common fMRI preprocessing pipelines.** *Front Neurosci* 2019;13:821 CrossRef Medline
50. Poldrack RM, Mumford JA, Nichols TE. *Handbook of Functional MRI Data Analysis.* Cambridge University Press; 2011
51. Simmons A, Tofts PS, Barker GJ, et al. **Sources of intensity nonuniformity in spin echo images at 1.5 T.** *Magn Reson Med* 1994;32:121–28 CrossRef Medline
52. Patel AX, Kundu P, Rubinov M, et al. **A wavelet method for modeling and despiking motion artifacts from resting-state fMRI time series.** *Neuroimage* 2014;95:287–304 CrossRef Medline
53. Power JD, Plitt M, Kundu P, et al. **Temporal interpolation alters motion in fMRI scans: Magnitudes and consequences for artifact detection.** *PLoS One* 2017;12:e0182939 CrossRef Medline
54. Tanabe J, Miller D, Tregellas J, et al. **Comparison of detrending methods for optimal fMRI preprocessing.** *Neuroimage* 2002;15:902–07 CrossRef Medline

55. Kopel R, Sladky R, Laub P, et al. **No time for drifting: comparing performance and applicability of signal detrending algorithms for real-time fMRI.** *Neuroimage* 2019;191:421–29 CrossRef Medline
56. Muschelli J, Nebel MB, Caffo BS, et al. **Reduction of motion-related artifacts in resting state fMRI using aCompCor.** *Neuroimage* 2014;96:22–35 CrossRef Medline
57. Middlebrooks EH, Frost CJ, Tuna IS, et al. **Reduction of motion artifacts and noise using independent component analysis in task-based functional MRI for preoperative planning in patients with brain tumor.** *AJNR Am J Neuroradiol* 2017;38:336–42 CrossRef Medline
58. Hallquist MN, Hwang K, Luna B. **The nuisance of nuisance regression: spectral misspecification in a common approach to resting-state fMRI preprocessing reintroduces noise and obscures functional connectivity.** *Neuroimage* 2013;82:208–25 CrossRef Medline
59. Power JD, Mitra A, Laumann TO, et al. **Methods to detect, characterize, and remove motion artifact in resting state fMRI.** *Neuroimage* 2014;84:320–41 CrossRef Medline
60. Fox MD, Zhang D, Snyder AZ, et al. **The global signal and observed anticorrelated resting state brain networks.** *J Neurophysiol* 2009;101:3270–83 CrossRef Medline
61. Aguirre GK, Zarahn E, D'Esposito M. **The inferential impact of global signal covariates in functional neuroimaging analyses.** *Neuroimage* 1998;8:302–06 CrossRef Medline
62. Macey PM, Macey KE, Kumar R, et al. **A method for removal of global effects from fMRI time series.** *Neuroimage* 2004;22:360–66 CrossRef Medline
63. Scholvinck ML, Maier A, Ye FQ, et al. **Neural basis of global resting-state fMRI activity.** *Proc Natl Acad Sci U S A* 2010;107:10238–43 CrossRef Medline
64. Yan CG, Cheung B, Kelly C, et al. **A comprehensive assessment of regional variation in the impact of head micromovements on functional connectomics.** *Neuroimage* 2013;76:183–201 CrossRef Medline
65. Satterthwaite TD, Wolf DH, Loughhead J, et al. **Impact of in-scanner head motion on multiple measures of functional connectivity: relevance for studies of neurodevelopment in youth.** *Neuroimage* 2012;60:623–32 CrossRef Medline
66. Power JD, Plitt M, Gotts SJ, et al. **Ridding fMRI data of motion-related influences: Removal of signals with distinct spatial and physical bases in multiecho data.** *Proc Natl Acad Sci U S A* 2018;115: E2105–14 CrossRef Medline
67. Lowe MJ, Mock BJ, Sorenson JA. **Functional connectivity in single and multislice echoplanar imaging using resting-state fluctuations.** *Neuroimage* 1998;7:119–32 CrossRef Medline
68. Vincent JL, Snyder AZ, Fox MD, et al. **Coherent spontaneous activity identifies a hippocampal-parietal memory network.** *J Neurophysiol* 2006;96:3517–31 CrossRef Medline
69. Joel SE, Caffo BS, van Zijl PC, et al. **On the relationship between seed-based and ICA-based measures of functional connectivity.** *Magn Reson Med* 2011;66:644–57 CrossRef Medline
70. Chai XJ, Castañón AN, Ongür D, et al. **Anticorrelations in resting state networks without global signal regression.** *Neuroimage* 2012;59:1420–28 CrossRef Medline
71. Anderson JS, Druzgal TJ, Lopez-Larson M, et al. **Network anticorrelations, global regression, and phase-shifted soft tissue correction.** *Hum Brain Mapp* 2011;32:919–34 CrossRef Medline
72. Murphy K, Birn RM, Handwerker DA, et al. **The impact of global signal regression on resting state correlations: are anti-correlated networks introduced?** *Neuroimage* 2009;44:893–905 CrossRef Medline
73. Gotts SJ, Saad ZS, Jo HJ, et al. **The perils of global signal regression for group comparisons: a case study of autism spectrum disorders.** *Front Hum Neurosci* 2013;7:356 CrossRef Medline
74. Hahamy A, Calhoun V, Pearlson G, et al. **Save the global: global signal connectivity as a tool for studying clinical populations with functional magnetic resonance imaging.** *Brain Connect* 2014;4:395–403 CrossRef Medline
75. Murphy K, Fox MD. **Towards a consensus regarding global signal regression for resting state functional connectivity MRI.** *Neuroimage* 2017;154:169–73 CrossRef Medline
76. Wee CY, Yap PT, Denny K, et al. **Resting-state multi-spectrum functional connectivity networks for identification of MCI patients.** *PLoS One* 2012;7:e37828 CrossRef Medline
77. Shirer WR, Jiang H, Price CM, et al. **Optimization of rs-fMRI preprocessing for enhanced signal-noise separation, test-retest reliability, and group discrimination.** *Neuroimage* 2015;117:67–79 CrossRef Medline
78. Risk BB, Murden RJ, Wu J, et al. **Which multiband factor should you choose for your resting-state fMRI study?** *Neuroimage* 2021;234:117965 CrossRef Medline
79. Van Dijk KR, Sabuncu MR, Buckner RL. **The influence of head motion on intrinsic functional connectivity MRI.** *Neuroimage* 2012;59:431–38 CrossRef Medline
80. Alakorkko T, Saarimäki H, Glerean E, et al. **Effects of spatial smoothing on functional brain networks.** *Eur J Neurosci* 2017;46:2471–80 CrossRef Medline
81. Mikl M, Mareček R, Hlustik P, et al. **Effects of spatial smoothing on fMRI group inferences.** *Magn Reson Imaging* 2008;26:490–503 CrossRef Medline
82. Kokkonen SM, Nikkinen J, Remes J, et al. **Preoperative localization of the sensorimotor area using independent component analysis of resting-state fMRI.** *Magn Reson Imaging* 2009;27:733–40 CrossRef Medline
83. Huang H, Ding Z, Mao D, et al. **PreSurgMapp: a MATLAB Toolbox for presurgical mapping of eloquent functional areas based on task-related and resting-state functional MRI.** *Neuroinformatics* 2016;14:421–38 CrossRef Medline
84. Friston KJ, Holmes AP, Poline JB, et al. **Analysis of fMRI time-series revisited.** *Neuroimage* 1995;2:45–53 CrossRef Medline
85. Ball T, Breckel TP, Mutschler I, et al. **Variability of fMRI-response patterns at different spatial observation scales.** *Hum Brain Mapp* 2012;33:1155–71 CrossRef Medline
86. Pajula J, Tohka J. **Effects of spatial smoothing on inter-subject correlation based analysis of fMRI.** *Magn Reson Imaging* 2014;32:1114–24 CrossRef Medline

# Diffusion-Weighted Imaging Reveals Impaired Glymphatic Clearance in Idiopathic Intracranial Hypertension

 Derrek Scharztz, Alan Finkelstein, Nhat Hoang, Matthew T. Bender,  Giovanni Schifitto, and Jianhui Zhong



## ABSTRACT

**BACKGROUND AND PURPOSE:** The pathophysiology underlying idiopathic intracranial hypertension (IIH) remains incompletely understood. While one theory postulates impaired cerebral glymphatic clearance in IIH, there is a paucity of methods to quantify glymphatic activity in human brains. The purpose of this study was to use advanced diffusion-weighted imaging to evaluate the glymphatic clearance of IIH patients and how it may relate to clinical severity.

**MATERIALS AND METHODS:** DWI was used to separately evaluate the diffusivity along the cerebral perivascular spaces and lateral association and projection fibers, with the degree of diffusivity used as a surrogate for glymphatic function (diffusion tensor image analysis along the perivascular space). Patients with IIH were compared with normal controls. Glymphatic clearance was correlated with several clinical metrics, including lumbar puncture opening pressure and Frisen papilledema grade (low grade: 0–2; high grade: 3–5).

**RESULTS:** In total, 99 patients with IIH were identified and compared with 6 healthy controls. Overall, patients with IIH had significantly lower glymphatic clearance based on DWI-derived diffusivity compared with controls ( $P = .005$ ). Additionally, in patients with IIH, there was a significant association between declining glymphatic clearance and increasing Frisen papilledema grade ( $P = .046$ ) but no correlation between opening pressure and glymphatic clearance ( $P = .27$ ). Furthermore, healthy controls had significantly higher glymphatic clearance compared with patients with IIH and low-grade papilledema ( $P = .015$ ) and high-grade papilledema ( $P = .002$ ). Lastly, patients with IIH and high-grade papilledema had lower glymphatic clearance compared with patients with IIH and low-grade papilledema ( $P = .005$ ).

**CONCLUSIONS:** Patients with IIH possess impaired glymphatic clearance, which is directly related to the extent of clinical severity. The DWI-derived parameters can be used for clinical diagnosis or to assess response to treatment.

**ABBREVIATIONS:** AQP = aquaporin; AUC = area under the curve; DTI-ALPS = DTI analysis along the perivascular space; FA = fractional anisotropy; IIH = idiopathic intracranial hypertension; ROC = receiver operating characteristic

Idiopathic intracranial hypertension (IIH) is a disease characterized by increased intracranial pressure of unknown etiology.<sup>1</sup> While generally considered multifactorial, a principal underlying process driving IIH pathophysiology has yet to be identified. A small number of groups have recently theorized that IIH might primarily be a consequence of abnormally functioning cerebral

glymphatics with impaired clearance of CSF and cerebral interstitial fluid.<sup>2–4</sup> Broadly, the cerebral glymphatic system is a “brain-wide pathway for fluid transport, which includes the para-arterial influx of subarachnoid CSF into the brain interstitium, followed by clearance of interstitial fluid along large-caliber draining veins.”<sup>5</sup> Nonetheless, experimental evidence supporting the dysfunctional glymphatic model for IIH remains sparse, largely due to a paucity of methods to measure glymphatic flow within the human brain.

Recently, MR imaging has been leveraged to noninvasively evaluate the cerebral glymphatic system.<sup>6–10</sup> More specifically, the diffusion tensor image analysis along the perivascular space (DTI-ALPS) technique has emerged as a robust imaging method to quantify the degree of glymphatic clearance and has been used in numerous prior studies.<sup>6–10</sup> DTI-ALPS allows the assessment of glymphatic activity without intravenous or intrathecal contrast agent injection. The glymphatic clearance assessed with DTI-ALPS has been shown to be correlated with that assessed with the


Received August 14, 2023; accepted after revision November 2.

From the Departments of Imaging Sciences (D.S., A.F., N.H., G.S., J.Z.), Neurosurgery (M.T.B.), and Neurology (G.S.), University of Rochester Medical Center, Rochester, New York.

Supported by the Department of Imaging Sciences, University of Rochester Medical Center, Fischer Fund Grant. Supported in part by National Institutes of Health Grants R01MH118020 and R01AG054328.

Derrek Scharztz and Alan Finkelstein contributed equally to this work.

Please address correspondence to Derrek Scharztz, MD, Department of Imaging Sciences, University of Rochester Medical Center, 601 Elmwood Ave, Rochester, NY 14642; e-mail: derrek\_scharztz@urmc.rochester.edu; @D\_ScharztzMD

 Indicates article with online supplemental data.

<http://dx.doi.org/10.3174/ajnr.A8088>

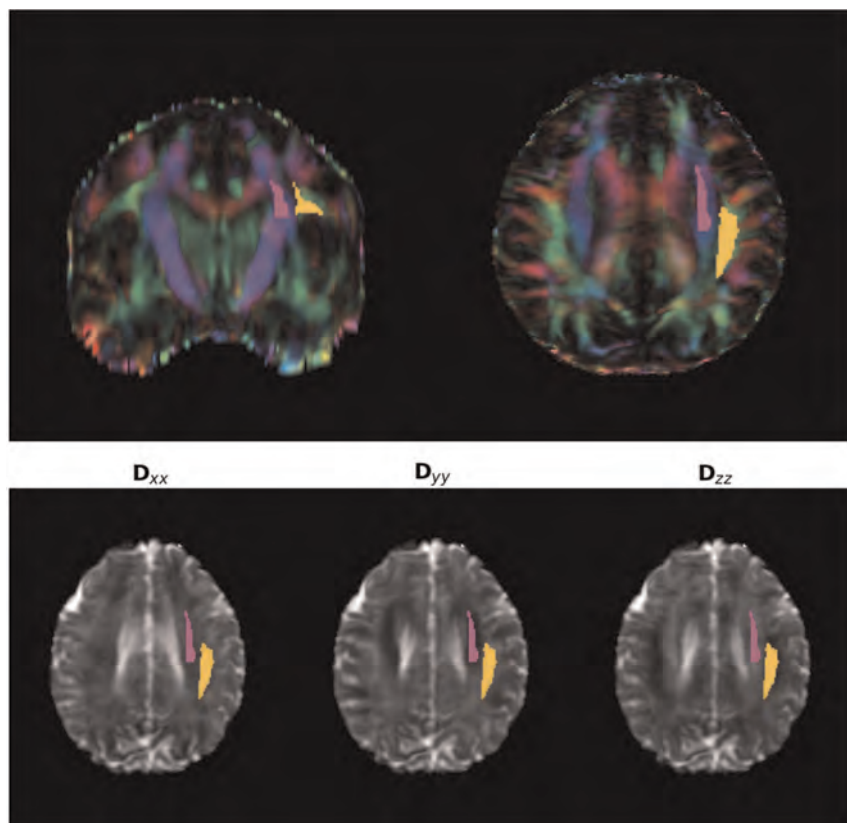


**FIG 1.** ROI by using atlas-based ALPS index. Top row: The projection (superior and posterior corona radiata, *magenta*) and association (superior longitudinal fasciculus, *yellow*) fibers were defined by the labels of the ICBM DTI-81 Atlas. Bottom row: Gray-scale maps of X, Y, and Z diffusion with ROIs.

direct intrathecal tracer-based measurement in humans.<sup>6-10</sup> In short, the DTI-ALPS method measures the diffusivity along the perivascular space compared with projection and association fibers adjacent to the lateral ventricle body, and serves as a measure of glymphatic outflow.<sup>5-10</sup> Here, we hypothesized that patients with IIH possessed impaired glymphatic clearance that could be directly identified and measured by using the DTI-ALPS method.

## MATERIALS AND METHODS

### Patient Cohort

In this retrospective study, approved by our Institutional Research Subject Review Board (STUDY00008280), 99 patients with clinically diagnosed IIH were retrospectively identified from our single-center tertiary care institution from 2016 to 2023. A small set of healthy controls ( $n = 6$ ) were also retrospectively identified who possessed no significant medical history (including no history of chronic headaches), and had normal brain MRIs. All subjects had previously undergone MR imaging as part of their standard of care (performed as part of a standardized MR imaging protocol), including structural T1-weighted imaging and DWI with 12 or 14 directions.

### Inclusion and Exclusion Criteria

Patients with clinically diagnosed IIH were enrolled according to diagnostic criteria as previously described by Friedman et al.<sup>11</sup> Patients with no other confounding neurologic disorders (eg,

brain tumor, migraine, multiple sclerosis, meningitis, etc) were retrospectively identified based on the inclusion of a T1-weighted scan and DWI with at least 12 directions. All imaging was completed within 3 months of clinical diagnosis and before any medical or interventional treatment. Patients up to the age of 50 were eligible for inclusion; patients older than 50 years were excluded because increasing age and small vessel disease have been shown to influence ALPS index and may function as a confounding variable.<sup>6,12</sup>

### Clinical Data

Clinical data on IIH patient demographics, presenting clinical features, and pertinent past medical history were collected and presented. Furthermore, documented Frisen papilledema grade at time of initial presentation and diagnosis was collected along with lumbar puncture opening pressure in the lateral decubitus position.

### Image Acquisition

All images were acquired on a 3T Discovery 750 MR imaging system (GE Healthcare) with an 8-channel head coil. Anatomic T1-weighted imaging was acquired as well as a standard clinical

DTI protocol with 12–14 diffusion-weighted directions with  $b = 1000$  seconds/mm<sup>2</sup> and 4  $b = 0$  reference images.

### Quantification with DTI-ALPS

This study leveraged the DTI-ALPS technique to quantify the degree of cerebral glymphatic function, which has been well described in prior studies.<sup>6-10</sup> DWI data were corrected for eddy current-induced distortion by using EDDY\_CORRECT in FSL (<https://fsl.fmrib.ox.ac.uk/fsl/fslwiki/eddy>). Susceptibility-induced distortion was corrected by using INVERSION consisting of inverse contrast normalization of T1-weighted data and diffeomorphic coregistration by using symmetric normalization in ANTs (<http://stnava.github.io/ANTs/>).<sup>13</sup> Diffusivity maps along the x-axis ( $D_{xx}$ ), y-axis ( $D_{yy}$ ), and z-axis ( $D_{zz}$ ) were computed in addition to fractional anisotropy (FA), mean diffusivity, axial diffusivity, and radial diffusivity by using DIPY (<https://dipy.org/index.html>). FA maps were coregistered to the FA map template FMRIB58 atlas by using ANTs. The FA registration matrix was used to warp all other DTI maps to standard space. Modified JHU ICBM white matter labels were used for the projection (superior corona radiata) and association fibers (superior longitudinal fasciculus) in the periventricular area.<sup>14</sup> As a quality assurance step, ROIs were defined in standard (MNI) space, and all diffusion directions were warped to MNI space. In addition, all subjects were individually reviewed for correct registration and ROI placement. An example atlas-based ROI determination can be seen in Figure 1. In accordance with prior studies, the DTI-ALPS

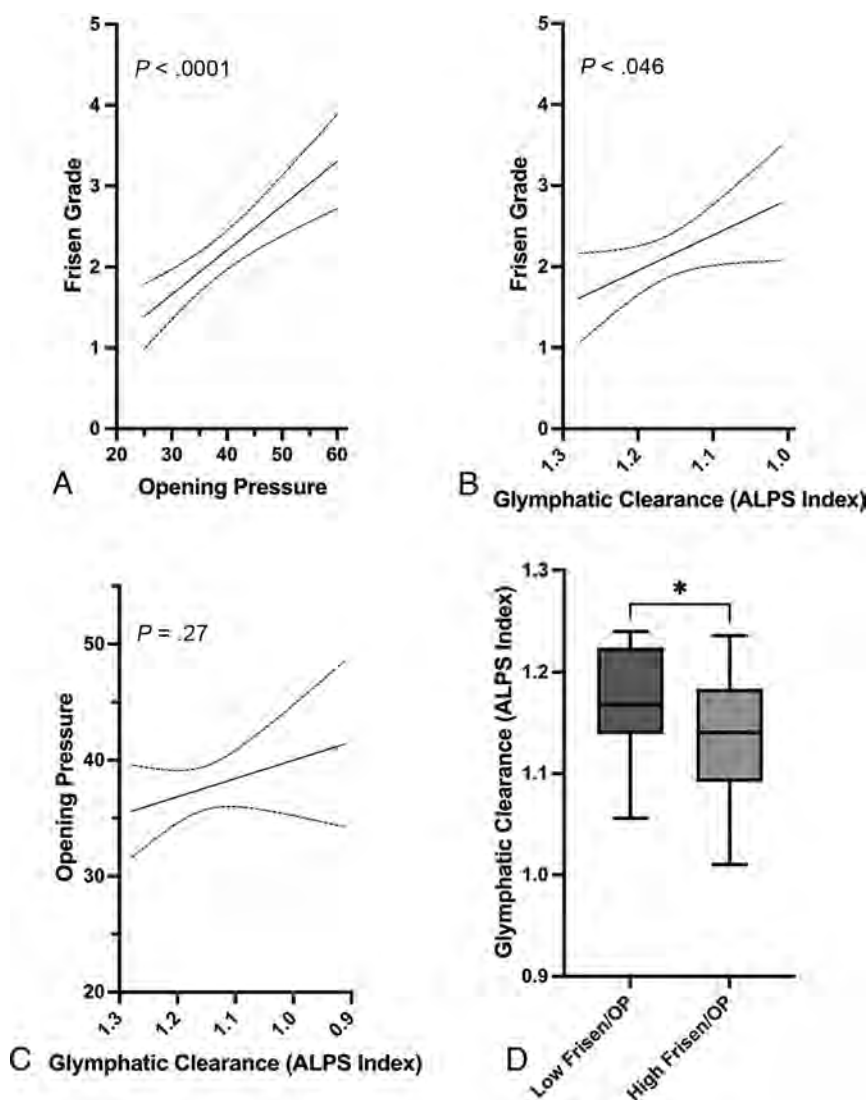


**FIG 2.** A, Association between lumbar puncture opening pressure and Frisen papilledema grade in patients with IIH. B, Association between glymphatic function (ALPS index) and Frisen papilledema grade. The glymphatic clearance on the x-axis is declining moving left to right. C, Association between glymphatic clearance and lumbar puncture opening pressure in patients with IIH. D, Box-and-whisker plot showing difference in glymphatic clearance between patients with IIH and low Frisen grade papilledema (0–2) and lower opening pressure (<50th percentile in cohort) compared with patients with IIH and high Frisen grade papilledema (3–5) and higher opening pressure ( $\geq 50$ th percentile). \* indicates  $P < .05$ .

index, which is used as a measure of glymphatic flow, was then computed by using these labels, defined by the following:

$$ALPS\ index = \frac{mean(Dxx_{proj}, Dxx_{assoc})}{mean(Dyy_{proj}, Dzz_{assoc})}$$

### Statistical Analysis

Correlations among continuous variables (opening pressure, Frisen papilledema grade, ALPS index, etc) were performed via linear regression. Differences between and among groups were assessed by an unpaired, 2-tailed  $t$  test or 1-way ANOVA. Additionally, receiver operating characteristic (ROC) curve analysis with calculation of the area under the curve (AUC) was completed to assess the diagnostic performance of the

ALPS index for patients with IIH versus controls and between less-severe and more-severe IIH cases. All statistical analyses were completed and graphed by using GraphPad Prism statistical software (version 10). For all statistical tests, a  $P$  value of  $\leq .05$  was used to indicate statistical significance.

## RESULTS

### Patient Clinical Characteristics

A total of 99 patients with clinically diagnosed IIH with sufficient MR imaging sequences for analysis were retrospectively identified. The average age at diagnosis was 29 years (SD: 8 years), 88% were female, and the average body mass index was 40.7 (SD: 8.3). Regarding presenting clinical features, 90% presented with a headache, 69.7% had visual disturbance, 94% had papilledema at presentation, and the mean opening pressure on lateral decubitus lumbar puncture was 37.6 cmH<sub>2</sub>O (SD: 9.4). Frisen papilledema grade was explicitly documented in 81 of the patients with IIH (median grade = 2). MRV was completed in 91 (92%) patients with IIH, and some degree of venous sinus stenosis was present in 82 (90%) cases. Complete pertinent clinical characteristics of the patients with IIH are shown in the Online Supplemental Data. Regarding healthy controls, 6 female patients were identified with a mean age of 25.2 (SD: 2.3) and mean body mass index of 27.2 (SD: 6.3). There was no significant difference in mean age between patients with IIH and controls ( $P = .2$ ). These 6 controls had normal brain MRIs and had no

significant past medical history, including no history of chronic headaches.

### Glymphatic Clearance and DWI Analysis

First, there was no statistical difference in the number of DTI diffusion directions between the subjects (mean, 17.529; SD: 9.4) and controls (mean, 16.5; SD: 4.5) ( $P = .45$ ). Overall, control patients had significantly higher glymphatic clearance (ALPS index mean, 1.23; SD, 0.04; coefficient of variation: 3.2%) compared with patients with IIH (mean, 1.15; SD, 0.07) ( $P = .005$ ). Additionally, there was a significant correlation between worsening/increasing Frisen papilledema grade and lumbar puncture opening pressure within the patients with IIH ( $P < .0001$ ) (Fig 2A). There was also a significant association between declining

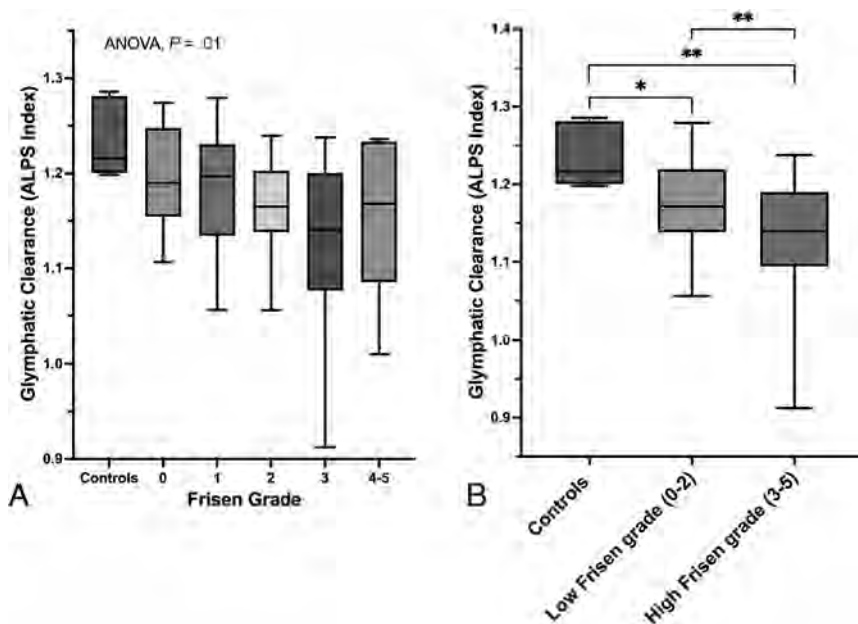


**FIG 3.** A, Box-and-whisker plot showing glymphatic clearance and how it relates between controls and patients with IIH and varying Frisen papilledema grades. B, Box-and-whisker plot showing difference in glymphatic clearance between controls and patients with IIH and low-grade papilledema (Frisen grade 0–2) and high-grade papilledema (Frisen grade 3–5). \* indicates  $P < .05$ ; \*\* indicates  $P < .01$ .

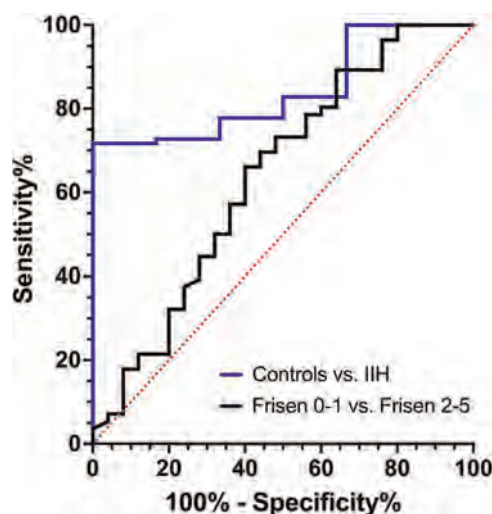


**FIG 4.** ROC curve analysis assessing the diagnostic performance of the ALPS index between patients with IIH versus controls and between patients with IIH and less-severe (Frisen papilledema grade 0–1) and more-severe (Frisen papilledema grade 2–5) disease.

glymphatic clearance and worsening Frisen grade ( $P = .046$ ) (Fig 2B). However, there was no significant relation between glymphatic outflow and lumbar puncture opening pressure ( $P = .27$ ) (Fig 2C). Given the significant association between Frisen grade and opening pressure (Fig 2A), we hypothesized that there may be a difference in glymphatic clearance between patients with IIH and both low Frisen grade (0–2) and lower opening pressure ( $< 50$  percentile of cohort) compared with patients with both high Frisen grade ( $\geq 3$ ) and higher opening pressure ( $\geq 50$  percentile). We found that patients with both a

high Frisen grade and higher opening pressure had significantly lower glymphatic clearance compared with those with a low Frisen grade and lower opening pressure ( $P = .029$ ) (Fig 2D).

Because we found that glymphatic clearance was significantly associated with the clinical severity of papilledema (Fig 2B), we investigated how the glymphatic outflow of controls compared with patients with IIH and varying Frisen grade. Between-groups ANOVA test demonstrated significantly different degrees of glymphatic clearance between controls and different Frisen grades ( $P = .01$ , Fig 3A). Furthermore, patients with low Frisen grade (0–2) papilledema had significantly lower glymphatic clearance compared with controls ( $P = .015$ ). Similarly, patients with high Frisen grade papilledema (3–5) also had significantly lower glymphatic clearance compared with healthy controls ( $P = .002$ ). Last, patients with IIH and high-grade papilledema also had significantly lower glymphatic clearance compared with patients with IIH and low-grade papilledema ( $P = .005$ ) (Fig 3B).

#### ROC Curve Analysis

ROC curve analysis was completed to assess the diagnostic performance of the ALPS index between IIH cases versus controls and between patients with IIH and less-severe (Frisen grade 0–1) and more-severe (Frisen grade 2–5) cases. Regarding IIH cases versus controls, ROC curve analysis demonstrated an AUC of 0.842 (SD, 0.06,  $P = .005$ ), where an ALPS index of  $< 1.197$  was found to have a sensitivity of 71.7% and a specificity of 100% (Fig 4). When comparing less-severe IIH cases to more-severe IIH cases, ROC curve analysis demonstrated an AUC of 0.64 (SD: 0.07,  $P = .045$ ), where an ALPS index of  $< 1.179$  had a sensitivity of 66.1% and a specificity of 60% (Fig 4). However, when comparing Frisen grade 0–2 versus Frisen grade 3–5, ROC curve analysis was not statistically significant (AUC: 0.62,  $P = .06$ ).

#### DISCUSSION

This study used the DTI-ALPS technique to evaluate the cerebral glymphatic system in patients with IIH. We found that overall patients with IIH had significantly lower glymphatic clearance compared with healthy controls ( $P = .005$ ). Additionally, we found a direct association between worsening clinical papilledema and declining glymphatic clearance ( $P = .046$ ). Moreover, this study demonstrated that, compared with controls, patients with IIH had lower glymphatic clearance with both low-grade ( $P = .015$ ) and high-grade papilledema ( $P = .002$ ). Overall, these findings suggest that there is impaired glymphatic clearance in IIH and that the degree of impaired clearance is directly associated with degree of clinical severity.

The pathophysiology of IIH remains incompletely understood. Though many consider the pathophysiology to be multifactorial, there is a developing hypothesis that IIH is principally due to impairment of the cerebral lymphatic system.<sup>2,3</sup> Likewise, some have postulated a link between aquaporin-4 (AQP4) alterations and impaired lymphatic outflow resulting in IIH.<sup>2,15</sup> However, this hypothesis is largely theoretical with limited experimental evidence to substantiate that lymphatic dysfunction is actually present in IIH. One of the reasons for this is a paucity of methods to evaluate the lymphatic system in patients.

While data are overall sparse, a few studies have suggested that impaired lymphatic flow is present in IIH. One of the first studies to suggest lymphatic dysfunction in IIH was by Alperin et al<sup>16</sup> who compared 11 patients with IIH with 11 controls by using MR imaging and showed increased gray matter interstitial volume in patients with IIH. Additionally, a prior study by using gadobutrol MR imaging tracer compared 15 patients with IIH with 15 controls and found delayed tracer clearance in patients with IIH, suggesting impaired lymphatic clearance.<sup>17</sup> It has also been shown that patients with IIH possess a higher quantity of cerebral perivascular spaces, a suspected pathway of the lymphatic system, which has indirectly suggested impaired lymphatic outflow in IIH.<sup>18</sup>

The presented analysis is the first study to demonstrate that the magnitude of lymphatic clearance as defined with diffusion measurement in IIH is directly associated with the extent of clinical severity (Figs 2B, 3B), suggesting that impaired lymphatic clearance underlies IIH pathophysiology and may drive disease. These findings, combined with impaired cerebral venous outflow thought to be involved in IIH, further suggest that IIH is a “glymphedema” of the brain.<sup>19</sup> Likewise, it has been previously hypothesized by Alperin et al<sup>16,20</sup> that resistance to cerebral venous return is the potential genesis leading to increased brain interstitial volume. Together, this could suggest that impaired cerebral venous return — possibly, via venous sinus stenosis, or other mechanisms — results in veno-glymphatic congestion and either causes or exacerbates the observed impaired lymphatic clearance. Future studies may investigate how diffusivity is related to extent of venous collaterals or degree of venous sinus stenosis.

Nonetheless, while our findings provide evidence for the IIH lymphatic dysfunction model, the underlying molecular mechanisms have yet to be elucidated. However, it has been theorized that defective AQPs involved in cerebral fluid transport and lymphatic outflow may be dysfunctional in IIH, possibly due to hormonal or genetic alterations.<sup>2</sup> Likewise, AQP4 has been shown to regulate water transport between the brain and CSF,<sup>5</sup> and has also been shown to be differentially expressed in IIH.<sup>21</sup> Similarly, AQP1 has been implicated in drug-induced IIH.<sup>22</sup> Regardless, further research is required to unravel the molecular mechanism between IIH and possible lymphatic dysfunction. Also, additional imaging analysis of other DTI parameters, such as perfusion or chemical exchange saturation transfer imaging, may yield clinically meaningful insights in patients with IIH.

This study has several limitations that need to be considered. First, this is a single-center retrospective analysis, which subjects it to the inherent biases of this study design, such as selection bias of the included participants. In addition, recent work has shown

the ALPS index to be a robust metric across scanning parameters, but that it can vary with the number of diffusion-weighting directions.<sup>6</sup> Additionally, an obvious limitation is the small number of healthy controls within our cohort ( $n = 6$ ). Given the retrospective design of this study, identifying healthy controls without any significant possibly confounding medical history, and with adequate MR imaging sequences for analysis, is challenging. Nonetheless, even with such a small number of controls, we still detected a significant overall difference in lymphatic clearance in patients with IIH (Fig 2). Moreover, we found that papilledema grade was directly related to the extent of impaired lymphatic clearance in IIH, which is inherently a control-independent analysis (Figs 2B, 3B). Regardless, we believe that future studies investigating the lymphatic system in patients with IIH should ideally be prospectively designed and with a larger number of controls.

## CONCLUSIONS

Based on DWI-derived diffusivity, patients with IIH possess impaired lymphatic clearance that correlates with the extent of disease severity, providing further evidence that primary lymphatic dysfunction may underlie IIH pathophysiology. These DWI-derived parameters can also be used for clinical diagnosis or to assess early response to treatment. Further studies are needed to assess the efficacy of DTI-ALPS as a diagnostic and prognostic biomarker in patients with IIH.

Disclosure forms provided by the authors are available with the full text and PDF of this article at [www.ajnr.org](http://www.ajnr.org).

## REFERENCES

1. Markey KA, Mollan SP, Jensen RH, et al. **Understanding idiopathic intracranial hypertension: mechanisms, management, and future directions.** *Lancet Neurol* 2016;15:78–91 CrossRef Medline
2. Lenck S, Radovanovic I, Nicholson P, et al. **Idiopathic intracranial hypertension: the veno lymphatic connections.** *Neurology* 2018;91:515–22 CrossRef Medline
3. Bezerra ML, Ferreira AC, de Oliveira-Souza R. **Pseudotumor cerebri and lymphatic dysfunction.** *Front Neurol* 2017;8:734 CrossRef Medline
4. Mangalore S, Rakshith S, Srinivasa R. **Solving the riddle of ‘idiopathic’ in idiopathic intracranial hypertension and normal pressure hydrocephalus: an imaging study of the possible mechanisms.** *Monro-Kellie 3.0. Asian J Neurosurg* 2019;14:440–52 CrossRef Medline
5. Iliff JJ, Wang M, Liao Y, et al. **A paravascular pathway facilitates CSF flow through the brain parenchyma and the clearance of interstitial solutes, including amyloid  $\beta$ .** *Sci Transl Med* 2012;4:147ra111 CrossRef Medline
6. Taoka T, Masutani Y, Kawai H, et al. **Evaluation of lymphatic system activity with the diffusion MR technique: diffusion tensor image analysis along the perivascular space (DTI-ALPS) in Alzheimer’s disease cases.** *Jpn J Radiol* 2017;35:172–78 CrossRef Medline
7. Siow TY, Toh CH, Hsu JL, et al. **Association of sleep, neuropsychological performance, and gray matter volume with lymphatic function in community-dwelling older adults.** *Neurology* 2022;98:e829–38 CrossRef Medline
8. Lee DA, Lee J, Park KM. **Glymphatic system impairment in patients with status epilepticus.** *Neuroradiology* 2022;64:2335–42 CrossRef Medline
9. Bae YJ, Kim JM, Choi BS, et al. **Altered brain lymphatic flow at diffusion-tensor MRI in rapid eye movement sleep behavior disorder.** *Radiology* 2023;307:e221848 CrossRef Medline

10. Bae YJ, Choi BS, Kim JM, et al. **Altered glymphatic system in idiopathic normal pressure hydrocephalus.** *Parkinsonism Relat Disord* 2021;82:56–60 CrossRef Medline
11. Friedman DI, Liu GT, Digre KB. **Revised diagnostic criteria for the pseudotumor cerebri syndrome in adults and children.** *Neurology* 2013;81:1159–65 CrossRef Medline
12. Zhang W, Zhou Y, Wang J, et al. **Glymphatic clearance function in patients with cerebral small vessel disease.** *Neuroimage* 2021;238:118257 CrossRef Medline
13. Bhushan C, Haldar JP, Choi S, et al. **Co-registration and distortion correction of diffusion and anatomical images based on inverse contrast normalization.** *Neuroimage* 2015;115:269–80 CrossRef Medline
14. Yokota H, Vijayasarithi A, Cekic M, et al. **Diagnostic performance of glymphatic system evaluation using diffusion tensor imaging in idiopathic normal pressure hydrocephalus and mimickers.** *Curr Gerontol Geriatr Res* 2019;2019:5675014 CrossRef Medline
15. Steinruecke M, Tiefenbach J, Park JJ, et al. **Role of the glymphatic system in idiopathic intracranial hypertension.** *Clin Neurol Neurosurg* 2022;222:107446 CrossRef Medline
16. Alperin N, Ranganathan S, Bagci AM, et al. **MRI evidence of impaired CSF homeostasis in obesity-associated idiopathic intracranial hypertension.** *AJNR Am J Neuroradiol* 2013;34:29–34 CrossRef Medline
17. Eide PK, Pripp AH, Ringstad G, et al. **Impaired glymphatic function in idiopathic intracranial hypertension.** *Brain Commun* 2021;3:fcab043 CrossRef Medline
18. Jones O, Cutsforth-Gregory J, Chen J, et al. **Idiopathic intracranial hypertension is associated with a higher burden of visible cerebral perivascular spaces: the glymphatic connection.** *AJNR Am J Neuroradiol* 2021;42:2160–64 CrossRef Medline
19. Nicholson P, Kedra A, Shotar E, et al. **Idiopathic intracranial hypertension: glymphedema of the brain.** *J Neuroophthalmol* 2021;41:93–97 CrossRef Medline
20. Alperin N, Lee SH, Mazda M, et al. **Evidence for the importance of extracranial venous flow in patients with idiopathic intracranial hypertension (IIH).** *Intracranial Pressure and Brain Monitoring XII* 2005 (pp. 129–132). Vienna: Springer-Verlag
21. Eide PK, Eidsvaag VA, Nagelhus EA, et al. **Cortical astrogliosis and increased perivascular aquaporin-4 in idiopathic intracranial hypertension.** *Brain Res* 2016;1644:161–75 CrossRef Medline
22. Stiebel-Kalish H, Eyal S, Steiner I. **The role of aquaporin-1 in idiopathic and drug-induced intracranial hypertension.** *Med Hypotheses* 2013;81:1059–62 CrossRef Medline

# Assessment of Collateral Flow in Patients with Carotid Stenosis Using Random Vessel-Encoded Arterial Spin-Labeling: Comparison with Digital Subtraction Angiography

Shanshan Lu, Chunqiu Su, Yuezhou Cao, Zhenyu Jia, Haibin Shi, Yining He, and Lirong Yan



## ABSTRACT

**BACKGROUND AND PURPOSE:** Collateral circulation plays an important role in steno-occlusive internal carotid artery disease (ICAD) to reduce the risk of stroke. We aimed to investigate the utility of planning-free random vessel-encoded arterial spin-labeling (rVE-ASL) in assessing collateral flows in patients with ICAD.

**MATERIALS AND METHODS:** Forty patients with ICAD were prospectively recruited. The presence and extent of collateral flow were assessed and compared between rVE-ASL and DSA by using Contingency (C) and Cramer V (V) coefficients. The differences in flow territory alterations stratified by stenosis ratio and symptoms, respectively, were compared between symptomatic ( $n = 19$ ) and asymptomatic ( $n = 21$ ) patients by using the Fisher exact test.

**RESULTS:** Good agreement was observed between rVE-ASL and DSA in assessing collateral flow ( $C = 0.762$ ,  $V = 0.833$ , both  $P < .001$ ). Patients with ICA stenosis of  $\geq 90\%$  were more likely to have flow alterations ( $P < .001$ ). Symptomatic patients showed a higher prevalence of flow alterations in the territory of the MCA on the same side of ICAD (63.2%), compared with asymptomatic patients (23.8%,  $P = .012$ ), while the flow alterations in the territory of anterior cerebral artery did not differ ( $P = .442$ ). The collateral flow to MCA territory was developed primarily from the contralateral internal carotid artery (70.6%) and vertebrobasilar artery to a lesser extent (47.1%).

**CONCLUSIONS:** rVE-ASL provides comparable information with DSA on the assessment of collateral flow. The flow alterations in the MCA territory may be attributed to symptomatic ICAD.

**ABBREVIATIONS:** ACA = anterior cerebral artery; AcomA = anterior communicating artery; ASL = arterial spin-labeling; ECA = external carotid artery; ICAD = internal carotid artery disease; pCASL = pseudocontinuous ASL; PcomA = posterior communicating artery; rVE-ASL = random vessel-encoded arterial spin-labeling; SS = super-selective; VBA = vertebrobasilar artery; VE = vessel-encoded

Collateral circulation plays a pivotal role in maintaining cerebral perfusion, metabolism, and function in patients with steno-occlusive internal carotid artery disease (ICAD).<sup>1</sup> The overall annual risk of stroke is  $\sim 9\%$ – $18\%$  in symptomatic patients with ICAD with compromised cerebral perfusion and poor collateral flow.<sup>2</sup> Adequate collateral circulation can prevent hemodynamic deterioration and lower the risk of stroke occurrence.<sup>2,3</sup> The primary collateral flow develops in the circle of Willis via the

anterior and posterior communicating arteries (AcomA and PcomA, respectively). Secondary collateral pathways include the external carotid artery (ECA) via the ophthalmic artery and leptomeningeal anastomoses at the brain surface, which are recruited when the primary collaterals are insufficient.<sup>4</sup> In clinical practice, DSA remains the reference standard to assess collateral circulations. However, this procedure is invasive and bears the risk of neurologic complications and ionizing radiation, limiting its availability for routine long-term surveillance.<sup>5,6</sup> A noninvasive method that demonstrates selective angiographic information is desired to investigate collateral blood flow.

Arterial spin-labeling (ASL) MR perfusion imaging offers a noninvasive approach to measuring cerebral perfusion.<sup>7–10</sup> Among the ASL variants, vessel-selective ASL techniques enable depicting flow territories and assessing collateral pathways, where an individual or groups of brain-feeding arteries are labeled.<sup>2,11–15</sup> Super-selective ASL (SS-ASL) and vessel-encoded ASL (VE-ASL) are 2 conventional vessel-selective ASL techniques that are based on pseudocontinuous ASL (pCASL) but employ additional

Received July 12, 2023; accepted after revision November 7.

From the Departments of Radiology (S.L., C.S.) and Interventional Radiology (Y.C., Z.J., H.S.), The First Affiliated Hospital of Nanjing Medical University, Nanjing, Jiangsu Province, China; and Department of Radiology (Y.H., L.Y.), Feinberg School of Medicine, Northwestern University, Chicago, Illinois.

S. Lu and C. Su contributed equally to this work.

Please address correspondence to Lirong Yan, Department of Radiology, Feinberg School of Medicine, Northwestern University, 737 N Michigan Ave, Suite 1600, Chicago, IL 60611; e-mail: lirong.yan@northwestern.edu



Indicates article with online supplemental data.

<https://dx.doi.org/10.3174/ajnr.A8100>

gradients in between the radiofrequency pulses.<sup>14-16</sup> SS-ASL enables the labeling of a single artery,<sup>14,15</sup> while VE-ASL can label multiple vessels simultaneously.<sup>16</sup> However, prior knowledge of the positions of the feeding arteries is required during the implementation of both SS-ASL and VE-ASL, which increases the complexity of the protocol setting and prolongs scan preparation time.<sup>12</sup> Furthermore, these conventional vessel-selective ASL techniques are vulnerable to field inhomogeneity at the labeling locations.<sup>17,18</sup> To address the limitations, a random VE-ASL (rVE-ASL) has been introduced,<sup>13</sup> which not only allows for mapping vascular territories without prior knowledge but also uniquely identifies the locations of the corresponding feeding arteries in the tagging plane.

In this study, we aimed to evaluate the clinical utility of rVE-ASL in assessing collateral flows by comparison with DSA as the reference standard in patients with ICAD. We further investigated the flow alterations between patients with symptomatic and asymptomatic ICAD.

## MATERIALS AND METHODS

### Patients

The ethics committee of our institution approved the study protocol, and written informed consent was obtained from all patients. From February 2018 to December 2021, we recruited 53 patients with ICAD presenting with ICA stenosis ( $\geq 50\%$ ) or occlusion on noninvasive imaging (CT angiography, MR angiography, or ultrasonography) who underwent DSA for further evaluation and agreed to participate in rVE-ASL imaging from our single center. Those patients either experienced recent neurologic events (acute ischemic stroke or transient ischemic attack) or nonspecific neurologic symptoms, such as dizziness and headache. For patients with nonspecific symptoms, DSA was considered by clinicians for further evaluation when patients presented with ICA stenosis of  $\geq 70\%$ , or with ICA stenosis of  $\geq 50\%$  and had unstable plaques on noninvasive images. The time interval between DSA and rVE-ASL was within 1 week. After imaging, those with severe motion artifacts ( $n = 8$ ) on rVE-ASL, bilateral ICA stenosis ( $n = 3$ ), or severe intracranial arterial stenosis ( $n = 2$ ) were excluded from further analyses. Finally, 40 patients (34 men, mean age  $68.0 \pm 10.8$  years) were enrolled, including 19 symptomatic patients and 21 asymptomatic patients.

### MR Imaging Protocol

All the experiments were performed on a 3T MR scanner (Magnetom Skyra, Siemens) by using a 20-channel head-neck coil. Compressed-sensing time-of-flight MRA (CS TOF-MRA) equipped with inline reconstruction was performed with the following parameters:<sup>19</sup> TR = 21 ms, TE = 3.49 ms, flip angle =  $18^\circ$ , FOV =  $220 \times 200$  mm<sup>2</sup>, matrix =  $368 \times 334$ , acquired resolution =  $0.6 \times 0.6 \times 0.6$  mm<sup>3</sup>, and reconstructed resolution =  $0.4 \times 0.4 \times 0.4$  mm<sup>3</sup>. The TOF coverage extended from the bifurcation of the common carotid artery to the body of the corpus callosum (16 cm). DWI was performed with the imaging parameters as follows: b-value = 1000 mm<sup>2</sup>/s, TR = 6400 ms, TE = 98 ms, FOV =  $220 \times 220$  mm<sup>2</sup>, matrix =  $192 \times 192$ , section thickness = 4 mm, 20 slices. T2-weighted FLAIR was performed with the following parameters: TR = 8000 ms, TE = 97 ms, TI =

**Table 1: Distribution of collaterals grades by rVE-ASL and DSA**

rVE-ASL collateral grade	DSA collateral grade				Total
	0	1	2	3	
0	0	0	0	0	0
1	0	12	2	0	14
2	0	1	4	0	5
3	0	0	0	21	21
Total	0	13	6	21	40

**Note:**— 0: poor, no visible collaterals; 1: intermediate, partial collateral flow to the side of stenosis/occlusion; 2: good, full collateral flow to the side of stenosis/occlusion; 3: normal antegrade flow.

2370 ms, FOV =  $230 \times 230$  mm<sup>2</sup>, matrix =  $256 \times 230$ , section thickness = 5 mm, 20 slices.

rVE-ASL scan with background suppressed single-shot 3D gradient- and spin-echo acquisition was performed with the following parameters: FOV =  $220 \times 220$  mm<sup>2</sup>, matrix =  $64 \times 64$ , TR = 3650 ms, TE = 36 ms, labeling duration = 1500 ms, post-labeling delay = 1500 ms, 12 slices with the section thickness of 8 mm, 60 pairs of encoding steps with random orientation, phase and wavelength were acquired with 2 additional pairs of global label/control, leading to a total scan time of 7 minutes 32 seconds.

### DSA Protocol

DSA was performed by using the modified Seldinger method with a DSA machine (Allura Xper FD20, Philips). A 5F headhunter catheter was introduced into the ascending aorta via the transfemoral route and navigated into the appropriate carotid or vertebral artery, as decided by the angiographer. The arteries were displayed in at least 2 projections by automatic injection of 6–8 mL of iodixanol 320 (Visipaque, GE Healthcare). DSA was performed with a 270-mm FOV and a 1024 matrix, yielding a measured pixel size of  $0.27 \times 0.27$  mm<sup>2</sup>. We used variable frames-per-second (fps) in the DSA protocol containing 3 phases (phase 1: 6 fps for 4 s; phase 2: 2 fps for 8 s; phase 3: 1 fps for the remaining acquisition).

### rVE-ASL Postprocessing

rVE-ASL analysis was performed in MATLAB (MathWorks). The images were subtracted pair-wise, resulting in 60 vessel-encoded perfusion maps and 2 global perfusion maps. Theoretical ASL signals at each location in the labeling plane were calculated by using the 60 sets of predefined encoding parameters. The locations of feeding arteries were identified by calculating the correlation coefficient between the acquired perfusion signal per voxel and the theoretical ASL signals, and the corresponding perfusion territorial maps were subsequently determined based on the maximum correlation coefficient of each voxel. We divided the perfusion territories into 3 regions: right ICA, left ICA, and vertebrobasilar artery (VBA) territories. These images were subsequently combined into a red-green-blue frame to demonstrate the spatial distribution of the 3 perfusion territories (right ICA territory as green, left ICA territory as red, and VBA territory as blue).

### Assessment of ICA Stenosis and Collateral Flow

The luminal stenosis ratio was calculated by 1 experienced neurointerventional radiologist (14 years of experience) on DSA

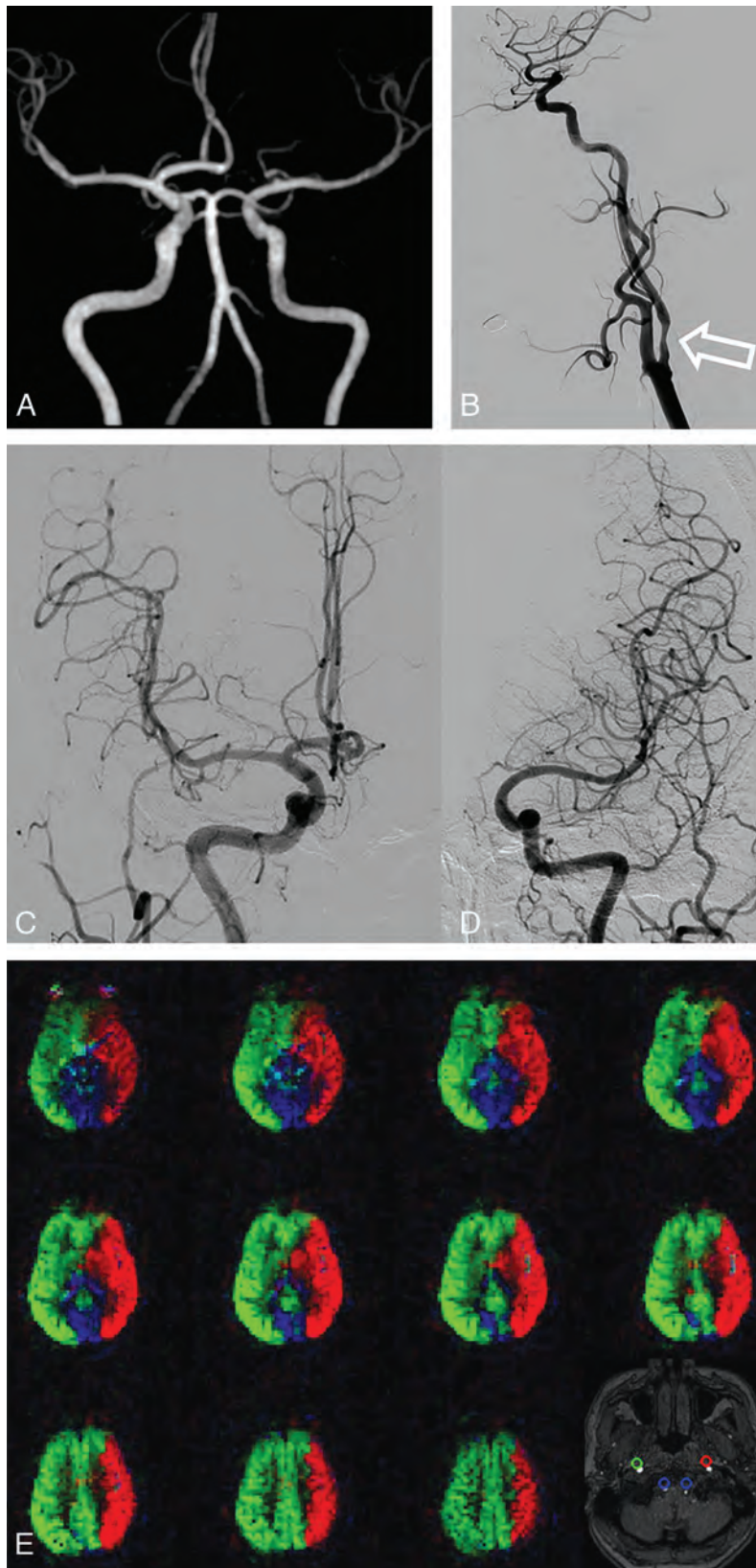


**FIG 1.** A 71-year-old male asymptomatic patient with left ICA stenosis. **A**, TOF-MRA shows the absence of the left A1 segment of the circle of Willis in this patient. **B–D**, DSA reveals a left ICA stenosis of 60%, but with a normal antegrade flow (grade III). The right ICA angiogram reveals normal antegrade flow to the left ACA territory. **E**, Vascular territory maps generated by rVE-ASL display flow territories of left ICA (red), right ICA (green), and VBA (blue), along with detected feeding arteries on the labeling plane. The right ICA supplies the left ACA territory, consistent with the findings on DSA.

according to the North American Symptomatic Carotid Endarterectomy Trial method:<sup>20</sup> stenosis ratio (%) =  $(1 - \text{artery diameter at the narrowest site} / \text{normal vessel diameter at the distal end of stenosis}) \times 100\%$ . If there were multiple stenoses in 1 segment, only the most stenotic site was selected for calculation.

The presence of collateral flow was assessed with reference to a previous report:<sup>21</sup> 1) anterior collateral flow: from the normal side across the AcomA to the A2 segment on the side of ICAD only or flow from the normal side across the AcomA and retrograde flow in the A1 segment on the stenotic side that supplies both the A2 segment and the MCA on the side of the ICAD; 2) posterior collateral flow: from the PcomA that supplies the vascular territory of MCA on the side of the ICAD; and 3) collateral flow in the leptomeningeal anastomoses was considered to be present if DSA showed cortical branches extending from the posterior cerebral artery or anterior cerebral artery (ACA) into the vascular territory of the MCA. It is worth noting that any changes in flow territories caused by normal anatomic variants of the circle of Willis, such as hypoplasia/absent A1 segment or fetal origin of posterior cerebral artery, were not considered as the presence of collateral flow in this study. However, in cases where there was no variation in ACA (hypoplasia/absent A1 segment), flow from the contralateral side passing through the AcomA to reach the A2 segment on the side of ICAD was considered as anterior collateral flow.

The extent of collateral flow was graded on both rVE-ASL and DSA at the ipsilateral hemisphere to the ICAD for each patient, respectively, giving a total of 40 hemispheres. Two neuroradiologists (10 and 6 years of experience, respectively) and 2 neurointerventional radiologists (14 and 8 years of experience, respectively) independently assessed the collateral grades, according to the following scale: 0: poor, no visible collaterals; 1: intermediate, partial collateral flow to the side of ICAD; 2: good, full collateral flow to the side of ICAD; 3: normal antegrade flow. Any

**Table 2: Flow alterations on rVE-ASL stratified by stenosis ratio**

	Stenosis Ratio	With Flow Alterations, n (%)	Without Flow Alterations, n (%)	P Value
Flow territory of MCA on the side of ICAD	< 90% (n = 24)	2 (8.3)	22 (91.7)	<.001
	≥ 90% (n = 16)	15 (93.8)	1 (6.2)	
Flow territory of ACA on the side of ICAD	< 90% (n = 24)	0 (0.0)	24 (100.0)	<.001
	≥ 90% (n = 16)	8 (50.0)	8 (50.0)	

**Table 3: Flow alterations on rVE-ASL stratified by symptoms**

	Patient Group	With Flow Alterations, n (%)	Without Flow Alterations, n (%)	P Value
Flow territory of MCA on the side of ICAD	Symptomatic (n = 19)	12 (63.2)	7 (36.8)	.012
	Asymptomatic (n = 21)	5 (23.8)	16 (76.2)	
Flow territory of ACA on the side of ICAD	Symptomatic (n = 19)	5 (26.3)	14 (73.7)	.442
	Asymptomatic (n = 21)	3 (14.3)	18 (85.7)	

disagreement between the readers was solved by another senior neuroradiologist (28 years of experience).

### Statistical Analysis

Quantitative data conforming to a normal distribution were represented as the mean  $\pm$  SD; otherwise, as the median (interquartile range presented as the 25th and 75th percentiles). Categorical data were recorded as counts and percentages. Cohen kappa coefficient was calculated to evaluate the interobserver reliability for assessing the extent of collaterals on rVE-ASL and DSA. Contingency (C) and Cramer V (V) coefficients were calculated with  $\chi^2$  statistics and were used to compare the collateral grades between rVE-ASL and DSA. The difference in flow alterations between symptomatic and asymptomatic patients was assessed by using the Fisher exact test. The *P* value was 2-sided, and *P* < .05 was considered statistically significant. All statistical analyses were conducted by using SPSS 22.0 (IBM).

## RESULTS

### Patient Characteristics

Of the 40 patients, 35 presented with ICA stenosis of 50%–99% and 5 presented with ICA occlusion. Anatomic variations of the circle of Willis were observed in 26 patients, including 16 patients with hypoplasia or absent A1 segment, 7 patients with fetal posterior cerebral artery, and 3 patients with both. The demographic, clinical, and imaging characteristics of patients are detailed in Online Supplemental Data.

### Comparison of Collateral Grades between rVE-ASL and DSA

The interreader agreement in grading collaterals by using rVE-ASL and DSA was found to be good to excellent, with kappa values of 0.876 and 0.764, respectively. Good agreement was achieved between rVE-ASL and DSA in grading collateral flow (C = 0.762; V = 0.833; *P* < .001). Of the 40 patients, only 2 cases that were graded as collateral grade II on DSA were misclassified as grade I on rVE-ASL, and 1 case showing grade I collaterals on DSA was classified as grade II on rVE-ASL. For the remaining 37 cases, the collaterals revealed by rVE-ASL match completely with the findings from DSA (Table 1). Figure 1 shows an example of the vascular territory maps revealed by rVE-ASL from an asymptomatic patient with left ICA stenosis of 60%, where a normal antegrade flow was observed, consistent with the DSA findings.

### Flow Alterations on rVE-ASL Stratified by Stenosis Ratio and Symptoms

Flow alterations were observed in 17 patients in the territory of MCA and 8 patients in the territory of ACA, respectively, on the side affected by ICAD (Online Supplemental Data). Notably, these flow alterations were more frequently observed in patients with high-grade ICA stenosis ( $\geq 90\%$ ) compared with those with <90% ICA stenosis, in both MCA and ACA vascular territories (*P* < .001 for both territories), as indicated in Table 2.

Symptomatic patients exhibited a high prevalence of flow alterations (63.2%) in the territory of MCA ipsilateral to ICAD, compared with asymptomatic patients (23.8%) (*P* = .012, as shown in Table 3). The collateral flow was primarily developed from the contralateral ICA via AcomA in 12 of 17 (70.6%) patients and from VBA via PcomA in 8 of 17 (47.1%) patients. Detailed information can be found in Online Supplemental Data. However, there were no significant differences in flow alterations in the territory of ACA between symptomatic and asymptomatic patients (*P* = .442). Figure 2 shows an example of an asymptomatic patient with right-side high-grade ICA stenosis. rVE-ASL demonstrated flow alterations in the territory of MCA with collaterals from the VBA, which was confirmed by DSA. Figure 3 shows a symptomatic case of ICAD with right ICA occlusion. Evident flow alterations in the territory of the right MCA with collaterals from the left ICA and the VBA were observed on rVE-ASL, consistent with DSA findings.

## DISCUSSION

In this study, we successfully demonstrated the feasibility of using rVE-ASL to assess collateral flows in patients with ICAD. Our results showed a good to excellent agreement between rVE-ASL and the reference standard of DSA in determining the presence and the extent of collaterals. Patients with a severe grade of ICA stenosis ( $\geq 90\%$ ) were more prone to experiencing flow alterations. The presence of flow alterations in the territory of the MCA may be linked to symptomatic ICAD.

The ability to determine the arterial source of blood supply to specific brain regions or lesions is crucial for the clinical evaluation and treatment of patients with ICAD. Some noninvasive methods, such as dynamic contrast-enhanced MRA, 4D flow MR imaging, or MR perfusion, can be considered to evaluate

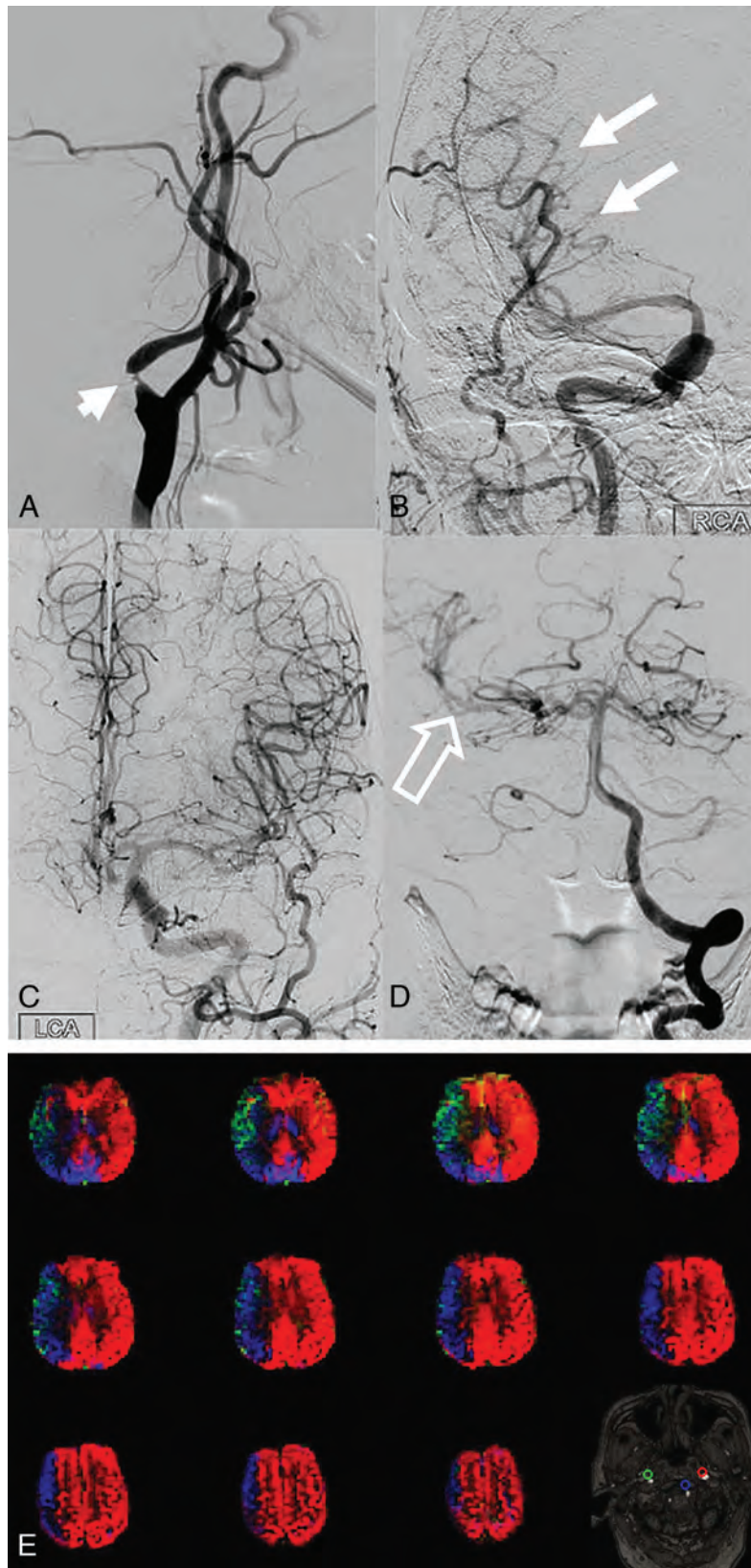


**FIG 2.** An 81-year-old male patient with dizziness for 2 years. *A–D*, DSA images reveal a very high-grade stenosis of the right ICA indicated by the white short arrow. The right ICA angiogram shows decreased flow to the right MCA territory (*white arrows*). The VBA angiogram shows significant collateral flow to the right MCA territory (*white hollow arrow*). The extent of collaterals is classified as grade I. *E*, Evident flow alterations are shown on vascular territory maps generated by rVE-ASL. The territory of right MCA is supplied by the right ICA (*green*) and VBA (*blue*), while the territory of right ACA is supplied by left ICA (*red*), consistent with the DSA findings. The extent of collaterals is also classified as grade I on rVE-ASL. The locations of the detected feeding arteries are shown in the bottom right of figure (*E*).

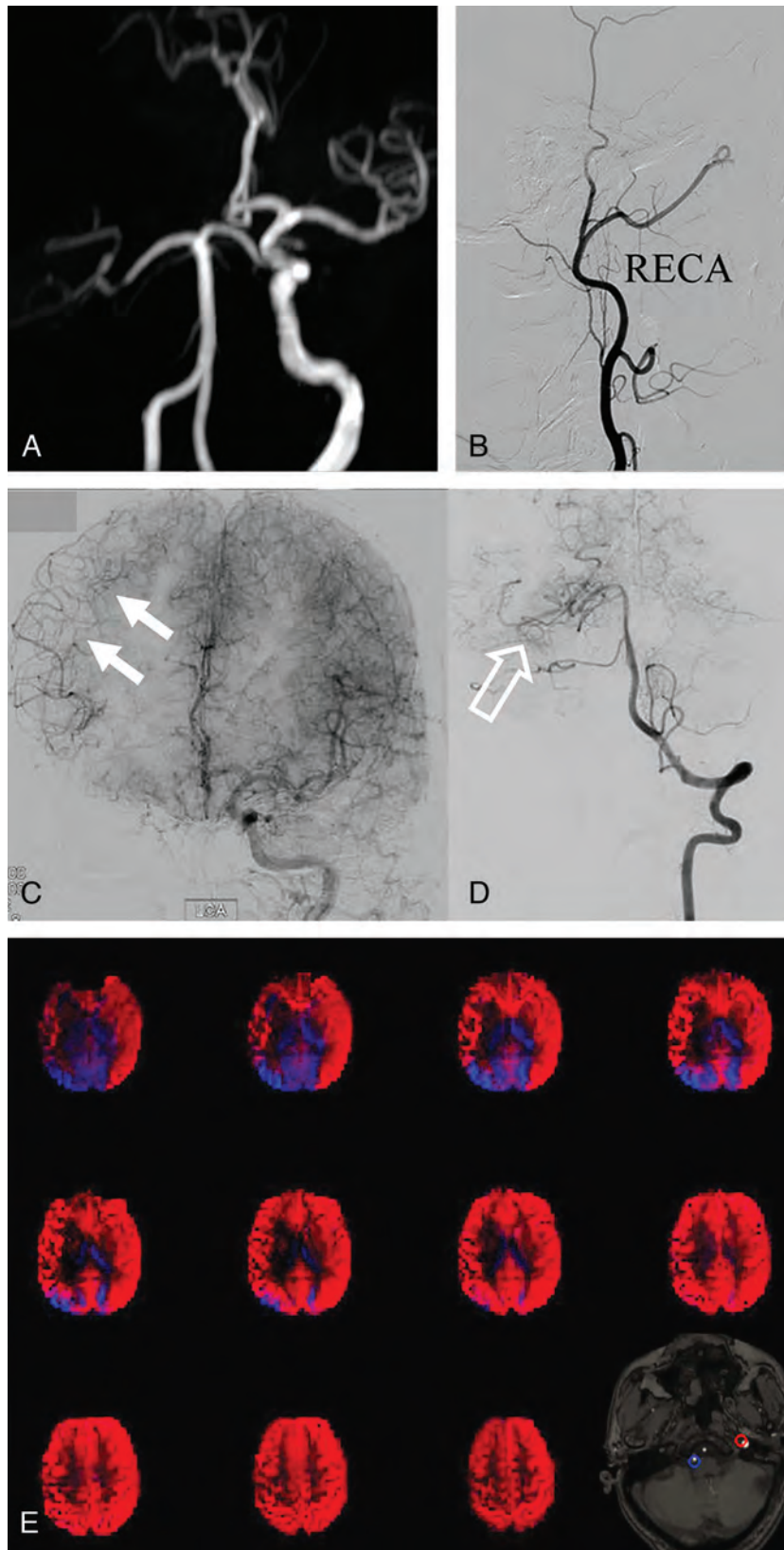


**FIG 3.** A 60-year-old man with left limb weakness for 3 days. A, TOF-MRA shows the occlusion in the right ICA and the absence of the right A1 segment of the circle of Willis in this patient. B–D, DSA confirms the occlusion of the right ICA, and the extent of collaterals is classified as grade I. The left ICA angiogram shows collateral flow to the right ACA and MCA territory via the AcomA and the leptomeningeal anastomoses (*white arrows*). The VBA angiogram shows collateral flow to the right MCA territory via the PcomA and leptomeningeal anastomoses (*white hollow arrow*). E, Vascular territory maps of rVE-ASL show flow territories of left ICA (*red*) and VBA (*blue*), while the flow territory of the right ICA (*green*) is absent. The territory of right MCA is mainly supplied by the left ICA, followed by VBA, consistent with the findings on DSA. The extent of collaterals is also classified as grade I on rVE-ASL. The locations of the detected feeding arteries are shown in the bottom right of figure (E).

patients with ICAD in clinical practice. Dynamic contrast-enhanced MRA and 4D flow MR imaging are considered “lumenography” and focus on depiction of dynamic blood flow patterns or measuring blood flow velocities in the cerebral vasculature. MR perfusion techniques, such as dynamic susceptibility contrast and conventional ASL, allow for CBF imaging. However, these MR imaging techniques can not characterize the collateral flow territories. Previous studies have suggested that vessel-selective ASL, such as VE-ASL and SS-ASL, could be a valuable tool for mapping the territories of main brain feeding arteries.<sup>7,22-24</sup> However, the conventional vessel-selective ASL techniques require prior knowledge of the locations of vessels to be tagged.<sup>12,17,18</sup> This in turn necessitates a collection of an angiogram and expertise in planning. In contrast, the rVE-ASL used in our study cannot only map vascular territories without the need for explicit planning but also identify the locations of corresponding source arteries in the tagging plane. This simplifies the scan procedure similar to conventional pCASL. In the conventional vessel-selective ASL based on pCASL, potential off-resonance at the locations of the arteries in the tagging plane can significantly impact the tagging efficiency. In contrast, rVE-ASL is insensitive to off-resonance effects similar to multiphase pseudocontinuous ASL.<sup>13</sup> Our study demonstrated a high consistency between vascular territory mapping by using rVE-ASL and DSA, indicating that rVE-ASL could serve as an alternative and noninvasive method to evaluate individual collateral pathways in patients with ICAD.

In this study, we observed that symptomatic patients with ICAD had a higher prevalence of flow alterations in the MCA territory on the affected side, compared with asymptomatic patients. However, there was no significant difference found in flow alterations in the ACA territory between symptomatic and asymptomatic patients. These findings are consistent with a previous study by van Laar et al,<sup>21</sup> which reported significant differences in the flow territories of the contralateral ICA and VBA in patients with symptomatic ICA occlusion compared with those in control subjects. They also reported that the MCA territory ipsilateral to the occluded ICA was primarily supplied by the VBA, whereas the flow territory of ACA on the occluded side was mainly supplied by the contralateral ICA. However, in contrast to their findings, our study found that collateral flow to the MCA territory on the side of ICAD was primarily developed from the contralateral ICA (70.6% via AcomA) and, to a lesser extent, from the VBA (47.1% via PcomA). These differences in the collateral flow patterns may be attributed to variations in the circle of Willis among individuals. Previous studies have also emphasized the importance of collateral flow from the contralateral ICA via AcomA or VBA.<sup>25-29</sup> Our results further support the significance of collateral flows from the contralateral ICA in maintaining blood flow in the MCA territory on the side of ICAD. In symptomatic patients without flow alteration, inadequate collateral compensation may lead to a borderzone infarct. Additionally, artery-to-artery embolism induced by vulnerable plaque can also contribute to the occurrence of stroke/TIA in these patients.

Our study also revealed a significant association between flow alterations and the degree of stenosis. Consistent with the

findings of Chen et al,<sup>30</sup> who reported the existence of high-grade stenosis associated with hemispheric asymmetry in flow territory map, we found that a high-grade ICA stenosis ( $\geq 90\%$ ) was most likely to result in flow alterations. Traditionally, the stenotic rate of ICA  $\geq 70\%$  is considered an indicator of hemodynamic impairment. However, our study indicates that patients with high-grade ICA stenosis could remain asymptomatic despite exhibiting flow alterations. These findings suggest that changes in flow territory may occur before CBF deficits manifest, and adequate compensating collateral flow may protect patients from the deterioration of clinical symptoms. Flow assessment by rVE-ASL can demonstrate the redistribution of CBF from the contralateral ICA and VBA, reflecting compensating patterns and the presence of collateral pathways in patients with ICAD, and may help predict the borderzone prone to infarction. Importantly, rVE-ASL offers several advantages, such as noninvasive imaging without radiation exposure, no requirement for additional contrast agents, and high compatibility with other routine MR imaging (eg, DWI). Therefore, rVE-ASL can be a valuable tool for longitudinal monitoring of disease progression in patients with ICAD and may assist in decision-making regarding patient selection for interventional therapy.

This study has limitations. First, this is a pilot study with limited sample size, which may affect the generalizability of the results. Future studies with larger cohorts are needed to further validate the clinical utility of the rVE-ASL method. Second, some secondary collateral pathways, such as the ECA via the ophthalmic artery, were not evaluated in our study. However, such secondary collaterals generally develop only in patients with near-total occlusion or total occlusion of ICA when primary collaterals are insufficient. There were 4 patients who showed secondary collateral pathways developed from the ECA via the ophthalmic artery on DSA in our study. Flow territories of the ECA were successfully detected by rVE-ASL. One representative case is shown in Online Supplemental Data. Third, the number of symptomatic patients with ICA stenosis of 50%–90% was relatively small, potentially introducing some bias in the interpretation of findings. Finally, prospective studies are still warranted to investigate the prognostic effect of compensating patterns in patients with ICAD, which could be helpful in guiding patient selection for interventional therapy.

## CONCLUSIONS
















Our study demonstrates the feasibility of using rVE-ASL to assess collateral flows in patients with ICAD, yielding results comparable to DSA. Patients with very high-grade ICA stenosis ( $\geq 90\%$ ) are prone to exhibit flow alterations. The collateral flow in the territory of MCA on the affected side is primarily developed from the contralateral ICA, and its presence could serve as a potential predictor of symptomatic ICAD. These findings emphasize the potential clinical utility of rVE-ASL in assessing collateral circulation and its possible role in predicting and managing ICAD.

**Disclosure forms** provided by the authors are available with the full text and PDF of this article at [www.ajnr.org](http://www.ajnr.org).

## REFERENCES

1. Liebeskind DS. **Collateral circulation.** *Stroke* 2003;34:2279–84 CrossRef Medline
2. Hartkamp NS, Petersen ET, Chappell MA, et al. **Relationship between haemodynamic impairment and collateral blood flow in carotid artery disease.** *J Cereb Blood Flow Metab* 2018;38:2021–32 CrossRef Medline
3. Vernieri F, Pasqualetti P, Matteis M, et al. **Effect of collateral blood flow and cerebral vasomotor reactivity on the outcome of carotid artery occlusion.** *Stroke* 2001;32:1552–58 CrossRef Medline
4. Hofmeijer J, Klijn CJ, Kappelle LJ, et al. **Collateral circulation via the ophthalmic artery or leptomeningeal vessels is associated with impaired cerebral vasoreactivity in patients with symptomatic carotid artery occlusion.** *Cerebrovasc Dis* 2002;14:22–26 CrossRef Medline
5. Henderson RD, Eliasziw M, Fox AJ, et al. **Angiographically defined collateral circulation and risk of stroke in patients with severe carotid artery stenosis.** North American Symptomatic Carotid Endarterectomy Trial (NASCET) Group. *Stroke* 2000;31:128–32 CrossRef Medline
6. Kaufmann TJ, Huston J 3rd, Mandrekar JN, et al. **Complications of diagnostic cerebral angiography: evaluation of 19,826 consecutive patients.** *Radiology* 2007;243:812–19 CrossRef Medline
7. Petersen ET, Zimine I, Ho YC, et al. **Non-invasive measurement of perfusion: a critical review of arterial spin labelling techniques.** *Br J Radiol* 2006;79:688–701 CrossRef Medline
8. Alsop DC, Detre JA, Golay X, et al. **Recommended implementation of arterial spin-labeled perfusion MRI for clinical applications: a consensus of the ISMRM perfusion study group and the European consortium for ASL in dementia.** *Magn Reson Med* 2015;73:102–16 CrossRef Medline
9. Detre JA, Leigh JS, Williams DS, et al. **Perfusion imaging.** *Magn Reson Med* 1992;23:37–45 CrossRef Medline
10. Williams DS, Detre JA, Leigh JS, et al. **Magnetic resonance imaging of perfusion using spin inversion of arterial water.** *Proc Natl Acad Sci USA* 1992;89:212–16 CrossRef Medline
11. Zhang X, Ghariq E, Hartkamp NS, et al. **Fast cerebral flow territory mapping using vessel encoded dynamic arterial spin labeling (VE-DASL).** *Magn Reson Med* 2016;75:2041–49 CrossRef Medline
12. Wong EC. **Vessel-encoded arterial spin-labeling using pseudocontinuous tagging.** *Magn Reson Med* 2007;58:1086–91 CrossRef Medline
13. Wong EC, Guo J. **Blind detection of vascular sources and territories using random vessel encoded arterial spin labeling.** *Magn Reson Mater Phys* 2012;25:95–101 CrossRef Medline
14. Dai W, Robson PM, Shankaranarayanan A, et al. **Modified pulsed continuous arterial spin labeling for labeling of a single artery.** *Magn Reson Med* 2010;64:975–82 CrossRef Medline
15. Helle M, Norris DG, Rufer S, et al. **Superselective pseudocontinuous arterial spin labeling.** *Magn Reson Med* 2010;64:777–86 CrossRef Medline
16. van Osch MJ, Teeuwisse WM, Chen Z, et al. **Advances in arterial spin labelling MRI methods for measuring perfusion and collateral flow.** *J Cereb Blood Flow Metab* 2018;38:1461–80 CrossRef Medline
17. Okell TW, Garcia M, Chappell MA, et al. **Visualizing artery-specific blood flow patterns above the circle of Willis with vessel-encoded arterial spin labeling.** *Magn Reson Med* 2019;81:1595–604 CrossRef Medline
18. Okell TW, Harston GW, Chappell MA, et al. **Measurement of collateral perfusion in acute stroke: a vessel-encoded arterial spin labeling study.** *Sci Rep* 2019;9:8181 CrossRef Medline
19. Zhang X, Cao YZ, Mu XH, et al. **Highly accelerated compressed sensing time-of-flight magnetic resonance angiography may be reliable for diagnosing head and neck arterial steno-occlusive disease: a comparative study with digital subtraction angiography.** *Eur Radiol* 2020;30:3059–65 CrossRef Medline
20. North American Symptomatic Carotid Endarterectomy Trial. **Methods, patient characteristics, and progress.** *Stroke* 1991;22:711–20 CrossRef Medline
21. van Laar PJ, Hendrikse J, Klijn CJ, et al. **Symptomatic carotid artery occlusion: flow territories of major brain-feeding arteries.** *Radiology* 2007;242:526–34 CrossRef Medline
22. Rutgers DR, Klijn CJ, Kappelle LJ, et al. **A longitudinal study of collateral flow patterns in the circle of Willis and the ophthalmic artery in patients with a symptomatic internal carotid artery occlusion.** *Stroke* 2000;31:1913–20 CrossRef Medline
23. Chng SM, Petersen ET, Zimine I, et al. **Territorial arterial spin labeling in the assessment of collateral circulation: comparison with digital subtraction angiography.** *Stroke* 2008;39:3248–54 CrossRef Medline
24. Arteaga DF, Strother MK, Davis LT, et al. **Planning-free cerebral blood flow territory mapping in patients with intracranial arterial stenosis.** *J Cereb Blood Flow Metab* 2017;37:1944–58 CrossRef Medline
25. Kluytmans M, van der Grond J, van Everdingen KJ, et al. **Cerebral hemodynamics in relation to patterns of collateral flow.** *Stroke* 1999;30:1432–39 CrossRef Medline
26. Hendrikse J, Hartkamp MJ, Hillen B, et al. **Collateral ability of the circle of Willis in patients with unilateral internal carotid artery occlusion: border zone infarcts and clinical symptoms.** *Stroke* 2001;32:2768–73 CrossRef Medline
27. Hoksbergen AW, Majoie CB, Hulsmans FJ, et al. **Assessment of the collateral function of the circle of Willis: three-dimensional time-of-flight MR angiography compared with transcranial color-coded duplex sonography.** *AJNR Am J Neuroradiol* 2003;24:456–62 Medline
28. Lee JH, Choi CG, Kim DK, et al. **Relationship between circle of Willis morphology on 3D time-of-flight MR angiograms and transient ischemia during vascular clamping of the internal carotid artery during carotid endarterectomy.** *AJNR Am J Neuroradiol* 2004;25:558–64 Medline
29. Fang H, Song B, Cheng B, et al. **Compensatory patterns of collateral flow in stroke patients with unilateral and bilateral carotid stenosis.** *BMC Neurol* 2016;16:39 CrossRef Medline
30. Chen YF, Tang SC, Wu WC, et al. **Alterations of cerebral perfusion in asymptomatic internal carotid artery steno-occlusive disease.** *Sci Rep* 2017;7:1841 CrossRef Medline

# Value of Immediate Flat Panel Perfusion Imaging after Endovascular Therapy (AFTERMATH): A Proof of Concept Study

 Adnan Mujanovic,  Christoph C. Kurmann,  Michael Manhart,  Eike I. Piechowiak,  Sara M. Pilgram-Pastor,  Bettina L. Serrallach,  Gregoire Boulouis,  Thomas R. Meinel,  David J. Seiffge,  Simon Jung,  Marcel Arnold,  Thanh N. Nguyen, Urs Fischer,  Jan Gralla,  Tomas Dobrocky, Pasquale Mordasini, and  Johannes Kaesmacher



## ABSTRACT

**BACKGROUND AND PURPOSE:** Potential utility of flat panel CT perfusion imaging (FPCT-PI) performed immediately after mechanical thrombectomy (MT) is unknown. We aimed to assess whether FPCT-PI obtained directly post-MT could provide additional potentially relevant information on tissue reperfusion status.

**MATERIALS AND METHODS:** This was a single-center analysis of all patients with consecutive acute stroke admitted between June 2019 and March 2021 who underwent MT and postinterventional FPCT-PI ( $n = 26$ ). A core lab blinded to technical details and clinical data performed TIC1 grading on postinterventional DSA images and qualitatively assessed reperfusion on time-sensitive FPCT-PI maps. According to agreement between DSA and FPCT-PI, all patients were classified into 4 groups: hypoperfusion findings perfectly matched by location (group 1), hypoperfusion findings mismatched by location (group 2), complete reperfusion on DSA with hypoperfusion on FPCT-PI (group 3), and hypoperfusion on DSA with complete reperfusion on FPCT-PI (group 4).

**RESULTS:** Detection of hypoperfusion (present/absent) concurred in 21/26 patients. Of these, reperfusion findings showed perfect agreement on location and size in 16 patients (group 1), while in 5 patients there was a mismatch by location (group 2). Of the remaining 5 patients with disagreement regarding the presence or absence of hypoperfusion, 3 were classified into group 3 and 2 into group 4. FPCT-PI findings could have avoided TIC1 overestimation in all false-positive operator-rated TIC1 3 cases (10/26).

**CONCLUSIONS:** FPCT-PI may provide additional clinically relevant information in a considerable proportion of patients undergoing MT. Hence, FPCT-PI may complement the evaluation of reperfusion efficacy and potentially inform decision-making in the angiography suite.

**ABBREVIATIONS:** AIS = acute ischemic stroke; eTIC1 = expanded Thrombolysis in Cerebral Infarction; FPCT-PI = flat panel CT perfusion imaging; MT = mechanical thrombectomy;  $T_{max}$  = time to maximum

The current standard for assessing reperfusion success after mechanical thrombectomy (MT) is 2D DSA and it is usually evaluated with the Thrombolysis in Cerebral Infarction (TIC1) scale.<sup>1</sup> Recognition, treatment, and individualized postinterventional care of residual distal vessel occlusions after MT for proximal large-vessel occlusions are of increasing relevance.<sup>2</sup> With the advent of devices dedicated to distal MT and the potential use of

intra-arterial thrombolytics after incomplete reperfusion, more treatment options are now available, but none are without risks.<sup>3–6</sup> A sensitive and correct assessment of the residual perfusion deficit — at best with an estimation of eloquence — allows for a thorough risk–benefit assessment, which can inform subsequent clinical decisions. However, interventionalists performing the procedure are prone to overestimating the technical success based on standard DSA, biasing the overall estimation of the reperfused territory.<sup>7,8</sup> Besides a general overestimation bias, specific locations may also be more prone to false-positive TIC1 3 ratings.<sup>7,8</sup>


Received September 12, 2023; accepted after revision November 14.

From the Departments of Diagnostic and Interventional Neuroradiology (A.M., C.C.K., E.I.P., S.M.P.-P., B.L.S., J.G., T.D., P.M., J.K.), Diagnostic, Interventional and Pediatric Radiology (C.C.K.), and Neurology (T.R.M., D.J.S., S.J., M.A., U.F.), University Hospital Bern, Inselspital, and Graduate School of Health Sciences (A.M., C.C.K.), University of Bern, Bern, Switzerland; Siemens Healthineers, Advanced Therapies (M.M.), Forchheim, Germany; Department of Diagnostic and Interventional Neuroradiology (G.B.), University Hospital Tours (Centre Val de Loire Region), Tours, France; Department of Neurology (T.N.N.), Boston Medical Center, Boston University Chobanian and Avedisian School of Medicine, Boston, Massachusetts; Department of Neurology (U.F.), University Hospital Basel, University of Basel, Basel, Switzerland; and Department of Diagnostic and Interventional Neuroradiology (P.M.), Cantonal Hospital St. Gallen, St. Gallen, Switzerland.

A. Mujanovic and C.C. Kurmann contributed equally to this work.

P. Mordasini and J. Kaesmacher contributed equally to this work.

Please address correspondence to Johannes Kaesmacher, MD, PhD, University Institute of Diagnostic and Interventional Neuroradiology, University Hospital Bern Inselspital, Freiburgstrasse 10, 3001 Bern, Switzerland; e-mail: johannes.kaesmacher@insel.ch; @adnan\_mujanovic; @chris\_kurmann; @TDobrocky; @Eikeip; @TotoMynell; @DavidSeiffge; @CheesmakerMD; @NguyenThanhMD; @gboulouis; @StrokeBern; @ScanNeuroradBE; @MedFacultyUniBE

 Indicates open access to non-subscribers at [www.ajnr.org](http://www.ajnr.org)

 Indicates article with online supplemental data.

<http://dx.doi.org/10.3174/ajnr.A8103>

Periprocedural perfusion imaging might serve as an adjunct for more accurate evaluation of reperfusion success,<sup>9-13</sup> especially in cases of subtle distal occlusions or overlapping capillary phase hypoperfusions, which are hard to detect on DSA runs alone.<sup>10-13</sup> Pronounced collaterals with competing flow in peripheral vessels, on the other hand, may result in an underestimation of reperfusion outcome. Postinterventional perfusion imaging might help guide decision-making on whether to pursue adjuvant treatments for patients with incomplete reperfusion.<sup>12,13</sup>

Presently, there is a paucity of data on feasibility, clinical utility, and diagnostic sensitivity of new-generation flat panel CT perfusion imaging (FPCT-PI) acquired after MT. In this proof-of-concept study, we aimed to qualitatively assess whether FPCT-PI obtained directly in the angiography suite at the end of the intervention could provide additional potentially relevant information on tissue reperfusion status compared with the current standard.

## MATERIALS AND METHODS

### Patient Population

This is a single-center retrospective observational study. The University Hospital Bern is a tertiary-level care center with a 24-hour stroke service, including availability of 24-hour MT treatment. The University Hospital Bern serves as a referral institution for all patients with acute ischemic stroke (AIS) in central Switzerland covering a population of ~2 million residents with >2000 patients with stroke treated annually. All consecutive patients with AIS admitted between June 2019 and March 2021 who underwent MT were screened for eligibility. Patients with internal carotid artery or middle cerebral artery (M1 or M2 segment) occlusion who had immediate postinterventional FPCT-PI were considered for the final analysis, as these occlusion patterns usually show highest interrater agreement with regard to grading of reperfusion success. Patient records and clinical charts were screened for any adverse events related to additional radiation or contrast exposure during the hospital stay. This study was approved by the local ethics committee (reference ID 231/14, 2019-00547, 2023-00892) and performed according to the standards of the Declaration of Helsinki. Study data are available from the corresponding author upon presentation of a research plan and clearance by the ethics committee. Reporting was performed according to the Strengthening of Reporting of Observational Studies in Epidemiology statement.<sup>14</sup>

### Flat Panel CT Imaging Acquisition and Perfusion Imaging Postprocessing

Details on FPCT-PI image acquisition have been previously reported.<sup>15</sup> In short, we used a biplane flat panel CT (Artis Icono and Artis Q; Siemens) with 10 rotational sweeps (5 seconds per sweep with 1-second turnaround) of the C-arm system with Z-axis covering the entire brain. Perfusion maps were computed by using an offline prototype software provided by Siemens Healthineers.<sup>16,17</sup> Perfusion maps were computed by using deconvolution-based perfusion analysis.<sup>18</sup> Present software demonstrated almost equivalent results to syngo.via (Siemens) when using time to maximum ( $T_{max}$ ) and TTP maps (Pearson correlation coefficient 0.95–0.98 for qualitative analysis).<sup>17,19</sup> Further details on FPCT-PI acquisition and perfusion postprocessing are available in the Online Supplemental Data.

### Rating on DSA and FPCT-PI

Study ratings for all imaging data were performed independently of the intervention by a core lab (years of neuroradiology training: >10, >4, and >3 years) blinded to technical details and clinical data. The interrater agreement is reported with Krippendorff alpha coefficient. Reperfusion grading was performed on the final anteroposterior and lateral whole-brain DSA runs, which were acquired immediately before the FPCT-PI. Degree of reperfusion was graded by using the expanded TICI (eTICI) scale on the final DSA series.<sup>1</sup> Locations of the residual occlusions after MT were classified into frontal, parietal, temporal, and occipital regions (Online Supplemental Data).<sup>20</sup> For comparative purposes, we also reported TICI reperfusion as graded by the operating interventionalist at the end of the procedure, by extracting the scores from the acute interventional report that was filled out immediately after the procedure. Whenever the eTICI is reported, it refers to the core lab adjudicated grading, whereas TICI refers to the operators' assessment, as no eTICI was available from the operators' reports.

Presence or absence of hypoperfusion findings was rated on postprocessed perfusion maps, which were acquired immediately after the intervention. Presence of hypoperfusion was defined as focal, wedge-shaped perfusion delay within the initial target territory, suggesting a residual vessel occlusion. Careful correlations with preadmission imaging were done, so that perfusion abnormalities related to chronic parenchyma deficits or cervical vessel stenosis were not considered as remaining vessel occlusions.  $T_{max}$  and TTP perfusion maps were used for qualitative visual evaluation of persisting perfusion deficits as per the definition stated above.  $T_{max}$  and TTP have the highest sensitivity for early detection of perfusion abnormalities caused by vessel occlusions and show the best correlation to the perfusion maps generated by commercially available software.<sup>10,17,19</sup> Classification of the location of the hypoperfusion on FPCT-PI was done by using the same regions as for the DSA maps (Online Supplemental Data). The Core lab was blinded to DSA findings for FPCT-PI evaluation and vice versa. For all patients with hypoperfusion on FPCT-PI, manual segmentation of the hypoperfused area was performed with 3D Slicer (<http://www.slicer.org>) to obtain hypoperfused tissue volumes (Online Supplemental Data and respective caption for Methodology).<sup>21</sup> Hypoperfusion on FPCT-PI was correlated with follow-up imaging at 24 hours regarding the evolution of new infarcts in the residually hypoperfused territory on FPCT-PI, ie, a new infarct occur in the area of hypoperfusion on FPCT-PI that was not evident on admission imaging (Online Supplemental Data and respective caption for Methodology).

### DSA and FPCT-PI Agreement

To determine the agreement between the findings on final DSA runs and FPCT-PI, all patients were allocated to 1 of 4 groups. Groups 1 and 2 included patients with concurring dichotomized classification of presence or absence of hypoperfusion on both imaging modalities. For this purpose, patients were classified into no evidence of hypoperfusion on DSA (ie, eTICI 3) or evidence of hypoperfusion on DSA (eTICI <3). Likewise, FPCT-PI findings were dichotomized into presence or absence of hypoperfused areas. Further specifications were made accordingly. In group 1,

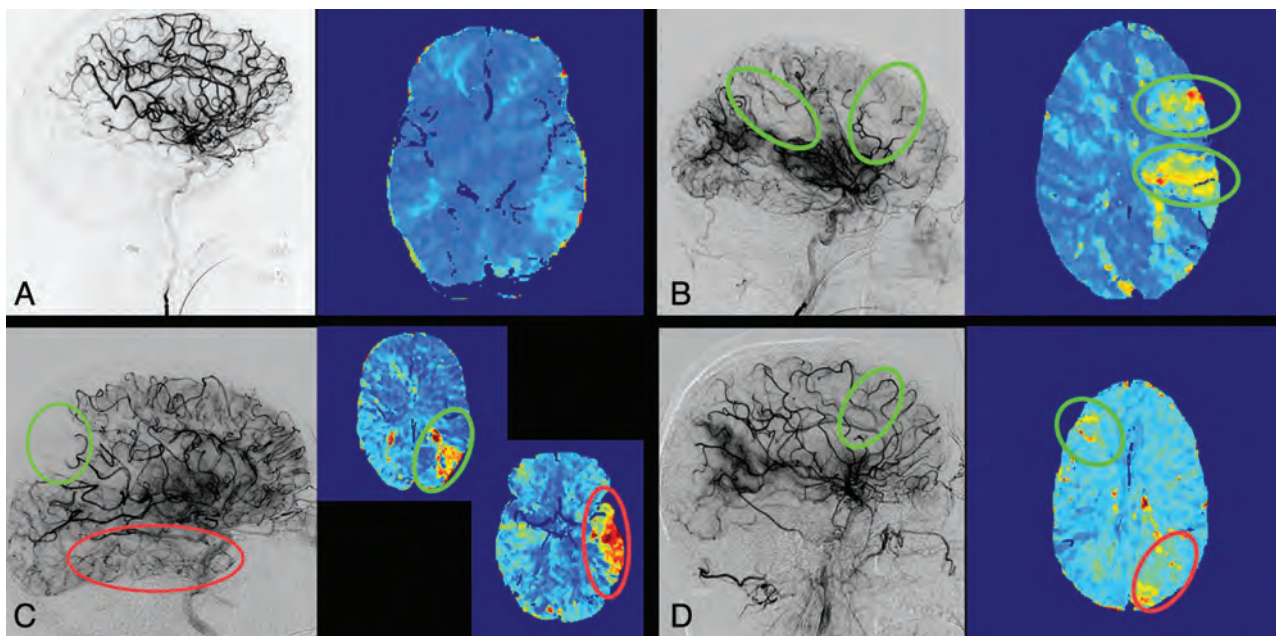


**FIG 1.** Concurring ratings regarding the presence of hypoperfusion. A, Patient with a left-M1 occlusion with complete reperfusion (eTICI 3) on the final angiography imaging and normal perfused tissue on FPCT-PI. B, Patient with a left-M1 occlusion with incomplete reperfusion (eTICI 2b50) on the final angiography imaging and corresponding frontal and parietal hypoperfusion deficits on the FPCT-PI. C, Patient with a left-M1 occlusion with incomplete reperfusion (eTICI 2b67) on the final angiography series, with a clear deficit in the parietal region. On follow-up FPCT-PI, the corresponding hypoperfusion is visible in the same area (*green circle*), with an additional hypoperfusion noted in the temporal region (*red circle*). The temporal branch occlusion was not noted by the core lab, but confirmed after making FPCT-PI available. D, Patient with a right-M2 occlusion with incomplete reperfusion on the final angiography series (eTICI 2b67, *green circle*) and hypoperfusion on the contralateral unaffected side (*red circle*).

hypoperfusion findings were perfectly matched by location, for example, TICI 2b hypoperfusion in the parietal area on DSA matched with hypoperfusion deficit in the same parietal area on FPCT-PI (Fig 1A, -B). In contrast, group 2 included patients with concurring dichotomized hypoperfusion findings but a mismatch in the locations of the hypoperfused areas between the two imaging modalities, for example, TICI 2b patient without reperfusion in the parietal area on the DSA but with hypoperfusion in both the parietal and temporal regions on the FPCT-PI (Fig 1C). Groups 3 and 4 included patients with discrepant dichotomized classification of presence or absence of hypoperfusion between the two imaging modalities. In group 3, this discrepancy was defined as complete reperfusion on the final DSA (ie, TICI 3) but clearly demarcated hypoperfusion on FPCT-PI (Fig 2A, -B). Group 4 patients had incomplete reperfusion on the final DSA run (TICI <3) but no hypoperfusion findings on FPCT-PI (Fig 2C). Results from groups 2, 3, and 4 were categorized as potentially clinically relevant, as dichotomized hypoperfusion findings in these 3 groups were mismatched and might reveal additional details on tissue reperfusion status. Core lab graded eTICI scores were used in the initial analysis of agreement between DSA and flat panel CT and for group allocation. To assess sensitivity, we also performed a subanalysis between DSA and FPCT-PI agreement based on operator-graded TICI scores.

## RESULTS

During the study period, 251 patients with AIS were treated with MT. One of 5 neurointerventionalists at our center acquired

postinterventional FPCT-PI during the study period. Fifty AIS cases were treated by this operator, and the decision to acquire FPCT-PI was with the operator, usually dependent on working hours versus off hours and the availability of a technician trained in acquiring FPCT-PI. During the initial study period, perfusion postprocessing failed in 4 patients due to failed timing of contrast bolus and the start of image acquisition. The remaining 26 patients were included in the agreement analysis (Fig 3). In the final study cohort, 69% of the patients were male; mean age was 77 years (IQR, 61–83); and median NIHSS score at admission was 15 (IQR, 11–20). Medium DSA-to-FPCT-PI time was 4 minutes 18 seconds (IQR 3 minutes 12 seconds–7 minutes 30 seconds). Median dose of contrast agent used for angiography and FPCT-PI was 200 mL (IQR, 183–228 mL). Hence, the median additional contrast dose required for FPCT-PI constituted 30% of the total contrast agent dose. Other baseline, interventional, and outcome characteristics are presented in Table and Online Supplemental Data. There were no differences between patients with and without FPCT-PI during the study period (Online Supplemental Data). Interrater agreement was very good (for DSA: 0.87, 95% CI, 0.74–0.94; for FPCT-PI: 0.88, 95% CI 0.82–0.94). Compared with the final DSA imaging, postinterventional perfusion imaging revealed new and potentially clinically relevant information in more than one-third of patients (10/26).

## Concurring Ratings Regarding the Presence of Hypoperfusion

The ratings of presence or absence of any hypoperfusion were concurring in 21/26 patients, and these constituted groups 1 and 2. In

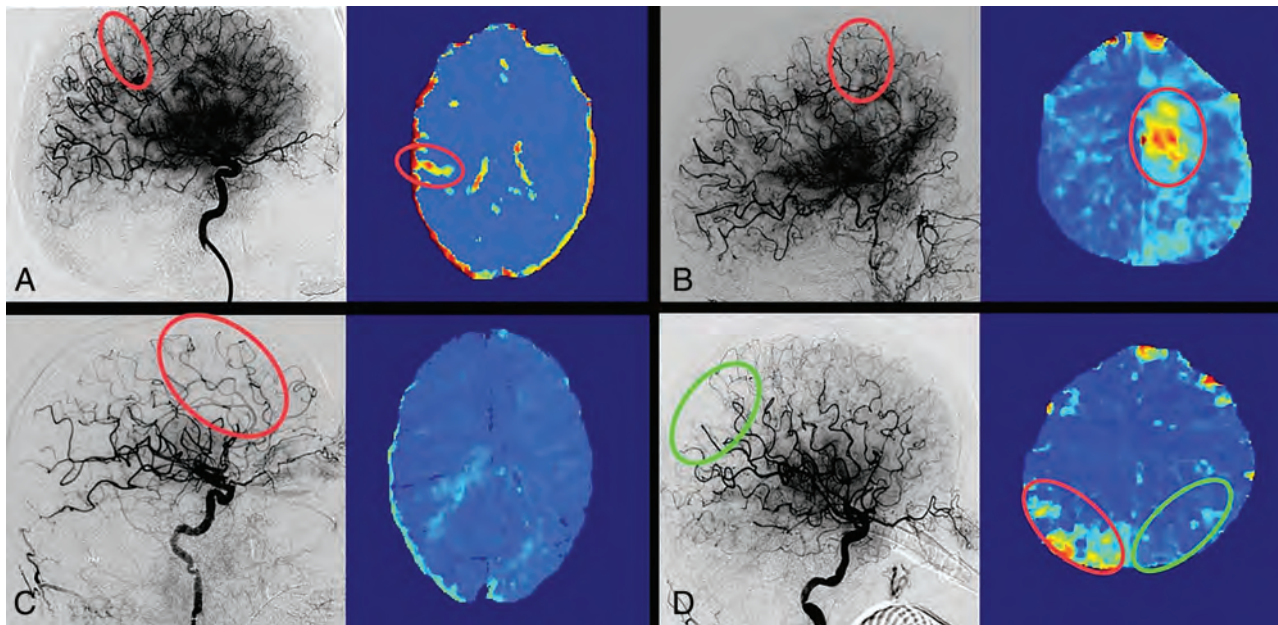


**FIG 2.** Discrepant ratings regarding the presence of hypoperfusion. A, Patient with a right-M1 occlusion rated as complete reperfusion (eTICI 3) on the final angiography imaging, but follow-up FPCT-PI revealed distal nonperfused tissue. A small residual M4 branch occlusion was confirmed by the core lab after making FPCT-PI available. B, Patient with a left-ICA occlusion rated as complete reperfusion (eTICI 3) on final angiography imaging, but follow-up FPCT-PI revealed a new hypoperfusion due to a distal frontal anterior cerebral artery branch occlusion. C, Patient with a left-M1 occlusion with incomplete reperfusion (eTICI 2b67) on the final angiography series with a clear capillary phase deficit in the frontal region. Follow-up FPCT-PI showed complete delayed reperfusion without any perfusion delays. D, Patient with a left-M1 occlusion with a small persisting deficit in the parietal region on the final angiography run (eTICI 2c, green circle). Follow-up FPCT-PI shows no perfusion delay on the left side; however, there was a hypoperfusion deficit on the contralateral side (red circle).

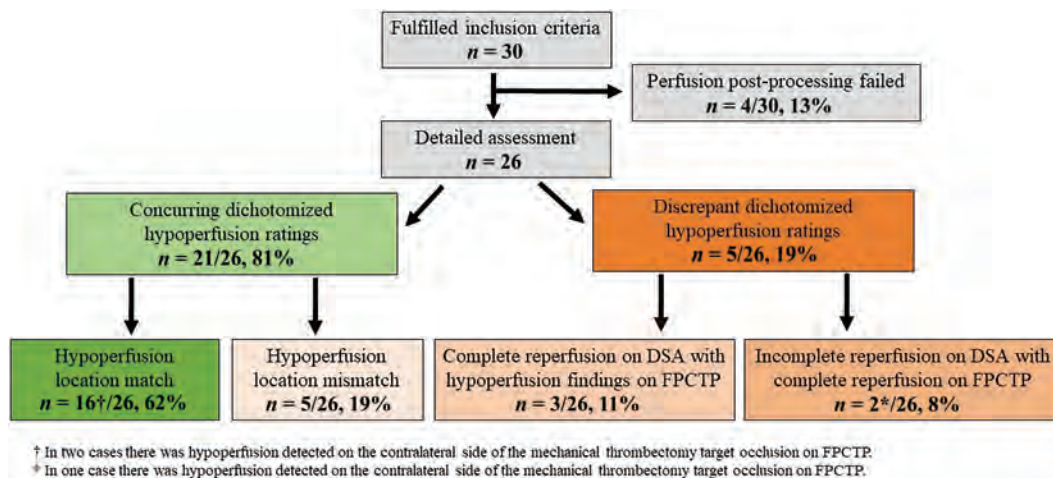


**FIG 3.** Study flow chart and patient allocation based on the agreement between the findings on final DSA runs and FPCT-PI.

group 1 (16/26), hypoperfusion findings were perfectly matched by location and size between the 2 imaging modalities. Three patients had complete reperfusion (eTICI 3) with corresponding findings on the FPCT-PI (ie, no hypoperfusion noted; Fig 1A). Thirteen patients had incomplete reperfusion on the final DSA run (eTICI <3), which precisely matched the areas and size of hypoperfusion on the FPCT-PI (Fig 1B). In group 2 (5/26), there were findings of hypoperfusion location mismatch, where on both imaging modalities there was a clear case of demarcated hypoperfusion, but the location and regions of hypoperfusions were

mismatched. In all 5 patients, the core lab found more hypoperfused area on FPCT-PI than on DSA (Fig 1C).

#### Discrepant Ratings Regarding the Presence of Hypoperfusion

Disagreements regarding the presence or absence of hypoperfusion were found in 5/26 patients encompassing groups 3 and 4. DSA-to-FPCT-PI time did not differ between the 5 patients with discrepant dichotomized hypoperfusion ratings and those with concordant dichotomized hypoperfusion ratings (4 minutes 12 seconds versus 4 minutes 18 seconds,  $P = .9$ ). In group 3 (3/26),

## Baseline and Interventional Characteristics

Variables	N = 26 <sup>a</sup>
Baseline	
Age	77 (61, 83)
Sex (male)	18 (69%)
NIHSS on admission	15 (11, 20)
Intervention	
eTICI score (core-lab adjudicated grading)	
2a	2 (8%)
2b50	2 (8%)
2b67	10 (38%)
2c	5 (19%)
3	7 (27%)
Time from DSA to FPCTP (min)	4.3 (3.2, 7.5)
Total contrast dose for both DSA and FPCTP (mL)	200 (183, 228)
Outcome	
NIHSS at 24 hours	6 (2, 15)
90-day mRS	
0	2 (7.7%)
1	8 (31%)
2	2 (7.7%)
3	4 (15%)
4	3 (12%)
5	1 (3.8%)
6	6 (23%)

<sup>a</sup> Data are median (IQR); n (%).

reperfusion was rated as complete (eTICI 3) on DSA, but there were hypoperfusion findings on the FPCT-PI. After making FPCT-PI for 2 group 3 patients available to the core lab, reassessment of the final DSA showed peripheral occlusions corresponding to the hypoperfusion findings on FPCT-PI (Fig 2A, -B). In group 4, 2 patients had incomplete reperfusion on the DSA run, but no hypoperfusion on FPCT-PI (Fig 2C). Upon reevaluation of DSA images, the core lab did not change their rating. Individual median DSA-to-FPCT-PI time for these 2 particular cases was 2 minutes 14 seconds and 10 minutes 31 seconds.

A sensitivity analysis for concurring and discrepant ratings regarding the presence or absence of hypoperfusion based on operator-graded TICI scores showed a higher number of potentially clinically relevant cases (13/26). The highest increase was seen in patients allocated to group 3, as operators had a tendency to rate more cases as complete reperfusion when using DSA alone (operator versus core lab adjudicated group 3 rates: 31% versus 11%, Online Supplemental Data). Contralateral to the affected hemisphere with the MT target territory, we noted hypoperfusion findings in 3 patients (Figs 1D–,2D; Online Supplemental Data and respective caption for Results).

## Perfusion Imaging and Clinical Outcomes

In total, operators graded reperfusion as complete on the final DSA (TICI 3) in 16/26 patients. Operator overestimation of final reperfusion score occurred in 10/26 patients compared with the core lab ratings on DSA (Online Supplemental Data), and all of these patients showed hypoperfusion on FPCT-PI. There were new infarcts on follow-up within area of FPCT-PI hypoperfusion in 10/26 cases, 5 of these belonging to group 1 and the other 5 to group 2.

Subanalyses on different patient subgroups (stratified by TICI, eTICI, presence or volume of perfusion deficit) indicated better clinical outcome for patients with higher reperfusion

scores, without perfusion deficits on FPCT-PI and with lower hypoperfusion volumes (Online Supplemental Data). Two patients had a marked increase in creatinine levels during the acute hospital stay (Online Supplemental Data), but only 1 of them fulfilled the diagnostic criteria for acute kidney injury.<sup>22</sup> In these 2 patients, acquisition of FPCT-PI constituted 30% and 37% of the total contrast media dose, respectively.

## DISCUSSION

This proof-of-concept study demonstrates that FPCT-PI provides additional and potentially clinically relevant information on tissue reperfusion status for more than one-third of patients undergoing immediate perfusion imaging after thrombectomy. In a considerable percentage of patients, interpreting final reperfusion status based on DSA alone will underestimate the total area of hypoperfused territory. Underestimation is even greater when considering assessments by the operators during the acute treatment phase. Other discrepant findings between DSA and FPCT-PI observed in this study may relate to persistent microvascular obstruction or early spontaneous reperfusion, findings that deserve further studies.

## Value of Perfusion Imaging

The additional value of immediate perfusion imaging after MT is unknown. Several studies performed perfusion imaging after MT, but timing of the follow-up images varied.<sup>12,23,24</sup> When using immediate perfusion imaging, we observed more sensitive delineation of hypoperfusion with additional territory involvement than with DSA alone. In 5/26 patients with matching dichotomized hypoperfusion grading, we observed additional territories of hypoperfused tissue on FPCT-PI. Interpretation of hypoperfused areas on gray-scale DSA images without spatial resolution can be complex, in particular when performed under time restraints or off-hours,<sup>25</sup> especially because most interventionalists tend to overestimate the percentage of reperfused tissue in the acute setting.<sup>7</sup> Notably, operators overestimated TICI reperfusion in a considerable number of cases; and in all cases, false TICI readings would have been revealed if perfusion maps had been available during or directly after the acute treatment. In this study, the decision on pursuing additional treatment was made by the interventionalist; processed FPCT-PI was not available at the time point of decision-making, only 4D angiography, which is automatically calculated from the acquisition. FPCT-PI was obtained with a prototype software package offline, and the software cannot yet be used for real-time decision-making.

Several studies have previously shown good correlation between perfusion maps on standardized CT and MR imaging protocols and FPCT-PI,<sup>26,27</sup> including a multicenter analysis.<sup>28</sup> The overall quality of FPCT-PI maps in this study was sufficient, and the percentage of maps that failed perfusion postprocessing on the FPCT-PI was comparable to the rates of failed postprocessing on standardized CT and MR imaging perfusion protocols.<sup>29</sup> Specifically, in all 4 patients with failed postprocessing, the failure was due to timing imbalances of contrast application and start of FPCT-PI rotational runs, a systematic error that occurred during the early study period.

### **Spontaneous Reperfusion**

In 2 patients, there were no hypoperfusion findings on FPCT-PI, although they clearly had incomplete reperfusion ( $eTICI < 3$ ) on the final DSA run. Spontaneous reperfusion after incomplete reperfusion is known to occur frequently.<sup>10,12,23</sup> Previous analysis on spontaneous reperfusion reported rates of up to 60% of patients when evaluating  $24 \pm 12$ -hour follow-up perfusion imaging.<sup>10,23</sup> Even when perfusion imaging is performed 30 minutes after the intervention, it revealed spontaneous reperfusion in almost one-half the patients with a final reperfusion grade of  $mTICI \geq 2b$ .<sup>12</sup> Excellent pial collaterals could have masked residual distal occlusion; however, in our 2 patients, we saw no rapid collateral blood flow to the ischemic territory on the final DSA runs. Potential explanation for spontaneous reperfusion could be that FPCT-PI was not thresholded to properly identify residual hypoperfusion. It could have also been an artifact finding, especially as in 1 of these 2 cases there was hypoperfusion on the contralateral, unaffected, side. In the other case, a longer DSA-to-FPCT-PI time (median time 10 minutes 30 seconds) could have increased the chances of delayed reperfusion on FPCT-PI.

New infarct on follow-up imaging was seen in 5/16 patients from group 1 and all patients from group 2. Five patients from group 1 who developed a new infarct in the area of FPCT-PI hypoperfusion generally had lower final reperfusion scores and slower collateral flow, which could explain the occurrence of new infarcts.<sup>10,30</sup> On the other hand, all patients in group 2 had additional perfusion deficit that was difficult to detect on DSA alone and could have been potentially treated if FPCT-PI were immediately available.

### **Persistent Microvascular Hypoperfusion**

Immediate postinterventional FPCT-PI could enable the evaluation of microvascular reperfusion and with it the discrepancy between microvascular and macrovascular reperfusion (ie, detection of the no-reflow phenomenon). Reports on detection of microvascular reperfusion on follow-up perfusion imaging are heterogeneous.<sup>12,23,24</sup> Even though tissue reperfusion is time-dependent,<sup>31</sup> these discrepant findings between the studies are probably related to the lack of standardized criteria for defining microvascular hypoperfusion.<sup>32</sup> We found 1 patient (group 3) with potential persistent microvascular hypoperfusion without any distal vessel occlusions on the retrospective DSA analysis (Online Supplemental Data). However, we would be reluctant to classify this as a no-reflow phenomenon because of uncertainties regarding its definition. Use of different perfusion imaging modalities, quantitative cutoffs, and follow-up times are the most likely reasons for discrepant definitions and rates of the no-reflow phenomenon across studies.<sup>32</sup>

### **Impact of FPCT-PI on the Workflow**

One advantage of FPCT-PI is that it offers a simple workflow. With this technique, it is possible to get information about the patients' perfusion and potentially tissue status, while options for intra-arterial treatment are still available. Currently, FPCT-PI is not available for all angiography suites, and commercial software packages are lacking. With more advanced tools and streamlined

workflows in the angiography suite, FPCT-PI may be a real-time evaluation tool for decision-making in the future.<sup>33</sup> Standardized training of nurses and interventionalists on the use of FPCT-PI is required; however, having a clear set of indications and scenarios for FPCT-PI could streamline its implementation in the operating protocol.<sup>33</sup> Other potential strategies to mitigate misinterpretations from the DSA could be with the use of validated deep learning-based approaches, especially in suspicion of distal thromboembolism.<sup>34</sup> Automating and quantifying perfusion deficits on DSA could minimize the risk of interobserver and intraobserver variability (eg, experience of the reader, inspection attentiveness, TICI scale variations).<sup>35</sup> Moreover, combination of standard DSA with perfusion imaging (ie, DSA perfusion) could be useful in quantifying the degree and nature of reperfusion after the intervention.<sup>33</sup>

### **Potential Risks of FPCT-PI**

FPCT-PI is not devoid of misinterpretations and artifacts.<sup>36</sup> Notably, postprocessing failed in 4/30 cases. However, deconvolution-based parametric maps could offer higher sensitivity to alteration in hemodynamics and higher quantitative reliability of perfusion deficits compared with DSA maps.<sup>36</sup> Moreover, if the interventionalist observes a perfusion deficit of FPCT-PI, it might prompt them to reevaluate the DSA for residual occlusion. Other potential risks of FPCT-PI could be related to the increased contrast agent and radiation doses.<sup>37</sup> However, there does not seem to be any difference between effective radiation dose from FPCT-PI and standard multidetector CT protocols (2.88 mSv versus 2.17 mSv) when using the current FPCT-PI protocols with collimation.<sup>38</sup> If FPCT-PI were to become standard of care, the theoretical minimal stochastic risks from such overexposure to radiation in a large pool of patients would have to be balanced by — yet to be shown — individual benefits of therapeutic approach modifications derived from FPCT-PI. Concerns have also been raised about the impact of administering additional contrast agent. In the present cohort, 2 patients had increased creatinine levels; however, it is difficult to determine whether this change is driven purely by additional contrast agent administered for FPCT-PI, especially considering that a more complex MT procedure can easily result in a comparable dose of total contrast. Overall, data consistently show a low risk of contrast-induced acute kidney injury after MT, even in patients with chronic kidney disease.<sup>39–41</sup> General consensus is that the benefits of detecting and evaluating eloquence of remaining residual occlusions are likely to outweigh the minimal risk of contrast medium-associated kidney failure.<sup>39–41</sup>

### **Limitations**

This is a single-center retrospective proof-of-concept study performed in highly selected patients, which prompts confounding and selection bias. Even though  $T_{max}$  and TTP maps are most sensitive to perfusion abnormalities,<sup>10</sup> they might not be sensitive enough to detect hypoperfusion on a microvascular level; other perfusion maps should be considered for a more comprehensive assessment of the microvasculature. Patient clinical outcome was not the focus of the present manuscript; because of the limited sample size, we advise caution when interpreting these results. Despite our best efforts to mitigate possible signal-induced errors in perfusion maps, there could still be effects that are masked or

unaccounted for. Specifically, there were fewer runs with FPCT-PI resulting in worse time-resolution than conventional CT perfusion imaging. Moreover, previous intra-arterial contrast injection and accumulation of that contrast in territories of brain-barrier breakdown could influence the calculation of attenuation-time curves.

## CONCLUSIONS

Immediate postinterventional FPCT-PI may provide additional clinically relevant information in a considerable percentage of patients undergoing MT. Potential benefits of FPCT-PI may be its high sensitivity for residual vessel occlusions, taking into account collaterals from different territories and determining anatomic location of hypoperfused areas. If these findings are confirmed, FPCT-PI may be used to complement the evaluation of reperfusion efficacy following acute stroke interventions in the future.

Disclosure forms provided by the authors are available with the full text and PDF of this article at [www.ajnr.org](http://www.ajnr.org).

## REFERENCES

1. Zaidat OO, Yoo AJ, Khatri P, STIR Thrombolysis in Cerebral Infarction (TICI) Task Force, et al. **Recommendations on angiographic revascularization grading standards for acute ischemic stroke: a consensus statement.** *Stroke* 2013;44:2650–63 CrossRef Medline
2. Samuels N, van de Graaf RA, van den Berg CAL, MR CLEAN Registry Investigators, et al. **Blood pressure in the first 6 hours following endovascular treatment for ischemic stroke is associated with outcome.** *Stroke* 2021;52:3514–22 CrossRef Medline
3. Mokin M, Fargen KM, Primiani CT, et al. **Vessel perforation during stent retriever thrombectomy for acute ischemic stroke: technical details and clinical outcomes.** *J Neurointerv Surg* 2017;9:922–28 CrossRef Medline
4. Diprose WK, Wang MT, Ghate K, et al. **Adjunctive intraarterial thrombolysis in endovascular thrombectomy: a systematic review and meta-analysis.** *Neurology* 2021;96:1135–43 CrossRef
5. Kaesmacher J, Bellwald S, Dobrocky T, et al. **Safety and efficacy of intra-arterial urokinase after failed, unsuccessful, or incomplete mechanical thrombectomy in anterior circulation large-vessel occlusion stroke.** *JAMA Neurol* 2022;77:318–26 CrossRef Medline
6. Kaesmacher J, Meinel TR, Kurmann C, et al. **Safety and efficacy of intra-arterial fibrinolytics as adjunct to mechanical thrombectomy: a systematic review and meta-analysis of observational data.** *J Neurointerv Surg* 2020;13:1073–80 CrossRef Medline
7. Zhang G, Marquering HA, Van Es AC, MR CLEAN Registry Investigators, et al. **Operator versus core-lab adjudication of reperfusion after endovascular treatment of acute ischemic stroke.** *Stroke* 2018;49:2376–82 CrossRef Medline
8. Pressman E, Waqas M, Sands V, et al. **Factors associated with decreased accuracy of modified thrombolysis in cerebral infarct scoring among neurointerventionalists during thrombectomy.** *Stroke* 2021;52:E733–38 CrossRef Medline
9. Mujanovic A, Kammer C, Kurmann CC, et al. **Association of intravenous thrombolysis with delayed reperfusion after incomplete mechanical thrombectomy.** *Clin Neuroradiol* 2022;33:87–98 CrossRef Medline
10. Mujanovic A, Jungi N, Kurmann CC, et al. **Importance of delayed reperfusion in patients with incomplete thrombectomy.** *Stroke* 2022;53:3350–58 CrossRef Medline
11. Fainardi E, Busto G, Rosi A, et al. **T<sub>max</sub> volumes predict final infarct size and functional outcome in ischemic stroke patients receiving endovascular treatment.** *Ann Neurol* 2022;91:878–88 CrossRef Medline
12. Rubiera M, Garcia-Tornel A, Olivé-Gadea M, et al. **Computed tomography perfusion after thrombectomy: an immediate surrogate marker of outcome after recanalization in acute stroke.** *Stroke* 2020;51:1736–42 CrossRef Medline
13. Brugnara G, Herweh C, Neuberger U, et al. **Dynamics of cerebral perfusion and oxygenation parameters following endovascular treatment of acute ischemic stroke.** *J Neurointerv Surg* 2021;neurintsurg-2020-017163 CrossRef Medline
14. von Elm E, Altman DG, Egger M, STROBE Initiative, et al. **The Strengthening the Reporting of Observational Studies in Epidemiology (STROBE) statement: guidelines for reporting observational studies.** *J Clin Epidemiol* 2008;61:344–49 CrossRef Medline
15. Kurmann CC, Kaesmacher J, Pilgram-Pastor S, et al. **Correlation of collateral scores derived from whole-brain time-resolved flat panel detector imaging in acute ischemic stroke.** *AJNR Am J Neuroradiol* 2022;43:1627–32 CrossRef Medline
16. Manhart MT, Kowarschik M, Fieselmann A, et al. **Dynamic iterative reconstruction for interventional 4-D C-arm CT perfusion imaging.** *IEEE Trans Med Imaging* 2013;32:1336–48 CrossRef Medline
17. Struffert T, Deuerling-Zheng Y, Kloska S, et al. **Dynamic angiography and perfusion imaging using flat detector CT in the angiography suite: a pilot study in patients with acute middle cerebral artery occlusions.** *AJNR Am J Neuroradiol* 2015;36:1964–70 CrossRef Medline
18. Fieselmann A, Kowarschik M, Ganguly A, et al. **Deconvolution-based CT and MR brain perfusion measurement: theoretical model revisited and practical implementation details.** *Int J Biomed Imaging* 2011;2011:467563 CrossRef Medline
19. Ortega-Gutierrez S, Quispe-Orozco D, Schafer S, et al. **Angiography suite cone-beam CT perfusion for selection of thrombectomy patients: a pilot study.** *J Neuroimaging* 2022;32:493–501 CrossRef Medline
20. Pressman E, Sands V, Flores G, et al. **Eloquence-based reperfusion scoring and its ability to predict post-thrombectomy disability and functional status.** *Interv Neuroradiol* 2022;28:538–46 CrossRef Medline
21. Fedorov A, Beichel R, Kalpathy-Cramer J, et al. **3D Slicer as an image computing platform for the Quantitative Imaging Network.** *Magn Reson Imaging* 2012;30:1323–41 CrossRef Medline
22. Morcos SK, Thomsen HS, Webb JA. **Contrast-media-induced nephrotoxicity: a consensus report.** *Eur Radiol* 1999;9:1602–13 CrossRef Medline
23. Tan Z, Parsons M, Bivard A, et al. **Optimal tissue reperfusion estimation by computed tomography perfusion post-thrombectomy in acute ischemic stroke.** *Stroke* 2021;52:E760–63 CrossRef Medline
24. Ng FC, Churilov L, Yassi N, et al. **Prevalence and significance of impaired microvascular tissue reperfusion despite macrovascular angiographic reperfusion (no-reflow).** *Neurology* 2022;98:E790–801 CrossRef Medline
25. Park JC, Kim JE, Kang HS, et al. **CT perfusion with angiography as a substitute for both conventional digital subtraction angiography and acetazolamide-challenged SPECT in the follow-up of postbypass patients.** *Cerebrovasc Dis* 2010;30:547–55 CrossRef Medline
26. Doerfler A, Göllitz P, Engelhorn T, et al. **Flat-panel computed tomography (DYNA-CT) in neuroradiology: from high-resolution imaging of implants to one-stop-shopping for acute stroke.** *Clin Neuroradiol* 2015;25 Suppl 2:291–97 CrossRef Medline
27. Struffert T, Deuerling-Zheng Y, Kloska S, et al. **Flat detector CT in the evaluation of brain parenchyma, intracranial vasculature, and cerebral blood volume: a pilot study in patients with acute symptoms of cerebral ischemia.** *AJNR Am J Neuroradiol* 2010;31:1462–69 CrossRef Medline
28. Kurmann CC, Kaesmacher J, Cooke DL, et al. **Evaluation of time-resolved whole brain flat panel detector perfusion imaging using RAPID ANGIO in patients with acute stroke: comparison with CT perfusion imaging.** *J Neurointerv Surg* 2023;15:387–92 CrossRef Medline

29. Demeestere J, Wouters A, Christensen S, et al. **Review of perfusion imaging in acute ischemic stroke: from time to tissue.** *Stroke* 2020;51:1017–24 CrossRef Medline
30. Cimflova P, Singh N, Kappelhof M, et al. **Effect of incomplete reperfusion patterns on clinical outcome: insights from the ESCAPE-NA1 trial.** *J Neurointerv Surg* 2023;9:1–7 CrossRef
31. d'Esterre CD, Boesen ME, Ahn SH, et al. **Time-dependent computed tomographic perfusion thresholds for patients with acute ischemic stroke.** *Stroke* 2015;46:3390–97 CrossRef Medline
32. Mujanovic A, Ng F, Meinel TR, et al. **No-reflow phenomenon in stroke patients: a systematic literature review and meta-analysis of clinical data.** *Int J Stroke* 2023;17474930231180434 CrossRef Medline
33. Kosior JC, Buck B, Wannamaker R, et al. **Exploring reperfusion following endovascular thrombectomy: a proof of concept using perfusion angiography.** *Stroke* 2019;50:2389–95 CrossRef Medline
34. Mittmann BJ, Braun M, Runck F, et al. **Deep learning-based classification of DSA image sequences of patients with acute ischemic stroke.** *Int J Comput Assist Radiol Surg* 2022;17:1633–41 CrossRef Medline
35. Su R, Cornelissen SA, van der Sluijs M, et al. **AutoTICI: automatic brain tissue reperfusion scoring on 2D DSA images of acute ischemic stroke patients.** *IEEE Trans Med Imaging* 2021;40:2380–91 CrossRef Medline
36. Vagal A, Wintermark M, Nael K, et al. **Automated CT perfusion imaging for acute ischemic stroke: pearls and pitfalls for real-world use.** *Neurology* 2019;93:888–98 CrossRef Medline
37. Zensen S, Guberina N, Opitz M, et al. **Radiation exposure of computed tomography imaging for the assessment of acute stroke.** *Neuroradiology* 2021;63:511–18 CrossRef Medline
38. Brehm A, Nguyen KA, Blackham KA, et al. **Effective dose measurements of the latest-generation angiographic system in patients with acute stroke: a comparison with the newest multidetector CT generation.** *AJNR Am J Neuroradiol* 2022;43:1621–26 CrossRef Medline
39. Jhou H, Chen P, Yang L, et al. **Contrast-associated acute kidney injury after endovascular therapy for acute ischemic stroke: a meta-analysis.** *Stroke Vasc Interv Neurol* 2022;2:1–11 doi: CrossRef
40. Brinjikji W, Demchuk AM, Murad MH, et al. **Neurons over nephrons.** *Stroke* 2017;48:1862–68 CrossRef Medline
41. Li X, Partovi S. **Save the brain first: CTA and mechanical thrombectomy in patients at risk for contrast-induced nephropathy.** *AJNR Am J Neuroradiol* 2020;41:637–38 CrossRef Medline

# Transarterial Embolization of Anterior Cranial Fossa Dural AVFs as a First-Line Approach: A Single-Center Study

 Carl A. J. Puylaert,  René van den Berg, Bert A. Coert, and Bart J. Emmer



## ABSTRACT

**BACKGROUND AND PURPOSE:** Endovascular treatment has been increasingly used for anterior cranial fossa dural AVFs. Evidence on the safety and efficacy of different endovascular treatment strategies is limited. We report clinical and angiographic outcomes of patients with anterior cranial fossa dural AVFs who underwent treatment using transarterial embolization with *n*-BCA as a first-line approach.

**MATERIALS AND METHODS:** Consecutive patients undergoing treatment for anterior cranial fossa dural AVFs at the Amsterdam University Medical Centers between 2010 and 2023 were retrospectively included. Transarterial embolization was used as a first-line approach, while transvenous treatment and surgery were used in cases of unsuccessful transarterial embolization. Treatment was evaluated on the basis of the angiographic cure rate, procedural complications, and clinical outcome.

**RESULTS:** Fourteen patients were included with 15 anterior cranial fossa dural AVFs. All patients underwent primary endovascular treatment (12 transarterial, 1 transvenous, and 1 combined). Complete occlusion using only transarterial embolization was reached in 69% of patients (9/13), while the overall complete occlusion by endovascular treatment was reached in 79% of patients (11/14). Navigation and embolization were performed through the ophthalmic artery in 13 patients, with no procedural complications. Visual acuity was preserved in all patients. Three patients underwent an operation after failed endovascular treatment. All patients had complete anterior cranial fossa dural AVF occlusion at follow-up.

**CONCLUSIONS:** Treatment of anterior cranial fossa dural AVFs using transarterial embolization with *n*-BCA as a first-line approach is a safe and feasible first-line treatment strategy. No visual complications due to embolization through the ophthalmic artery occurred in this study.

**ABBREVIATIONS:** ACF = anterior cranial fossa; dAVF = dural AVF

Anterior cranial fossa (ACF) dural AVFs (dAVFs) are a rare and relatively aggressive subtype of intracranial dural dAVF. Because of their drainage through cortical veins and the associated risk of hemorrhage, treatment is recommended in nearly all cases.<sup>1</sup> The most common primary arterial feeders of ACF-dAVFs are formed by ethmoidal branches from the ophthalmic artery, with possible secondary contribution through collateral branches from the internal maxillary and middle meningeal arteries. Following advances in endovascular

microcatheters and embolic agents, endovascular treatment of ACF-dAVFs has become the primary treatment technique in the past decade.<sup>2</sup> However, no consensus exists on the optimal endovascular approach, either transarterial or transvenous, or if microsurgical disconnection is preferred over these techniques.<sup>3–6</sup>

Transarterial embolization is most commonly performed through the ophthalmic artery. A common concern with this approach is occlusion of the central retinal artery due to excessive reflux of embolic agent.<sup>3</sup> Thus, some authors have proposed transvenous embolization as a preferred first-line approach.<sup>4,7</sup> However, a venous approach carries the risk of venous perforation, and catheter positioning can be arduous in case of a tortuous venous anatomy.<sup>3,4,7</sup>

A recent study evaluated the use of transarterial embolization of ACF-dAVFs as a first-line approach, though primary transarterial embolization was only performed in 54% of patients (19/34), with central retinal artery occlusion occurring in 1 patient after

Received August 11, 2023; accepted after revision November 2.

From the Departments of Radiology and Nuclear Medicine (C.A.J.P., R.v.d.B., B.J.E.), and Neurosurgery (B.A.C.), Amsterdam University Medical Centers, Amsterdam, the Netherlands.

Please address correspondence to C.A.J. Puylaert, MD, Amsterdam University Medical Centers, University of Amsterdam, Department of Radiology and Nuclear Medicine, Meibergdreef 9, 1105 AZ, Amsterdam, the Netherlands; e-mail: c.a.puylaert@amsterdamumc.nl; @CarlPuylaert



Indicates article with online supplemental data.

<http://dx.doi.org/10.3174/ajnr.A8092>

embolization using Onyx (Medtronic).<sup>3</sup> Ethylene-vinyl alcohol copolymers dissolved in dimethyl sulfoxide, such as Onyx or Squid (Balt), have been increasingly used in recent years for dAVF embolization, because they allow long injection times and controlled embolization. However, in contrast to *n*-BCA, copolymers require reflux for distal progression of the liquid agent, which is unwanted in embolization through the ophthalmic artery due to the proximity of the central retinal artery. The aim of this study was to report on outcomes of patients who underwent treatment of ACF-dAVFs using transarterial embolization through the ophthalmic artery with *n*-BCA as the first-line approach.

## MATERIALS AND METHODS

### Study Design

We retrospectively retrieved consecutive patients with ACF-dAVFs who were treated at Amsterdam University Medical Centers between January 2010 and April 2023. Of 14 eligible patients, 13 were previously included in a large cohort investigating the association between dAVFs and cerebral venous thrombosis, though without a description of the current subgroup and specific outcome measures.<sup>8</sup> For this observational study, the ethics committee of the Amsterdam University Medical Centers waived the necessity for formal approval. In accordance with the General Data Protection Regulation, all eligible patients received an information letter about the study, with the option of refusing the use of their pseudonymized data. The current study was performed in accordance with Strengthening the Reporting of Observational Studies in Epidemiology (STROBE) guidelines.<sup>9</sup>

### Treatment and Follow-Up

All referred patients were discussed in our neurovascular multidisciplinary team meeting to determine the indication for endovascular or surgical treatment. When possible, a first-line endovascular approach was preferred due to a less invasive nature than surgery. A primary transarterial approach was used, except in cases with unfavorable arterial anatomy or unfavorable (high) flow conditions. Depending on the angiographic anatomy, a primary route was chosen through the ophthalmic artery, ethmoidal branches, or middle meningeal artery. As a first choice, catheterization of the ophthalmic artery was attempted in all cases, regardless of the caliber or angle of origin. Flow-directed microcatheters (Magic 1.2F or 1.5F; Balt) in combination with microguidewires were used for selective microcatheterization. The size of the microcatheter was chosen depending on the caliber of the (distal) feeding branch from the ophthalmic artery. This choice allowed very distal catheterization with the goal of obtaining, as much as possible, a wedged microcatheter position. No vasodilators were used. A mixture of *n*-BCA (Histoacryl; B. Braun) and ethiodized oil (Lipiodol; Guerbet) was used for embolization with a ratio ranging from 1:1.5 to 1:4, depending on the estimated distance, flow speed, and size of the catheterized vessel. A wedged position of the microcatheter was preferred to allow maximum forward progression of *n*-BCA. Embolization through the ophthalmic artery was only performed if a safe position could be reached far enough distal to the origin of the central retinal artery. Injection with *n*-BCA was stopped after successful occlusion of the venous

outlet or in case of progressive reflux nearing the origin of the central retinal artery. In cases of partial occlusion or when no embolization could be attempted, a transvenous approach could be considered, depending on the estimated risk of venous perforation. In cases of unsuccessful endovascular treatment, patients were referred for surgical disconnection. All endovascular procedures were performed by neurointerventional radiologists with extensive experience in endovascular procedures. Operations were performed by vascular neurosurgeons with extensive experience in dAVF surgery. Frontal or frontotemporal approaches were used with subsequent selective surgical disconnection.

### Data Collection

Patient data on demographics, medical history, symptoms, and clinical outcome were retrieved from our electronic patient file system. Clinical outcome was defined on the basis of the presenting symptoms of the ACF-dAVF and classified as asymptomatic, improvement of symptoms, worsening of symptoms, or death. Visual function was subjectively assessed after treatment, while advanced assessment was performed in cases of suspected visual symptoms. Overall functional outcome at the last follow-up visit was retrospectively assessed using the mRS. An mRS  $\geq 3$  was defined as a poor (unfavorable) outcome.<sup>10</sup> Follow-up imaging studies were reviewed for each patient.

The angiographic anatomy of each lesion was detailed by describing the arterial feeders, venous drainage pattern, and the presence of venous ectasia. Each lesion was classified according to the Cognard classification.<sup>11</sup> Angiographic outcomes after embolization were complete or partial occlusion; the latter was defined as residual flow through the fistulous point and/or early venous filling of the draining vein of the dAVF.

### Statistical Analysis

All analyses were performed using SPSS Statistics 28.0 (IBM). Continuous variables were described using mean (SD) or median with interquartile range, depending on their distribution.

## RESULTS

### Patient Characteristics

Fourteen patients were included in the study (Online Supplemental Data). The mean age was 59 (SD, 11) years with a range of 34–79 years. Sixty-four percent of patients were men (9/14). Medical history showed evidence of hypertension ( $n = 1$ ), a previous cerebrovascular accident ( $n = 4$ ), and previous cranial surgery ( $n = 2$ ). Ten patients (71%) were past smokers, though none were active smokers. No patients had known previous head trauma. ACF-dAVF diagnosis was made by CT in 3 patients, MR imaging in 5 patients, and angiography in the remaining 6 patients. Twelve patients (86%) were symptomatic. Three patients presented with hemorrhage, namely SAH ( $n = 1$ ) and frontal intraparenchymal hemorrhage ( $n = 2$ ), the latter in 1 case combined with a subdural hematoma. Two patients were asymptomatic; in both, the ACF-dAVF was discovered incidentally.

### Angiographic Anatomy

A total of 15 ACF-dAVFs were described for 14 patients, because 1 patient was found to have 2 ACF-dAVFs with separate arterial

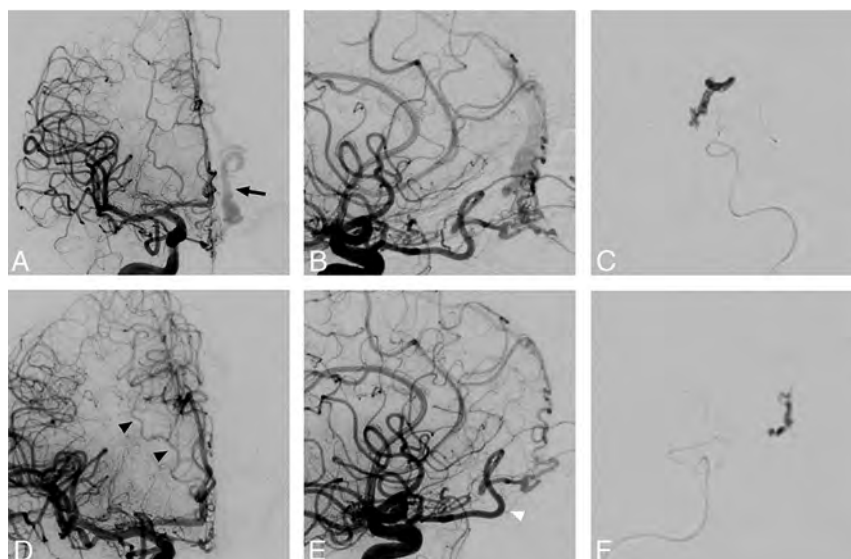


**FIG 1.** A patient with 2 dAVFs with separate arterial feeders and venous drainage. A right-sided injection of the ICA shows a dAVF with supply from the right ophthalmic artery with drainage through a dilated cortical vein on the left side (arrow) into the superior sagittal sinus (A and B). After successful embolization through 1 of the 2 ethmoidal branches of the left ophthalmic artery (C), a repeat right ICA injection clearly shows the second remaining fistula with separate transtethmoidal supply refluxing into a nondilated vein on the right-sided cortical frontal vein (arrowheads) into the superior sagittal sinus. The bayonet sign is seen, signifying the origin of the central retinal artery (white arrowhead, D and E). Because the first embolization was performed without substantial arterial reflux, the second fistula was again successfully embolized through the right ophthalmic artery (F).

#### Treatment characteristics

Variable	Value (%) (No.)
Primary endovascular treatment	100% (14/14)
Transarterial	86% (12/14)
Transvenous	7% (1/14)
Combined	7% (1/14)
Secondary surgery after failed endovascular treatment	21% (3/14)
Endovascular outcome	
Complete occlusion	79% (11/14)
Partial occlusion	7% (1/14)
No embolization attempt	14% (2/14)
Clinical outcome <sup>a</sup>	
Asymptomatic	29% (4/14)
Improvement of symptoms	71% (10/14)
Worsening of symptoms	0% (0/14)
Death	0% (0/14)
Procedural complications	
Endovascular treatment	0% (0/14)
Surgery	67% (2/3)
Seizure	33% (1/3)
Anosmia	33% (1/3)

<sup>a</sup> This concerns symptoms attributed to the dAVF.

feeders and venous drainage (Fig 1). All ACF-dAVFs were supplied by the ophthalmic artery; in 67% of cases ( $n = 10$ ), there was bilateral supply from the ophthalmic artery. Additional dural feeders were seen from the internal maxillary artery ( $n = 5$ ), middle meningeal artery ( $n = 3$ ), and facial artery. Pial feeders were seen in 1 ACF-dAVF through a branch from the orbitofrontal artery. All ACF-dAVFs showed drainage through cortical veins

before entering the venous sinus (Borden type III). All ACF-dAVFs drained to the superior sagittal sinus, while 2 showed additional drainage to the cavernous sinus ( $n = 2$ ) and superficial middle cerebral vein, connected through the vein of Labbé to the sigmoid sinus ( $n = 1$ ).

#### Treatment and Outcome

All patients underwent primary endovascular treatment (Table). Complete occlusion using endovascular treatment was achieved in 79% of patients (11/14). In 13 patients, transarterial catheterization was performed. In 11 of these patients with 12 ACF-dAVFs, embolization was attempted with a total of 14 glue injections through the ophthalmic artery (10 unilateral and 2 bilateral) with a mean injection time of 31 (SD, 8) seconds; range, 25–38 seconds). Additionally, 1 glue injection was through the middle meningeal artery, and 1 glue injection, through a pial feeder from the orbitofrontal artery. Using only transarterial embolization, we achieved complete occlusion in 69%

of patients (9/13) (Fig 2). In 1 patient with unsuccessful transarterial embolization, subsequent transvenous embolization was performed in the same session with complete occlusion of the ACF-dAVF. A primary transvenous approach was used in 1 patient because of high fistulous flow and very unfavorable vascularization through multiple small dural arteries. Treatment resulted in complete occlusion of the ACF-dAVF by glue embolization of the proximal part of the draining vein.

Endovascular treatment was unsuccessful in 3 of 14 patients (21%). One ACF-dAVF was only partially occluded despite multiple transarterial embolization attempts, which had to be halted due to progressive reflux of the embolic agent (Fig 3). In the remaining 2 patients, no embolization attempt was made because a distal-enough microcatheter position could not be obtained to allow safe embolization. All 3 patients were referred for surgery, with successful surgical disconnection of the ACF-dAVF.

No procedural complications of endovascular treatment were seen. Visual acuity was preserved in all patients. Procedural complications were seen in 2 of 3 patients who underwent surgery. One patient developed postoperative anosmia, while another patient had transient postoperative symptoms attributed to a seizure.

#### Follow-Up

All patients had clinical follow-up with a median length of 13 months (range, 4–94 months). At last follow-up, 12 patients (86%) had an mRS of 0–2. Two patients had a poor clinical outcome (mRS 3 and 4) related to neurologic damage from the initial hemorrhage.

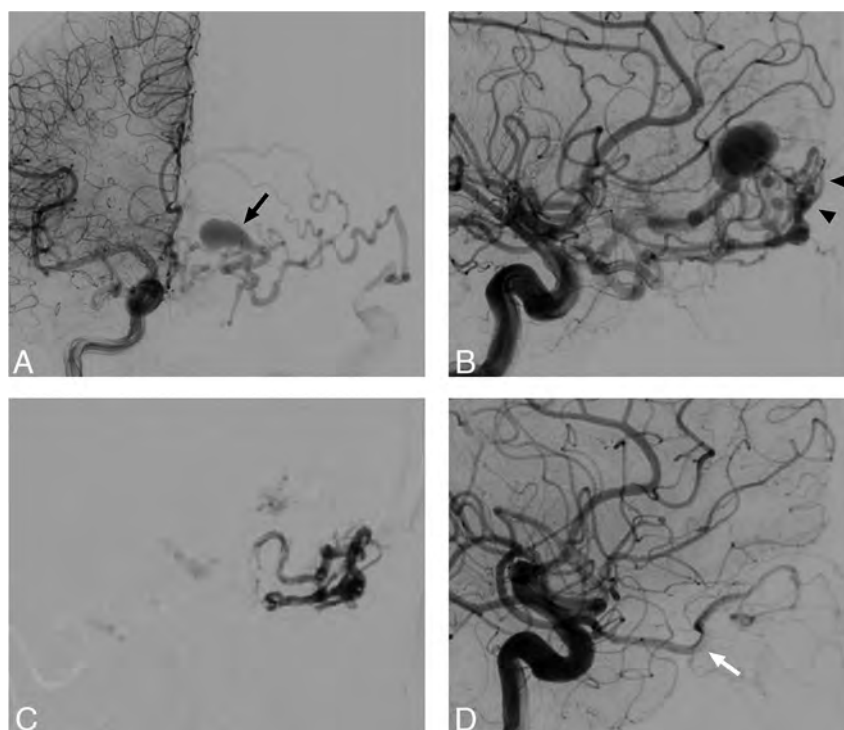


**FIG 2.** A patient who presented with transient aphasia. Angiography demonstrated a dAVF with arterial feeding through ethmoidal branches of the right ophthalmic artery in a posterior-anterior projection (A), the left ophthalmic artery in a lateral projection (arrowheads) (B), and the frontal branch of the left middle meningeal artery (not shown). Cortical venous reflux is seen through ectatic left-sided cortical veins (arrow) toward the superficial middle cerebral vein before ending in the sigmoid sinus (A and B). Embolization through the right ophthalmic artery, with filling of the proximal refluxing vein with a minor spill of glue in the more distal venous territory (C). Complete occlusion of the fistula was achieved. The bayonet sign is seen, signifying the origin of the central retinal artery (white arrow) (D). The patient was asymptomatic at follow-up.

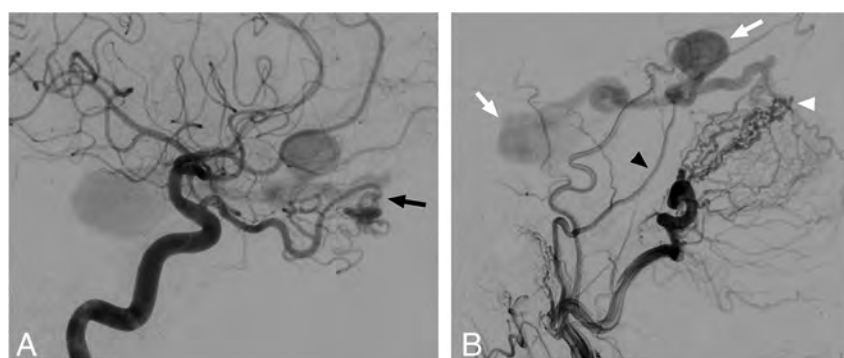


**FIG 3.** A patient with a complex dAVF with extensive arterial supply from both ophthalmic arteries (arrow), right middle meningeal artery (arrowhead), and infraorbital branch from the maxillary artery (white arrowhead). Due to proximal elongation, the exact location of the bayonet cannot be determined (A and B). Multiple venous ectasias are visible along the cortical draining vein (white arrows). Embolization was attempted through both ophthalmic arteries, which had to be halted due to reflux before glue could reach the venous outlet. The patient finally underwent surgery, with successful disconnection of the fistula.

## DISCUSSION

In this study, we describe outcomes of patients who were treated for ACF-dAVF using transarterial embolization with *n*-BCA as a first-line approach. Transarterial embolization reached direct, complete occlusion in 69% of patients. Overall, endovascular

treatment including transvenous and combined approaches reached complete occlusion in 79% of patients. No procedural complications from endovascular treatment were seen. Visual acuity was preserved in all patients. Three patients underwent secondary surgery after failed endovascular treatment. All patients had complete ACF-dAVF occlusion at follow-up.

ACF-dAVFs are exceedingly rare lesions. The classification of “aggressive” subtype should be nuanced because modern literature has shown relatively lower rates of hemorrhage, ranging from 27% to 57%,<sup>3-5</sup> compared with the high rates of hemorrhage (62%–91%) reported in earlier literature.<sup>12,13</sup> The hemorrhage rate of 21% in our study supports this notion and underlines the importance of a noninvasive first-line treatment approach. Previous studies on endovascular treatment of ACF-dAVFs have shown complete occlusion rates ranging from 53% to 92% and complication rates ranging from 3.6% to 12%.<sup>2-5,14</sup> In a recent study, 23 patients underwent transarterial ACF-dAVF embolization using varying types of embolic agents (*n*-BCA, Onyx, and Squid).<sup>3</sup> In this study, 1 case of central retinal artery occlusion occurred due to excessive reflux of Onyx. To our knowledge, no other cases of central retinal artery occlusion after embolization through the ophthalmic artery have been published, though this complication is likely underreported. When one performs embolization through the ophthalmic artery, only minimal reflux is allowed due to the proximity of the central retinal artery.<sup>15</sup> Because copolymers require reflux to provide forward push of the embolic agent, from a procedural point of view, these are unfavorable in this procedure compared with *n*-BCA, which allows better control of reflux. In our study, only 13% of *n*-BCA injections through the ophthalmic artery (2/15) had to be aborted due to reflux, and this reflux could be safely managed without

embolic material nearing the origin of the central retinal artery. In all other cases, no reflux occurred proximal to the tip of the microcatheter.

The experience of the neurointerventionalist does play an important role in the choice of the embolic agent, which might

explain the predominant use of Onyx in all major studies on transarterial embolization of ACF-dAVF.<sup>3-5,14,16,17</sup> Two recent case reports have indicated that micro-balloon-assisted embolization might be used to avoid Onyx reflux through the ophthalmic artery.<sup>18,19</sup> However, the more difficult navigation and risk of vessel perforation due to balloon inflation should be taken in account under these circumstances. In our opinion, the use of *n*-BCA in our study is an important factor in the relatively high rate of successful transarterial embolization without occurrence of complications.

Several technical aspects are important to consider when using a transarterial approach. In our center, we prefer very distal catheterization of the ophthalmic artery with very soft-flow-directed microcatheters allowing injection of diluted *n*-BCA for treatment of ACF-dAVFs. This approach allows control of the antegrade injection of the embolic agent with only very sparse reflux. The aim of embolization should be occlusion of the proximal venous outlet. Partial or absent occlusion of the proximal venous outlet and persistent outflow after occlusion of the primary arterial feeder might induce the development of secondary feeders through collateral arteries, with persistent flow through the dAVF and a continued risk of hemorrhage. Reflux of the embolic agent should not be allowed close to the origin of the central retinal artery. In most cases, the origin of the central retinal artery can be found where the ophthalmic artery crosses the optic nerve with the classically described “bayonet” appearance.<sup>15</sup> However, under arteriovenous high-flow conditions, the ophthalmic artery will show elongation, making identification of the bayonet more challenging. In addition, the central retinal artery will hardly be opacified because of the steal effect toward the fistula. In such cases, any risks should be minimized by obtaining a very distal position and by allowing only minimal reflux. Furthermore, a wedge position of the microcatheter is preferred to reduce reflux. A transvenous approach can be used in cases with drainage to the superior sagittal sinus, though it is important to evaluate the venous anatomy, tortuosity, and presence of venous ectasia to estimate the likelihood of safely obtaining a distal position for embolization.

Limitations of our study included the retrospective nature of the study, which prohibited exhaustive data collection. However, patients were included consecutively, and a consistent treatment approach was used during the study period. Although several larger multicenter studies on endovascular treatment of ACF-dAVFs have been published, these have inconsistencies in treatment approaches, technique, and types of embolic agents used for embolization.<sup>3-5,14</sup> Our study is the largest single-center study on transarterial embolization of ACF-dAVFs to date. Prospective registry studies could be used for comparison of treatment strategies of ACF-dAVFs.

## CONCLUSIONS

Our study shows that endovascular treatment using transarterial embolization with *n*-BCA as a first-line approach is a safe and feasible treatment strategy for ACF-dAVF. Although copolymers have seen increased usage compared with *n*-BCA, we recommend maintaining experience with *n*-BCA for specific indications such as ACF-dAVF.

Disclosure forms provided by the authors are available with the full text and PDF of this article at [www.ajnr.org](http://www.ajnr.org).

## REFERENCES

- Gross BA, Moon K, Kalani MYS, et al. **Clinical and anatomic insights from a series of ethmoidal dural arteriovenous fistulas at Barrow Neurological Institute.** *World Neurosurg* 2016;93:94–99 CrossRef Medline
- Xu B, Wang Z, Bai W, et al. **Treatment of cavernous sinus dural arteriovenous fistula using different surgical approaches: analysis of 32 consecutive cases.** *J Interv Med* 2019;2:118–22 CrossRef Medline
- Trivelato FP, Smajda S, Saleme S, et al. **Endovascular treatment of anterior cranial base dural arteriovenous fistulas as a first-line approach: a multicenter study.** *J Neurosurg* 2022;137:1758–65 CrossRef Medline
- Dabus G, Kan P, Diaz C, et al. **Endovascular treatment of anterior cranial fossa dural arteriovenous fistula: a multicenter series.** *Neuroradiology* 2021;63:259–66 CrossRef Medline
- Sanchez S, Raghuram A, Wendt L, et al. **Natural history, angiographic presentation and outcomes of anterior cranial fossa dural arteriovenous fistulas.** *J Neurointerv Surg* 2023;15:903–08 CrossRef Medline
- Su X, Gao Z, Ma Y, et al. **Correspondence on “Natural history, angiographic presentation and outcome of anterior cranial fossa dural arteriovenous fistulas” by Sanchez et al.** *J Neurointerv Surg* 2023;15:932 CrossRef Medline
- Limucci N, Leone G, Nappini S, et al. **Transvenous embolization of ethmoidal dural arteriovenous fistulas: case series and review of the literature.** *World Neurosurg* 2018;110:e786–93 CrossRef Medline
- Kuiper L, Sánchez van Kammen M, Coert BA, et al. **Association between dural AVFs and cerebral venous thrombosis.** *AJNR Am J Neuroradiol* 2022;43:1722–29 CrossRef Medline
- Vandenbroucke JP, von Elm E, Altman DG, et al; STROBE Initiative. **Strengthening the Reporting of Observational Studies in Epidemiology (STROBE): explanation and elaboration.** *Int J Surg* 2014;12:1500–24 CrossRef Medline
- van Swieten JC, Koudstaal PJ, Visser MC, et al. **Interobserver agreement for the assessment of handicap in stroke patients.** *Stroke* 1988;19:604–07 CrossRef Medline
- Cognard C, Gobin YP, Pierot L, et al. **Cerebral dural arteriovenous fistulas: clinical and angiographic correlation with a revised classification of venous drainage.** *Radiology* 1995;194:671–80 CrossRef Medline
- King WA, Martin NA. **Intracerebral hemorrhage due to dural arteriovenous malformations and fistulae.** *Neurosurg Clin N Am* 1992;3:577–90 CrossRef Medline
- Halbach VV, Higashida RT, Hieshima GB, et al. **Dural arteriovenous fistulas supplied by ethmoidal arteries.** *Neurosurgery* 1990;26:816–23 CrossRef Medline
- Mayercik VA, Sussman ES, Pulli B, et al. **Efficacy and safety of embolization of dural arteriovenous fistulas via the ophthalmic artery.** *Interv Neuroradiol* 2021;27:444–50 CrossRef Medline
- Akdemir Aktaş H, Mine Ergun K, Tatar İ, et al. **Investigation into the ophthalmic artery and its branches by superselective angiography.** *Interv Neuroradiol* 2022;28:737–45 CrossRef Medline
- Piergallini L, Tardieu M, Cagnazzo F, et al. **Anterior cranial fossa dural arteriovenous fistula: transarterial embolization from the ophthalmic artery as first-line treatment.** *J Neuroradiol* 2021;48:207–14 CrossRef Medline
- Cannizzaro D, Peschillo S, Cenato M, et al. **Endovascular and surgical approaches of ethmoidal dural fistulas: a multicenter experience and a literature review.** *Neurosurg Rev* 2018;41:391–98 CrossRef Medline
- Kular S, Tse G, Pahwa B, et al. **Micro-balloon-assisted embolization of anterior cranial fossa dural arteriovenous fistula via a trans-ophthalmic approach: a technical report and case series.** *Neuroradiology* 2022;64:1269–74 CrossRef Medline
- Pulli B, Sussman ES, Mayercik V, et al. **Initial experience with the Scepter Mini dual-lumen balloon for transophthalmic artery embolization of anterior cranial fossa dural arteriovenous fistulae.** *J Neurointerv Surg* 2020;12:1132–36 CrossRef Medline

# Safety and Efficacy of Low-Profile Braided Stents versus Flow Diverters in the Reconstructive Technique in the Treatment of Patients with Vertebrobasilar Dolichoectasia Aneurysms: A Cohort of 47 Patients with Long-Term Follow-Up

 Zhe Ji, Chuan He, Jingwei Li,  Jiewen Geng,  Peng Hu, Guilin Li, and  Hongqi Zhang



## ABSTRACT

**BACKGROUND AND PURPOSE:** Vertebrobasilar dolichoectasia aneurysm is a rare type of cerebrovascular disorder with a poor natural history, and endovascular treatment is widely accepted. Whether a high-profile braided stent (flow diverter) could promote occlusion of vertebrobasilar dolichoectasia aneurysm without increasing the complications rather than a low-profile braided stent remains uncertain. The aim of the study was to present a single-center experience of the safety and efficacy of a low-profile braided stent versus a flow diverter in treating patients with vertebrobasilar dolichoectasia aneurysms.

**MATERIALS AND METHODS:** The retrospective review was conducted on a total of 432 consecutive patients diagnosed with posterior circulation aneurysms who underwent endovascular treatment in our center from August 2013 to December 2021. Among these patients, 47 individuals with vertebrobasilar dolichoectasia aneurysms who were treated with low-profile braided stents or flow diverters were included. Vertebrobasilar dolichoectasia aneurysms involving only the vertebral artery were excluded. Patients were divided into 2 groups: the low-profile braided stent group and the flow diverter group based on the device used. Safety and efficacy outcomes were subsequently analyzed.

**RESULTS:** There were 25 total patients enrolled in low-profile braided stent group and 22 patients in flow diverter group. The safety of low-profile braided stents and flow diverters in the treatment of vertebrobasilar dolichoectasia aneurysms was evaluated by clinical outcome, a new neurologic deficit due to procedural complications, and neurologic death. The rates of good clinical outcome were similar between the 2 groups (low-profile braided stent, 56%, versus flow diverter, 59.1%;  $P = .831$ ), and the rates of neurologic death were also similar (low-profile braided stent, 12%, versus flow diverter, 9.1%;  $P = .747$ ). Higher rates of new neurologic deficits due to procedural complications were observed in the flow diverter group, but the difference was not significant (low-profile braided stent, 24%, versus flow diverter, 40.9%;  $P = .215$ ). The efficacy was evaluated by angiographic occlusion of vertebrobasilar dolichoectasia aneurysms and progression of mass effect resulting from these aneurysms. Significantly higher rates of complete occlusion of vertebrobasilar dolichoectasia aneurysms were shown in the flow diverter group (41.2%;  $P = .028$ ) than in the low-profile braided stent group (10%).

**CONCLUSIONS:** Both low-profile braided stents and flow diverters have similar high risks in reconstructive techniques in the treatment of vertebrobasilar dolichoectasia aneurysms, while a flow diverter is more effective in promoting complete occlusion of vertebrobasilar dolichoectasia aneurysm than a low-profile braided stent. A flow diverter may be a better alternative for carefully selected patients with vertebrobasilar dolichoectasia aneurysms.

**ABBREVIATIONS:** FD = flow diverter; LPBS = low-profile braided stent; VBDA = vertebrobasilar dolichoectasia aneurysm

Vertebrobasilar dolichoectasia aneurysm (VBDA) is a rare type of cerebrovascular disorder resulting in ectasia, elongation, and tortuosity of the vertebrobasilar artery. Flemming et al<sup>1</sup>

assumed that the incidence was  $<0.05\%$ , while Ince and Alpaslan<sup>2</sup> revealed that a VBDA was detected in approximately 2.06% of the first-ever stroke population. Patients with VBDAs commonly present with ischemic stroke, intracranial hemorrhage, and compression of the brainstem and/or cranial nerves, which could lead to

Received September 6, 2023; accepted after revision November 2.

From the Department of Neurosurgery, China International Neuroscience Institute, Xuanwu Hospital, Capital Medical University, Xicheng District, Beijing, China.

This study was supported by the Beijing Scientific and Technologic Project x, Z201100005520021, National Key Research Development Program x, 2016YFC1300800.

Chuan He and Hongqi Zhang contributed equally to this article.

We appreciate Jian Ren for drawing the artistic illustration.

Please address correspondence to Hongqi Zhang, MD, PhD, Department of Neurosurgery, China International Neuroscience Institute, Xuanwu Hospital, Capital Medical University, 45 Changchun St, Xicheng District, Beijing, China; e-mail: xwzhanghq@163.com

 Indicates article with online supplemental data.

<http://dx.doi.org/10.3174/ajnr.A8091>

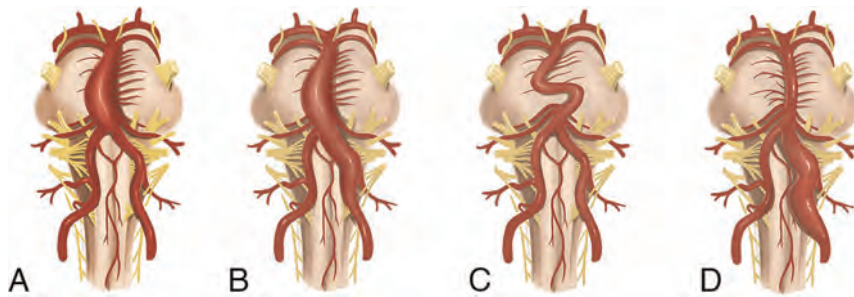


**FIG 1.** Artistic illustration of the inclusion criteria: VBD A involving the basilar artery (A), and VBD A involving both basilar and vertebral arteries (B) with superimposed dilation of a portion of the arterial segment. Artistic illustration of the exclusion criteria: A VBD A presenting with only elongation and/or tortuosity but without ectasia (C), and a VBD A only involving only the vertebral artery (D). The pictures are drawn by courtesy of Dr Jian Ren.

high rates of morbidity and mortality.<sup>3–7</sup> The natural history of VBD A is poor, and the cumulative proportion of survivors free of adverse health events was 54.1% at 5 years, 39.5% at 10 years, and 23.5% at 15 years.<sup>8</sup> Such a poor natural history indicated that professional intervention was necessary. However, treatment of VBD As was also challenging.

Surgical treatment of VBD As is rarely reported, and even the most experienced team reported an extremely high mortality in surgical outcome.<sup>9,10</sup> Endovascular treatment is more widely accepted and relatively simple in comparison. The low-profile braided stent (LPBS) has proved to be effective and relatively safe in treating VBD A during short-term follow-up, but it showed limited effectiveness in improving long-term prognosis and clinical outcome of patients with compressive symptoms.<sup>11–13</sup> The flow diverter (FD) has revolutionized the treatment of intracranial aneurysms and showed great potential in treating such nonsaccular intracranial aneurysms. However, complication rates using a FD in treating posterior circulation aneurysms are much higher than those for the anterior circulation.<sup>14</sup> Additionally, patients with basilar artery aneurysms have even significantly higher rates of mortality than those with vertebral artery aneurysms due to a high profile and existence of pontine perforators.<sup>15</sup> Whether a high-profile braided stent (FD) could promote occlusion of VBD As without increasing the complications more than LPBSs remains questionable. Therefore, we aimed to present our single-center experience based on 47 patients with VBD As treated with LPBSs and FDs.

## MATERIALS AND METHODS

### Study Design

This was a single-center retrospective study; it was approved by the ethics committee and local institutional review board of Xuanwu Hospital, Capital Medical University, Beijing, China (Nos. NO.2017024 and No 2017082). The requirement for written informed consent was waived because of the retrospective nature. The retrospective review was conducted on a total of 432 consecutive patients diagnosed with posterior circulation aneurysms who underwent endovascular treatment in our center from August 2013 to December 2021. The diagnosis of all enrolled patients with VBD As was radiologically confirmed by DSA after admission. The inclusion criteria for the subjects were as

follows: 1) untreated and unruptured VBD As meeting the diagnostic criteria defined as uniform aneurysmal dilation of an artery of  $>1.5$  times normal involving the basilar artery with a superimposed dilation of a portion of the basilar trunk;<sup>1</sup> and 2) use of a reconstructive technique with an LPBS or FD for treatment, with or without adjunctive coils. The exclusion criteria for the subjects were as follows: 1) a VBD A presenting with only elongation and/or tortuosity but without ectasia (Fig 1C); 2) a VBD A involving only the vertebral artery (Fig 1D). A VBD A without significant dilation was not

included due to its relatively benign natural history. A VBD A involving only the vertebral artery was also excluded because the difficulty and risk of the treatment was largely different whether or not the basilar trunk was involved due to the existence of pontine perforators. Finally, 47 patients with VBD As were included. All enrolled patients were classified into 2 groups: the LPBS group and the FD group according to the device used.

### Procedures

All procedures were performed with the patient under general anesthesia, with a femoral approach used in all patients. A 5F or 6F Navien intermediate catheter (Medtronic) was placed in the vertebral artery within a 6F Envoy DA guiding catheter (Codman Neuro), a 6F or 8F Envoy guiding catheter, or a 6F Neuron MAX long sheath (Penumbra). Marksman (Medtronic), Phenom 27 (Medtronic), or a Fast-track (MicroPort) microcatheter was introduced over a 0.014-inch Synchro guidewire (Stryker) into the distal posterior cerebral artery. Two types of LPBS, LVIS stent (MicroVention) and LEO stent (Balt Extrusion), and 2 types of FDs, the Pipeline Embolization Device (Medtronic) and the Tubridge Embolization Device (MicroPort), were used for treatment.

### Anticoagulation and Antiplatelet Management

Before endovascular treatment, routine daily doses of dual antiplatelet therapy, including at least 100 mg of aspirin combined with 75 mg of clopidogrel, were given for at least 3 days. However, platelet function testing was not conducted systematically because of the retrospective nature of the study. Intraoperative unfractionated heparin was given according to the patients' weight at a dose of 0.67 mg/kg once the endovascular treatment approach was established, and an additional dose was given depending on the length of the procedure. Additional postoperative tirofiban (0.1  $\mu$ g/kg/min) was administered at the discretion of the operators. All patients would continue 100 mg of aspirin daily for at least 12 months and 75 mg of clopidogrel for at least 6 months.

### Follow-Up and Outcome Measurements

Clinical follow-up was conducted at least 6 months after endovascular treatment, and the mRS was used to evaluate the clinical outcome. An mRS score of  $\leq 2$  was considered a favorable clinical

**Table 1: Baseline patient and VBDA imaging characteristics**

Factors	Different Groups		
	LPBS (n = 25)	FD (n = 22)	P Value
Patient characteristics			
Age (mean) (yr)	58.6 (SD, 10.2)	59.4 (SD, 8.7)	.445
Sex (male)	21 (84%)	17 (77.3%)	.654
Medical history			
Hypertension	23 (92%)	19 (86.4%)	.532
Diabetes	4 (16%)	1 (4.5%)	.204
Smoking	10 (40%)	8 (36.4%)	.798
Preoperative mRS score			
0	4 (16%)	5 (22.7%)	.582
1	10 (40%)	5 (22.7%)	
2	8 (32%)	9 (40.9%)	
3	3 (12%)	2 (9.1%)	
4	0	1 (4.6%)	
5	0	0	
VBDA imaging characteristic			
Length of VBDA (mean) (mm)	33.6 (SD, 11.9)	38.4 (SD, 13.8)	.551
Diameter of VBDA (mean) (mm)	15.2 (SD, 5.1)	15.4 (SD, 5.2)	.924
Brainstem compression resulting from VBDA	13 (52%)	13 (59.1%)	.626
Cerebral infarction around VBDA territory	7 (28%)	9 (40.9%)	.351

outcome, and an mRS score of  $\geq 3$  was considered an unfavorable clinical outcome. Changes in the mRS score were used to evaluate changes in clinical outcomes from admission to the latest clinical follow-up. A radiologic examination was also conducted at least 6 months postoperatively. Angiographic occlusion was evaluated by DSA,<sup>16</sup> and the result was categorized as complete (100% volume of dilation was occluded), near-complete ( $>90\%$  volume of dilation was occluded), or incomplete ( $<90\%$  volume of dilation was occluded). Progression of a mass effect resulting from a VBDA was evaluated by MR imaging. Measurements of the maximum transverse diameter of the vessel wall were performed at the same level on preoperative and follow-up MR imaging. Progression of mass effect was defined as enlargement of the maximum transverse diameter of the vessel wall of  $\geq 5$  mm, or the result would be considered as no progression.

All complications thought to be procedural were reported. Complications were classified as intracranial hemorrhagic and ischemic. Procedural ischemic complications were defined as any ischemic events with definite clinical expression that contributed to an increase of  $\geq 1$  point on the NIHSS and radiographically confirmed fresh cerebral infarction around posterior circulation territories. Procedural hemorrhagic complications were defined as any intracranial bleeding events, radiographically confirmed intracranial or subarachnoid hemorrhage on CT.

All the above evaluations were conducted independently by 2 neurointerventionalists with  $>5$  years of experience and confirmed by a neurointerventionalist with  $>15$  years of experience.

### Statistical Analysis

Descriptive statistics were used. Categorical variables are presented as numbers and percentages. Continuous variables are presented as mean and range. Differences in baseline characteristics, clinical outcomes, and radiologic outcomes between groups were analyzed using *t* tests and  $\chi^2$  tests. SAS software, Version 9.4 (SAS Institute) was used for statistical analyses.

## RESULTS

### Baseline Characteristics

The study included a total of 47 consecutive patients with VBDA according to the inclusion and exclusion criteria above. The mean age of the patients enrolled was 59 years (range, 43–79 years). Thirty-eight (80.9%) patients were men, hypertension was observed in 42 (89.4%) patients, and 41 (87.2%) patients had an mRS score of  $\leq 2$  at admission. The mean length of the VBDA was 35.8 mm (range, 14.4–70.1 mm), and the mean diameter of the VBDA was 15.3 mm (range, 7.2–26 mm). All patients were classified into 2 groups according to the device used, with 25 patients in the LPBS group and 22 patients in the FD group. There were no statistically significant differences in baseline patient and

VBDA imaging characteristics between groups. The detailed baseline patient and VBDA imaging characteristics are shown in Table 1 and the Online Supplemental Data.

### Safety Results

The safety of the LPBS and FD in the treatment of VBDA was evaluated by clinical outcome, new neurologic deficits due to procedural complications, and neurologic death. Clinical follow-up data were available for all 47 patients. The median duration of clinical follow-up was 28 months for the LPBS group and 23 months for the FD group. The rates of good clinical outcome were similar between 2 groups (LPBS, 56%, versus FD, 59.1%;  $P = .831$ ), and there was also no significant difference in changes in symptoms. Higher rates of new neurologic deficits due to procedural complications were observed in the FD group, while ischemic complications accounted for the most deficits, but the difference was not significant (LPBS, 24%, versus FD, 40.9%;  $P = .215$ ). Additionally, some patients presented with excellent recovery after treatment of symptoms, and the rates of mild-to-severe disability due to procedural complications were similar. Similar rates of neurologic death were also shown between 2 groups (LPBS, 12%, versus FD, 9.1%;  $P = .747$ ). Two patients died of brainstem function failure resulting from brainstem infarction, 2 patients died of intracerebral hemorrhage resulting from thrombolysis from brainstem infarction, and 1 died directly from intracranial hemorrhage. Another 2 patients died of uncorrelated heart failure and pneumonia. The detailed safety results are shown in Table 2 and the Online Supplemental Data.

### Efficacy Results

The efficacy of LPBS and FD in the treatment of VBDA was evaluated by angiographic occlusion of VBDA and progression of the mass effect resulting from VBDA. Radiologic follow-up data were available for 37 (78.7%) patients. Five deceased patients and 5 surviving patients were lost to radiologic imaging follow-up due to poor status except 1 patient. The median duration of radiologic

follow-up was 24 months for the LPBS group and 19 months for the FD group. Significantly higher rates of complete occlusion of VBDA were shown in the FD group than in the LPBS group (LPBS, 10%, versus FD, 41.2%;  $P = .028$ ). Lower rates of incomplete occlusion of VBDA were shown in the FD group than in the LPBS group, but the difference was not significant (LPBS, 30%, versus FD, 17.1%;  $P = .383$ ). Although there was no significant difference, the FD group showed advancement in slowing

down progression of mass effect resulting from the VBDA. The detailed radiologic follow-up outcomes are shown in Table 2 and the Online Supplemental Data.

### Illustrated Cases

**Case 1.** The patient (case No. 10) had choking, dysphagia, and weakness of the lower extremities with an mRS score of 2 and was admitted to our center 5 years ago. Further DSA showed vertebro-

basilar dolichoectasia (VBD), while T2-weighted MR imaging indicated mild brainstem compression (Fig 2A, -B). Considering that the patient had compressive symptoms and obvious dilation of the basal-inferior segment, 2 LEO stents were implanted (Fig 2C). Two years later, the patient returned with choking recurrence, dysphagia, and weakness of the lower extremities accompanied by tinnitus. Follow-up DSA indicated partial occlusion of the VBD lesion, while T2-weighted MR imaging revealed progressive brainstem compression (Fig 2D, -E). Another LEO stent implantation was performed to obtain better direction of blood flow. Although the 5-year follow-up DSA showed that the VBD lesion was relatively stable, remarkable progression of brainstem compression was observed on the 5-year follow-up MR imaging (Fig 2F, -G). Meanwhile, the patient had aggravation of gait instability, choking, and dysphagia. Further FD implantation was planned for the patient, but

**Table 2: Safety and efficacy results**

Factors	Different Groups		
	LPBS (n = 25)	FD (n = 22)	P Value
Safety results			
Clinical outcome <sup>a</sup>			
Good (mRS ≤2)	14 (56%)	13 (59.1%)	.831
Poor (mRS ≥3)	11 (44%)	9 (40.9%)	
Changes in symptoms			
Nonaggravated	13 (52%)	14 (63.6%)	.421
Aggravated	12 (48%)	8 (36.4%)	
New neurologic deficits due to procedural complications			
Total	6 (24%)	9 (40.9%)	.215
Hemorrhagic	1 (4%)	2 (9.1%)	.476
Ischemic	5 (20%)	9 (40.9%)	.118
Mild-to-severe disability	6 (24%)	6 (27.3%)	.861
Neurologic death	3 (12%)	2 (9.1%)	.747
Efficacy results			
Angiographic occlusion <sup>b</sup>			
Complete	2 (10%)	7 (41.2%)	.028
Near-complete	12 (60%)	7 (41.2%)	.254
Incomplete	6 (30%)	3 (17.6%)	.383
Progression of mass effect			
Nonprogressed	10 (50%)	12 (70.6%)	.204
Progressed	10 (50%)	5 (29.4%)	

<sup>a</sup> Clinical follow-up data were available for all 47 of the 47 patients included.

<sup>b</sup> Radiologic imaging follow-up data for evaluating angiographic occlusion and progression of mass effect was available for 37 of the 47 patients included, 20 of the 25 patients in LPBS group and 17 of the 22 patients in FD group. Three surviving patients were lost to radiologic imaging follow-up due to poor status.

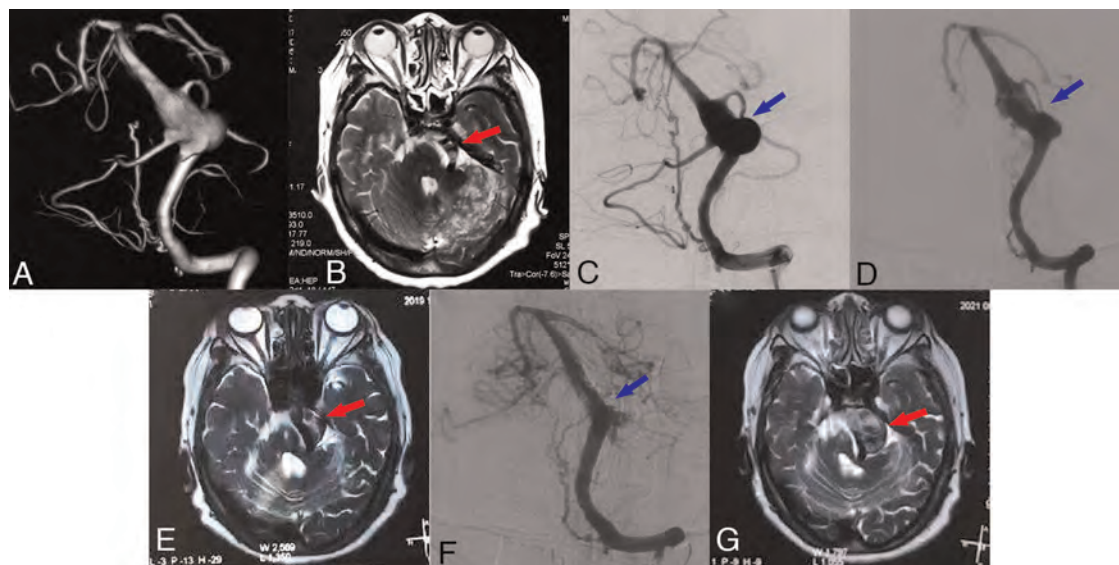


**FIG 2.** Preoperative DSA (A) and MR imaging (B) showing a VBDA and mild brainstem compression (red arrow). Angiography (C) after 2 LEO stents were implanted (blue arrow). Two-year follow-up DSA (D) indicating partial occlusion of the VBDA lesion (blue arrow), with MR imaging (E) revealing progressive brainstem compression (red arrow). Five-year follow-up DSA (F) showing further angiographic occlusion of the VBDA lesion (blue arrow), with MR imaging (G) revealing obvious progression of brainstem compression (red arrow).

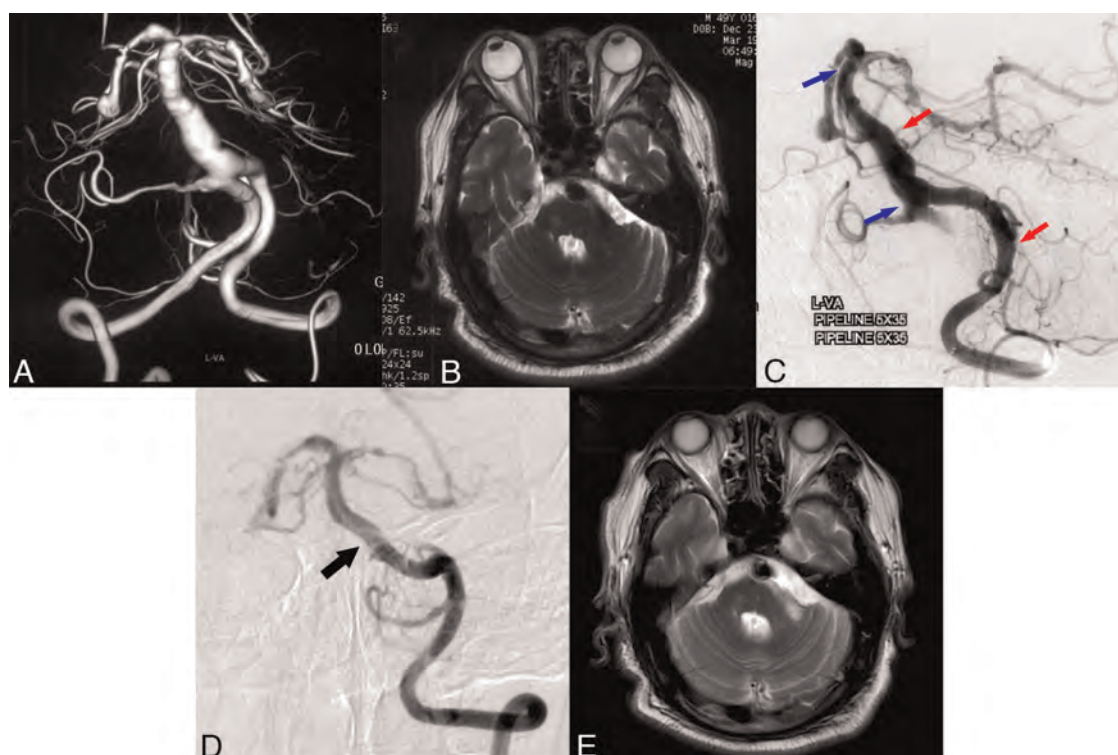


**FIG 3.** Preoperative DSA (A) showing a VBDA, with MR imaging (B) indicating no obvious brainstem compression. Angiography (C) after endovascular treatment with 2 Pipeline Embolization Devices was conducted. The blue arrows point to the proximal and distal edges of the first 5 × 35 cm Pipeline Embolization Device. The red arrows point to the proximal and distal edges of the second 5 × 35 cm Pipeline Embolization Device. Nine-month follow-up DSA (D) shows good healing of the dilation (black arrow) with no obvious progression of compression on MR imaging (E).

unfortunately, the patient refused. The patient was unable to take care of herself at the latest follow-up with an mRS of 4. The long-term effectiveness of LPBSs in preventing recanalization and increased mass effect of the VBD remains questionable.

**Case 2.** The patient (case No. 40) had dizziness and weakness of the lower extremities with an mRS score of 2 at admission, and planned DSA showed VBD, while MR imaging indicated no obvious brainstem compression or obvious dilation of the lesion (Fig 3A, -B). Endovascular treatment with 2 Pipeline Embolization Devices was performed (Fig 3C), and no periprocedural complications occurred. Nine-month follow-up DSA showed good healing of the dilation, with no obvious progression of compression observed on MR imaging (Fig 3D, -E). The patient also considered the symptoms to have gradually improved after endovascular treatment with FDs at the latest 2-year follow-up visit.

## DISCUSSION

Both LPBSs and FDs have high risks in the reconstructive technique in the treatment of VBDA, but whether a VBDA should be treated and the indications for the VBDA still remain confusing. The natural history of VBDA is poor, and the cumulative proportion of survivors free of adverse health events was 54.1% at 5 years, 39.5% at 10 years, and 23.5% at 15 years.<sup>8</sup> However, except for radiologic progression of the VBDA, which has been suggested to be associated with poor clinical outcome, no other defined risk factors have been reported.<sup>17,18</sup> Specific radiographic features that indicate VBDA tend to change from benign, even

asymptomatic, to malignant and require treatment remain unanswerable. According to a recent meta-analysis, patients with VBDA could not benefit significantly from endovascular treatment in comparison with the natural history. Therefore, the indications of VBDA are of great importance.<sup>19</sup> Patients with VBDA who underwent endovascular treatment in our cohort usually presented with prominent clinical symptoms, obvious dilation with high rupture risk, or enlargement during follow-up. We prefer conservative treatment and regular follow-up for patients with VBDA who remain asymptomatic or VBDA without dilation due to their relatively benign natural history.<sup>1</sup> However, all treatment decision-making processes still depend on the discretion of operator instead of uniform consensus.

Previous reports had concluded that the high profile of the FD either mechanically blocks the orifice of the side branch or narrows it to an insufficient size, accounting for the occurrence of perforator infarction.<sup>20</sup> Perforator infarction was associated with a significantly higher risk of posterior circulation aneurysms, especially the aneurysm around brainstem, due to a lack of collaterals and delicate perfusion.<sup>21</sup> However, safety outcomes between the LPBS and FD groups were similar according to the result, on the basis of our experience. Although higher rates of new neurologic deficits due to procedural complications were observed in the FD group, while rates of ischemic complications in the FD group were 2 times higher than those of the LPBS group, the difference was not significant. Additionally, the rates of mild-to-severe disability due to procedural complications and clinical outcome were similar between groups.

The result was also consistent with a recent systematic review and meta-analysis, which showed no significant difference in favorable clinical outcomes between stent-assisted coiling and FD placement in the treatment of posterior circulation nonsaccular aneurysms.<sup>22</sup> Early reports of VBDA treatment with an FD showed a very high complication rate of >50%,<sup>23</sup> which has extremely restricted the application in the early stage. The telescope technique with multiple FDs may account for the poor results, and the technique was strictly limited in our cohort unless the dilated segment of the VBDA was too long, so the safety result was relatively acceptable. In addition, postoperative dual antiplatelet therapy with oral anticoagulation was reported to have a significantly better clinical outcome than dual antiplatelet therapy for patients with VBDA treated with an FD;<sup>24</sup> similar regimens were also recommended for further treatment.

According to a recent systematic review and meta-analysis, no significant difference was shown in rates of complete/near-complete occlusion between stent-assisted coiling and FD placement in the treatment of posterior circulation nonsaccular aneurysms.<sup>22</sup> This study had similar results in rates of complete/near-complete occlusion, but significantly higher rates of complete occlusion of VBDA were shown in FD group than in the LPBS group. A large case series reported 28 subjects similar to VBDA in our cohort; the result revealed that 42.8% of patients had good angiographic results, which was almost consistent with our results.<sup>25</sup> A multicenter study reported a total of 131 posterior circulation aneurysms treated with FDs, and the complete occlusion rates of fusiform aneurysms similar to VBDA in our cohort was 59.7%, which was higher than our results.<sup>16</sup> The VBDA in our cohort were larger in diameter, while VBDA only involving the vertebral artery being excluded may account for such results. In a study of 19 consecutive patients with VBDA treated with LPBSs, the results showed that 84.2% of patients had good reconstruction of the VBDA during radiographic follow-up, a percentage that was also higher than our results.<sup>11</sup> A significant proportion with adjunctive coils may account for such results. However, a similar strategy with LPBS and adjunctive coils was attempted in our cohort at an early stage, but rates of procedural complications were so high that adjunctive coils have been used with great caution since then.

Brainstem compression resulting from VBDA was also a great therapeutic challenge. Although no significant difference was shown, the LPBS proved to be less effective in preventing progression of mass effect. As shown in illustrated case 1, despite favorable angiographic occlusion of the VBD lesion on DSA, mass effect still progressed and resulted in a poor prognosis. Another study reached a similar conclusion that the effects of LPBS were limited for patients with VBDA presenting with compressive symptoms.<sup>12</sup> The result reported by another team suggested that parent artery occlusion and flow diversion were better alternatives for VBDA with brainstem compression, also partly consistent with our results.<sup>26</sup> Last, different from other intracranial aneurysms, importance should be given to evaluating not only angiographic occlusion but also the progression of mass effect of the VBDA in follow-up because it was often ignored but could result in poor prognosis.

## LIMITATIONS

This is a single-center retrospective study, but the sample size is large compared with similar studies. The VBDA is a rare type of cerebrovascular disorder, so the result is still acceptable. Results based on comparison between contemporaneous clinical and radiologic follow-up would be more persuasive, but such comparison is difficult to conduct because of the retrospective nature. Additionally, platelet function testing was also limited because of the retrospective nature. Only a subset of patients underwent platelet function testing, and the adjustment of antiplatelet regimens based on the results was also empirical.

## CONCLUSIONS

There is no significant difference in the safety results between the LPBS and FD groups, but both strategies carry high risks. An FD is more effective in promoting complete occlusion of VBDA than LPBS. An FD may be a better alternative for carefully selected patients with VBDA. However, advanced-level studies such as randomized controlled trials are still necessary and desired.

**Disclosure forms** provided by the authors are available with the full text and PDF of this article at [www.ajnr.org](http://www.ajnr.org).

## REFERENCES

1. Flemming KD, Wiebers DO, Brown RD Jr, et al. **The natural history of radiographically defined vertebrobasilar nonsaccular intracranial aneurysms.** *Cerebrovasc Dis* 2005;20:270–79 CrossRef Medline
2. Ince B, Alpaslan BG. **Vertebrobasilar dolichoectasia and stroke risk factors.** *Thrombosis Research* 2016;141:S37–38 CrossRef
3. Aurora SK, Tietjen GE. **Vertebrobasilar artery ectasia presenting as hydrocephalus.** *J Stroke Cerebrovasc Dis* 2000;9:192–95 CrossRef Medline
4. AbdelHamid M, John K, Rizvi T, et al. **Hemifacial spasm due to vertebrobasilar dolichoectasia: a case report.** *Radiol Case Rep* 2015;10:65–67 CrossRef Medline
5. Förster A, Wenz H, Al-Zghloul M, et al. **Vertebrobasilar dolichoectasia is associated with cerebral microbleeds and intracerebral hemorrhage in the posterior circulation.** *Eur Stroke J* 2016;1:82 CrossRef
6. Cheng-Ching E, Chahine L, Hussain MS, et al. **Giant dolichoectatic vertebrobasilar system: clinical presentation and endovascular approach: a case report.** *J Neuroimaging* 2010;20:93
7. Nasr DM, Flemming KD, Lanzino G, et al. **Natural history of vertebrobasilar dolichoectatic and fusiform aneurysms: a systematic review and meta-analysis.** *Cerebrovasc Dis* 2018;45:68–77 CrossRef Medline
8. Passero SG, Rossi S. **Natural history of vertebrobasilar dolichoectasia.** *Neurology* 2008;70:66–72 CrossRef Medline
9. Nakatomi H, Kiyofuji S, Ono H, et al. **Giant fusiform and dolichoectatic aneurysms of the basilar trunk and vertebrobasilar junction: clinicopathological and surgical outcome.** *Neurosurgery* 2020;88:82–95 CrossRef Medline
10. Lawton MT, Abla AA, Rutledge WC, et al. **Bypass surgery for the treatment of dolichoectatic basilar trunk aneurysms: a work in progress.** *Neurosurgery* 2016;79:83–99 CrossRef Medline
11. He X, Duan C, Zhang J, et al. **The safety and efficacy of using large woven stents to treat vertebrobasilar dolichoectasia.** *J Neurointerv Surg* 2019;11:1162–66 CrossRef Medline
12. Wang J, Jia L, Yang X, et al. **Outcomes in symptomatic patients with vertebrobasilar dolichoectasia following endovascular treatment.** *Front Neurol* 2019;10:610 CrossRef Medline
13. Wu X, Xu Y, Hong B, et al. **Endovascular reconstruction for treatment of vertebrobasilar dolichoectasia: long-term outcomes.** *AJNR Am J Neuroradiol* 2013;34:583–88 CrossRef Medline

14. Zhou G, Su M, Yin YL, et al. **Complications associated with the use of flow-diverting devices for cerebral aneurysms: a systematic review and meta-analysis.** *Neurosurg Focus* 2017;42:E17 CrossRef Medline
15. Wang CB, Shi WW, Zhang GX, et al. **Flow diverter treatment of posterior circulation aneurysms: a meta-analysis.** *Neuroradiology* 2016;58:391–400 CrossRef Medline
16. Griessenauer CJ, Ogilvy CS, Adeeb N, et al. **Pipeline embolization of posterior circulation aneurysms: a multicenter study of 131 aneurysms.** *J Neurosurg* 2018;130:923–35 CrossRef Medline
17. Ubogu EE, Zaidat OO. **Vertebrobasilar dolichoectasia diagnosed by magnetic resonance angiography and risk of stroke and death: a cohort study.** *J Neurol Neurosurg Psychiatry* 2004;75:22–26 Medline
18. Mangrum WI, Huston J, Link MJ, et al. **Enlarging vertebrobasilar nonsaccular intracranial aneurysms: frequency, predictors, and clinical outcome of growth.** *J Neurosurg* 2005;102:72–79 CrossRef Medline
19. Bin-Alamer O, Qedair J, Palmisciano P, et al. **Dolichoectatic vertebrobasilar aneurysms: a systematic review and meta-analysis of management strategies and outcomes.** *Neurosurg Focus* 2023;54:E9 CrossRef Medline
20. Kulcsár Z, Ernemann U, Wetzel SG, et al. **High-profile flow diverter (Silk) implantation in the basilar artery: efficacy in the treatment of aneurysms and the role of the perforators.** *Stroke* 2010;41:1690–96 CrossRef Medline
21. Brinjikji W, Murad MH, Lanzino G, et al. **Endovascular treatment of intracranial aneurysms with flow diverters: a meta-analysis.** *Stroke* 2013;44:442–47 CrossRef Medline
22. Domingo RA, Tripathi S, Perez-Vega C, et al. **Treatment of posterior circulation non-saccular aneurysms with flow diversion versus stent-assisted coiling: a systematic review and meta-analysis.** *J Neurointerv Surg* 2021;13:159–63 CrossRef Medline
23. Natarajan SK, Lin N, Sonig A, et al. **The safety of Pipeline flow diversion in fusiform vertebrobasilar aneurysms: a consecutive case series with longer-term follow-up from a single US center.** *J Neurosurg* 2016;125:111–19 CrossRef Medline
24. Siddiqui AH, Monteiro A, Hanel RA, et al. **Triple therapy versus dual-antiplatelet therapy for dolichoectatic vertebrobasilar fusiform aneurysms treated with flow diverters.** *J Neurointerv Surg* 2023;15:655–63 CrossRef Medline
25. Bhogal P, Pérez MA, Ganslandt O, et al. **Treatment of posterior circulation non-saccular aneurysms with flow diverters: a single-center experience and review of 56 patients.** *J Neurointerv Surg* 2017;9:471–81 CrossRef Medline
26. Cho DY, Kim BS, Choi JH, et al. **The fate of unruptured intracranial vertebrobasilar dissecting aneurysm with brain stem compression according to different treatment modalities.** *AJNR Am J Neuroradiol* 2019;40:1924–31 CrossRef Medline

# Discrimination of Hemorrhage and Contrast Media in a Head Phantom on Photon-Counting Detector CT Data

Franka Risch, Ansgar Berlis, Thomas Kroencke, Florian Schwarz, and Christoph J. Maurer



## ABSTRACT

**SUMMARY:** In this anthropomorphic head phantom study, samples containing blood and contrast agent with concentrations ranging from 0 to 6 mg iodine per milliliter and another set of samples without blood for reference were scanned with a photon-counting detector CT using a standard cranial protocol. It was demonstrated that photon-counting detector CT can reliably distinguish hemorrhage and contrast media, including density determination of the latter. The technology promises to add value in several neuroimaging applications.

**ABBREVIATIONS:** CM = contrast media; ME70 = virtual monoenergetic image at 70 keV; PCD = photon-counting detector; VNC = virtual noncontrast

In recent years, the field of intracranial endovascular intervention has gained expertise and application due to the therapeutic benefit that minimally invasive treatment provides.<sup>1</sup> Intracranial interventions, such as recanalization or embolization procedures, usually require an unenhanced control CT scan to rule out possible bleeding. However, distinguishing hemorrhage from contrast enhancement that may have passed the BBB during the intervention is challenging due to their similar x-ray attenuation.<sup>2,3</sup>

Photon-counting detector CT (PCD-CT) is a promising technology that has the potential to facilitate the differentiation of contrast-enhancement media and hemorrhage following neuro-interventional procedures in clinical routine. This scanner inherently acquires spectral information that allows postprocessing steps including material differentiation.<sup>4</sup> Accordingly, a CT scan can be separated into the attenuation resulting from remaining iodine and soft tissue, generating contrast media (CM) maps and virtual noncontrast (VNC) series. The instant availability of this information promises to improve the diagnostic confidence and the associated therapeutic decision.

The purpose of this in vitro study was to evaluate the ability of PCD-CT to precisely distinguish between blood and iodine at various iodine concentrations, including the precise

determination of the CM attenuation within an anthropomorphic head phantom.

## MATERIALS AND METHODS

### Phantom

The phantom used in this study replicates the human brain anatomy and comprises brain-equivalent tissue with constant CT values, surrounded by high x-ray-absorbing structures that simulate the skull and temporal bones (PFO-Kalotte; Quality assurance in Radiology and Medicine). Additionally, 3 cylindric holes at the center, anterior, and lateral aspects, directly beneath the skull, allow inserts.

### Insert Composition

Iodine concentrations from 0 to 6 mg/mL with 1 mg/mL increments were included in this study. As a reference, 1 series of concentrations consisted solely of iodine (30 mg/mL) and sodium chloride (0.9%). The second series was designed to represent the actual clinical scenario of iodine mixed with blood. Red cells from an outdated blood donation were diluted with glucose (40%) and mixed with iodine and sodium chloride in a constant ratio (2 shares of blood, 1 share of glucose, 1 share of iodine diluted with sodium chloride) to simulate blood. All solutions were adjusted to a total volume of 120 mL to fill the whole of the phantom with a stand-off on both sides.

### CT Protocol

All samples were scanned on a novel PCD-CT (NAEOTOM Alpha; Siemens) with a standard clinical cranial CT protocol at all 3 phantom insert positions, respectively. Scans were acquired single-source at a tube voltage of 120 kV(peak) in a spiral mode with

Received September 22, 2023; accepted after revision November 7.

From the Departments of Diagnostic and Interventional Radiology (F.R., T.K., F.S.) and Diagnostic and Interventional Neuroradiology (A.B., C.J.M.), University Hospital Augsburg, Augsburg, Germany; Centre for Advanced Analytics and Predictive Sciences (T.K.), University Augsburg, Augsburg, Germany; and Medical Faculty (F.S.), Ludwig Maximilian University Munich, Munich, Germany.

F. Schwarz and C. J. Maurer contributed equally to this work.

Please address correspondence to Christoph Maurer, MD, Department of Diagnostic and Interventional Neuroradiology, University Hospital Augsburg, Stenglinstrasse 2, 86156 Augsburg, Germany; e-mail: christoph.maurer@uk-augsburg.de; @Podaleirios5

<http://dx.doi.org/10.3174/ajnr.A8093>

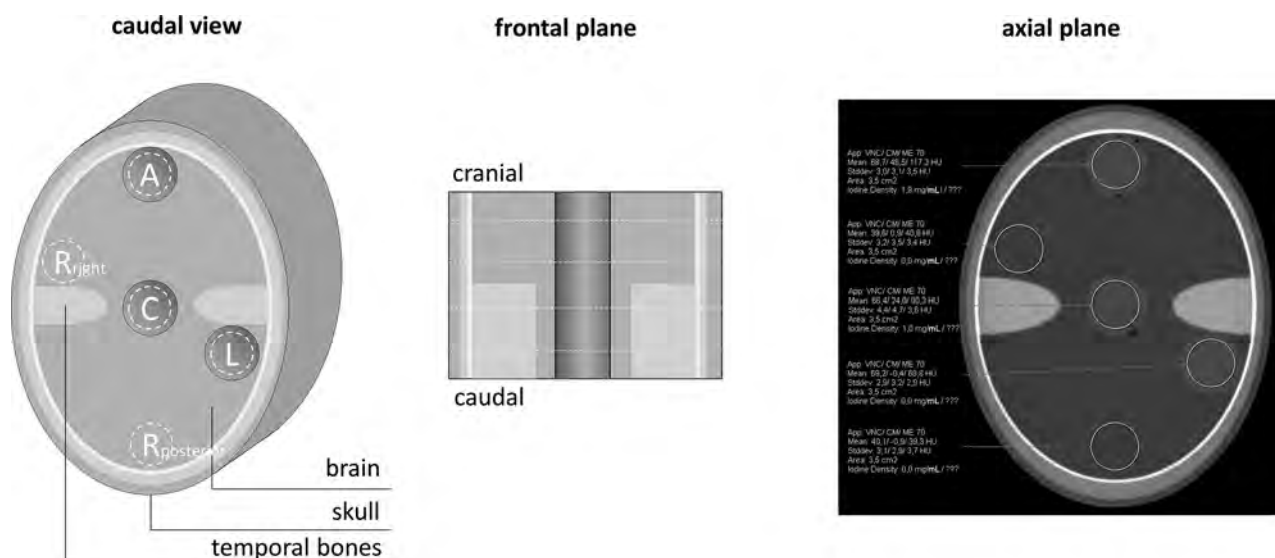


**FIG 1.** The schematic structure of the phantom and the respective positions of measurement. A indicates anterior; C, central; L, left; R<sub>posterior</sub>, posterior reference; R<sub>right</sub>, right reference).

a pitch of 0.55. The reference tube current time product was adjusted by setting the image quality level to 280, and the single/total collimation was 0.4/38.4 mm.

### Image Reconstruction

Images were iteratively reconstructed (Q2, quantum iterative reconstruction, QIR; Siemens) on the scanner console (Version VA50A) using a quantitative regular kernel (Qr40). Spectral post-processing series were generated to fully preserve spectral image information for further analyses. Section thickness and increment were set to 1.0/0.4 mm.

### Image Analysis

Image analysis was performed on a dedicated workstation (syngo, via, Version VB70A; Siemens) in a dual-energy workflow (virtual unenhanced application profile). Four different axial section positions were considered, 2 within and 2 out of the temporal bone section, approximately equally distributed from the cranial-to-caudal direction (Fig 1). Circular ROIs with a constant area of 3.5 cm<sup>2</sup> were positioned centrally within the inserts, excluding possible air bubbles. In addition to the positions anterior (A), central (C), and left (L), 2 further reference measurements posterior (R<sub>posterior</sub>) and right (R<sub>right</sub>), which were arranged symmetrically to the axis of rotation. The calculated iodine concentration in milligrams per milliliter, as well as the mean and SD of CT values in Hounsfield units for the CM map, the virtual monoenergetic image at 70 keV (ME70), and the VNC image were recorded. The noise level was defined as the SD of CT values measured within the reference ROIs (R<sub>posterior</sub> and R<sub>right</sub>).

### Statistical Analyses

Statistical analyses were conducted using Python (Version 3.9). Data were tested for normal distribution using the Shapiro-Wilk test. To assess differences, we used the paired *t* test and the Wilcoxon signed-rank test for parametric and nonparametric data, respectively. In case of multiple comparisons, *P* values were

adjusted using the Bonferroni method. Continuous data are given as mean (SD) or as median (interquartile range) for parametric or nonparametric data. The accuracy of linear regression analysis was assessed using the coefficient of determination (*r*<sup>2</sup>). Statistical significance was set at *P* values < .05.

### RESULTS

The effective milliamperere-seconds, volume CT dose index, and dose-length product were 170 mAs, 30.6 mGy, and 533 mGy × cm for each scan, respectively.

The general noise level was 3.5 (3.3–3.7) HU. All measurements of CT values within the reference and the blood samples are demonstrated in Fig 2. The reference probes without blood show low CT values for an actual iodine attenuation of 0 mg/mL with means of 3.8, 13.7, and 9.9 for CM, ME70, and VNC, respectively. With increasing iodine concentrations, Hounsfield units of CM and ME70 rise accordingly in ~22-HU steps with a significant (all, *P* < .01), albeit a small, constant distance of <10 HU from each other, attributable to the attenuation of the sodium chloride. Meanwhile VNC CT values remained constant around 9 HU. Results from blood-containing probes were even more accurate. At zero iodine concentration, ME70 and VNC showed no significant difference (*P* = .12), and the mean CT values on CM were close to 0 HU (−0.9 [SD, 1.6] HU). A linear increase of CT values of ME70 and CM was observed with increasing iodine attenuation, but with a larger distance in measurement to each other (~67 HU) due to the blood attenuation. On VNC, CT values were consistent with smaller SDs compared with the non-blood samples.

Figure 3 shows the regression analysis between the actual and measured iodine concentrations of the reference samples without blood and the samples with blood and glucose. The regression lines demonstrate a perfect linear relationship with an *r*<sup>2</sup> value of 1.0. However, the measured iodine concentrations are slightly underestimated with increasing actual concentration, indicated by the slope of 0.9. ROI positioning above or next to the

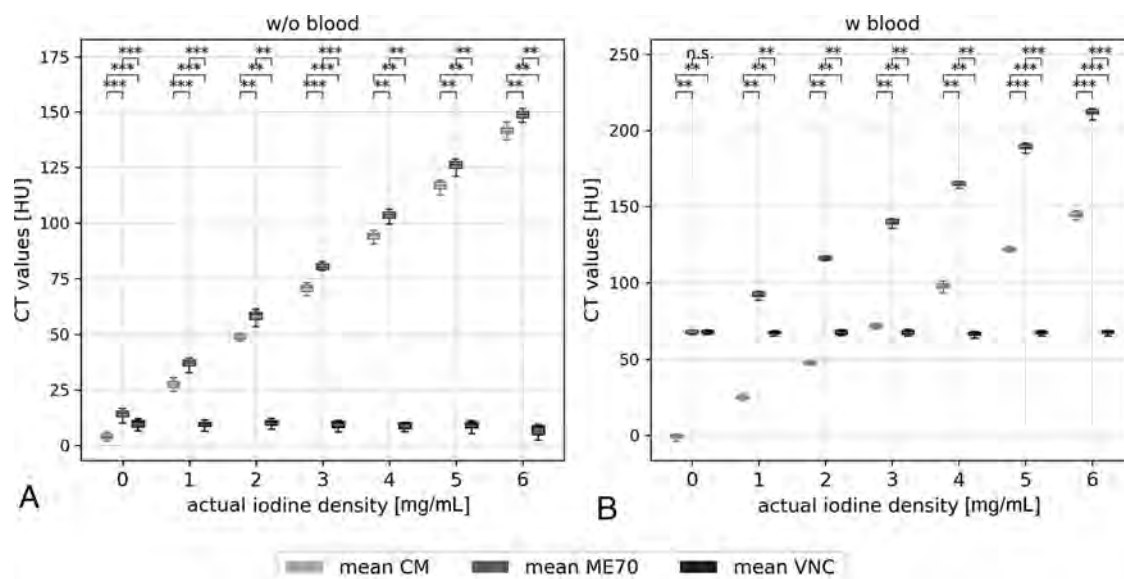


**FIG 2.** Measured CT values within the samples without (A) and with (B) blood, at all positions (anterior, center, left) and on all slices (next and above the temporal bone structures) presented in boxplots. CT values are compared among ME70, the CM map, and VNC. Statistically significant differences are marked. n.s. indicates  $P > .05$ ; \*,  $P < .05$ ; \*\*,  $P < .01$ ; \*\*\*,  $P < .001$ .

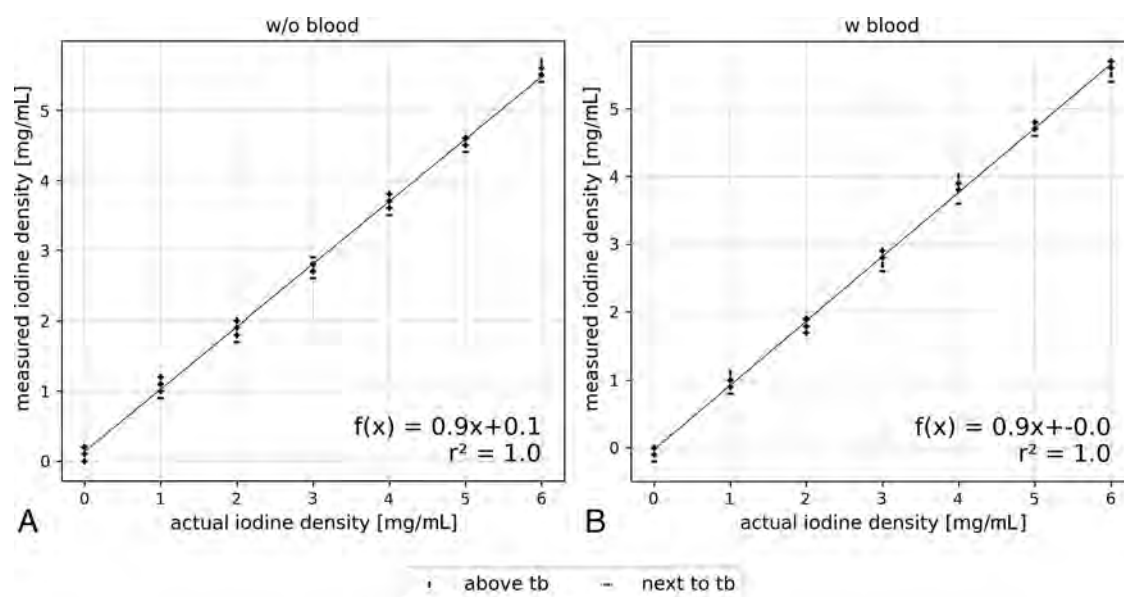


**FIG 3.** Linear regression of initial and measured iodine concentration of the samples. Reference samples without (A) and with (B) blood including all positions (anterior, center, left) and the compared between-sections above and next to temporal bone (tb) structures.

temporal bone structures showed no influence on the measurement and largely overlapped. Figure 4 shows that the mean difference between the actual and measured iodine concentrations is  $-0.2$  mg/mL, which is consistent for both reference and the blood samples.

## DISCUSSION

In this study, we analyzed several blood samples with iodine concentrations ranging from 0 to 6 mg/mL in an anthropomorphic head phantom and tested the ability of PCD-CT to discriminate CM and to determine its exact concentration. We found that the

spectral data of PCD-CT provide reliable differentiation between iodine- and noniodine-caused attenuation, regardless of the presence of blood or the height of CM concentration. Moreover, we demonstrated the feasibility of iodine concentration determination using PCD-CT.

In patients with acute ischemic stroke, the BBB disruption can lead to contrast enhancement of the infarcted area in the first few hours following mechanical thrombectomy. Distinguishing between contrast pooling and subarachnoid or parenchymal hemorrhage is crucial for patient management and outcome.<sup>5,6</sup> Additionally, this differentiation is important for other neurointerventions, such as embolization procedures for aneurysms,

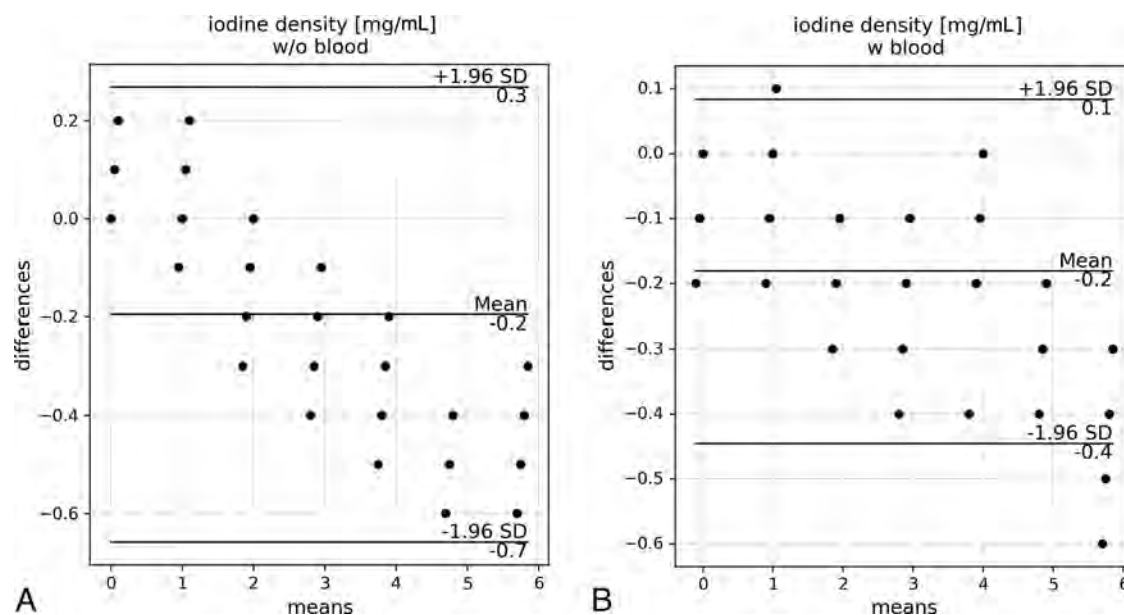


**FIG 4.** Bland-Altman plots showing the means and differences between the measured and actual iodine concentrations in samples without (A) and with (B) blood. All positions (anterior, center, and left) and sections (above and next to temporal bone structures) are considered. W/o indicates without; w, with.

AVMs, dural AVFs, and, more recently, embolization of the middle meningeal artery for treatment of chronic subdural hematomas.<sup>7-9</sup> During these interventions, hemorrhages can easily occur and must be distinguished from extravasation of CM or contrast enhancement.

CT is the imaging technique of choice because it is widely available and allows a rapid and accurate diagnosis. With conventional single-energy CT, however, a differentiation of blood and CM is extremely difficult due to the similar attenuation behavior of x-rays.<sup>10</sup> Spectral information, such as provided by dual-energy CT, allows performing material decomposition into attenuation shares caused by contrast and noncontrast media<sup>11</sup> and, therefore, has a wide range of application in neuroradiologic interventions.<sup>7</sup> The introduction of PCD-CT into clinical routine provides inherently spectral information and simultaneously overcomes limitations of conventional energy-integrating detectors with higher spatial resolution and the absence of electronic noise.<sup>4</sup>

This study used the standard cranial CT protocol for the anthropomorphic head phantom, to achieve dose results comparable with those of clinical in vivo scans. Analysis of Hounsfield units showed that iodine and blood are clearly distinguishable regardless of the underlying iodine attenuation. Furthermore, material decomposition of iodine and noniodine shares appears to be more accurate in samples with blood than in reference samples with only sodium chloride. Furthermore, differences of 1 mg/mL in iodine concentration can clearly be discriminated in CT values. The automated calculation of the underlying iodine attenuation shows a perfect linear correlation to the actual one, albeit with an increasing underestimation for higher concentrations. However, these inaccuracies may be partly due to several limitations. First, the accuracy of the instruments used and possible human error could affect the samples and their actual iodine concentrations. Second, a homogeneous distribution of CM

within the volume of the sample could not be guaranteed, possibly having led to local variation and, therefore, measurement errors. Third, the experiment is of an in vitro nature, and further studies are necessary to translate the results into clinical benefits for patient care.

## CONCLUSIONS

PCD-CT proved to be a reliable tool for differentiating blood and iodine and accurately determining several iodine concentrations in an anthropomorphic head phantom. These findings suggest the potential of PCD-CT for various applications in neuroimaging. Further studies should investigate the use of PCD-CT for imaging of brain hemorrhage with differentiation between calcification and hemorrhage, prediction of hematoma expansion on unenhanced CT and CTA,<sup>12</sup> as well as the identification of hemorrhagic tumors in hemorrhages of unknown origin.<sup>13</sup>












**Disclosure forms** provided by the authors are available with the full text and PDF of this article at [www.ajnr.org](http://www.ajnr.org).

## REFERENCES

- Eskey CJ, Meyers PM, Nguyen TN, et al; American Heart Association Council on Cardiovascular Radiology and Intervention and Stroke Council. **Indications for the performance of intracranial endovascular neurointerventional procedures: a scientific statement from the American Heart Association.** *Circulation* 2018;137:e661-89 CrossRef Medline
- Lummel N, Schulte-Altedorneburg G, Bernau C, et al. **Hyperattenuated intracerebral lesions after mechanical recanalization in acute stroke.** *AJNR Am J Neuroradiol* 2014;35:345-51 CrossRef Medline
- Kim JT, Heo SH, Cho BH, et al. **Hyperdensity on non-contrast CT immediately after intra-arterial revascularization.** *J Neurol* 2012;259:936-43 CrossRef Medline
- Flohr T, Petersilka M, Henning A, et al. **Photon-counting CT review.** *Phys Med* 2020;79:126-36 CrossRef Medline

5. Neuberger U, Kickingereder P, Schönenberger S, et al. **Risk factors of intracranial hemorrhage after mechanical thrombectomy of anterior circulation ischemic stroke.** *Neuroradiology* 2019;61:461–69 CrossRef Medline
6. Riederer I, Fingerle AA, Zimmer C, et al. **Potential of dual-layer spectral CT for the differentiation between hemorrhage and iodinated contrast medium in the brain after endovascular treatment of ischemic stroke patients.** *Clin Imaging* 2021;79:158–64 CrossRef Medline
7. Gibney B, Redmond CE, Byrne D, et al. **A review of the applications of dual-energy CT in acute neuroimaging.** *Can Assoc Radiol J* 2020;71:253–65 CrossRef Medline
8. Nakagawa I, Park HS, Kotsugi M, et al. **Enhanced hematoma membrane on DynaCT images during middle meningeal artery embolization for persistently recurrent chronic subdural hematoma.** *World Neurosurg* 2019;126:e473–79 CrossRef Medline
9. Zaouak Y, Sadeghi N, Sarbu N, et al. **Differentiation between cerebral hemorrhage and contrast extravasation using dual energy computed tomography after intra-arterial neuro interventional procedures.** *J Belg Soc Radiol* 2020;104:70 CrossRef Medline
10. Choi Y, Shin NY, Jang J, et al. **Dual-energy CT for differentiating acute intracranial hemorrhage from contrast staining or calcification: a meta-analysis.** *Neuroradiology* 2020;62:1617–26 CrossRef Medline
11. Heismann BJ, Schmidt BT, Flohr T. *Spectral Computed Tomography*. 2012; SPIE Press
12. Bodanapally UK, Shanmuganathan K, Gunjan YP, et al. **Quantification of iodine leakage on dual-energy CT as a marker of blood-brain barrier permeability in traumatic hemorrhagic contusions: prediction of surgical intervention for intracranial pressure management.** *AJNR Am J Neuroradiol* 2019;40:2059–65 CrossRef Medline
13. Kim SJ, Lim HK, Lee HY, et al. **Dual-energy CT in the evaluation of intracerebral hemorrhage of unknown origin: differentiation between tumor bleeding and pure hemorrhage.** *AJNR Am J Neuroradiol* 2012;33:865–72 CrossRef Medline

# Quantification of T2-FLAIR Mismatch in Nonenhancing Diffuse Gliomas Using Digital Subtraction

 Nicholas S. Cho,  Francesco Sanvito, Viên Lam Le, Sonoko Oshima,  Ashley Teraishi,  Jingwen Yao, Donatello Telesca,  Catalina Raymond,  Whitney B. Pope,  Phioanh L. Nghiemphu,  Albert Lai,  Timothy F. Cloughesy,  Noriko Salamon, and  Benjamin M. Ellingson



## ABSTRACT

**BACKGROUND AND PURPOSE:** The T2-FLAIR mismatch sign on MR imaging is a highly specific imaging biomarker of isocitrate dehydrogenase (*IDH*)-mutant astrocytomas, which lack 1p/19q codeletion. However, most studies using the T2-FLAIR mismatch sign have used visual assessment. This study quantified the degree of T2-FLAIR mismatch using digital subtraction of fluid-nulled T2-weighted FLAIR images from non-fluid-nulled T2-weighted images in human nonenhancing diffuse gliomas and then used this information to assess improvements in diagnostic performance and investigate subregion characteristics within these lesions.

**MATERIALS AND METHODS:** Two cohorts of treatment-naïve, nonenhancing gliomas with known *IDH* and 1p/19q status were studied ( $n = 71$  from The Cancer Imaging Archive (TCIA) and  $n = 34$  in the institutional cohort). 3D volumes of interest corresponding to the tumor were segmented, and digital subtraction maps of T2-weighted MR imaging minus T2-weighted FLAIR MR imaging were used to partition each volume of interest into a T2-FLAIR mismatched subregion (T2-FLAIR mismatch, corresponding to voxels with positive values on the subtraction maps) and nonmismatched subregion (T2-FLAIR nonmismatch corresponding to voxels with negative values on the subtraction maps). Tumor subregion volumes, percentage of T2-FLAIR mismatch volume, and T2-FLAIR nonmismatch subregion thickness were calculated, and 2 radiologists assessed the T2-FLAIR mismatch sign with and without the aid of T2-FLAIR subtraction maps.

**RESULTS:** Thresholds of  $\geq 42\%$  T2-FLAIR mismatch volume classified *IDH*-mutant astrocytoma with a specificity/sensitivity of 100%/19.6% (TCIA) and 100%/31.6% (institutional);  $\geq 25\%$  T2-FLAIR mismatch volume showed 92.0%/32.6% and 100%/63.2% specificity/sensitivity, and  $\geq 15\%$  T2-FLAIR mismatch volume showed 88.0%/39.1% and 93.3%/79.0% specificity/sensitivity. In *IDH*-mutant astrocytomas with  $\geq 15\%$  T2-FLAIR mismatch volume, T2-FLAIR nonmismatch subregion thickness was negatively correlated with the percentage T2-FLAIR mismatch volume ( $P < .0001$ ) across both cohorts. The percentage T2-FLAIR mismatch volume was higher in grades 3–4 compared with grade 2 *IDH*-mutant astrocytomas ( $P < .05$ ), and  $\geq 15\%$  T2-FLAIR mismatch volume *IDH*-mutant astrocytomas were significantly larger than  $< 15\%$  T2-FLAIR mismatch volume *IDH*-mutant astrocytoma ( $P < .05$ ) across both cohorts. When evaluated by 2 radiologists, the additional use of T2-FLAIR subtraction maps did not show a significant difference in interreader agreement, sensitivity, or specificity compared with a separate evaluation of T2-FLAIR and T2-weighted MR imaging alone.

**CONCLUSIONS:** T2-FLAIR digital subtraction maps may be a useful, automated tool to obtain objective segmentations of tumor subregions based on quantitative thresholds for classifying *IDH*-mutant astrocytomas using the percentage T2 FLAIR mismatch volume with 100% specificity and exploring T2-FLAIR mismatch/T2-FLAIR nonmismatch subregion characteristics. Conversely, the addition of T2-FLAIR subtraction maps did not enhance the sensitivity or specificity of the visual T2-FLAIR mismatch sign assessment by experienced radiologists.

**ABBREVIATIONS:** AUC = area under curve; *IDHm* = isocitrate dehydrogenase mutant; *IDHm-A* = isocitrate dehydrogenase mutant astrocytoma; *IDHm-O* = isocitrate dehydrogenase mutant oligodendroglioma; *IDHwt* = isocitrate dehydrogenase wild-type; NAWM = normal-appearing white matter; ROC = receiver operating characteristic; TCIA = The Cancer Imaging Archive; T2FM = T2-FLAIR mismatch; T2FNM = T2-FLAIR nonmismatch; VOI = volume of interest

The prognosis and management of human gliomas are dependent on the tumor molecular classification, particularly

isocitrate dehydrogenase (*IDH*) mutational status.<sup>1,2</sup> While *IDH* wild-type (*IDHwt*) tumors have poor prognosis<sup>2</sup> and warrant


Received September 23, 2023; accepted after revision November 10.

From the UCLA Brain Tumor Imaging Laboratory (N.S.C., F.S., V.L.L., S.O., A.T., J.Y., C.R., B.M.E.), Center for Computer Vision and Imaging Biomarkers, Department of Bioengineering (N.S.C., V.L.L., B.M.E.), Henry Samueli School of Engineering and Applied Science, Department of Biostatistics (D.T.), Fielding School of Public Health, University of California, Los Angeles, Los Angeles, California; Department of Radiological Sciences (N.S.C., F.S., V.L.L., S.O., A.T., J.Y., C.R., W.B.P., N.S., B.M.E.), Medical Scientist Training Program (N.S.C.), UCLA Neuro-Oncology Program (P.L.N., A.L., T.F.C.), Department of Neurology (P.L.N., A.L., T.F.C.), Department of Neurosurgery (B.M.E.), and Department of Psychiatry and Biobehavioral Sciences (B.M.E.), David Geffen School of Medicine, University of California, Los Angeles, Los Angeles, California.

This work was supported by the National Institutes of Health National Institute of General Medical Sciences, T32GM008042 (N.S.C.); National Institutes of Health

National Cancer Institute, F30CA284809 (N.S.C.); National Institutes of Health National Cancer Institute, R01CA270027 (B.M.E., T.F.C.); National Institutes of Health National Cancer Institute, R01CA279984 (B.M.E.), DoD CDMRP CA220732 (B.M.E., T.F.C.); and National Institutes of Health National Cancer Institute, P50CA211015 (B.M.E., T.F.C.).

Please address correspondence to Benjamin M. Ellingson, PhD, Departments of Radiological Sciences, Psychiatry, and Neurosurgery, David Geffen School of Medicine, University of California, Los Angeles, 924 Westwood Blvd, Ste 615, Los Angeles, CA 90024; e-mail: bellingson@mednet.ucla.edu

 Indicates article with online supplemental data.  
<http://dx.doi.org/10.3174/ajnr.A8094>

aggressive therapy, *IDH*-mutant (*IDHm*) tumors have a much more favorable prognosis.<sup>2,3</sup> Treatment plans for *IDHm* gliomas can include observation following surgery<sup>3</sup> to balance treatment-related morbidity from chemoradiation and may also soon include mutant *IDH*-inhibitor targeted therapies, which have recently shown significant benefit in a Phase III clinical trial.<sup>4,5</sup> However, because the molecular classification of gliomas requires histologic analyses, the inherently invasive nature of sampling brain tumor tissue either from biopsy or during tumor resection may also support the need for noninvasive methods to molecularly classify human gliomas in the up-front setting.

The presence of the T2-FLAIR mismatch sign (T2FM sign) on MR imaging, first described by Patel et al,<sup>6</sup> has become a well-known and validated<sup>7-13</sup> noninvasive imaging biomarker with ~100% specificity albeit low sensitivity for diagnosing *IDHm* astrocytomas (1p/19q-intact; *IDHm*-A) and ruling out *IDHm* oligodendrogliomas (1p/19q-codeleted; *IDHm*-O) and *IDHwt* gliomas. Patel et al originally described this imaging biomarker as the “presence or absence of complete/near-complete hyperintense signal on T2WI, and relatively hypointense signal on FLAIR except for a hyperintense peripheral rim,”<sup>6</sup> and the authors reported a specificity of 100% in the 2 cohorts they tested and sensitivities of 22.0% and 45.5%.<sup>6</sup> Other subsequent studies have also noted 100% specificity<sup>7,8</sup> along with some instances of false-positives resulting in specificities ranging from 76.5% to 98%.<sup>9-12</sup> There is also the potential for less conservative definitions of the T2FM sign, such as Lasocki et al<sup>8</sup> proposing that a reader-estimated  $\geq 25\%$  T2FM volume was sufficient to assign as T2FM sign positivity, which still yielded 100% specificity with 63% sensitivity;<sup>8</sup> Li et al<sup>14</sup> proposing simply a T2-weighted FLAIR hyperintense rim with a hypointense core regardless of appearance on T2-weighted MR imaging, which also yielded 100% specificity with 71.3% sensitivity; and Lee et al<sup>15</sup> proposing a partial T2FM sign in grade 4 *IDHm* gliomas when assessing only grade 4 gliomas, which yielded 99.6% specificity with 26.4% sensitivity. Less conservative definitions have also been proposed to explain the findings of Juratli et al<sup>10</sup> of 76% specificity with 73% sensitivity.<sup>13</sup>

However, despite the inherently quantitative nature of the T2FM sign based on the relative extent of T2FM volume within a tumor, to our knowledge, studies on the T2FM sign have mostly remained qualitative on the basis of reader studies. A prior study by Mohammed et al<sup>16</sup> has previously used a geographically-weighted regression-based classification model that resulted in the classification of *IDHm*-A with very high sensitivity and specificity. Another study by Lee et al<sup>17</sup> used a “hot-spot” assessment of T2FM areas by assessing relative T2-weighted and T2-weighted FLAIR hyperintensity in the T2FM core region for glioma classification,<sup>17</sup> but the study did not assess the whole-tumor quantification of T2FM volume. Quantifying T2FM volume could be valuable to assess whether there is a quantitative percentage T2FM volume that is analogous to T2FM sign positivity for achieving 100% specificity for *IDHm*-A, such as the reader-estimated  $\geq 25\%$  T2FM volume of Lasocki et al<sup>8</sup> or other volumetric thresholds.

As a result, there remains a continued need for methods for visualization and volumetric quantification of T2FM to specifically

study *IDHm*-A exhibiting the T2FM sign. For example, *IDHm*-A with the T2FM sign are known for intratumoral heterogeneity because the T2FM core subregion is known for the presence of microcysts or enlarged intercellular space on histology.<sup>12,18</sup> These findings may also demonstrate the need for a reliable method to study *IDHm*-A with the T2FM sign specifically in the context of characterizing T2FM and T2-FLAIR nonmismatch (T2FNM) sub-region differences. One such method could be subtraction maps of coregistered MR images, which have already shown utility for T1 post-/precontrast MR imaging for assessing contrast-enhancing tumor volume in glioblastomas.<sup>19</sup> While similar mathematics of relative T2-weighted and T2-weighted FLAIR hyperintensity signal has been used to study the T2FM sign only in the mismatched core region,<sup>17</sup> to our knowledge, whole-brain subtraction maps have not yet been applied for T2-weighted and T2-weighted FLAIR images to quantify the extent of T2FM from a whole-tumor, volumetric perspective.

The present study explored the use of T2-weighted and T2-weighted FLAIR subtraction maps to study T2FM in nonenhancing gliomas. We hypothesized the following: 1) There is a tumor percentage T2FM volume threshold based on subtraction map values that can classify *IDHm*-A with 100% specificity; 2) the percentage T2FM volume may be associated with tumor volume and tumor grade; and 3) the visual evaluation of T2-FLAIR subtraction maps would improve the sensitivity, specificity, and inter-reader agreement of the T2FM sign in a reader study.

## MATERIALS AND METHODS

### Patient Selection

Two cohorts of patients with gliomas who underwent preoperative MR imaging from 2 different institutions were screened for analysis: 1) a test cohort from The Cancer Imaging Archive (TCIA) University of California San Francisco Preoperative Diffuse Glioma MR imaging dataset (UCSF-PDGM) ( $n = 495$  total)<sup>20-22</sup> and 2) a validation cohort consisting of patients at our institution enrolled in prospective trials (institutional review board Nos. 14-001261, 21-000514, 21-002112) and/or assessed in a prior study<sup>23</sup> ( $n = 150$  total). All patients in the institutional cohort provided written informed consent. Patients with the following inclusion criteria were included in the study: 1) nonenhancing, adult-type diffuse glioma according to the World Health Organization 2021 classification,<sup>1</sup> 2) no prior pharmacologic or radiation treatment, 3) no prior surgery except for biopsy, 4) known *IDH*-mutational status, 5) if *IDH*-mutant, known 1p/19q status, and 6) supratentorial location (Online Supplemental Data). All patients in the TCIA UCSF-PDGM were treatment-naïve except for biopsy. The tumor molecular diagnosis ground truth was based on histopathologic analysis. *IDH* status was determined by targeted next-generation DNA sequencing for the TCIA cohort<sup>24</sup> and by polymerase chain reaction sequencing and/or immunohistochemistry for the institutional cohort.<sup>25</sup> 1p/19q codeletion status was determined using fluorescence in situ hybridization for both cohorts. A total of 70 patients from the TCIA UCSF-PDGM and 34 patients from the institutional cohort were included in the study (Online Supplemental Data). Two distinct lesions in the left and right hemispheres of 1 patient

**Table 1: Patient data**

Characteristic	TCIA Cohort ( <i>n</i> = 70 Patients with <i>n</i> = 71 Lesions)	Institutional Cohort ( <i>n</i> = 34 Patients/Lesions)
Age (mean) (range)	43 (22–78)	42 (22–79)
Sex: male/female	41/29	18/16
Diagnosis (No.) (%)		
IDHm-A	46 (64.8%)	19 (55.9%)
Grade 2	33	11
Grade 3	13	7
Grade 4	0	1
IDHm-O	9 (12.7%)	9 (26.5%)
Grade 2	9	8
Grade 3	0	1
IDHwt glioma	16 (22.5%)	6 (17.6%)

in the TCIA cohort were assessed separately. Patient data are summarized in Table 1.

### Image Acquisition and Preprocessing

Both cohorts were scanned using 3T scanners (TCIA: GE Healthcare Discovery 750; institutional: Siemens Prisma, Skyra, Trio, Vida) and underwent standardized protocols for T2-weighted and T2-weighted FLAIR MR imaging: TCIA, 3D T2-weighted sagittal FSE: TR/TE = 2200/100 ms; section thickness = 1.2 mm; in-plane resolution = 1 × 1 mm;<sup>21</sup> TCIA, 3D T2-weighted FLAIR coronal FSE: TR/TE/TI = 5700/115/1650 ms; section thickness = 1.2 mm; in-plane resolution = 1 × 1 mm;<sup>21</sup> institutional, 2D T2-weighted axial FSE: TR = 4381–8450 ms; TE = 86–116 ms; section thickness = 3 mm; in-plane resolution = 0.31–0.94 × 0.31–0.94 mm; institutional, 3D T2-weighted sagittal FSE (*n* = 1 patient): TR/TE = 3200/412 ms; section thickness = 1 mm; in-plane resolution = 0.98 × 0.98 mm; institutional, T2-weighted FLAIR 2D axial: TR = 7080–9980 ms; TE = 81–89 ms; TI = 2500 ms; section thickness = 3 mm; in-plane resolution = 0.47–0.94 × 0.47–0.94 mm.

The provided TCIA data were already preprocessed as follows:<sup>20,21</sup> scans were registered to the 3D T2-weighted FLAIR image (Advanced Normalization Tools software package; <http://stnava.github.io/ANTs/>) and then skull-stripped using the open-source, deep-learning algorithm brain\_mask ([https://www.github.com/ecalabr/brain\\_mask/](https://www.github.com/ecalabr/brain_mask/)). The institutional data were preprocessed similarly: scans were registered to the 3D T1-post-contrast image (tkregister2; FreeSurfer <https://surfer.nmr.mgh.harvard.edu/fswiki/tkregister2><sup>26</sup> and the FMRIB Linear Image Registration Tool, FLIRT, <https://fsl.fmrib.ox.ac.uk/fsl/fslwiki/FLIRT/UserGuide>)<sup>27</sup> and then skull-stripped using the open-source, deep-learning algorithm HD-BET<sup>28</sup> (<https://github.com/MIC-DKFZ/HD-BET>).

### T2-FLAIR Subtraction Maps and Tumor Imaging Analysis

T2-FLAIR subtraction maps were generated as follows: 1) skull-stripped T2-weighted MR imaging was further precisely registered to skull-stripped T2-weighted FLAIR MR imaging using FLIRT; 2) T2-weighted MR imaging and T2-weighted FLAIR MR imaging were normalized using *z* score normalization and then by performing voxelwise subtraction by the mean T2-weighted and T2-weighted FLAIR signal intensity, respectively, of the normal-appearing white matter (NAWM) using 3 spheric volumes of interest (VOIs) within the contralesional superior

centrum semiovale, avoiding T2/FLAIR hyperintensities as described previously<sup>23,29</sup> so that the resulting signal intensity in the NAWM would be ~0; and then 3) performing voxelwise subtraction of the normalized T2-weighted MR imaging and the normalized T2-weighted FLAIR MR imaging (normalized T2-weighted minus normalized T2-weighted FLAIR). Tumor VOIs of the T2-weighted hyperintensity of the institutional cohort were created by a lab member with 2 years of experience in tumor-segmentation analysis (N.S.C.)

using a semiautomated thresholding method involving Analysis of Functional NeuroImages (AFNI) software<sup>30</sup> (<https://afni.nimh.nih.gov>) as previously described.<sup>19,31</sup> The provided TCIA segmentations were also refined using this thresholding technique for consistency. Voxels corresponding to CSF and macroscopic cysts (characterized as having round shape, well-defined borders, CSF-like signal intensity, and lacking wall enhancement) were excluded from the tumor VOIs. All final tumor VOIs were inspected by a radiologist (S.O.) with 11 years of experience in neuroimaging analysis who was blinded to the tumor molecular diagnosis.

The whole-tumor VOIs were then split using the T2-FLAIR subtraction maps into T2FM (positive values in the T2-FLAIR subtraction map) and T2FNM (negative values in T2-FLAIR subtraction map) subregion VOIs using a consistent threshold of zero. Thus, tumor T2FM subregions would be defined as regions where the normalized T2-weighted MR imaging signal intensity is greater than the normalized T2-weighted FLAIR signal intensity, while the remaining voxels in the tumor mask would be assigned to the T2FNM subregion. T2FM and T2FNM subregion volumes were obtained. Tumor percentage T2FM volume (% T2FM volume) was calculated as T2FM subregion volume divided by total tumor volume. To assess the potential impacts of slight image misregistration on the percentage T2FM volume calculation, we generated 2 deliberately misregistered T2-FLAIR subtraction maps using the AFNI Nudge Dataset plugin (<https://afni.nimh.nih.gov/>)—one from a 2-voxel posterior shift of the coregistered T2-weighted MR imaging and one from 2° counterclockwise shift of the coregistered T2-weighted MR imaging—and tumor VOIs were split again into T2FM and T2FNM subregions. The median thickness of the peripheral T2FNM subregion for tumors exhibiting T2FM subregions was calculated using AFNI software by creating a 1-voxel-wide border segmentation of the T2FNM subregion VOI (3dDepthMap, rimify; [https://afni.nimh.nih.gov/pub/dist/doc/program\\_help/3dDepthMap.html](https://afni.nimh.nih.gov/pub/dist/doc/program_help/3dDepthMap.html)) followed by manually removing nonperipheral voxels and then creating a 3D depth map from the T2FM-subregion voxels after cluster filtering T2FM-subregion voxels at a threshold of >30 voxels. The external border segmentation was then encoded with the distance from the T2FM subregion via voxelwise multiplication of the depth map (Fig 1), and the median value was taken to be the T2FNM subregion thickness.

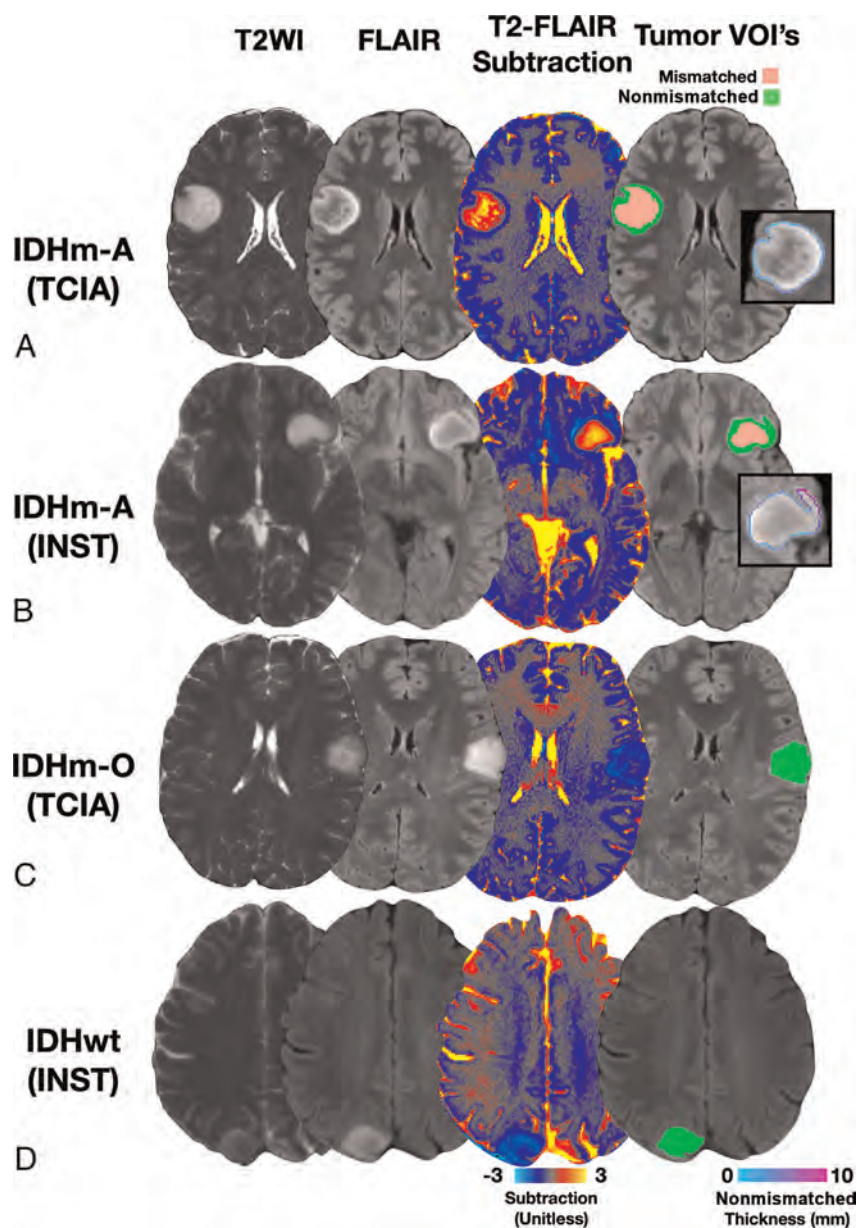


**FIG 1.** Representative true-positive and true-negative typical cases with T2-FLAIR subtraction maps and tumor segmentations. A, Patient A is a 38-year-old woman from the TCIA cohort diagnosed with a grade 2 *IDHm-A* demonstrating 59.6% T2-FLAIR mismatch volume (true-positive result). B, Patient B is a 23-year-old man from the institutional cohort diagnosed with grade 2 *IDHm-A* demonstrating 48.0% T2-FLAIR mismatch volume (true-positive result). C, Patient C is a 35-year-old woman from the TCIA cohort diagnosed with grade 2 *IDHm-O* demonstrating heterogeneous T2-weighted and T2-weighted FLAIR hyperintensity and no T2-FLAIR mismatch on the subtraction map (true-negative result). D, Patient D is a 59-year-old woman from the institutional cohort diagnosed with grade 4 *IDHwt* glioblastoma. The relative hypointense central T2-weighted FLAIR signal with a peripheral hyperintense rim may mimic a T2FM sign at first glance, but the corresponding absence of T2FM on the subtraction map from the heterogeneous T2-weighted hyperintensity clearly shows the lack of T2FM (true-negative result). Corresponding tumor segmentation VOIs of T2FM (pink) and T2FNM (green) subregions (A–D) as well as the T2FNM subregion external borders encoded with thickness (A/C) are shown. INST indicates institutional.

#### Reader Study: T2FM Sign Using T2-FLAIR Subtraction Maps

Two radiologists with 7 years (F.S., reader 1) and 11 years (S.O., reader 2) of neuroimaging experience who were blinded to the molecular diagnosis performed a reader study. For this analysis, the 2 cohorts were pooled. The readers were first given only the

coregistered T2-weighted and T2-weighted FLAIR MR images and asked to assess the presence of the T2FM sign as first described by Patel et al<sup>6</sup> (“presence or absence of complete/near-complete hyperintense signal on T2WI, and relatively hypointense signal on FLAIR except for a hyperintense peripheral rim”) and to estimate the percentage T2FM volume, similar to the proposed semiquantitative definition of  $\geq 25\%$  T2FM volume of Lasocki et al<sup>8</sup> as sufficient for the T2FM sign. The readers were then provided the T2-FLAIR subtraction maps in the same session and asked to repeat their assessments before assessing the next patient. T2-FLAIR subtraction maps were visualized using a standardized color bar with values ranging from  $-3$  to  $+3$ , in which red-to-yellow shades represented mismatched voxels with positive values, teal-to-blue shades represented non-mismatched voxels with negative values, and gray represented voxels with values close to zero (Fig 1).

#### Statistical Analysis

Statistical analysis was performed using GraphPad Prism Software (Version 8.4; GraphPad Software). Receiver operating characteristic (ROC) curves were first generated on the TCIA cohort to assess the performance of the empiric percentage T2FM volume thresholds for classifying *IDHm-A* versus *IDHm-O*/*IDHwt* gliomas. ROC curves were also computed in the institutional cohort, and the same percentage T2FM volume thresholds were applied to validate their diagnostic performance. For group comparisons, data sets were tested for normality using the Shapiro-Wilk test to determine whether to apply nonparametric/parametric statistical methods. Contingency tables for *IDHm-A* distribution based on cohort, tumor grade, and percentage T2FM volume were assessed using Fisher exact tests. Tumor characterization analyses comparing T2FM and T2FNM subregions were conducted only in *IDHm-A* that demonstrated both subregions at an empiric threshold of  $\geq 15\%$  T2FM volume. Differences in percentage T2FM volume and tumor volume were assessed using either *t* tests or Mann-Whitney tests. Correlations in T2FNM subregion thickness and percentage T2FM volume were assessed using either Pearson or Spearman

monstrated both subregions at an empiric threshold of  $\geq 15\%$  T2FM volume. Differences in percentage T2FM volume and tumor volume were assessed using either *t* tests or Mann-Whitney tests. Correlations in T2FNM subregion thickness and percentage T2FM volume were assessed using either Pearson or Spearman

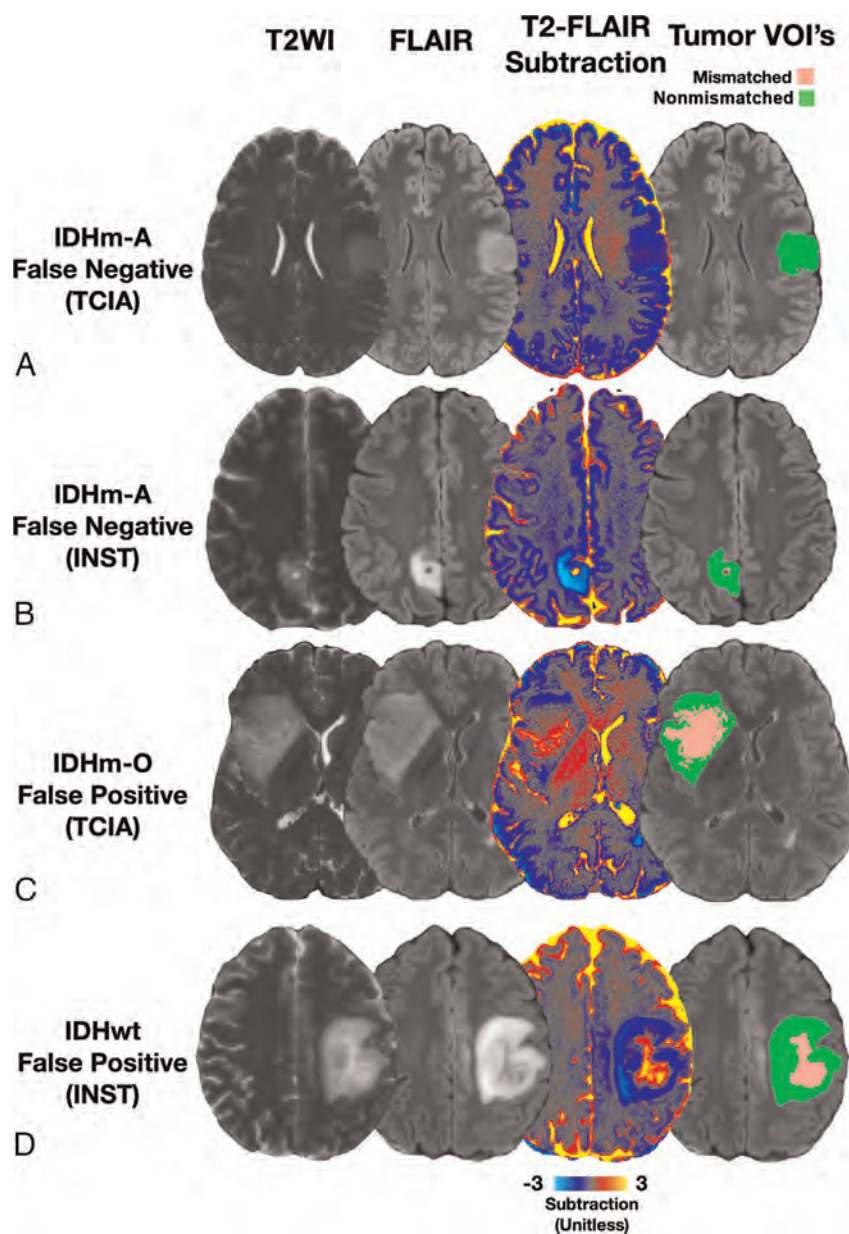


**FIG 2.** Representative false-negative and false-positive cases with T2-FLAIR subtraction maps and tumor segmentations. *A*, Patient A is a 38-year-old man from the TCIA cohort diagnosed with grade 2 *IDHm-A* with no T2-FLAIR mismatch on the subtraction map (false-negative result). *B*, Patient B is a 36-year-old woman from the institutional cohort diagnosed with grade 2 *IDHm-A* with no T2-FLAIR mismatch on the subtraction map excluding the cystic portion (false-negative result). *C*, Patient C is a 45-year-old man from the TCIA cohort diagnosed with grade 2 *IDHm-O* demonstrating 35.0% T2FM volume, which was assessed as a false-positive for the T2FM sign by 1 reader using subtraction maps (false-positive result). *D*, Patient D is a 35-year-old woman diagnosed with *IDHwt* glioblastoma demonstrating 12.5% T2FM volume, which was assessed as a false-positive for the T2-FLAIR mismatch sign by both readers using subtraction maps. Corresponding tumor-segmentation VOIs of T2FM (pink) and T2FNM (green) subregions are shown (*A–D*) (false-positive result).

correlations, and the relationships of T2FNM subregion thickness based on percentage T2FM volume categorizations were assessed using the Kruskal-Wallis test with post hoc Dunn Test for multiple comparisons. For the reader study, interreader agreement Cohen  $\kappa$  scores were calculated, and the Wald test was performed to assess overall changes in reader sensitivity and specificity for

*IDHm-A*. Significance was set to  $P < .05$ . All bar graphs with error bars display the mean and SD.

## RESULTS

### Representative Cases

Eight representative cases across both cohorts are shown in Figs 1 and 2. Figure 1 displays typical true-positive and true-negative cases in the reader study. Patients 2A and 2B were diagnosed with *IDHm-A*, and T2-FLAIR subtraction maps clearly visualize T2FM subregions within these tumors and demonstrate 59.6% and 48.0% T2FM volume, respectively (Fig 1A–B, true-positive results). Patients 2C and 2D were diagnosed with *IDHm-O* and *IDHwt* glioblastomas, respectively, which demonstrate heterogeneous T2-weighted FLAIR hyperintensity, but T2-FLAIR subtraction maps demonstrated no corresponding T2FM subregions (Fig 1C, -D, true-negative results). Figure 2 demonstrates typical false-negative and atypical false-positive cases. Patients 3A and 3B were diagnosed with *IDHm-A*, but T2-FLAIR subtraction maps do not show T2FM subregions (Fig 2A, -B, false-negative results). Patients 3C and 3D were diagnosed with *IDHm-O* and *IDHwt* glioblastomas, respectively. These patients were interpreted as having the T2-FLAIR mismatch sign when using T2-FLAIR subtraction maps by at least one of the readers and demonstrated 35.0% and 12.5% T2FM volume, respectively (Fig 2C, -D, false-positive results).

### Diagnostic Performance of Quantitative Percentage T2FM Volume

In the TCIA cohort, percentage T2FM volume was significantly higher in *IDHm-A* (mean, 18.0%; 95% CI, 11.4%–24.6%) compared with *IDHm-O/IDHwt* gliomas (mean, 5.38%; 95% CI, 0.94%–9.81%;  $P = .03$ ; Fig 3A). ROC curves using percentage T2FM volume to classify *IDHm-A* versus

*IDHm-O/IDHwt* gliomas demonstrated an area under curve (AUC) of 0.657 ( $P = .03$ ) (Fig 3B). A threshold of  $\geq 42\%$  T2FM volume was sufficient to achieve 100% specificity while also having 19.6% sensitivity; a threshold of  $\geq 25\%$  T2FM volume showed 92.0% specificity and 32.6% sensitivity; and a threshold of  $\geq 15\%$  T2FM volume showed 88.0% specificity

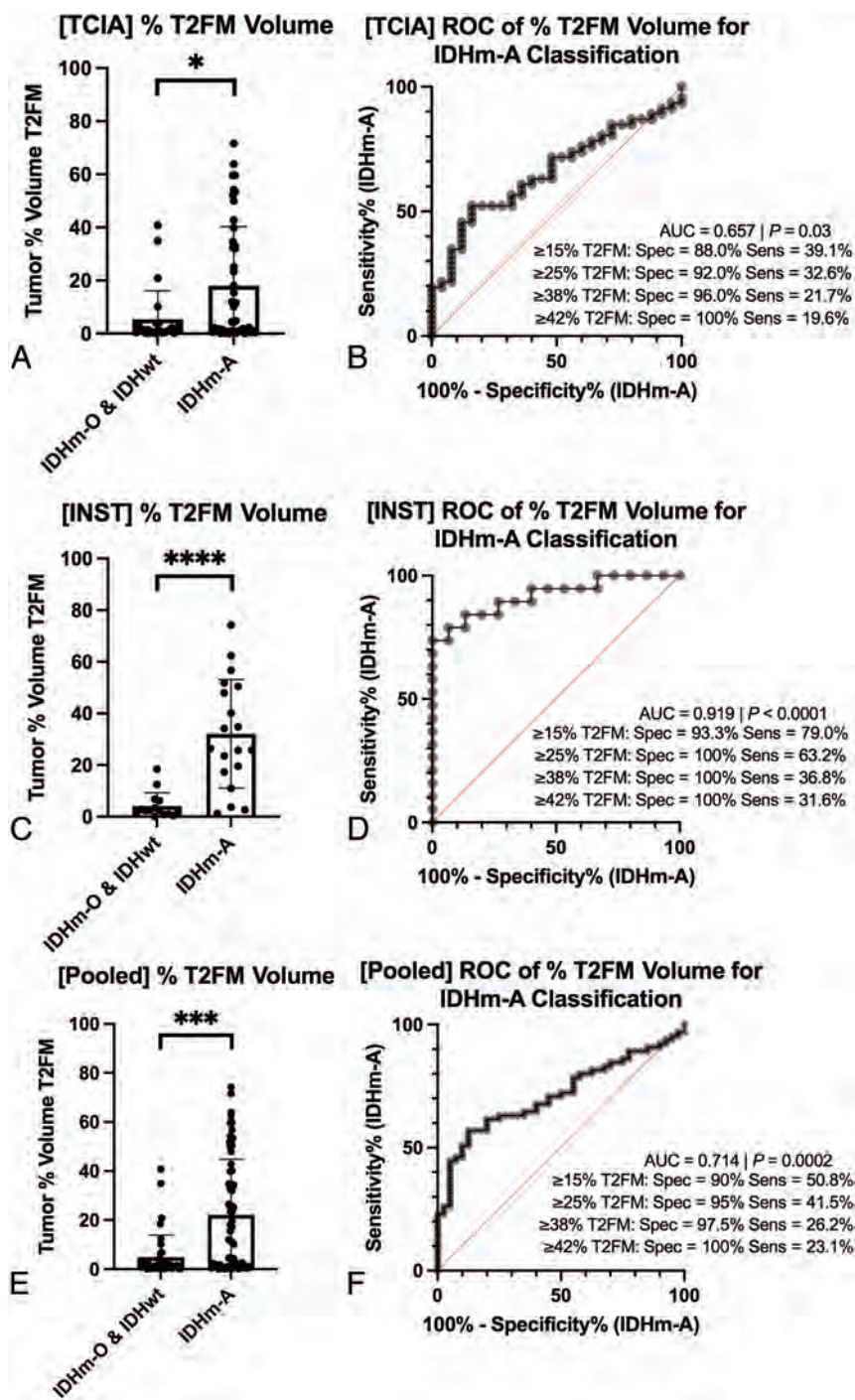


**FIG 3.** Tumor percentage of T2FM volume and diagnostic performance for *IDHm-A* classification. Results are shown for both the TCIA cohort (A and B) and the institutional cohort (C and D). *IDHm-A* had a higher percentage T2FM volume (% T2FM volume) compared with the other molecular signatures (A and C). ROC curves show that a specificity of 100% for the *IDHm-A* diagnosis could be achieved with a threshold of  $\geq 42\%$  T2FM volume in both cohorts (B and D), though in the validation cohort, a threshold of  $\geq 25\%$  T2FM volume sufficed (D). The summary results when pooling the 2 cohorts are also shown (E and F). INST indicates institutional; Spec, specificity; Sens, sensitivity; \*,  $P < .05$ ; \*\*\*,  $P < .001$ ; \*\*\*\*,  $P < .0001$ .

and 39.1% sensitivity for *IDHm-A* (Fig 3B). An optimal threshold maximizing the likelihood ratio at 5.44 was  $\geq 38\%$  T2FM volume, which showed 96.0% specificity and 21.7% sensitivity.

Similar results were shown in the institutional validation cohort. The percentage T2FM volume was significantly higher in *IDHm-A* (mean, 32.1%; 95% CI, 21.9%–42.2%) versus *IDHm-O/IDHwt* gliomas (mean, 4.14%; 95% CI, 1.32%–6.97%;  $P < .0001$ ; Fig 3C). ROC curve analyses showed an AUC = 0.919 ( $P < .0001$ , Fig 3D), and using the same thresholds as in the TCIA cohort, a threshold of  $\geq 42\%$  T2FM volume showed 100% specificity and 31.6% sensitivity; a threshold of  $\geq 25\%$  T2FM volume showed 100% specificity and 63.2% sensitivity; and a threshold of  $\geq 15\%$  T2FM volume showed 93.3% specificity and 79.0% sensitivity for *IDHm-A*. The TCIA optimal threshold of  $\geq 38\%$  T2FM volume showed 100% specificity and 36.8% sensitivity. There was a significantly higher proportion of *IDHm-A* with  $\geq 25\%$  T2FM volume in the institutional cohort compared with the TCIA cohort ( $P = .03$ ; Online Supplemental Data).

The diagnostic results when pooling both cohorts showed a significantly higher percentage T2FM volume in *IDHm-A* (mean, 22.1%; 95% CI, 16.5%–27.8%) compared with *IDHm-O/IDHwt* gliomas (mean, 4.91%; 95% CI, 2.04%–7.79%;  $P = .0002$ ; Fig 3E), and the ROC curve AUC was 0.714 ( $P = .0002$  [percentage T2FM volume threshold: specificity/sensitivity]  $\geq 42\%$  T2FM volume: 100%/23.1%;  $\geq 38\%$  T2FM volume: 97.5%/26.2%;  $\geq 25\%$  T2FM volume: 95%/41.5%;  $\geq 15\%$  T2FM volume: 90%/50.8%; Fig 3F).

When assessing the potential impact of slight image misregistration on the percentage T2FM volume, the mean magnitude difference in percentage T2FM volume across both cohorts was 1.04%; 95% CI, 0.88%–1.20% (Online Supplemental Data). By considering empiric thresholds of 1.0% and 5.0% T2FM volume as potential “noise floors” when using T2-FLAIR subtraction maps, the sensitivity values for *IDHm-A* at a threshold of  $\geq 1.0\%$  T2FM volume were 73.9%, 100%, and 81.5% for the TCIA,

institutional, and pooled cohorts, respectively, and for  $\geq 5.0\%$  T2FM volume, they were 45.7%, 84.2%, and 56.9% for the TCIA, institutional, and pooled cohorts, respectively (Online Supplemental Data).

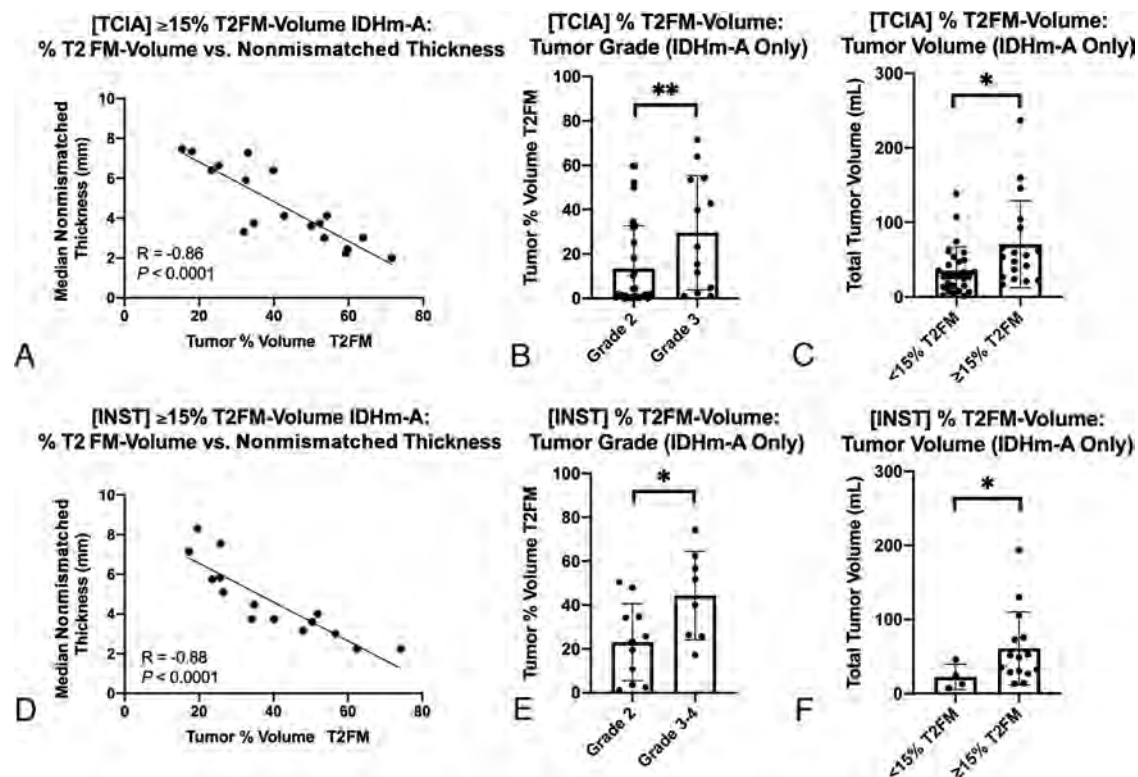


**FIG 4.** T2FNM thickness, tumor grade, and tumor volume relationships based on tumor percentage T2FM volume. In both cohorts, tumor percentage T2FM volume (% T2FM volume) was significantly negatively correlated with T2FNM subregion thickness (A and C,  $P < .0001$ ). Grade 3–4 *IDHm-A* had significantly higher percentage T2FM volume compared to grade 2 *IDHm-A* (B, TCIA,  $P = .008$ ; E, institutional,  $P = .03$ ), and tumor volumes were significantly greater in  $\geq 15\%$  T2FM volume *IDHm-A* compared with  $< 15\%$  T2FM volume *IDHm-A* (C, TCIA,  $P = .01$ ; F, institutional,  $P = .04$ ). INST indicates institutional; \*,  $P < .05$ , \*\*,  $P < .01$ .

#### Relationships among Tumor Subregions, Volumes, and Histopathologic Grade

In both cohorts, there was a significant negative correlation between T2FNM subregion thickness and percentage T2FM volume (TCIA:  $R = -0.86$ ,  $P < .0001$ ; institutional:  $R = -0.88$ ,  $P < .0001$ ; Fig 4A, -D). When categorizing *IDHm-A* as 15%–25% T2FM volume, 25%–42% T2FM volume, and  $\geq 42\%$  T2FM volume, there was an overall significant difference in T2FNM subregion thickness within each cohort with similar results (TCIA:  $P = .001$ ; 15%–25% T2FM volume: mean, 7.08 mm; 95% CI, 5.62–8.54 mm; 25%–42% T2FM volume: mean, 5.55 mm; 95% CI, 3.84–7.26 mm;  $\geq 42\%$  T2FM volume: mean, 3.14 mm; 95% CI, 2.53–3.76 mm; institutional:  $P = .001$ ; 15%–25% T2FM volume: mean, 7.06 mm; 95% CI, 3.88–10.3 mm; 25%–42% T2FM volume: mean, 5.07 mm; 95% CI, 3.54–6.60 mm;  $\geq 42\%$  T2FM volume: mean, 3.04 mm; 95% CI, 2.29–3.79 mm) (Online Supplemental Data).

The percentage T2FM volume was significantly lower in grade 2 *IDHm-A* compared to grade 3–4 *IDHm-A* in both cohorts (TCIA:  $P = .008$ ; 13.4% T2FM [95% CI, 6.56%–20.3%] versus 29.6% T2FM [95% CI, 14.1%–45.2%]; institutional:  $P = .03$ ; 23.2% T2FM [95% CI, 11.4%–34.9%] versus 44.4% T2FM [95% CI, 27.5%–61.2%]; Fig 4B, -E). There were no significant differences in the frequencies of grade 2 versus grade 3–4 *IDHm-A* between the TCIA and institutional cohorts or within each cohort based on a threshold of  $\geq 25\%$  T2FM volume ( $P < .05$ ; Online Supplemental Data). There were also no

significant relationships between percentage T2FM volume with patient age or sex in either cohort ( $P > .05$ ; Online Supplemental Data).

Tumor volumes were also significantly higher in *IDHm-A* with  $\geq 15\%$  T2FM volume compared with *IDHm-A* with  $< 15\%$  T2FM volume in both cohorts (TCIA:  $P = .01$ ; 35.5 mL [95% CI, 23.3–47.7 mL] versus 70.7 mL [95% CI, 41.7–99.7 mL]; institutional:  $P = .04$ ; 22.5 mL [95% CI, -4.85–49.8 mL] versus 60.8 mL [95% CI, 33.4–88.2 mL]; Fig 4C, -F).

#### Reader Study Results

The pooled sensitivity and specificity from the 2 cohorts using quantitative percentage T2FM volume and by visual assessment are summarized in the Online Supplemental Data. The reader study results across all patients are summarized in Tables 2 and 3. When assessing the T2FM sign using the definitions by Patel et al<sup>6</sup> and Lasocki et al<sup>8</sup> without subtraction maps, there were significant differences in the sensitivity and specificity for reader 1 ( $P = .001$ ) and a trend toward significance for reader 2 ( $P = .052$ ). Using the definitions of Patel et al<sup>6</sup> and Lasocki et al<sup>8</sup> without subtraction maps, reader 1 interpreted 24 (1 false-positive) and 37 cases (4 false-positives) of the T2FM sign, respectively, and reader 2 interpreted 23 (4 false-positives) and 30 (3 false-positives) cases of the T2FM sign, respectively. Specificity was unchanged for reader 2 (92.5%) between definitions, while it was slightly decreased for reader 1 using the definition of Lasocki et al<sup>8</sup> (90.0%) compared with that of Patel et al<sup>6</sup> (97.5%). The

**Table 2: Reader study results of T2FM sign: Sensitivity and specificity**

Classification Definition/Reader	With Subtraction Map	Sensitivity (95% CI)	Specificity (95% CI)
Patel et al <sup>6</sup>	No	35.4 (23.9–48.2)	97.5 (86.8–99.9)
	Yes	36.9 (25.3–49.8)	92.5 (79.6–98.4)
	No	30.8 (19.9–43.5)	92.5 (79.6–98.4)
	Yes	38.5 (26.7–51.4)	92.5 (79.6–98.4)
Lasocki et al <sup>8</sup>	No	50.8 (38.1–63.4)	90.0 (76.3–97.2)
	Yes	55.4 (42.5–67.7)	85.0 (70.2–94.3)
	No	41.5 (29.4–54.4)	92.5 (79.6–98.4)
	Yes	49.2 (36.6–61.9)	92.5 (79.6–98.4)

**Table 3: Reader study results of T2FM sign: Interreader agreement**

Classification Definition/with Subtraction Map	Cohen $\kappa$ (95% CI)
Patel et al <sup>6</sup>	
No	0.70 (0.53–0.87)
Yes	0.78 (0.64–0.92)
Lasocki et al <sup>8</sup>	
No	0.76 (0.63–0.89)
Yes	0.78 (0.65–0.90)

Lasocki et al<sup>8</sup> definition had slightly improved sensitivity (50.8% reader 1 and 41.5% reader 2) compared with that of Patel et al<sup>6</sup> (35.4% reader 1 and 30.8% reader 2).

For both readers, there were no significant changes in sensitivity and specificity after the inclusion of T2-FLAIR subtraction maps ( $P > .05$ ). Specificity was unchanged for reader 2, and there was a slight decrease in specificity for reader 1 with T2-FLAIR subtraction maps with the definition of Patel et al<sup>6</sup> (97.5% versus 92.5%; unchanged at 92.5%) and the definition of Lasocki et al<sup>8</sup> (90.0% versus 85.0%; unchanged at 92.5%). There was slightly improved sensitivity using either the definition of Patel et al<sup>6</sup> (reader 1: 35.4%, without the subtraction map, versus 36.9%, with the subtraction map; reader 2: 30.8% versus 38.5%) or the definition of Lasocki et al<sup>8</sup> (reader 1: 50.8% versus 55.4%; reader 2: 41.5% versus 49.2%).

Interreader agreement for the T2FM sign was substantial<sup>32</sup> for both definitions and with/without subtraction maps (Cohen  $\kappa$ : 0.70–0.78; Table 2). There were also slight, nonsignificant ( $P > .05$ ) improvements in interreader agreement using T2-FLAIR subtraction maps with the definition of either the Patel et al<sup>6</sup> (Cohen  $\kappa$ : 0.70 versus 0.78) or Lasocki et al<sup>8</sup> (0.76 versus 0.78).

## DISCUSSION

The primary objective of the present study was to add to the current literature by quantifying T2FM and T2FNM subregion volumes in nonenhancing gliomas using T2-FLAIR subtraction maps, with the main aim of diagnosing *IDHm-A* with near-100% specificity. The collective findings demonstrate that percentage T2FM volume thresholds may serve as a quantitative threshold for classifying *IDHm-A* with 100% specificity as demonstrated in 2 independent cohorts. The percentage T2FM volume is influenced by tumor volume and grade in *IDHm-A*, and T2-FLAIR subtraction maps may be more useful as an objective tool for

quantitative tumor imaging analysis than for visual assessment of the T2FM sign by experienced radiologists. The present study adds to the current literature by providing a method for the automated quantification of percentage T2FM volume and performing subregion segmentations in *IDHm-A* using T2-FLAIR subtraction maps. The present study also expands on a previous study assessing the relative signal intensity of T2FM in a hot-spot region within the T2FM core<sup>17</sup> by creating a

subtraction map for whole-tumor visualization and assessment.

Quantitative T2-FLAIR subtraction maps may serve as a useful, complementary tool for studying the T2FM sign in *IDHm-A*. The finding that  $\geq 42\%$  T2FM volume can classify *IDHm-A* with 100% specificity suggests that percentage T2FM volume calculated from quantitative subtraction maps may help radiologists avoid false-positives as shown in Fig 2 and serve as a potential imaging biomarker of *IDHm-A* in combination with the radiographic T2FM sign.<sup>6–13</sup> In the present study, we purposely did not describe the subtraction map-defined T2FM and T2FNM subregions synonymously as the “core” and “rim” subregions in *IDHm-A*, respectively, as in previous radiographic studies on the T2FM sign.<sup>6</sup> While T2-FLAIR subtraction maps allow determining the presence of T2FM subregions, the present use of T2-FLAIR subtraction maps may be limited in determining the presence of the corresponding hyperintense T2-weighted FLAIR rim specifically distinct from more broadly-defined T2FNM subregions that are also present in gliomas not exhibiting the T2FM sign.

The present findings of a threshold of  $\geq 42\%$  T2FM volume demonstrating 100% specificity for *IDHm-A* and lower thresholds of  $\geq 15\%$  and  $\geq 25\%$  T2FM volume demonstrating 88.0%–100% specificity may also be perceived as similar to those of other studies proposing a less conservative definition of the T2FM sign<sup>8,14,15</sup> and as demonstrated in our representative false-positive cases, particularly when considering that T2FM subtraction maps do not explicitly account for the hyperintense T2-weighted FLAIR rim. Nevertheless, percentage T2FM volume was also found to be inversely related to T2FNM subregion thickness in *IDHm-A*, possibly demonstrating that T2FNM subregions are potentially synonymous with a T2-weighted FLAIR hyperintense rim as the T2FM sign *IDHm-A* grows.

As for sensitivity, the present study demonstrates that high sensitivity cannot be achieved by lowering the percentage T2FM volume threshold, findings in line with those of previous studies reporting a low sensitivity of the T2FM sign.<sup>6–8</sup> Indeed, even when we dramatically lowered to a  $\geq 5.0\%$  T2FM volume threshold, which can be considered close to a noise floor, the sensitivity was 45.7%–84.2% in the 2 cohorts. We believe the low sensitivity may be related to the biology of *IDHm-A*, which can seemingly lack any extent of mismatch in a non-negligible percentage of cases. For example, the differing AUC performance may be explained by the higher proportion of nonmismatched *IDHm-A*

in the TCIA cohort compared with the institutional validation cohort, though both cohorts demonstrated 100% specificity for *IDHm-A* using a high percentage T2FM volume threshold.

These findings potentially demonstrate a limitation of percentage T2FM volume as a continuous measure for AUC-based classification compared with a categorical measure for 100% specificity-based classification through a percentage T2FM volume threshold (ie,  $\geq 42\%$  T2FM volume) at the cost of sensitivity. Additionally, even though there was no significant difference in the tumor grade distribution of *IDHm-A* with or without a  $\geq 25\%$  T2FM volume threshold, which is in line with the literature showing no *IDHm-A* tumor grade differences based on T2FM-sign,<sup>7,9,12</sup> the percentage T2FM volume was significantly higher in grade 3–4 *IDHm-A* compared with grade 2 and in tumors with larger volumes compared with smaller volumes in both cohorts. We speculate that percentage T2FM volume development may be associated with tumor growth; however, a longitudinal assessment is warranted to verify this claim.

The present study demonstrates that T2-FLAIR subtraction maps may be useful to obtain partitioned segmentations of T2FM/T2FNM subregions in *IDHm-A* for quantitative studies of the T2FM sign in gliomas. Previous studies have shown that mismatched areas show either microcystic changes or enlarged intercellular spaces on histology.<sup>6,18</sup> Future studies could use T2-FLAIR subtraction maps to objectively partition subregion segmentations to assess intratumoral heterogeneity because there have been studies using quantitative MR imaging to assess the tumor microenvironment of *IDHm-A* with the T2FM sign,<sup>17,33</sup> and use of the radiographic sign is now expanding and even being explored in pediatric populations.<sup>34</sup> In addition, the generation of T2-FLAIR subtraction maps uses readily available, open-source software and involves relatively routine preprocessing steps that are conducted for many quantitative imaging studies, including NIfTI conversion, image coregistration, skull-stripping, normalization, and voxelwise arithmetic (ie, subtraction), which could be performed by nonclinicians. Although off-line processing was required for this first demonstration study, it is conceivable that use of these maps could eventually be extended beyond research settings and expanded for clinical practice because the processing steps are not computationally demanding.

In the reader study portion of the present study, the interreader agreements without (0.70–0.76) and with subtraction maps (0.78) were in line with values previously reported in the literature.<sup>6,7</sup> Additionally, the specificity of the definition of Patel et al<sup>6</sup> applied by the readers (specificity ranging from 92.5% to 97.5%) was similar to that of the  $\geq 25\%$  T2FM volume threshold (95%). The specificity for the definition of Lasocki et al<sup>8</sup> (specificity ranging from 85% to 92.5%) was similar to that of the  $\geq 15\%$  T2FM volume threshold (90%). The sensitivity values were also comparable between the definition of Patel et al<sup>6</sup> and the  $\geq 25\%$  T2FM volume threshold (30.8%–38.5% versus 41.5%) and between the definition of Lasocki et al<sup>8</sup> and the  $\geq 15\%$  T2FM volume threshold (50.8% versus 41.5–55.4%, respectively).

Interestingly, there were no significant differences in sensitivity, specificity, or interreader agreement of T2FM sign when adding T2-FLAIR subtraction maps for either the Patel et al<sup>6</sup> or Lasocki et al<sup>8</sup> definitions, though there was a significant difference

when comparing the definitions of Patel et al<sup>6</sup> and Lasocki et al<sup>8</sup> for 1 reader and a significant trend in the other reader. There are possible reasons to explain these results. First, these findings may further support that the radiographic definitions of the T2FM sign are very robust in definition and that additional tools such as T2-FLAIR subtraction maps may not provide additional diagnostic benefit for estimating the percentage T2FM volume for T2FM sign positivity, especially for experienced radiologists. Second, the reader study design involved using a standardized T2-FLAIR subtraction map windowing and color scale with gray voxels depicting voxels around zero (either positive or negative), so the reader's interpretation of the gray voxels may have impacted their assessments. In the future, reader studies involving radiologists with less experience and a more binarized color bar without an intermediate color zone may be useful to better understand the potential diagnostic utility of T2-FLAIR subtraction maps. Although subtraction maps did not show a striking benefit as a tool for qualitative evaluations, their potential quantitative use to compute percentage T2FM volume and T2FM/T2FNM subregions is considered a valuable complementary tool that does not have interreader variability. The interreader agreement for the T2FM sign in both ours and previous studies was substantial, but not perfect, and, speculatively, may also be worse in less experienced readers, further supporting this notion.

There are several limitations to this study. First, the sample size was limited, so further studies assessing the potential usefulness of T2-FLAIR subtraction maps in other, expanded cohorts are warranted. Second, given that the T2FM sign is known to be impacted by pulse sequence parameters,<sup>11</sup> it is conceivable that there may be institutional- or patient-specific thresholds to better distinguish T2FM from T2FNM subregions compared with the positive- and negative-value thresholds, respectively, used in the current study. For example, lower FLAIR TIs have been shown to increase the visibility of the T2FM sign,<sup>11</sup> which may analogously lead to a larger percentage T2FM volume, and other sequence parameter variations may have similar effects. However, we believe that the use of straightforward positive- and negative-value thresholds with intensity-normalized anatomic images to minimize the impact of sequence parameter differences and additional NAWM normalization to further minimize patient-specific differences is valid as a first demonstration of the potential utility of T2-FLAIR subtraction maps for consistent analyses across and within our multi-institutional cohorts.

Nevertheless, a more thorough investigation of the impact of acquisition parameters on the T2FM sign, T2-FLAIR subtraction maps, and the percentage T2FM volume calculation may be warranted. A potential approach to overcome the inherent low sensitivity of T2FM could be represented by a combination of T2-FLAIR subtraction maps with advanced imaging such as diffusion,<sup>17,33</sup> perfusion,<sup>17,33</sup> and chemical exchange saturation transfer MR imaging<sup>35</sup> as did some prior studies on the visual T2FM-sign. Lastly, while the reader study results did not show marked improvement in T2FM sign assessment using T2-FLAIR subtraction maps in experienced radiologists, future reader studies assessing the potential usefulness of T2-FLAIR subtraction maps, including perhaps for radiology trainees, may be warranted.

## CONCLUSIONS

T2-FLAIR subtraction maps may be a useful tool to quantitatively assess the T2FM sign in nonenhancing gliomas and to obtain objective segmentations of T2FM and T2FNM subregions based on specific thresholds. Whole-tumor quantification of percentage T2FM volume may complement the T2FM sign for classifying IDHm-A with 100% specificity. Conversely, there appeared to be no significant benefit in using T2-FLAIR subtraction maps for visual assessment of the T2FM sign by experienced radiologists.

Disclosure forms provided by the authors are available with the full text and PDF of this article at [www.ajnr.org](http://www.ajnr.org).

## REFERENCES

- Louis DN, Perry A, Wesseling P, et al. The 2021 WHO Classification of Tumors of the Central Nervous System: a summary. *Neuro Oncol* 2021;23:1231–51 CrossRef Medline
- Yan H, Parsons DW, Jin G, et al. IDH1 and IDH2 mutations in gliomas. *N Engl J Med* 2009;360:765–73 CrossRef Medline
- Miller JJ, Gonzalez Castro LN, McBrayer S, et al. Isocitrate dehydrogenase (IDH) mutant gliomas: a Society for Neuro-Oncology (SNO) consensus review on diagnosis, management, and future directions. *Neuro Oncol* 2023;25:4–25 CrossRef Medline
- Mellinghoff IK, Lu M, Wen PY, et al. Vorasidenib and ivosidenib in IDH1-mutant low-grade glioma: a randomized, perioperative Phase 1 trial. *Nat Med* 2023;29:615–22 CrossRef Medline
- Mellinghoff IK, van den Bent MJ, Blumenthal DT, et al. INDIGO Trial Investigators. Vorasidenib in IDH1- or IDH2-mutant low-grade glioma. *N Engl J Med* 2023;389:589–601 CrossRef Medline
- Patel SH, Poisson LM, Brat DJ, et al. T2-FLAIR mismatch, an imaging biomarker for IDH and 1p/19q status in lower-grade gliomas: a TCGA/TCIA project. *Clin Cancer Res* 2017;23:6078–85 CrossRef Medline
- Broen MP, Smits M, Wijnenga MM, et al. The T2-FLAIR mismatch sign as an imaging marker for non-enhancing IDH-mutant, 1p/19q-intact lower-grade glioma: a validation study. *Neuro Oncol* 2018;20:1393–99 CrossRef Medline
- Lasocki A, Buckland ME, Drummond KJ, et al. Conventional MRI features can predict the molecular subtype of adult grade 2–3 intracranial diffuse gliomas. *Neuroradiology* 2022;64:2295–305 CrossRef Medline
- Corell A, Ferreyra Vega S, Hoefling N, et al. The clinical significance of the T2-FLAIR mismatch sign in grade II and III gliomas: a population-based study. *BMC Cancer* 2020;20:450 CrossRef Medline
- Juratli TA, Tummala SS, Riedl A, et al. Radiographic assessment of contrast enhancement and T2/FLAIR mismatch sign in lower grade gliomas: correlation with molecular groups. *J Neurooncol* 2019;141:327–35 CrossRef Medline
- Kinoshita M, Arita H, Takahashi M, et al. Impact of inversion time for FLAIR acquisition on the T2-FLAIR mismatch detectability for IDH-mutant, non-CODEL astrocytomas. *Front Oncol* 2020;10:596448 CrossRef Medline
- Deguchi S, Oishi T, Mitsuya K, et al. Clinicopathological analysis of T2-FLAIR mismatch sign in lower-grade gliomas. *Sci Rep* 2020;10:10113 CrossRef Medline
- Jain R, Johnson DR, Patel SH, et al. “Real world” use of a highly reliable imaging sign: “T2-FLAIR mismatch” for identification of IDH mutant astrocytomas. *Neuro Oncol* 2020;22:936–43 CrossRef Medline
- Li M, Ren X, Chen X, et al. Combining hyperintense FLAIR rim and radiological features in identifying IDH mutant 1p/19q non-codeleted lower-grade glioma. *Eur Radiol* 2022;32:3869–79 CrossRef Medline
- Lee MD, Patel SH, Mohan S, et al. ReSPOND Consortium. Association of partial T2-FLAIR mismatch sign and isocitrate dehydrogenase mutation in WHO grade 4 gliomas: results from the ReSPOND consortium. *Neuroradiology* 2023;65:1343–52 CrossRef Medline
- Mohammed S, Ravikumar V, Warner E, et al. Quantifying T2-FLAIR mismatch using geographically weighted regression and predicting molecular status in lower-grade gliomas. *AJNR Am J Neuroradiol* 2022;43:33–39 CrossRef Medline
- Lee MK, Park JE, Jo Y, et al. Advanced imaging parameters improve the prediction of diffuse lower-grade gliomas subtype, IDH mutant with no 1p19q codeletion: added value to the T2/FLAIR mismatch sign. *Eur Radiol* 2020;30:844–54 CrossRef Medline
- Yamashita S, Takeshima H, Kadota Y, et al. T2-fluid-attenuated inversion recovery mismatch sign in lower grade gliomas: correlation with pathological and molecular findings. *Brain Tumor Pathol* 2022;39:88–98 CrossRef Medline
- Ellingson BM, Kim HJ, Woodworth DC, et al. Recurrent glioblastoma treated with bevacizumab: contrast-enhanced T1-weighted subtraction maps improve tumor delineation and aid prediction of survival in a multicenter clinical trial. *Radiology* 2014;271:200–10 CrossRef Medline
- Calabrese E, Villanueva-Meyer JE, Rudie JD, et al. The University of California San Francisco Preoperative Diffuse Glioma MRI Dataset. *Radiol Artif Intell* 2022;4:e220058 CrossRef Medline
- Calabrese E, Villanueva-Meyer JE, Rudie JD, et al. The University of California San Francisco Preoperative Diffuse Glioma MRI Dataset. *Radiology Artif Intell* 2022;4:e220058 CrossRef Medline
- Clark K, Vendt B, Smith K, et al. The Cancer Imaging Archive (TCIA): maintaining and operating a public information repository. *J Digit Imaging* 2013;26:1045–57 CrossRef Medline
- Cho NS, Hagiwara A, Sanvito F, et al. A multi-reader comparison of normal-appearing white matter normalization techniques for perfusion and diffusion MRI in brain tumors. *Neuroradiology* 2023;65:559–68 CrossRef Medline
- Kline CN, Joseph NM, Grenert JP, et al. Targeted next-generation sequencing of pediatric neuro-oncology patients improves diagnosis, identifies pathogenic germline mutations, and directs targeted therapy. *Neuro Oncol* 2017;19:699–709 CrossRef Medline
- Lai A, Kharbanda S, Pope WB, et al. Evidence for sequenced molecular evolution of IDH1 mutant glioblastoma from a distinct cell of origin. *J Clin Oncol* 2011;29:4482–90 CrossRef Medline
- Fischl B. FreeSurfer. *Neuroimage* 2012;62:774–81 CrossRef Medline
- Smith SM, Jenkinson M, Woolrich MW, et al. Advances in functional and structural MR image analysis and implementation as FSL. *Neuroimage* 2004;23(Suppl 1):S208–19 CrossRef Medline
- Isensee F, Schell M, Pfueger I, et al. Automated brain extraction of multisequence MRI using artificial neural networks. *Hum Brain Mapp* 2019;40:4952–64 CrossRef Medline
- Hagiwara A, Oughourlian TC, Cho NS, et al. Diffusion MRI is an early biomarker of overall survival benefit in IDH wild-type recurrent glioblastoma treated with immune checkpoint inhibitors. *Neuro Oncol* 2022;24:1020–28 CrossRef Medline
- Cox RW. AFNI: software for analysis and visualization of functional magnetic resonance neuroimages. *Comput Biomed Res* 1996;29:162–73 CrossRef Medline
- Ellingson BM, Harris RJ, Woodworth DC, et al. Baseline pretreatment contrast enhancing tumor volume including central necrosis is a prognostic factor in recurrent glioblastoma: evidence from single and multicenter trials. *Neuro Oncol* 2017;19:89–98 CrossRef Medline
- Viera AJ, Garrett JM. Understanding interobserver agreement: the kappa statistic. *Fam Med* 2005;37:360–63 Medline
- Foltyn M, Nieto Taborda KN, Neuberger U, et al. T2/FLAIR-mismatch sign for noninvasive detection of IDH-mutant 1p/19q non-codeleted gliomas: validity and pathophysiology. *Neurooncol Adv* 2020;2:vdaa004 CrossRef Medline
- Wagner MW, Nobre L, Namdar K, et al. T2-FLAIR mismatch sign in pediatric low-grade glioma. *AJNR Am J Neuroradiol* 2023;44:841–45 CrossRef Medline
- Mancini L, Casagrande S, Gautier G, et al. CEST MRI provides amide/amine surrogate biomarkers for treatment-naïve glioma sub-typing. *Eur J Nucl Med Mol Imaging* 2022;49:2377–91 CrossRef Medline

# Comparison of HASTE versus EPI-Based DWI for Retinoblastoma and Correlation with Prognostic Histopathologic Parameters

Manish Sharma, Amit Gupta, Manisha Jana, Seema Kashyap, Sameer Bakhshi, and Sanjay Sharma



## ABSTRACT

**BACKGROUND AND PURPOSE:** Non-EPI-based DWI has shown better performance in head and neck pathologies owing to lesser susceptibility artifacts compared with EPI-DWI. However, only sporadic studies have investigated the feasibility of non-EPI-based DWI in retinoblastoma (RB). We qualitatively and quantitatively compared EPI-DWI and HASTE-DWI in RB and correlated the tumor ADC values obtained from these 2 techniques with histopathologic markers.

**MATERIALS AND METHODS:** Twenty-one treatment-naïve patients with RB underwent 1.5T orbital MR imaging. EPI-DWI and HASTE-DWI were acquired at 3 b-values (0, 500, and 1000 s/mm<sup>2</sup>). All patients subsequently underwent surgical enucleation. For qualitative image assessment, scoring of overall image quality, artifacts, tumor sharpness, and tumor conspicuity was done by using a 5-point Likert scale. Quantitative assessment included calculations of SNR, contrast-to-noise ratio (CNR), geometric distortion, and ADC. Qualitative scores were compared by using the Wilcoxon signed-rank test, and quantitative parameters were analyzed with a t test.

**RESULTS:** All 21 patients had unilateral RB; 15 were male and 6 were female with a median age of 36 months (range, 9–72 months). On histopathology, patients had either poorly differentiated ( $n=13/21$ ) or moderately differentiated ( $n=8/21$ ) RB. Other poor prognostic markers evaluated were optic nerve invasion ( $n=10/21$ ), choroidal invasion ( $n=12/21$ ), and anterior eye segment enhancement on MRI ( $n=6/21$ ). HASTE-DWI demonstrated higher image quality scores than EPI-DWI ( $P<.01$ ), except for tumor conspicuity score, which was higher for EPI-DWI ( $P<.001$ ). HASTE-DWI showed lower SNR, CNR, and geometric distortion than EPI-DWI ( $P<.001$ ). The average acquisition times of EPI-DWI and HASTE-DWI were ~1 and 14 minutes, respectively. The mean tumor ADC value on EPI-DWI was  $0.62 \pm 0.14 \times 10^{-3}$  mm<sup>2</sup>/s and on HASTE-DWI was  $0.83 \pm 0.17 \times 10^{-3}$  mm<sup>2</sup>/s. A significant correlation between EPI-DWI and HASTE-DWI ADC values ( $r=0.8$ ;  $P=.01$ ) was found. Lower ADC values were found in tumors with poor prognostic markers, but none reached a statistically significant difference.

**CONCLUSIONS:** HASTE-DWI shows improved overall image quality; however, it lacks in terms of tumor conspicuity, SNR, CNR, and longer acquisition time compared with EPI-DWI. ADC values derived from HASTE-DWI show no advantage over EPI-DWI in correlation with histopathologic prognostic markers.

**ABBREVIATIONS:** CNR = contrast-to-noise ratio; EPI-DWI = EPI-based DWI; RB = retinoblastoma

DWI is an fMRI technique based on Brownian motion of water molecules within the tissues. ADC value derived from DWI is an objective measure of free diffusion in the tissue.<sup>1</sup> There is abundant literature available on the utility of DWI for detection and characterization of various neoplasms, including malignant and benign orbital masses.<sup>1–5</sup> In retinoblastoma (RB), a fair correlation of tumor ADC values has been shown with poor prognostic markers, such as poorly differentiated tumor on histopathology,

tumor bilaterality, optic nerve invasion, and choroidal invasion.<sup>6–8</sup> However, the studies report a wide range of ADC values ( $0.38 \times 10^{-3}$  to  $0.74 \times 10^{-3}$  mm<sup>2</sup>/s) associated with these markers with no consistent definite cutoff values.<sup>6,7</sup> Nonetheless, tumor ADC values could have implications for medical and surgical management of RB.

The most commonly used EPI-based DWI (EPI-DWI) sequences allow short scan times but have marked susceptibility

Received September 8, 2023; accepted after revision October 29.

From the Departments of Radiodiagnosis and Interventional Radiology (M.S., A.G., M.J., S.S.), and Pathology (S.K.), All India Institute of Medical Sciences, New Delhi, India; and Department of Medical Oncology (S.B.), Institute of Rotary Cancer Hospital, All India Institute of Medical Sciences, New Delhi, India.

M. Sharma and A. Gupta contributed equally to this work as co-first authors.

Please address correspondence to Prof. Sanjay Sharma, Room 53, Dr. R. P. Centre for Ophthalmic Sciences, Department of Radiodiagnosis, All India Institute of Medical Sciences, New Delhi, Ansari Nagar 110029, India; e-mail: drssharmall@gmail.com



Indicates article with online supplemental data.

<http://dx.doi.org/10.3174/ajnr.A8084>

artifacts, especially at bone–air interfaces. Substantial anatomic distortion on orbital EPI-DWI is well known.<sup>9</sup> The use of non-EPI-based DWI for head and neck pathologies is well documented, especially for diagnosis of recurrent postoperative cholesteatomas, where it has been shown to outperform the traditional EPI-DWI in terms of image quality as well as diagnostic sensitivity and specificity.<sup>10,11</sup> HASTE-DWI is one such non-EPI technique, which has been in use for many years and is currently considered the reference standard MR imaging sequence for detection of cholesteatomas.<sup>12,13</sup> Similarly in cases of RB, we hypothesize that HASTE-DWI could potentially facilitate better coregistration with conventional MR images with better visual tumor delineation and perhaps provide a more robust ADC value correlation as an imaging prognostic marker. However, the use of non-EPI-based DWI for detection and characterization of RB has been reported only in few preliminary studies with limited sample sizes.<sup>14,15</sup>

To the best of our knowledge, there is no study available in the literature comparing both EPI-DWI and HASTE-DWI in the same patients with RB cohort. Also, there are no data regarding the correlation of prognostic markers in RB with ADC values derived from HASTE-DWI. The purpose of our study was to qualitatively and quantitatively compare the images acquired from EPI-DWI and HASTE-DWI in eyes with RB and correlate the derived ADC values with histopathologic prognostic markers.

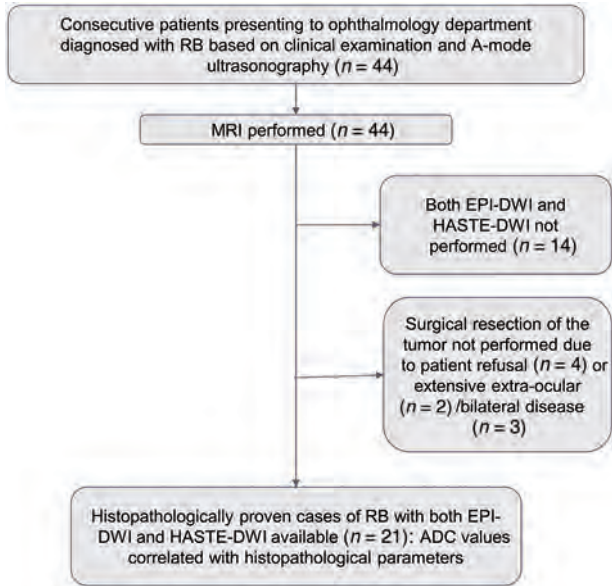


**FIG 1.** Flow chart showing patient inclusion and exclusion in the study.

**MATERIALS AND METHODS**

This prospective observational study was conducted after obtaining Institutional Ethics Committee approval. After taking informed parental consent, a total of 44 consecutive children with RB referred for MR imaging from our tertiary care ophthalmology center were recruited. The diagnosis of RB was based on clinical examination and A-mode ultrasonography. Patients who did not undergo surgical enucleation ( $n = 9$ ) because of either extensive bilateral/extra-ocular disease or guardian’s refusal were excluded. Also, the patients in whom both EPI-DWI and HASTE-DWI could not be performed ( $n = 14$ ) were excluded from the study. Thus, a total of 21 treatment-naïve patients with RB formed the final study group (Fig 1). There was no minimum tumor size criterion for inclusion into the study analysis.

Orbital MR imaging was performed under general anesthesia by using a 1.5T system (Avanto; Siemens) with a standard quadrature head coil (FOV 20 cm). Conventional sequences included thin-section spin-echo fat-suppressed T2-weighted orbital images in axial, coronal, and oblique sagittal planes, fat-suppressed T1-weighted orbital images in the axial plane followed by postcontrast orbital fat-suppressed T1-weighted images in all 3 planes, and postcontrast brain imaging after intravenous administration of gadopentetate dimeglumine (Magnevist). DWI ( $n = 21$ ) of the orbits was acquired in the axial plane with b-values of 0, 500, and 1000 mm<sup>2</sup>/s by using both EPI-DWI and HASTE-DWI (Online Supplemental Data). ADC maps were generated automatically for EPI-DWI and manually for HASTE-DWI.

Qualitative image assessment was performed by a radiologist (S.S., with 20 years’ experience in orbital imaging) on the  $b = 1000$  s/mm<sup>2</sup> images. The overall image quality, artifacts, tumor sharpness, and tumor conspicuity were scored by using a 5-point Likert scale as shown in Table 1. For quantitative image quality assessment, a single radiologist (A.G., with 8 years’ experience in body imaging) placed ROIs on the tumor and temporalis muscle in the same axial section to measure the signal values on  $b = 0$  s/mm<sup>2</sup> images on both EPI-DWI and HASTE-DWI and subsequently transferred the same ROIs to corresponding  $b = 500$  and 1000 s/mm<sup>2</sup> images (Online Supplemental Data). SNR was defined as signal of tumor divided by the SD. Contrast-to-noise ratio (CNR) was defined as the absolute signal difference of tumor and muscle divided by the SD of muscle signal. For quantification of geometric distortion (measured by a single radiologist A.G., with 8 years’ experience in body imaging), the maximum transverse and anteroposterior diameters of the eye globe on axial T2-weighted images were taken as the standard of reference. The distortion was assessed by measuring the deviations in the orbital diameters on both EPI-DWI and HASTE-DWI on the same axial section as T2-weighted image.

**Table 1: Qualitative image assessment based on the 5-point Likert scale**

Score	Overall Image Quality	Artifacts	Tumor Sharpness	Tumor Conspicuity
1	Nondiagnostic	Nondiagnostic	Nondiagnostic	Mass unidentifiable
2	Substantial deficiency in image quality	Marked impact on diagnosis	Not sharp	No differentiation between mass and vitreous
3	Moderate image quality	Moderate impact on diagnosis	Little sharp	Subtle mass lesion
4	Good image quality	Minimal impact on diagnosis	Moderately sharp	Well-seen mass lesion
5	Excellent image quality	No artifact	Good sharpness	Very well-seen mass lesion

**Table 2: Patient characteristics (n = 21)**

Characteristic	Value
Median age at enucleation	36 months (range, 9–72 months)
Sex	Male: 15 (71.4%) Female: 6 (29.6%)
Tumor laterality	Unilateral: 21 (100%) Bilateral: 0 Right eye: 13 (61.9%) Left eye: 8 (38.1%)
Median tumor size	15.3 mm (range, 10.2–36 mm)
Mean follow-up period	265.4 days (range, 155–410 days)

Quantitative analysis of the ADC map was performed by a single radiologist (M.S., with 10 years' experience in pediatric body imaging). Three circular ROIs of 0.12 cm<sup>2</sup> size were placed manually over the mass on the ADC map with simultaneous referencing of the T2-weighted and postcontrast images. Tumor ADC values were calculated as a mean of these 3 ROIs. The ROIs were drawn corresponding to the enhancing portion of the mass. Areas showing high signal on T2-weighted images with scarce or no contrast enhancement were considered as necrotic areas and were avoided during ROI placement. Similarly, dark foci suspicious of calcifications were not included in the ROI.

The postcontrast MR images were assessed for anterior eye segment enhancement by a single radiologist (M.S., with 20 years' experience in orbital imaging). Anterior eye segment enhancement was considered positive if there was an abnormal high signal on postcontrast MR imaging just anterior to the lens in the axial section showing maximum cross-section of the lens (ie, in the location of iris).

All patients underwent surgical enucleation, either upfront or preceded by neoadjuvant chemotherapy, within 20–30 days (mean duration of 27.1 days) after MR imaging. Various histopathologic parameters were evaluated. Tumor grade was classified as well (>50% rosettes), moderately (<50% rosettes), or poorly (no rosettes) differentiated. Optic nerve invasion was categorized as absent, prelaminar (optic nerve head), and postlaminar. Choroidal invasion was also noted. Invasion of iris, ciliary body, anterior chamber, and sclera was also assessed.

Qualitative scores were compared by using the Wilcoxon signed-rank test, and quantitative image quality parameters (SNR, CNR, and geometric distortion) were compared with a paired *t* test after testing for normality. Pearson correlation coefficient was used to correlate tumor ADC values on both DWI techniques. Correlation of tumor ADC values with various histopathologic parameters was statistically analyzed by using an independent *t* test. All statistical analysis was done by using statistical software SPSS (version 20.0; SPSS). *P* value <.05 at the CI of 95% was considered significant.

## RESULTS

A total of 21 patients (15 males and 6 females) were included in this study, with a median age of 36 months (range 9–72 months) at the time of enucleation. All patients had unilateral tumor (13 right eye and 8 left eye). The median tumor size was 15.3 mm (range 10.2–36 mm). On histopathology, the patients had either poorly differentiated (*n* = 13/21, 61.9%) or moderately differentiated (*n* = 8/21, 38.1%) tumor. Other poor prognostic markers

evaluated were optic nerve invasion (*n* = 10/21, 47.6%), choroidal invasion (*n* = 12/21, 57.1%), and anterior eye segment enhancement on postcontrast MR imaging (*n* = 6/21, 28.6%). None of the patients had invasion of the iris, ciliary body, anterior chamber, or sclera on histopathology. The mean duration of clinical follow-up after surgery was 265.4 days (range, 155–410 days). All patients survived during the duration of clinical follow-up, and none developed recurrence. Various demographic and clinical patient characteristics are summarized in Table 2.

### Qualitative Image Assessment

HASTE-DWI demonstrated higher image quality scores than EPI-DWI on the overall image quality, artifacts, and tumor sharpness. The average scores for HASTE-DWI versus EPI-DWI were as follows: overall image quality 4.19 versus 3.33, artifacts 4.38 versus 3.67, and tumor sharpness 4.14 versus 3.24 (*P* < .001), respectively. However, the tumor itself was more conspicuous and easily visualized on EPI-DWI compared with HASTE-DWI with an average score of 4.33 versus 3.52 for tumor conspicuity (*P* < .001) (Fig 2). The average acquisition times of EPI-DWI compared with HASTE-DWI were ~1 and 14 minutes, respectively.

### Quantitative Image Quality Assessment

In the anteroposterior direction, which is the frequency encoding axis in the scan, the average geometric distortion of orbital diameter on EPI-DWI was 6.105 ± 1.82 mm and on HASTE-DWI was 0.643 ± 0.43 mm (*P* < .001). However, there was no significant difference in distortion of transverse (phase-encoding direction) orbital diameter on EPI-DWI and HASTE-DWI with means of 0.610 ± 0.301 and 0.648 ± 0.339 mm, respectively (*P* = .568). The average SNR of EPI-DWI was 10.616 ± 1.844, 10.268 ± 1.843, and 9.578 ± 1.48 compared with that of 8.283 ± 1.691, 7.875 ± 1.124, and 7.461 ± 1.1 on HASTE-DWI on *b* = 0, 500, and 1000 s/mm<sup>2</sup> (*P* < .001, *P* < .001, and *P* < .001), respectively. The average CNR of EPI-DWI was 10.529 ± 1.553, 10.12 ± 1.254, and 9.4 ± 1.789 compared with that of 8.3 ± 1.527, 7.553 ± 1.33, and 7.295 ± 1.368 on HASTE-DWI on *b* = 0, 500, and 1000 s/mm<sup>2</sup> (*P* < .001, *P* < .001, and *P* < .001), respectively.

The various qualitative and quantitative image quality parameters are summarized in Table 3.

### EPI-DWI ADC versus HASTE-DWI ADC Value of the Tumor

The mean tumor ADC value on EPI-DWI was 0.62 ± 0.14 × 10<sup>-3</sup> mm<sup>2</sup>/s (range, 0.41–1.04 × 10<sup>-3</sup> mm<sup>2</sup>/s) and on HASTE-DWI was 0.83 ± 0.17 × 10<sup>-3</sup> mm<sup>2</sup>/s (range, 0.59–1.17 × 10<sup>-3</sup> mm<sup>2</sup>/s). Pearson correlation coefficient was used to correlate tumor ADC values on both DWI techniques. We found a significant correlation of EPI-DWI ADC values with HASTE-DWI ADC values (*r* = 0.8; *P* = .01); however, a linear correlation could not be established. HASTE-DWI ADC values were consistently higher than corresponding EPI-DWI ADC values (Online Supplemental Data).

### Correlation of Tumor ADC Values with Prognostic Parameters

The mean and SD of tumor ADC values on both DWI techniques in relation to histopathologic characteristics are shown in Table 4. Lower ADC values were found in tumors with poor

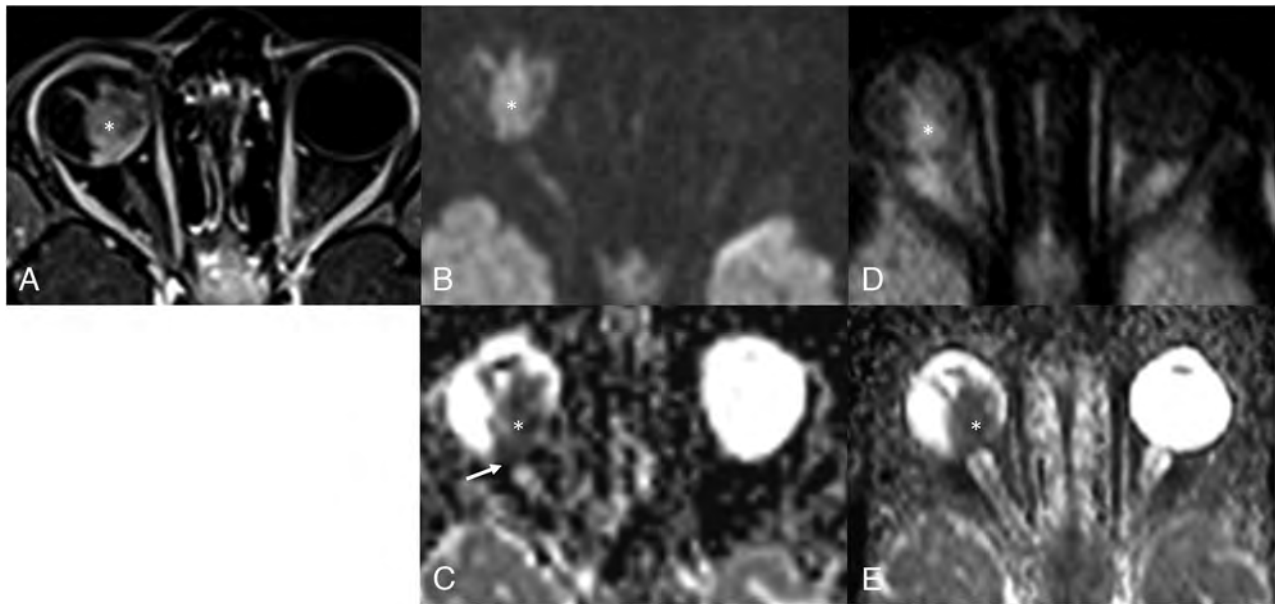


**FIG 2.** Comparison of EPI-DWI and HASTE-DWI quality. Axial postcontrast T1-weighted image (A) shows heterogeneously enhancing mass (asterisk) in the posterior segment of the right eye globe. EPI (B) and HASTE (D) axial DWI (b-value, 1000 s/mm<sup>2</sup>) at the same level show high signal intensity in the mass (asterisk) with corresponding hypointensity on ADC maps (C and E, respectively, for EPI-DWI and HASTE-DWI), suggestive of diffusion restriction. There is mild elongation (arrow in C) of eye globe in EPI ADC map in contrast to maintained shape of globe in HASTE ADC map. However, there is a decreased SNR in case of HASTE-DWI and its ADC map.

**Table 3: EPI-DWI versus HASTE-DWI quality assessment**

Parameter	EPI-DWI	HASTE-DWI	P Value
Qualitative parameters (n = 21): 5-point Likert scale			
Overall image quality	3.33	4.19	<.001
Artifacts	3.67	4.38	<.001
Tumor sharpness	3.24	4.14	<.001
Tumor conspicuity	3.52	4.33	<.001
Quantitative parameters (n = 21)			
Geometric distortion			
Transverse ocular diameter deviation (mean ± SD)	0.610 ± 0.301 mm	0.648 ± 0.339 mm	.568
Anteroposterior ocular diameter deviation (mean ± SD)	6.105 ± 1.82 mm	0.643 ± 0.43 mm	<.001
SNR			
b = 0	10.616 ± 1.844	8.283 ± 1.691	<.001
b = 500	10.268 ± 1.843	7.875 ± 1.124	<.001
b = 1000	9.578 ± 1.48	7.461 ± 1.1	<.001
CNR			
b = 0	10.529 ± 1.553	8.3 ± 1.527	<.001
b = 500	10.12 ± 1.254	7.553 ± 1.33	<.001
b = 1000	9.4 ± 1.789	7.295 ± 1.368	<.001

prognostic markers, such as poorly differentiated tumor (Fig 3; Online Supplemental Data), postlaminar optic nerve invasion (Fig 4; Online Supplemental Data), presence of choroid invasion (Fig 5; Online Supplemental Data), and large tumor size. The mean tumor ADC values in the presence of these markers ranged from  $0.52$  to  $0.59 \times 10^{-3}$  mm<sup>2</sup>/s on EPI-DWI and  $0.69$  to  $0.81 \times 10^{-3}$  mm<sup>2</sup>/s on HASTE-DWI compared with  $0.65$  to  $0.68 \times 10^{-3}$  mm<sup>2</sup>/s and  $0.81$  to  $0.89 \times 10^{-3}$  mm<sup>2</sup>/s in their absence, respectively; however, none reached a statistically significant difference. A higher mean tumor ADC value  $0.7 \times 10^{-3}$  mm<sup>2</sup>/s on EPI-DWI and  $0.91 \times 10^{-3}$  mm<sup>2</sup>/s on HASTE-DWI was seen in the presence of anterior eye segment enhancement (Online Supplemental Data) compared with that in its absence

( $0.58 \times 10^{-3}$  mm<sup>2</sup>/s and  $0.8 \times 10^{-3}$  mm<sup>2</sup>/s, respectively); however, the difference was not statistically significant.

## DISCUSSION

MR imaging plays a crucial role in diagnosis, staging, and therapeutic planning of patients with RB in the current practice.<sup>16,17</sup> Presence of restricted diffusion on DWI can help in ocular tumor characterization, especially in cases of indeterminate solid masses.<sup>5</sup> Most of the published literature regarding utility of DWI in patients with RB is based on EPI-DWI technique with studies showing encouraging results for potential utility of ADC values as a noninvasive imaging prognostic biomarker.<sup>6-8</sup> However, EPI-based technique has anatomic distortion and

**Table 4: Correlation of tumor ADC values on EPI-DWI and HASTE-DWI with prognostic parameters<sup>b</sup>**

Prognostic Parameter	Mean ADC Value for EPI-DWI ( $\times 10^{-3} \text{ mm}^2/\text{s}$ )	P Value for EPI-DWI	Mean ADC Value for HASTE-DWI ( $\times 10^{-3} \text{ mm}^2/\text{s}$ )	P Value for HASTE-DWI
Tumor grade				
Poorly differentiated ( $n = 13$ )	$0.59 \pm 0.16$	.37	$0.79 \pm 0.16$	.22
Moderately differentiated ( $n = 8$ )	$0.65 \pm 0.09$		$0.89 \pm 0.18$	
Tumor size				
$<15 \text{ mm}$ ( $n = 9$ )	$0.66 \pm 0.16$	.2	$0.89 \pm 0.19$	.14
$>15 \text{ mm}$ ( $n = 12$ )	$0.58 \pm 0.11$		$0.78 \pm 0.14$	
Optic nerve invasion				
Absent ( $n = 11$ )	$0.65 \pm 0.17$	.35 <sup>b</sup>	$0.88 \pm 0.20$	.14 <sup>b</sup>
Prelaminar ( $n = 5$ )	$0.64 \pm 0.07$		$0.86 \pm 0.13$	
Postlaminar ( $n = 5$ )	$0.52 \pm 0.04$		$0.69 \pm 0.05$	
Choroid invasion				
Present ( $n = 12$ )	$0.57 \pm 0.11$	.086	$0.81 \pm 0.18$	.66
Absent ( $n = 9$ )	$0.68 \pm 0.15$		$0.85 \pm 0.16$	
Anterior eye segment enhancement on postcontrast MRI				
Present ( $n = 6$ )	$0.70 \pm 0.18$	.056	$0.91 \pm 0.23$	.15
Absent ( $n = 15$ )	$0.58 \pm 0.10$		$0.80 \pm 0.13$	

<sup>a</sup>Other histopathologic characteristics (eg, invasion of iris, ciliary body, anterior chamber, and sclera) were not found in any patient.

<sup>b</sup>P value is for ADC values in cases with postlaminar invasion versus cases with prelaminar or absent invasion.

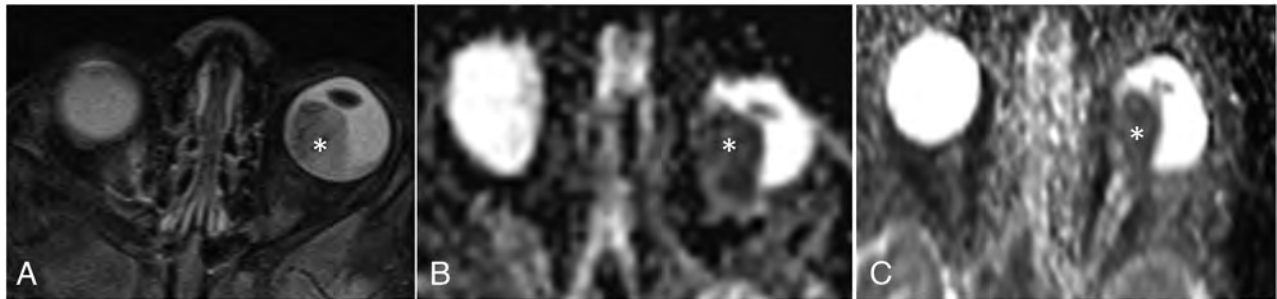


**FIG 3.** Poorly differentiated RB on histopathology. Axial T2-weighted image (A) shows a heterogeneously hypointense mass (asterisk) occupying the posterior segment of left eye globe. EPI (B) and HASTE (C) ADC maps show corresponding hypointense signal in the mass, suggestive of diffusion restriction. Mass showed low ADC values on both EPI-DWI and HASTE-DWI (mean ADC value being  $0.48 \times 10^{-3} \text{ mm}^2/\text{s}$  and  $0.70 \times 10^{-3} \text{ mm}^2/\text{s}$  for EPI-DWI and HASTE-DWI, respectively).



**FIG 4.** Histopathologically proved optic nerve invasion. Axial postcontrast T1-weighted image (A) at same level shows homogeneously enhancing mass with abnormal thickening and enhancement in the optic disc extending in postlaminar part of optic nerve (arrow), suggestive of postlaminar optic nerve invasion. EPI (B) and HASTE (C) ADC maps at the same level show corresponding hypointensity suggestive of diffusion restriction. Mass showed low ADC values on both EPI-DWI and HASTE-DWI (mean ADC value being  $0.52 \times 10^{-3} \text{ mm}^2/\text{s}$  and  $0.67 \times 10^{-3} \text{ mm}^2/\text{s}$  for EPI-DWI and HASTE-DWI, respectively).

magnetic susceptibility-induced artifacts in orbital imaging. In this study, we showed that, although HASTE-DWI, which is one of the non-EPI-based DWI techniques, had superior image quality and less geometric distortion than EPI-DWI, it lagged in terms of tumor conspicuity, SNR, and CNR; it showed no

significant benefit in tumor characterization by using ADC maps. Both techniques produced diagnostic quality DWI enabling tumor delineation. Also, because all of the tumors in our study were either medium or large-sized ( $>10 \text{ mm}$  in size), susceptibility artifacts in EPI-DWI did not appreciably affect tumor evaluation in any case.

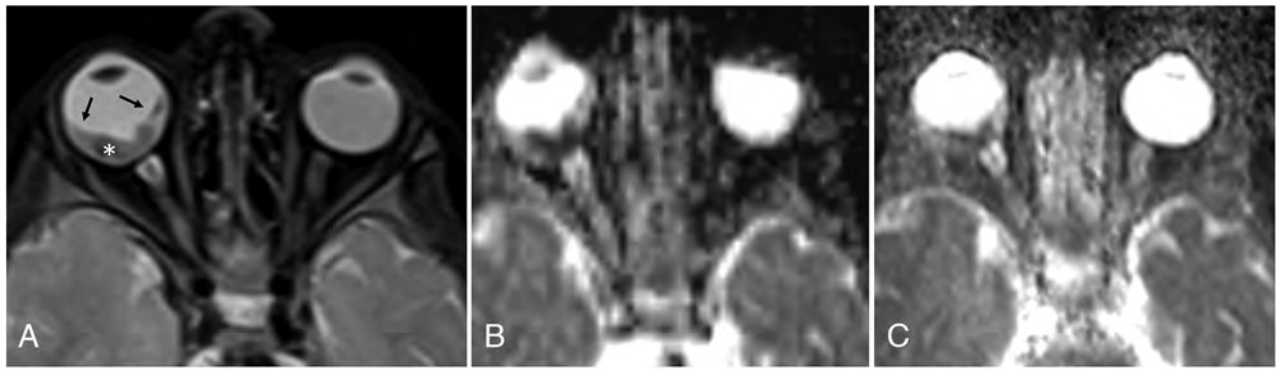


**FIG 5.** Histopathologically proved choroid invasion. Axial T2-weighted image (A) shows a hypointense small mass in the posterior segment of right eye with associated retinal detachment (arrows). EPI (B) and HASTE (C) ADC maps show corresponding hypointensity on ADC maps suggestive of diffusion restriction. Mass showed low ADC values on both EPI and HASTE-DWI (mean ADC value being  $0.51 \times 10^{-3} \text{ mm}^2/\text{s}$  and  $0.87 \times 10^{-3} \text{ mm}^2/\text{s}$  for EPI-DWI and HASTE-DWI, respectively).

This is especially relevant in our cohort where RB is usually diagnosed at a later stage with larger tumor size due to lack of a routine RB screening program at birth or in neonates and infants.<sup>18-20</sup>

Markedly longer acquisition times of the order of >10 times in HASTE-DWI MR imaging compared with EPI-DWI was a major drawback, especially as it prolongs the duration of general anesthesia, potentially risking the attendant complications in these children. Longer acquisition time of HASTE-DWI MR imaging is a consequence of its inherently low SNR, which must be compensated for by obtaining multiple signal averages.

We further correlated tumor ADC values obtained on both EPI-DWI and HASTE-DWI with histopathologic prognostic parameters. We found lower ADC values ( $0.52\text{--}0.59 \times 10^{-3} \text{ mm}^2/\text{s}$  on EPI-DWI and  $0.69\text{--}0.81 \times 10^{-3} \text{ mm}^2/\text{s}$  on HASTE-DWI) in tumors with adverse prognostic histopathologic factors; however, the difference was not statistically significant. These results are in keeping with the overall ambivalent results of the previous studies showing ADC correlation with some of the prognostic parameters and absence of any association with others (Online Supplemental Data). The lack of statistically significant ADC values in our study could be ascribed to a multitude of factors: use of 1.5T MR imaging, standard head coil rather than orbital surface coil, small sample size, relatively larger mean tumor size, and only few well or moderately differentiated tumors. Another factor limiting the clinical correlation of ADC values as an imaging biomarker for poor prognostic features of RB is its high variability ( $0.38 \times 10^{-3}$  to  $0.74 \times 10^{-3} \text{ mm}^2/\text{s}$ ) and lack of definite cutoff values.<sup>6-8</sup> In our study, we found that mean tumor ADC values were consistently higher in HASTE-DWI compared with EPI-DWI. While there was significant correlation between the ADC values obtained from both techniques, no linear correlation was found. This variability in the numerical values further complicates the use of ADC values in RB as a tool for the interpreting radiologist.

Previous studies have demonstrated a correlation of anterior segment enhancement on postcontrast MR imaging with aggressive tumor behavior including invasion of the optic nerve and choroid.<sup>21-23</sup> To our knowledge, no study has correlated tumor ADC value with anterior segment enhancement. In our study, we found that eyes showing anterior segment enhancement had higher tumor ADC values ( $0.7 \times 10^{-3} \text{ mm}^2/\text{s}$  on EPI-DWI and

$0.91 \times 10^{-3} \text{ mm}^2/\text{s}$  on HASTE-DWI), contrary to the expected low ADC values associated with aggressive tumors. However, this difference was not found to be statistically significant. Enhancement of the anterior eye segment on postcontrast MR imaging in RB is recognized to be either due to hyperemia secondary to iris neovascularization (rubeosis iridis) or secondary to infiltration by the tumor itself. Of note, no tumor showed anterior segment invasion on histopathology in our study. Thus, anterior eye segment enhancement in our cases is presumably due to tumor-induced aseptic cellulitis and consequent hyperemia. Higher ADC values in these tumors may be a result of areas of necrosis that were inadvertently included in the ROIs.

Apart from having a relatively small sample size, our study had a few other limitations. The measured mean ADC value from the entire tumor may not be truly representative of the whole tumor presumably due to tumor heterogeneity. More than one prognostic factor was present in several patients. Therefore, the low ADC values cannot be ascribed to any one particular poor prognostic parameter (confounding factors). Inadvertent inclusion of some part of necrotic tumor in the ROI placed for tumor ADC calculation may have led to falsely high ADC values. Correlation of data with long-term survival or mortality outcomes could not be done.

## CONCLUSIONS








Although HASTE-DWI is a frequently used sequence in MR imaging protocols for detection of cholesteatomas, most of the centers do not use this sequence for orbital MR imaging. Our study further reiterates the limitations and lack of any incremental benefit of including non-EPI-DWI in an orbital MR imaging protocol for children with RB. In conclusion, although HASTE-DWI shows an improved overall image quality with less orbital distortion and artifacts, it lacks in terms of tumor conspicuity, SNR, and CNR compared with EPI-DWI. ADC values derived from HASTE-DWI show no advantage over EPI-DWI in correlation with histopathologic prognostic markers in RB. A major drawback of HASTE-DWI is its markedly long acquisition time prolonging the duration of general anesthesia for MR imaging.

**Disclosure forms** provided by the authors are available with the full text and PDF of this article at [www.ajnr.org](http://www.ajnr.org).

## REFERENCES

1. Koh DM, Collins DJ. Diffusion-weighted MRI in the body: applications and challenges in oncology. *AJR Am J Roentgenol* 2007;188:1622–35 CrossRef Medline
2. Cameron CA, Tong JY, Juniat V, et al. Diagnostic utility of diffusion-weighted imaging and apparent diffusion coefficient for common orbital lesions: a review. *Ophthalmic Plast Reconstr Surg* 2022;38:515–21 CrossRef Medline
3. Politi LS, Forghani R, Godi C, et al. Ocular adnexal lymphoma: diffusion-weighted MR imaging for differential diagnosis and therapeutic monitoring. *Radiology* 2010;256:565–74 CrossRef Medline
4. Sepahdari AR, Aakalu VK, Kapur R, et al. MRI of orbital cellulitis and orbital abscess: the role of diffusion-weighted imaging. *AJR Am J Roentgenol* 2009;193:W244–50 CrossRef Medline
5. Sepahdari AR, Aakalu VK, Setabutr P, et al. Indeterminate orbital masses: restricted diffusion at MR imaging with echo-planar diffusion-weighted imaging predicts malignancy. *Radiology* 2010;256:554–64 CrossRef Medline
6. Abdel Razek AA, ElKhamary S, Al-Mesfer S, et al. Correlation of apparent diffusion coefficient at 3T with prognostic parameters of retinoblastoma. *AJNR Am J Neuroradiol* 2012;33:944–48 CrossRef Medline
7. Cui Y, Luo R, Wang R, et al. Correlation between conventional MR imaging combined with diffusion-weighted imaging and histopathologic findings in eyes primarily enucleated for advanced retinoblastoma: a retrospective study. *Eur Radiol* 2018;28:620–29 CrossRef Medline
8. Sepahdari AR, Kapur R, Aakalu VK, et al. Diffusion-weighted imaging of malignant ocular masses: initial results and directions for further study. *AJNR Am J Neuroradiol* 2012;33:314–19 CrossRef Medline
9. Le Bihan D, Poupon C, Amadon A, et al. Artifacts and pitfalls in diffusion MRI. *J Magn Reson Imaging* 2006;24:478–88 CrossRef Medline
10. Benson JC, Carlson ML, Lane JI. Non-EPI versus multishot EPI DWI in cholesteatoma detection: correlation with operative findings. *AJNR Am J Neuroradiol* 2021;42:573–77 CrossRef Medline
11. Dudau C, Draper A, Gkagkanasiou M, et al. Cholesteatoma: multi-shot echo-planar vs non echo-planar diffusion-weighted MRI for the prediction of middle ear and mastoid cholesteatoma. *BJR Open* 2019;1:20180015 CrossRef Medline
12. Schwartz KM, Lane JI, Bolster BD Jr, et al. The utility of diffusion-weighted imaging for cholesteatoma evaluation. *AJNR Am J Neuroradiol* 2011;32:430–36 CrossRef Medline
13. Amoodi H, Mofti A, Fatani NH, et al. Non-echo planar diffusion-weighted imaging in the detection of recurrent or residual cholesteatoma: a systematic review and meta-analysis of diagnostic studies. *Cureus* 2022;14:e32127 CrossRef Medline
14. de Graaf P, Pouwels PJ, Rodjan F, et al. Single-shot turbo spin-echo diffusion-weighted imaging for retinoblastoma: initial experience. *AJNR Am J Neuroradiol* 2012;33:110–18 CrossRef Medline
15. Hiwatashi A, Togao O, Yamashita K, et al. 3D turbo field echo with diffusion-sensitized driven-equilibrium preparation technique (DSDE-TFE) versus echo planar imaging in evaluation of diffusivity of retinoblastoma. *Br J Radiol* 2016;89:20160074 CrossRef Medline
16. Silvera VM, Guerin JB, Brinjikji W, et al. Retinoblastoma: what the neuroradiologist needs to know. *AJNR Am J Neuroradiol* 2021;42:618–26 CrossRef Medline
17. de Graaf P, Göricke S, Rodjan F, European Retinoblastoma Imaging Collaboration (ERIC), et al. Guidelines for imaging retinoblastoma: imaging principles and MRI standardization. *Pediatr Radiol* 2012;42:2–14 CrossRef Medline
18. Singh U, Katoch D, Kaur S, et al. Retinoblastoma: a sixteen-year review of the presentation, treatment, and outcome from a tertiary care institute in Northern India. *Ocul Oncol Pathol* 2017;4:23–32 CrossRef Medline
19. Yan J, Zhang H, Li Y. Establishment of the relationship between tumor size and range of histological involvement to evaluate the rationality of current retinoblastoma management. *PLoS One* 2013;8:e80484 CrossRef Medline
20. Vempuluru VS, Kaliki S. Screening for retinoblastoma: a systematic review of current strategies. *Asia Pac J Ophthalmol (Phila)* 2021;10:192–99 CrossRef Medline
21. de Graaf P, van der Valk P, Moll AC, et al. Contrast-enhancement of the anterior eye segment in patients with retinoblastoma: correlation between clinical, MR imaging, and histopathologic findings. *AJNR Am J Neuroradiol* 2010;31:237–45 CrossRef Medline
22. Galluzzi P, Cerase A, Hadjistilianou T, et al. Retinoblastoma: abnormal gadolinium enhancement of anterior segment of eyes at MR imaging with clinical and histopathologic correlation. *Radiology* 2003;228:683–90 CrossRef Medline
23. Deike-Hofmann K, von Lampe P, Eerikainen M, et al. Anterior chamber enhancement predicts optic nerve infiltration in retinoblastoma. *Eur Radiology* 2022;32:7354–64 CrossRef Medline

# MRI-Based Brain Volume Scoring in Cerebral Malaria Is Externally Valid and Applicable to Lower-Resolution Images

 Manu S. Goyal,  Lorena Vidal,  Karen Chetcuti,  Cowles Chilingulo, Khalid Ibrahim, Jeffrey Zhang, Dylan S. Small,  Karl B. Seydel, Nicole O'Brien,  Terrie E. Taylor, and  Douglas G. Postels

## ABSTRACT

**BACKGROUND AND PURPOSE:** Children with cerebral malaria have an elevated risk of mortality and neurologic morbidity. Both mortality and morbidity are associated with initially increased brain volume on MR imaging, as graded by the Brain Volume Score, a subjective ordinal rating scale created specifically for brain MRIs in children with cerebral malaria. For the Brain Volume Score to be more widely clinically useful, we aimed to determine its independent reproducibility and whether it can be applicable to lower-resolution MRIs.

**MATERIALS AND METHODS:** To assess the independent reproducibility of the Brain Volume Score, radiologists not associated with the initial study were trained to score MRIs from a new cohort of patients with cerebral malaria. These scores were then compared with survival and neurologic outcomes. To assess the applicability to lower-resolution MRI, we assigned Brain Volume Scores to brain MRIs degraded to simulate a very-low-field (64 mT) portable scanner and compared these with the original scores assigned to the original nondegraded MRIs.

**RESULTS:** Brain Volume Scores on the new cohort of patients with cerebral malaria were highly associated with outcomes (OR for mortality = 16,  $P < .001$ ). Scoring of the simulated degraded images remained consistent with the Brain Volume Scores assigned to the original higher-quality (0.35 T) images (intraclass coefficients  $> 0.86$ ).

**CONCLUSIONS:** Our findings demonstrate that the Brain Volume Score is externally valid in reproducibly predicting outcomes and can be reliably assigned to lower-resolution images.

**ABBREVIATIONS:** BVS = Brain Volume Score; CM = cerebral malaria

Malaria continues to be a leading cause of childhood mortality in sub-Saharan Africa.<sup>1</sup> A subset of children bitten by infectious mosquitoes develop cerebral malaria (CM), clinically defined as coma, *Plasmodium falciparum* infection, and no other obvious cause of illness. In endemic areas, CM is a driver of public health, contributing to both child mortality and poor neurodevelopmental

outcomes among survivors.<sup>2,3</sup> Although many of the steps between *P falciparum* infection and death from CM are clear, the lack of an animal model has resulted in an incomplete pathophysiologic understanding of the disease.<sup>4</sup> Standard of care treatments are IV antimalarial drugs and supportive care. Currently, there are no adjunctive therapies proved to improve outcomes.

Brain MR imaging has been used to better understand CM pathogenesis.<sup>5-10</sup> Some children with clinical CM develop increased brain volume on MRIs, identified by the presence of ventricular, sulcal, and/or cisternal effacement; blurring of the gray-white junction; and/or brain herniation. Brain volume in CM is graded using an 8-point scale, the Brain Volume Score (BVS) (Table 1).<sup>7</sup> Scores of 1 and 2 indicate atrophy, 3 is normal brain volume, and 4–8 indicate increasing severity of ventricular, sulcal, and cisternal effacement; blurring of the gray-white junction; and (with a score of 8) brain herniation. Scores of 7 and 8, termed “highly increased brain volume,” are strongly associated with increased mortality risk.<sup>7</sup> The original studies that created and validated this 8-point scale were performed using a Signa Ovation (GE Healthcare) fixed magnet. In these

Received June 28, 2023; accepted after revision November 6.

From the Mallinckrodt Institute of Radiology (M.S.G.), Washington University School of Medicine, St. Louis, Missouri; Children's Hospital of Philadelphia (L.V.), Philadelphia, Pennsylvania; Department of Radiology (K.C.) and Blantyre Malaria Project, (K.B.S., N.O., T.E.T., D.G.P.), Kamuzu University of Health Sciences, Blantyre, Malawi; Department of Radiology (K.C., C.C.), Queen Elizabeth Central Hospital, Blantyre, Malawi; Department of Statistics and Data Science (J.Z., D.S.S.), The Wharton School, University of Pennsylvania, Philadelphia, Pennsylvania; College of Osteopathic Medicine (K.B.S., T.E.T., K.I.), Michigan State University, East Lansing, Michigan; Nationwide Children's Hospital (N.O.), Center for Food Allergy and Asthma Research (K.I.), Northwestern University, Evanston, Illinois; Division of Pediatric Critical Care, Columbus, Ohio; and Division of Neurology (D.G.P.), The George Washington University, Children's National Medical Center, Washington, DC. This work was supported by National Institutes of Health grants R01 AI034969 and U01 AI126610.

Please address correspondence to Manu S. Goyal, MD, MSc, Campus Box 8131-50-5, 510 S. Kingshighway Blvd, St. Louis, MO 63110; e-mail: goyalm@wustl.edu

<http://dx.doi.org/10.3174/ajnr.A8098>

**Table 1: MRI criteria for assignment of brain volume scores**

BVS	Brief Description	Features
1	Severe atrophy	Markedly atypical for age with diffuse prominence of the cisternae, ventricles, and sulci
2	Mild atrophy	Subtle prominence of the cisternae, ventricles, and sulci for age
3	Normal	Typical for age
4	Mild increased volume	Mildly increased brain volume for age, but with normal cisternae, ventricles, and sulci
5	Mild swelling	Some localized or regional loss of cisternae, ventricles, and sulci
6	Moderate swelling	Diffuse involvement with incomplete effacement of the cisternae, ventricles, and sulci
6.5 <sup>a</sup>	Moderate-to-severe swelling	Features between 6 and 7, eg, near-complete effacement of the sulci without cisternal/ventricular effacement or significant cisternal/ventricular effacement with partial loss of the sulci
7	Severe swelling	Loss of all sulci with cisternal and ventricular effacement and decreased gray/white matter delineation
8	Severe swelling with herniation	Loss of all sulci with cisternal and ventricular effacement with herniation

<sup>a</sup> Score of 6.5 was not included in the original BVS.

studies, interrater reliability was very good-to-excellent.<sup>7,11</sup> Given these findings, the BVS is now intended to be used as a clinical tool to estimate prognosis and for enrichment of clinical trial samples (eg, selecting participants at higher risk of death).

The BVS was formulated and evaluated using a single 0.35 T MR imaging scanner.<sup>7</sup> Because fixed magnets of this strength (or stronger) are not widely available in malaria endemic regions, there is a need to test the validity of the BVS and its association with outcomes on lower-resolution MRIs. Very-low-field (64 mT) portable MR imaging scanners have recently become available and may provide an opportunity to expand the availability and usefulness of neuroimaging in resource-limited settings.<sup>12,13</sup> Portable scanners are less expensive than fixed magnets, but at a compromise of resolution and signal-to-noise.

We recently showed that BVS values assigned by different radiologists were similar to those assigned by an objective statistical model.<sup>11</sup> Combined with human interrater reliability results, this finding suggests that the BVS is internally valid. To our knowledge, external validation of the association of BVS with outcomes has not been previously assessed.

Here, to evaluate the external validity of the BVS, we aimed to determine the association between outcomes and the BVSs obtained in a new, independent cohort of children with CM. Additionally, to evaluate whether BVS assignment is valid using lower-resolution images, we compared the scores assigned to brain MRIs degraded to simulate a very-low-field MR imaging with the scores previously assigned to the original higher-resolution MRIs.

## MATERIALS AND METHODS

We performed a retrospective analysis of MRIs collected from children 3 months to 12 years of age with a clinical diagnosis of CM (Blantyre coma scale score  $\leq 2$ , peripheral parasitemia with *P. falciparum* of any density, and no other identifiable cause of coma). Enrollment in the parent studies occurred on the Pediatric Research Ward, a hospital unit specialized in the evaluation and care of children with CM, located at Queen Elizabeth Central Hospital in Blantyre, Malawi. Participants received standard of care therapies for pediatric CM, including IV artesunate (according to Malawi national guidelines) and close supportive care.

Seizures, both convulsive and nonconvulsive, were treated with IV antiseizure medications. Medical complications were

treated as they arose. At the time of hospital discharge, survivors were examined by a physician experienced in the care of children with CM for the presence of neurologic sequelae including motor, special sensory (blindness, deafness), or developmental abnormalities. If the parent thought that the child had returned to his or her prehospital baseline and the neurologic examination findings were normal, the survivor was classified as alive and normal. If findings of either the parental report or the examination were abnormal, the child was classified as alive with neurologic sequelae.

A parent or guardian accompanying the patient provided written informed consent at study enrollment. Ethics approval was obtained from the University of Malawi College of Medicine and the Michigan State University institutional review boards.

### Brain MRI Protocol

Children with CM who had baseline brain MRIs and recorded clinical outcomes suitable for testing the external validity of the BVS were included in this study. Participants underwent MR imaging as soon as possible after clinical stabilization, typically within 4 hours of hospital presentation. Images were obtained on a Signa Ovation 0.35 T MR imaging scanner. Imaging sequences in children admitted before and including 2014 have been previously described.<sup>7</sup> In 2014 and after, the brain MRI protocol included a sagittal 1.5-mm<sup>3</sup>-resolution T1 spin-echo sequence, an axial T2 spin-echo sequence, a coronal T2 spin-echo sequence, an axial T1 sequence, and an axial DWI sequence. If scanning protocols needed to be shortened due to patient factors (clinical instability or motion), the axial and coronal T2 sequences and sagittal T1 sequence were preferentially acquired. Contrast was not administered.

### BVS Education and Methodology of Radiologists

Three radiologists participated in this study, all practicing, medical school-affiliated attendings now with at least 6 years of experience (M.S.G., neuroradiology fellowship completed 2014; L.V., pediatric neuroradiology fellowship completed 2017; and K.C., pediatric radiology fellowship completed 2015). All 3 radiologists underwent initial training with one of the radiologists who developed the BVS. Training included a virtual didactic session and review of 50 MRIs including the full range of possible BVSs (the “training set”). The radiologists tested their BVS assignment abilities by next independently scoring 47 test case MRIs (the “test

set”) blinded to the original (reference standard) BVS assigned by one of the radiologists who developed the BVS.

After the 3 radiologists completed this training, 2 of them (M.S.G. and L.V.) re-assigned consensus BVSs to the same 47 test set MRIs but blinded to the original scores, approximately 2 years later. This was to confirm that their consensus scores remained closely calibrated with the reference standard BVS scores. Consensus was achieved after concurrent review of images using teleconferencing software (Zoom; Zoom Video Communications) and arriving at a single consensus score. During this process, several cases were identified in which differentiating between a BVS of 6 and 7 was challenging. Accordingly, a score of 6.5 was allowed in the consensus scores for these cases (Table 1).

### **Evaluating the Reproducibility and External Validity of the Association between BVS and Outcomes in Pediatric CM**

After completion of training, the same 2 radiologists (M.S.G. and L.V.) also independently assigned consensus BVS ratings to 94 brain MRIs obtained from a new cohort of children with CM. The radiologists were blinded to patient outcomes when assigning the BVS. To determine the potential benefit of modification of the BVS criteria by adding a score of 6.5 to the current whole-number-based system, we evaluated whether the outcomes of children whose BVS was 6.5 were more like outcomes seen in children whose MRIs were scored as 6, 7, or neither.

### **Testing the External Validity of BVS Assignment in Lower-Resolution MRIs**

To evaluate whether BVS can be validly assigned using lower-resolution MRIs, we obtained degraded versions of 37 of the training set and 47 of the test set MRIs (all from the 0.35 T MR imaging scanner and used previously for BVS assignment training) based on a proprietary algorithm from Hyperfine Research (Guilford, Connecticut). This step resulted in a set of brain images with lower resolution and greater noise, aiming to simulate scans obtainable with the 64 mT Swoop portable MRI (Hyperfine).

To first calibrate BVS assignment to the now-degraded images, 3 radiologists (M.S.G., L.V., and K.C.) reviewed the 37 degraded training set MRIs along with their corresponding non-degraded images. Once they finished this calibration step, each radiologist then independently assigned a BVS to each of the 47 degraded test set MRIs, while blinded to their corresponding nondegraded images. This step allowed us to test the reliability of the BVS assignment of the degraded MRIs by determining the concordance between the BVS assigned to the degraded test set MRIs and the original BVS assigned to their corresponding nondegraded images, which had been obtained using the 0.35 T scanner.

### **Statistical Analysis**

Statistical analyses were performed in Excel 2016 (Microsoft) and R Version 4.0.2 or higher (<https://www.r-project.org/>). The Fisher exact test was used to calculate ORs and 95% CIs. To assess the concordance of BVS assignment between the original resolution and degraded MRIs, we used the intraclass correlation coefficient function from the irr package for R (<https://cran.r-project.org/web/packages/irr/index.html>). For intraclass correlation

coefficients, lower-bound 95% CI values between 0.5 and 0.75 were considered moderate; 0.75 and 0.90, good; and >0.90, excellent estimates of reliability.<sup>14</sup>

## **RESULTS**

The mean age of the 94 children with CM whose MRIs were evaluated for external validity in this study was 49.5 months (range, 3–148 months), and 46% were male.

### **Calibration of the 2 Independent Radiologists' Consensus BVS Scoring**

Two-radiologist consensus BVS scoring of the nondegraded 47 test set brain MRIs had a good intraclass coefficient (0.925; 95% CI, 0.870–0.958) compared with reference standard scores assigned by the original radiologist who helped develop the BVS. The mean difference between the consensus scores and the original reference standard scores was very small (0.043; paired Student *t* test, *P* = .69), confirming that the independent consensus BVS scoring was well-calibrated against the reference standard scoring.

### **Reproducibility and External Validity of the Association of BVS and Outcomes in Pediatric CM**

Two-radiologist consensus BVSs for the 94 newly obtained brain MRIs ranged from 2 to 8. Six was the most frequent score. All children whose MRIs had scores of ≤4 were alive and neurologically normal at hospital discharge (*n* = 12). The 4 children whose MRIs had a score of 8 either died (*n* = 3) or were alive with neurologic sequelae (*n* = 1). Outcomes of those with BVS values of 5–7 were intermediate. In those children with a score of 5 (*n* = 20), one (5%) died and 3 of the 19 survivors (16%) were alive with neurologic sequelae. Of the 27 children whose MRIs had a BVS of 6, five (19%) died; the remainder were alive and neurologically normal. Of the 16 children with images assigned a BVS of 7, nine (56%) died, one was alive with neurologic sequelae (6%), and 6 were alive and neurologically normal. Among 15 cases given an intermediate score of 6.5, none died, one was alive with neurologic sequelae (7%), and the rest (93%) were alive and neurologically normal. The outcomes of children with a BVS of 6.5 were more similar to those in children whose BVS was 6 and less similar to children with scores of 7. Outcomes according to 3 categories (≤5, 6 or 6.5, and 7 or 8) are shown in Fig 1.

In the original outcome study, children with BVSs of 7 or 8, described as having “highly increased brain volume,” had a high mortality risk.<sup>7</sup> To evaluate the reproducibility and external validity of this finding, we compared the outcomes of children with scores of 7 or 8 (*n* = 20) with the outcomes of children with a BVS of ≤6.5 (*n* = 74). Children whose scans had a BVS of 7 or 8 had a 60% mortality risk and, if they survived, a 70% chance of a poor neurologic outcome. Conversely, those with a BVS of ≤6.5 had an 8% mortality risk and an 86% chance of survival with a good neurologic outcome. Compared with the outcomes of children with scores of ≤6.5, the odds of death in children whose BVS was 7 or 8 was 16.2 (95% CI, 4.3–69.7). These odds are similar to those reported in previous studies (Table 2). If we defined “highly increased brain volume” as a BVS of 6–8, the odds of death for children with higher scores was 11.5 (95% CI, 1.6–503.7), compared with children with a BVS of ≤5.

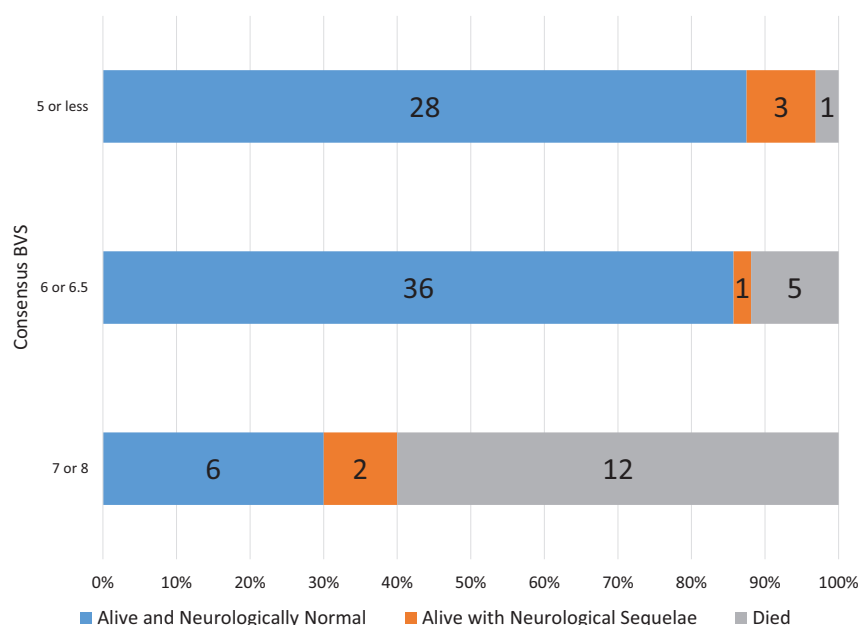


**FIG 1.** Outcomes of children by the initial consensus BVS. Proportional outcomes of consensus BVS are demonstrated when trichotomized into 3 categories,  $\leq 5$ , 6 or 6.5, and 7 or 8.

**Table 2: ORs for mortality at a BVS threshold of 7 or 6**

Fisher Test	OR	95% CI	P Value
7–8 vs $\leq 6.5$	16.17	4.3–69.7	<.001
6–8 vs $\leq 5$	11.50	1.6–503.7	.005
Seydel et al <sup>7</sup> (7–8 vs $\leq 6$ )	13.75 <sup>a</sup>	4.3–58.6 <sup>a</sup>	<.001

<sup>a</sup>The OR and CI reported in Seydel et al<sup>7</sup> used logistic regression and was 14.0 (4.5–43.4). Here we use Fisher exact test instead because of its increased accuracy for sample sizes in this study, which was then also applied to Seydel et al<sup>7</sup> to make these results comparable. Accordingly, the recalculated OR and CI are slightly different than that reported in Seydel et al<sup>7</sup>.

### Consistency of BVS Assignment on Lower-Resolution MRIs

Despite the images being of lower resolution, MRIs degraded to simulate the output of lower-field scanners showed similar characteristics compared with the original images obtained at 0.35 T (Fig 2). The CSF spaces, including the sulci, cisterns, and ventricles, could be differentiated from brain parenchyma, allowing assessment of whether they were effaced. In contrast, blurring of the gray-white junction was less visible using the degraded images compared with those that were not degraded.

For the degraded 47 test set MRIs, the intraclass coefficients for BVS scores assigned by each of the 3 radiologists compared with the original BVS scores for the nondegraded MRIs ranged from 0.867 to 0.901 (Table 3). The mean bias for all 3 was  $<0.5$ , and the mean absolute deviation was approximately 0.6. If we used the median BVS from the 3 radiologists assigned on the lower-resolution images and compared it with the BVS score assigned using higher-resolution images, this step modestly improved the intraclass coefficient to 0.928, while slightly reducing the bias (0.128) and mean absolute deviation (0.468).

## DISCUSSION

Brain MR imaging is a prognostic biomarker in pediatric CM and can be used to identify children who may most benefit from aggressive or targeted interventions. The whole-number system of BVS assignment is prognostically valid. In our study,

noninteger intermediate scoring (ie, BVS = 6.5) yielded no additional prognostic information. Using 2-radiologist consensus scoring, our study confirms the reproducibility and external validity of the association of the integer-based BVS and outcomes in CM. Moreover, assignment of BVS remains consistent when applied to degraded images with lower resolution.

A fundamental challenge in applying any scale to describe the severity of a pathologic process is in determining the appropriate resolution of that scale. With respect to the BVS, if gradations finer than the currently used ordinal integer scale are used, one radiologist could assign a score of 6.4 to a case, while a second could assign a score of 6.6. Although the assigned grades differ minimally, if one is forced to round to the nearest whole number, the original scores would more widely differ.

This difference becomes important at thresholds (eg, between BVS of 6 and 7) at which mortality risk changes. Conversely, using a more finely graded scale may not improve the reliability or accuracy. Here, we assessed the validity of a single in-between score, 6.5, and found that outcomes were more like those in children with a score of 6 than with a score of 7. On this basis, we suggest that the original 8-integer-based ordinal scale for the assignment of BVS currently remains appropriate, though future refinements should continue to be investigated.

In our study, children with CM whose MR imaging scans were scored independently as a BVS of 7 or 8 had a mortality risk of 60%. Conversely, only 1 of 32 children with a score of  $\leq 5$  died. For cases assigned a score of 6, mortality was intermediate. Our results suggest that the BVS may be more useful if trichotomized into “no significant increase in brain volume” (BVS of  $\leq 5$ ), “moderate increase in brain volume” (BVS of 6), and “highly increased brain volume” (BVS of 7 or 8). Children with the lowest range of scores have low mortality, those with a score of 6 have intermediate mortality, and scores of 7 or 8 are associated with a high mortality risk. Of note, among survivors, the relationship between morbidity and BVS scores is less clear. Thus, future studies to confirm and extend these findings are warranted.

Images acquired for this study were from a single 0.35 T MR imaging scanner with a minimally varying imaging protocol. Portable lower-field scanners are increasingly being tested and used in a variety of clinical settings, including evaluating brain volume in children<sup>15</sup> with pathogenic processes that result in brain injury and edema<sup>16</sup> and when assessing brain herniation.<sup>17</sup> To evaluate whether this more easily scalable imaging technique might work in the assignment of BVSs to children with CM, we determined score assignment concordance when images from the 0.35 T MR imaging scanner were degraded to simulate a 64 mT MR imaging scanner. Despite image degradation, BVS scoring showed good-to-excellent reliability between images obtained on

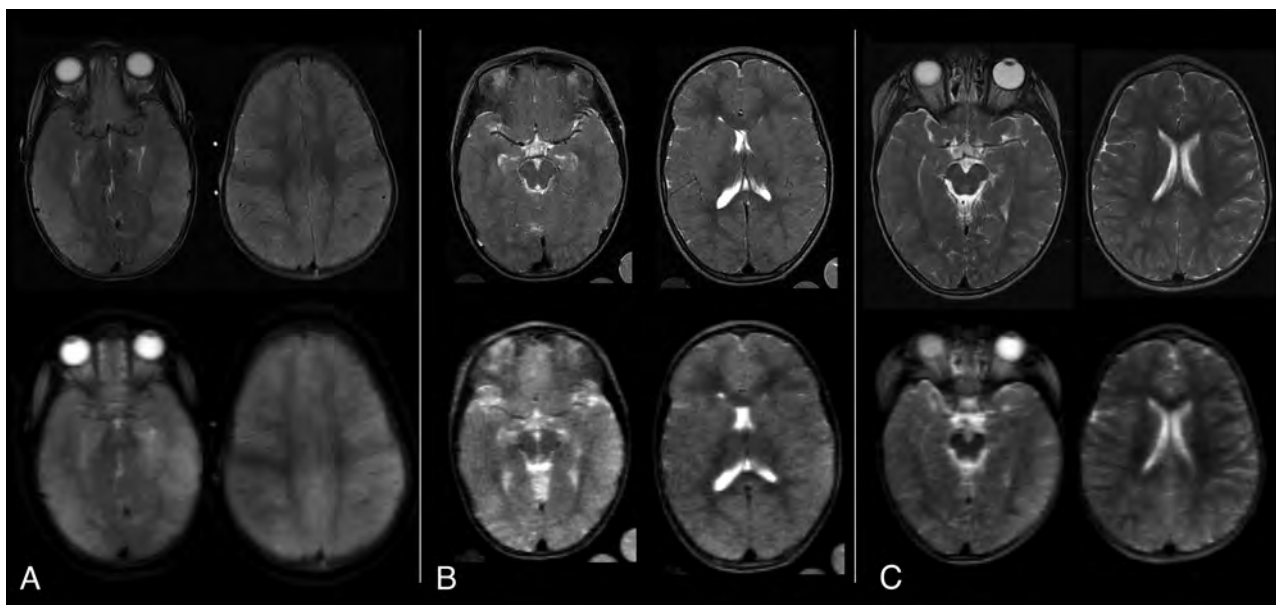


**FIG 2.** Sample T2w original and simulated MRIs from children with CM. The original brain MRIs were obtained on a Signa Ovation 0.35 T magnet (upper row) and corresponding axial images were obtained after image degradation to simulate the resolution of a very-low-field scanner (lower row). A, A BVS of 8 was assigned to the original scan as well as to the degraded images by all 3 radiologists. B, A BVS of 6 was assigned to the original scan, and 6 or 7, to the degraded images. C, A BVS of 4 was assigned to the original scan, and 5 or 3, to the degraded images.

**Table 3: BVS assigned to degraded MRIs compared with original criterion standard BVS assigned to nondegraded scans**

Test Statistic	R1	R2	R3	Median
Intraclass coefficient (95% CI)	0.901 (0.830–0.944)	0.878 (0.777–0.932)	0.867 (0.762–0.926)	0.928 (0.874–0.959)
Mean bias	+0.170	–0.340	+0.319	+0.128
Mean absolute deviation	0.553	0.596	0.617	0.468

a 0.35 T fixed magnet and those simulating output of a portable 64 mT scanner. Our findings should be considered preliminary because they used proprietary-algorithm-based simulated images rather than those obtained independently by the very-low-field scanner itself. Optimally, MRIs from a single patient using both a 0.35 T fixed magnet and a portable 64 mT magnet should be compared. Ethically, this comparison may be challenging due to the fragile clinical status of critically ill children with CM and the long scanning times required. Another method to validate BVSs derived from very-low-field scanners as prognostic biomarkers in pediatric CM would be to assess the association between BVS and outcomes using images only obtained from a portable 64 mT magnet. Nevertheless, our current findings suggest but cannot establish that the BVS is a valid prognostic biomarker across MR imaging scanners of varying field strengths.

Our study has several limitations. Most important, the study radiologists are all experienced in BVS assignment in children with CM. The generalizability of the findings of our study to radiologists who have not undergone a rigorous educational program of BVS assignment is unknown. The training and test set MRIs in this study were used repeatedly for training, calibration of BVS scores, and testing of the BVS on degraded images. Although months or years separated each of these tasks, it is possible that memory of the previously assigned BVS affected a radiologist's later BVS scoring. Our reuse of images through time was required due to the numeric rarity of MR imaging scans obtained from children with CM. The validity of the BVS as a prognostic biomarker was derived using images obtained at hospital admission.

It is possible that changes in BVS through time may be a better prognostic biomarker or provide additional insights into CM pathogenesis. We used the neurologic status at hospital discharge to indicate the presence of neurologic sequelae. The duration of posthospital follow-up for children included in this study varied across the clinical protocols in which they were enrolled. Because these posthospital follow-up times were not standardized for all participants included here, only the hospital discharge status was used in our analyses. However, because neurologic sequelae in CM survivors may appear or resolve through time, it is possible that the estimates of the strength of the association between BVS and neurologic sequelae may change if a standard posthospital neurologic status was used in the analyses.

## CONCLUSIONS

In pediatric CM, independent MRI-based assessment of the BVS reproducibly predicts outcomes and can be reliably performed with lower-resolution images.

## ACKNOWLEDGMENTS

We are grateful to all families whose children took part in this study. We would also like to thank Dr Sam Kampondeni for assisting in the initial training of the study radiologists on assigning brain volume scores.

**Disclosure forms** provided by the authors are available with the full text and PDF of this article at [www.ajnr.org](http://www.ajnr.org).

## REFERENCES

1. World Health Organization. *World Malaria Report 2022*. World Health Organization; 2022
2. Idro R, Carter JA, Fegan G, et al. **Risk factors for persisting neurological and cognitive impairments following cerebral malaria.** *Arch Dis Child* 2006;91:142–48 CrossRef Medline
3. Postels DG, Taylor TE, Molyneux M, et al. **Neurologic outcomes in retinopathy-negative cerebral malaria survivors.** *Neurology* 2012;79:1268–72 CrossRef Medline
4. Guenther G, Muller D, Moyo D, et al. **Pediatric cerebral malaria.** *Curr Trop Med Rep* 2021;8:69–80 CrossRef Medline
5. Kampondeni SD, Potchen MJ, Beare NA, et al. **MRI findings in a cohort of brain injured survivors of pediatric cerebral malaria.** *Am J Trop Med Hyg* 2013;88:542–46 CrossRef Medline
6. Potchen MJ, Kampondeni SD, Seydel KB, et al. **Acute brain MRI findings in 120 Malawian children with cerebral malaria: new insights into an ancient disease.** *AJNR Am J Neuroradiol* 2012;33:1740–46 CrossRef Medline
7. Seydel KB, Kampondeni SD, Valim C, et al. **Brain swelling and death in children with cerebral malaria.** *N Engl J Med* 2015;372:1126–37 CrossRef Medline
8. Sahu PK, Hoffmann A, Majhi M, et al. **Brain magnetic resonance imaging reveals different courses of disease in pediatric and adult cerebral malaria.** *Clin Infect Dis* 2021;73:e2387–96 CrossRef Medline
9. Looareesuwan S, Wilairatana P, Krishna S, et al. **Magnetic resonance imaging of the brain in patients with cerebral malaria.** *Clin Infect Dis* 1995;21:300–09 CrossRef Medline
10. Mohanty S, Benjamin LA, Majhi M, et al. **Magnetic resonance imaging of cerebral malaria patients reveals distinct pathogenetic processes in different parts of the brain.** *mSphere* 2017;2:e00193–17 CrossRef Medline
11. Tu D, Goyal MS, Dworkin JD, et al. **Automated analysis of low-field brain MRI in cerebral malaria.** *Biometrics* 2022;79:2417–29 CrossRef Medline
12. Chetcuti K, Chilingulo C, Goyal M, et al. **Implementation of a low-field portable MRI scanner in a resource-constrained environment: our experience in Malawi.** *AJNR Am J Neuroradiol* 2022;43:670–74 CrossRef Medline
13. Webb A, Obungoloch J. **Five steps to make MRI scanners more affordable to the world.** *Nature* 2023;615:391–93 CrossRef Medline
14. Koo TK, Li MY. **A guideline of selecting and reporting intraclass correlation coefficients for reliability research.** *J Chiropr Med* 2016;15:155–63 CrossRef Medline
15. Deoni SC, Bruchhage MM, Beauchemin J, et al. **Accessible pediatric neuroimaging using a low field strength MRI scanner.** *Neuroimage* 2021;238:118273 CrossRef Medline
16. Beekman R, Crawford A, Mazurek MH, et al. **Bedside monitoring of hypoxic ischemic brain injury using low-field, portable brain magnetic resonance imaging after cardiac arrest.** *Resuscitation* 2022;176:150–58 CrossRef Medline
17. Sheth KN, Yuen MM, Mazurek MH, et al. **Bedside detection of intracranial midline shift using portable magnetic resonance imaging.** *Sci Rep* 2022;12:67 CrossRef Medline

# Incidental Thalamic Lesions Identified on Brain MRI in Pediatric and Young Adult Patients: Imaging Features and Natural History

 Vinicius de Padua V. Alves,  Marguerite M. Care, and  James L. Leach



## ABSTRACT

**BACKGROUND AND PURPOSE:** Nonspecific, localized thalamic signal abnormalities of uncertain significance are occasionally found on pediatric brain MR imaging. The goal of this study is to describe the MR imaging appearance and natural history of these lesions in children and young adults.

**MATERIALS AND METHODS:** This retrospective study evaluated clinically acquired brain MR imaging examinations obtained from February 1995 to March 2022 at a large, tertiary care pediatric hospital. Examinations with non-mass-like and nonenhancing thalamic lesions were identified based on term search of MR imaging reports. A total of 221 patients formed the initial group for imaging assessment. Additional exclusions during imaging review resulted in 171 patients. Imaging appearance and size changes were assessed at baseline and at follow-up examinations.

**RESULTS:** A total of 171 patients (102 male) at a median age of 11 years (range: 1–23 years), 568 MR imaging examinations, and 180 thalamic lesions were included. Median time from baseline to the last follow-up MR imaging was 542 days (range: 46–5730 days). No lesion enhanced at any time point. On imaging follow-up, 11% of lesions (18/161) became smaller, 10% (16/161) resolved, 73% (118/161) remained stable, and 6% (9/161) increased in size at some point during evaluation. Median time interval from baseline to enlargement was 430 days (range: 136–1074 days).

**CONCLUSIONS:** Most incidental, non-mass-like thalamic signal abnormalities were stable, decreased in size, or resolved on follow-up imaging and are likely of no clinical significance. Surveillance strategies with longer follow-up intervals may be adequate in the management of such findings.

**ABBREVIATIONS:** AP = anteroposterior; EMR = electronic medical record; GRE = gradient recalled-echo; PD = proton density; TR = transverse

Increasing utilization and technical advances in MR imaging have led to the frequent identification of incidental findings (unexpected imaging findings likely unrelated to clinical presentation) on pediatric brain MR imaging examinations performed for both clinical and research purposes.<sup>1–5</sup> In our pediatric neuroradiology practice, we often identify nonspecific lesions within the thalami on brain examinations obtained for a wide variety of indications. While some of these incidental findings may have immediate clinical implications, most are of uncertain significance and may produce confusion among clinicians and concern among patients and their families.<sup>6</sup> In addition, subsequent evaluations of these findings may lead to cascades of additional imaging and testing and

increased health care expenses. Outcomes-based research is an important pillar in the development of management recommendations for incidental findings.<sup>7,8</sup> While prior studies have assessed incidentally identified, mass-like, potentially neoplastic signal abnormalities in the thalamus in children,<sup>6,9</sup> we are unaware of any investigation assessing the imaging appearance, distribution, and natural history of non-mass-like, nonspecific, areas of signal abnormality in the thalamus in the pediatric population. Based upon our clinical experience, we hypothesized that these signal abnormalities rarely change on follow-up imaging and rarely have definite clinical significance. The purpose of our study was to assess the imaging appearance of these signal abnormalities and their natural history on follow-up examinations (when available), describe basic clinical associations, and define reasonable MR imaging follow-up guidelines.


## MATERIALS AND METHODS

This retrospective study was approved by the Institutional Review Board at Cincinnati Children's Hospital Medical Center.

Received September 19, 2023; accepted after revision November 6.

From the Department of Radiology (V.d.P.V.A., M.M.C., J.L.L.), Cincinnati Children's Hospital Medical Center, Cincinnati, Ohio; and Department of Radiology (M.M.C., J.L.L.), University of Cincinnati College of Medicine, Cincinnati, Ohio.

Please address correspondence to James L. Leach, MD, 3333 Burnet Ave, Kasota Building MLC 5031, Cincinnati, OH 45226; e-mail: james.leach@cchmc.org; @CincyKidsRad

 Indicates open access to non-subscribers at [www.ajnr.org](http://www.ajnr.org)

<http://dx.doi.org/10.3174/ajnr.A8090>

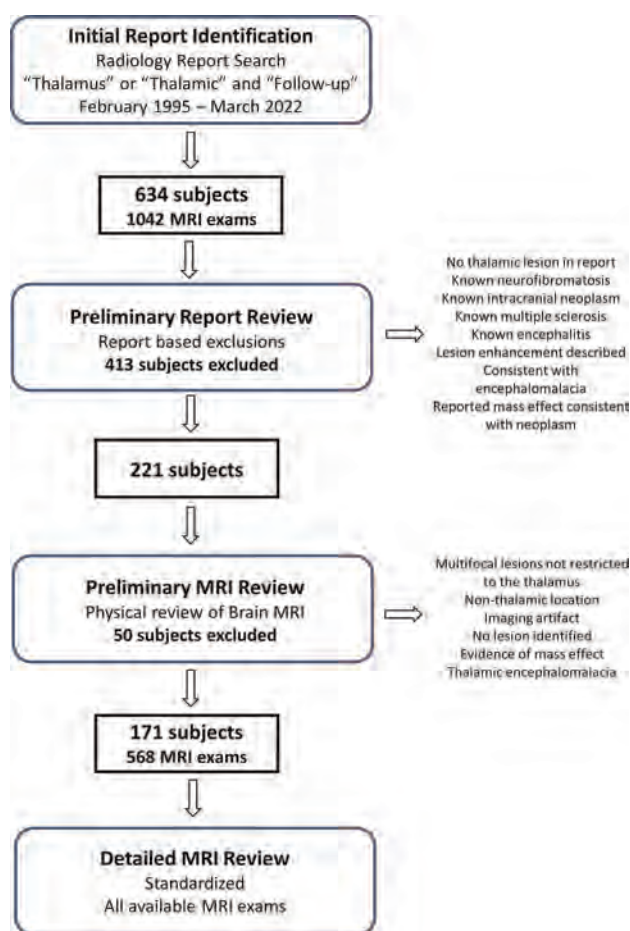


**FIG 1.** Flow chart of study participant selection process. Conditions on right denote exclusion criteria.

All research activities were Health Insurance Portability and Accountability Act compliant, and the need for patient informed consent was waived.

### Sample Selection

Patients were identified by performing a radiology report search (Illuminate Insight, Softek) of brain MR imaging examinations performed between February 1995 and March 2022 (Fig 1). Reports were selected that included both the terms “thalamic” and/or “thalamus” and “follow-up” in the radiology report. A total of 634 potential patients (1042 MR imaging examinations) were identified on initial report search. A preliminary radiology report review was performed by 2 board-certified pediatric neuroradiologists (both with >20 years clinical experience; J.L.L., M.M.C.) with the following exclusions: No thalamic lesion described in the identified report; known history of neurofibromatosis, intracranial neoplasm, multiple sclerosis, or encephalitis at the time of reporting; and reported contrast enhancement on the baseline examination, thalamic encephalomalacia, or thalamic lesions with mass effect consistent with neoplasm. A total of 413 patients were excluded by this preliminary report review. Then, a preliminary imaging review of the report-identified MR imaging examinations in the remaining 221 patients was performed by the same 2 board-certified pediatric neuroradiologists. Additional exclusions

during preliminary imaging review included the following: multifocal lesions not restricted to the thalamus, nonthalamic location of the reported signal abnormality, imaging artifact responsible for the abnormality, no lesion identified on imaging review, evidence of mass effect (including distortion of internal thalamic structures, expansion of the thalamus, deformity of adjacent CSF spaces indicating mass effect), or imaging findings consistent with thalamic encephalomalacia. An additional 50 patients were excluded after preliminary MR imaging review for a final cohort of 171 patients with nonspecific, non-mass-like thalamic signal abnormalities. All previous and follow-up brain MR imaging examinations available in our institutional PACS were identified in this cohort for a total of 568 brain MR imaging examinations.

### Extraction of Clinical Data

Clinical and demographic data were acquired from the electronic medical record (EMR) (Epic Systems) and imaging reports by a research fellow (V.d.P.V.A.). The clinical indication for the examination on the radiology report was extracted. If a patient had multiple follow-ups, the clinical indication for the MR imaging was extracted from the first examination where the thalamic abnormality was mentioned. The EMR was systematically searched utilizing the most recent clinical notes available and the continually updated problem list and extracted for the patients with known medical conditions. The results were summarized into pertinent categories based on the timing of the initial MR imaging where the thalamic lesion was identified and based on a combination of radiology report clinical indications and the EMR search.

### Standardized MR Imaging Review of Thalamic Abnormalities

Detailed imaging review of brain MR imaging studies was performed by the same 2 board-certified neuroradiologists (J.L.L., M.M.C.). An initial 10 training studies were evaluated by both reviewers together to define and agree upon measurement method and lesion characteristic assessment. Subsequently, all examinations were independently evaluated by each examiner. One reviewer (J.L.L.) evaluated 65% of examinations (368/568), whereas the other (M.M.C.) evaluated 35% (200/568) of the examinations. For patients with multiple MR imaging examinations, the first occurrence of a thalamic lesion was considered the baseline MR imaging examination. Image assessment and lesion measurement were performed utilizing the clinical PACS system at our institution. Imaging reviewers were not blinded to the clinical MR imaging report. The reviewers assessed thalamic lesion characteristics and their longitudinal change on each examination utilizing a standardized electronic form. Lesion location was defined by nuclear group (anterior, posterior, lateral, and medial) utilizing a standardized template reference<sup>10</sup> and brain hemisphere lateralization (left and right). Lesion signal intensity was visually characterized for each sequence compared with the ipsilateral caudate nucleus (hypointense, isointense, hyperintense) or nonvisible/indistinguishable from normal thalamus for each available sequence, including T1-weighted, T2-weighted, proton attenuation (PD), T2-weighted FLAIR, DWI, ADC maps, and gradient recalled-echo or susceptibility weighted imaging (GRE/SWI). Signal was described as heterogeneous or homogeneous, and

**Table 1: Clinical scenario for baseline MR imaging examinations (n = 171)**

MR Imaging Examination Indication	n	%
Migraine headache	53	31
Seizures/epilepsy	40	23.4
NOS headache	20	11.7
Other <sup>a</sup>	18	10.5
Behavioral/developmental <sup>b</sup>	13	7.6
Head injury	8	4.7
Movement disorder	5	2.9
Ophthalmologic	4	2.3
Psychiatric	4	2.3
Hearing loss	3	1.8
Idiopathic intracranial hypertension	3	1.8

**Note:**— NOS indicates not otherwise specified.

<sup>a</sup> Includes precocious puberty, hypopituitarism, central sleep apnea or congenital central hypoventilation, focal neurologic findings, Fanconi anemia, lymphoma, Li-Fraumeni syndrome screening, unspecified neck pain, Chiari syndrome, syncope, prior stroke, and vertigo.

<sup>b</sup> Includes attention deficit/hyperactivity disorder, autism spectrum disorder, fine and gross motor delay, intermittent explosive disorder, and language delay.

margins as ill-defined or well-defined. Well-defined margins were defined as sharply circumscribed transitions around the entire circumference of the lesion. The MR imaging sequence allowing best visualization of the lesion was used for measurement (typically, the axial T2-weighted or T2 FLAIR sequence). Anteroposterior (AP) and transverse (TR) linear measurements were performed and recorded for each lesion. Any change from prior examinations were denoted. Assessment and documentation of any MR imaging studies performed before identification of the thalamic abnormality were also performed. Patient sex and age were obtained from imaging reports at the time of first MR imaging (if more than 1 examination was present).

### MR Imaging Procedures

A total of 373 (66%, 373/568) examinations were performed on 1.5T MR scanners, and 195 (34%, 195/568) were performed on 3T MR scanners. Given the retrospective nature and time frame of the study, MR imaging protocols and scanner manufacturer varied, but each examination included at least T1-weighted and T2-weighted pulse sequences, at a maximum of 6 mm section thickness (range: 1–6 mm, median: 4 mm). Additional pulse sequences, available on a case-by-case basis included the following: PD, T2 FLAIR, DWI, ADC maps, and GRE/SWI. A total of 343 (60%, 343/568) examinations were performed on GE Healthcare scanners, 171 (30%, 171/568) on Philips Healthcare scanners, and 52 (10%, 52/568) on Siemens scanners. A total of 408 (70.5%, 408/578) studies included the administration of gadolinium-based contrast agents during initial identification and/or follow-up of the thalamic signal abnormalities.

### Statistical Analysis

A descriptive analysis of demographic and clinical data was performed to summarize sample and imaging characteristics. All statistical analyses were performed with Excel Version 2209 Build 16.0 (Microsoft). Categorical variables were presented as percentages. For enlarging lesions, AP and TR dimensional cross product at each imaging time point was plotted overtime to graphically demonstrate growth characteristics.

## RESULTS

### Study Sample Characteristics

A total of 171 patients (102 male, 69 female) with 568 MR imaging examinations and 180 thalamic lesions were included in this study. Median age at baseline MR imaging was 11 years (range: 1–23 years). The 2 most common indications for the MR imaging examination were headaches (43%, 73/171) and seizures/epilepsy (23%, 40/171) (Table 1). No patient had a clinical diagnosis of neurofibromatosis or multiple sclerosis at the time of the initial examination, or subsequently, by review of the EMR up until December 1, 2022.

### Thalamic Lesion Characteristics at Baseline MR Imaging

Among all lesions, 91 (50.5%, 91/180) were located in the right thalamus and 89 (49.5%, 89/180) in the left thalamus. A total of 109 lesions (61%, 109/180) were identified in the posterior, 51 (28%, 51/180) in the lateral, 17 (10%, 17/180) in the medial, and 3 (1%, 3/180) in the anterior thalamic nuclear regions. Imaging examples of typical lesions are provided in Figure 2. The median size of the lesions was as follows: AP, 4 mm (range: 2–21 mm); TR, 5 mm (range: 1–18 mm). For border definition, 128 lesions (71%, 128/180) were considered ill-defined, whereas 52 lesions (29%, 52/180) were classified as well-defined. For internal architecture, most lesions (97%, 174/180) were deemed homogeneous and a minority (3%, 6/180) were categorized as heterogeneous. No lesion exhibited contrast enhancement on any follow-up examinations. Table 2 provides the signal characteristics of the lesions based on different MR imaging sequences. Lesions were best seen on T2 or T2-FLAIR sequences and were most commonly hyperintense on T2 and T2 FLAIR (77.3%, 79.9%, respectively) and isointense to hypointense on T1-weighted images (42.5%) compared with the caudate. While most lesions were not identified on DWI/DTI, some (11.1%) exhibited increased diffusivity relative to the thalamus and caudate. None demonstrated relative diffusion restriction on ADC maps.

### Longitudinal Analysis on Follow-up MR Imaging

A total of 152 (89%, 152/171) patients had follow-up examinations with a median of 2 follow-up examinations (range: 1–12 examinations). A total of 87 subjects (51% of total cohort) had 1-year or greater follow-up: 1–2 years: 21; 2–3 years: 21; 3–4 years: 19; 4–5 years: 13; >5 years: 13. A 3-month follow-up interval was most commonly recommended in baseline scan reports (44%, 76/171), ranging from 1 to 12 months (Table 3). Median time from baseline to the last follow-up MR imaging was 542 days (range: 46–5730 days). A total of 161 lesions (89%, 161/180) were followed up longitudinally. Of those, 18 (11%, 18/161) became smaller, 16 (10%, 16/161) resolved, 118 (73%, 118/161) remained stable, and 9 (6%, 9/161) were larger at any follow-up point (of these: 1 had no further follow-up, 6 were subsequently stable or smaller, and 1 resolved) (Fig 3). One enlarging lesion (maximum dimension of 10 × 8 mm) was treated with radiation therapy for presumed thalamic glioma (without histologic confirmation) with a subsequent decrease in size (Fig 3C). Among the enlarging lesions, the median interval from baseline to initial identified enlargement was 430 days

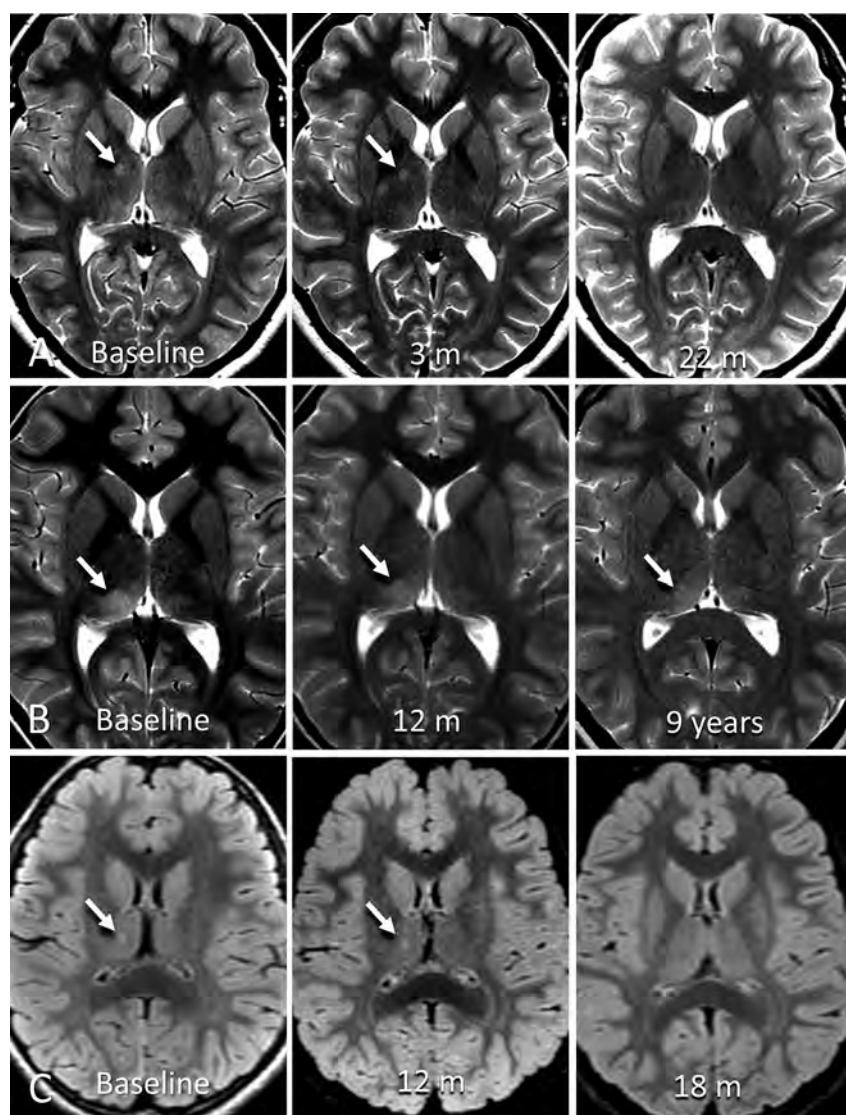


**FIG 2.** Example cases of incidental thalamic lesions identified in this study. A, Axial T2-weighted images of a 13-year-old adolescent girl with headache show a focal thalamic lesion (arrow) within the anterior lateral right thalamus on baseline MR imaging. The lesion was stable on the 3-month follow-up and resolved at 22-month follow-up. B, Axial T2-weighted images of a 9-year-old girl with headache show ill-defined thalamic signal (arrow) in the posterior right thalamus on baseline MR imaging. At 1-year follow-up, the lesion was slightly less defined and smaller. At 9-year follow-up, the lesion was smaller and less defined. This patient had 12 follow-up scans for this lesion over a 9-year period. C, Axial T2 FLAIR images of a 5-year-old girl after a single seizure episode. Baseline MR imaging shows a small focal signal abnormality in the right thalamus (arrow). This lesion slightly enlarged at 1-year follow-up and resolved at 18-month follow-up imaging.

**Table 2: Thalamic lesion signal characteristics on baseline MR imaging (n = 180 lesions)**

Signal	PD	T1	T2	T2 FLAIR	DWI	ADC	GRE/SWI
Hypointense	0.0	26.5	0.0	0.0	1.8	0.0	0.0
Isointense	42.8	16.0	21.0	19.0	19.8	1.8	16.5
Hyperintense	52.4	1.7	77.3	79.9	11.1	53.1	55.3
Not visible	9.5	55.8	1.1	1.1	68.5	46.3	29.8

(range: 136–1074 days). Four lesions enlarged within 1 year, and 4 within 2 years. Graphical representation of lesion growth is provided in Figure 4. No lesions were biopsied. No other subject, by review of the EMR up until December 1, 2022, had clinical diagnosis of intracranial neoplasm.

In subjects with  $\geq 2$  years follow-up (excluding the radiation therapy treated subject), no lesion that had been stable or smaller (including those that had previously enlarged and were subsequently stable or smaller) by 2 years continued to enlarge. One subject (Subject B, Fig 3) had an enlargement time point at 2.9 years (1074 days); however, this patient had no interval studies from their initial brain MR imaging. This subject was followed for an additional 4656 days (12.8 years) with long-term stability.

A total of 26 patients had MR imaging examinations performed before the identification of thalamic signal abnormalities. Mean time from the most recent prior study (where no thalamic lesion was identified) to the first MR imaging examination demonstrating a thalamic lesion was 1882 days (range: 148–5437 days). Six subjects had 2 thalamic lesions at initial diagnosis, all stable on subsequent follow-up (6 months to 2 years). Three subjects developed a new thalamic lesion on follow-up imaging for an existing thalamic lesion. One did not have follow-up imaging after the new lesion was identified (6 years after the initial examination); thus, growth potential cannot be documented. Of those that had follow-up, 1 new lesion was stable at subsequent 2-year follow-up, and 1 new lesion was smaller at subsequent 4-month follow-up. No subjects with resolved thalamic lesions had subsequent follow-up brain imaging studies.

Most thalamic lesions, even those described as having ill-defined margins, were well delineated relative to the remainder of the thalamus. During data analysis, a subgroup of thalamic lesions, all within the pulvinar of the posterior thalamus ( $n = 21$ ), were identified with very ill-defined margins that made differentiation of lesion borders challenging (Fig 2B). In these patients, measurements were often difficult. There was no thalamic expansion or mass effect (by definition).

Of the 20 lesions in this subgroup with follow-up imaging, 19 were stable and 1 resolved.

No thalamic imaging finding specifically correlated with the clinical scenario at diagnosis. After the baseline examination, no

Table 3: MR imaging follow-up recommendations available on baseline imaging reports (n = 171 patients)<sup>a</sup>

None <sup>b</sup>	1 Month <sup>c</sup>	2 Months	3 Months	4 Months	6 Months	9 Months	12 Months	NOS <sup>d</sup>
3	4	7	76	24	41	3	7	6

**Note:**— NOS indicates not otherwise specified.  
<sup>a</sup> Values are absolute numbers.  
<sup>b</sup> Study report did not provide recommendations for follow-up imaging.  
<sup>c</sup> In the case an interval range of follow-up was given, the smallest interval was considered.  
<sup>d</sup> Imaging follow-up was recommended but no specified time interval.

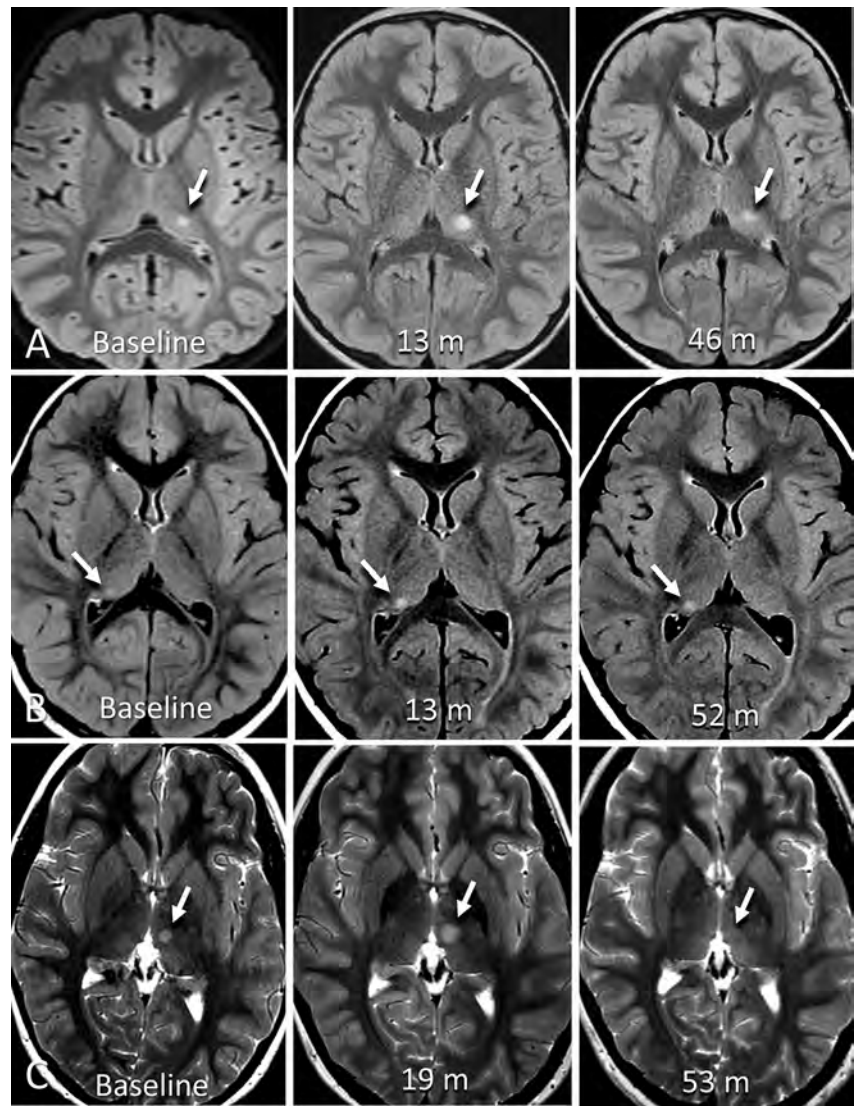


**FIG 3.** Example cases of enlarging incidental thalamic lesions identified in this study. A, Axial T2 FLAIR images of a 6-year-old boy with headache show a focal thalamic lesion (arrow) within the posterior left thalamus on baseline MR imaging. At 13-month follow-up, the lesion was enlarged. At 46-month follow-up, the lesion was more ill-defined and slightly decreased posteriorly. B, Axial T2 FLAIR images part of routine follow-up of a 4-year-old boy with history of right cerebellar complex developmental venous anomaly. Baseline MR imaging shows a small focus of increased signal in the posterior right thalamus, enlarged at 13-month follow-up, then stable 52 months after baseline MRI. C, Axial T2-weighted images of an 8-year-old girl with history of head trauma and headache showing a focal lesion within the left medial thalamus (7 × 5 mm). There was slow interval enlargement over 5 MR imaging studies for 19 months, at which point the lesion was classified as presumed low-grade glioma, and was treated with a total of 50.4 Gy fractionated radiation therapy over 8 weeks. Following therapy, there was a decrease in the site over subsequent 34 months.

subject developed a diagnosis of multiple sclerosis, neurofibromatosis, metabolic condition, or other condition that could be specifically related to the thalamic abnormality.

DISCUSSION

Pediatric brain MR imaging studies conducted for clinical and research purposes often harbor incidental imaging findings.<sup>1</sup> The reported rates of such findings vary from 10% to 26% of examinations.<sup>3,4,6,11</sup> Our retrospective study included 171 children, adolescents, and young adults who underwent brain MR imaging for various indications, the most common being headache, seizures, and epilepsy. We found that incidentally identified, non-mass-like, nonspecific, thalamic lesions were mostly (94%) stable, smaller, or resolved on follow-up imaging. Among the lesions that enlarged (6%), most were subsequently stable, smaller, or resolved. One enlarging lesion was treated with radiation therapy as a presumed thalamic neoplasm with subsequent decrease in size. The thalamic lesions were most frequently located in the posterior and lateral thalamic groups and were ill-defined and exhibited no diffusion restriction. No lesions were biopsied or underwent resection. No lesion with follow-up imaging that included contrast administration subsequently enhanced. None of the thalamic imaging findings was definitely correlated with the examination clinical scenario. Together, our study suggests that most of these small, nonspecific, non-mass-like thalamic signal abnormalities are of limited clinical significance.

Developing effective imaging follow-up and management strategies for incidentally identified findings on brain MR imaging requires a thorough understanding of their imaging characteristics and outcomes and has been little studied in pediatric patients.<sup>1,8,9</sup> Zaazoue et al<sup>6</sup> evaluated 144 pediatric patients with incidental brain lesions on MR imaging indeterminate for tumor, including 26 patients with thalamic lesions. In their study, only 3 patients with thalamic lesions showed an increase in lesion size on follow-up imaging, and none required surgical intervention. Like our

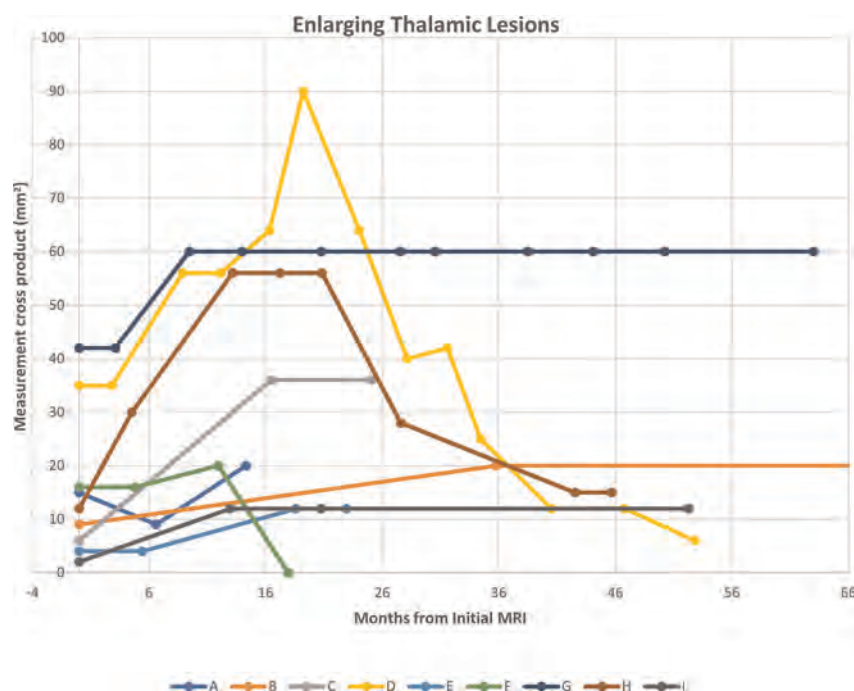


**FIG 4.** Growth trajectories of 9 thalamic lesions that enlarged at any time during follow-up MR imaging. Patient D, an 8-year-old girl with history of head trauma and headache, was treated with radiation therapy 19 months after initial lesion identification after growth identified with a subsequent decrease in size. Patient B, a 14-year-old adolescent boy with history of fetal alcohol syndrome and tethered cord, had additional stable follow-up examinations at 138 and 190 months (not shown).

investigation, those with typical syndromic characteristics, such as NF1, NF2, and tuberous sclerosis, were excluded. However, the authors included only lesions thought to potentially represent neoplasms, and included lesions with mass effect which makes their cohort essentially different from ours. Although their numbers were small, their outcomes were comparable to ours, and they concluded that patients with thalamic lesions are less likely to progress or require surgical intervention than those in other locations.<sup>6</sup>

Additional research on pediatric MR imaging has focused primarily on thalamic lesions with mass effect or high suspicion for neoplasm.<sup>6,9</sup> For instance, Kozyrev et al<sup>9</sup> investigated 58 children with space-occupying thalamic lesions incidentally identified on MR imaging, of whom 21 underwent surgery due to clinician suspicion of high-grade tumor, change in lesion characteristic, or growth on follow-up imaging. In their study, contrast-enhancing lesions were included and most operated patients were found to have low-grade or high-grade gliomas on histopathologic analyses. In contrast, we excluded all lesions demonstrating mass effect and/or contrast enhancement. However, because many of their thalamic neoplasms, including those that were both low and high grade, were nonenhancing, enhancement characteristics may not be a key distinguishing factor.

In our study, no histopathology analyses were performed in any of the thalamic lesions, which prevents confirmation of etiology. The differential diagnosis for an imaging lesion in the thalamus is wide ranging.<sup>12</sup> Some of the lesions may represent small, indolent, or spontaneously regressing neoplasms. Prior studies

have reported on spontaneous resolution of low-grade tumors in pediatric patients.<sup>13,14</sup> Transient edema or inflammation may account for the complete resolution of some lesions observed in imaging, particularly in patients with a history of seizures or epilepsy. Investigations involving patients with prolonged status epilepticus have revealed thalamic DWI and FLAIR hyperintensities on the same side as the epileptiform activity,<sup>15,16</sup> often ill-defined signal within the pulvinar.<sup>17</sup> Thalamic involvement has also been associated with venous vasculitis conditions, such as Behcet disease, or connective tissue disorders, such as Sjogren syndrome.<sup>15</sup> These lesions often appear hyperintense in T2 and FLAIR sequences and occasionally exhibit enhancement in gadolinium-enhanced T1-weighted imaging.<sup>15</sup> Finally, these lesions may represent isolated dysplastic or hamartomatous changes of the thalamus, such as in cases of NF1<sup>12,18</sup> (although no subject in our study had this diagnosis).

Our study has several limitations. As this was a retrospective analysis of examinations from a single institution,

there is potential for selection bias in our results. Therefore, future prospective and multicenter studies are needed to confirm our findings. The inclusion of images dating back to 1995 means that there were substantial differences in acquisition protocols and techniques between examinations, which may have impacted the identification and characterization of thalamic lesions. In addition, differences in section thickness selection between examinations may have contributed to apparent changes in lesion size as many lesion dimensions were near or below the section thickness of examinations. Without histopathology, the potential etiologies of the lesions remain speculative. Our image reviews were subjective and relied on the expertise of 2 readers who assessed different cases, which may have introduced variability in our results. However, both neuroradiologists reviewed a common training set of 10 subjects to define measurement technique and subjective assessment, trained in an identical fashion at the same institutions, and have been working in the same institution together since 2007, limiting this potential confounding factor. Of 171 subjects, 66 subjects (39%) had imaging follow-up for >2 years. This does limit our assessment for very slow growing tumors and could occur for a number of many reasons including: no report recommendations for continued follow-up, clinician/patient choice, transfer to adult or other pediatric institutions, or loss of medical follow-up. This limits our ability to establish definitive data on very long-term follow-up of these findings and is an unavoidable limitation of a retrospective study. On clinical chart review, none of our subjects had a subsequent diagnosis of tumor or other clearly related clinical condition (other than the

subject treated with radiation therapy for presumed glioma without histologic proof, which enlarged at 7 months after identification).

The findings of this study may be used to guide and improve imaging follow-up recommendations for incidental, nonspecific, thalamic lesions. Considering that all enlarging lesions (ie, more concerning for neoplasia) in our cohort did so by 3 years from initial imaging, a less aggressive surveillance strategy may be adequate. Based on imaging reports, the suggested follow-up intervals from our cohort (Table 3) were predominantly  $\leq 6$ -month intervals, which may have been unnecessarily conservative, given our outcome findings. Additionally, assessing our subset of subjects with longer-term follow-up, no lesion with prior follow-up imaging followed for  $> 2$  years demonstrated enlargement. One lesion enlarged at 2.9 years after initial diagnosis (without previous follow-up imaging), and was subsequently stable for 12.8 years. Conclusions, however, are limited by lack of  $> 1$  year imaging follow-up in many subjects. If follow-up imaging is deemed necessary, it may be beneficial to extend the follow-up period to 6–12 months initially, followed by yearly follow-ups thereafter for at least 3 years after diagnosis. By adopting this management approach, we can ensure that patients receive appropriate monitoring while additionally minimizing unnecessary diagnostic testing.

## CONCLUSIONS










In our retrospective study of 171 children, adolescents, and young adults who underwent brain MR imaging for various neurologic or screening indications, most incidentally identified, non-mass-like thalamic signal abnormalities were stable, smaller, or resolved on follow-up imaging and likely of minimal to no clinical significance. Of lesions that enlarged with subsequent follow-up imaging, 1 continued to enlarge, concerning for neoplasm. Therefore, less conservative surveillance strategies of such incidental findings with longer follow-up intervals may be adequate to guarantee both optimized and cost-effective care for these patients.

Disclosure forms provided by the authors are available with the full text and PDF of this article at [www.ajnr.org](http://www.ajnr.org).

## REFERENCES

- Li Y, Thompson WK, Reuter C, ABCD Consortium, et al. **Rates of incidental findings in brain magnetic resonance imaging in children.** *JAMA Neurol* 2021;78:578–87 CrossRef Medline
- Fisch N, Konen O, Halevy A, et al. **Incidental multifocal white matter lesions in pediatric magnetic resonance imaging.** *Pediatr Neurol* 2012;47:7–12 CrossRef Medline
- Maher CO, Piatt JH, Ragheb J, Section on Neurologic Surgery, American Academy of Pediatrics, et al. **Incidental findings on brain and spine imaging in children.** *Pediatrics* 2015;135:e1084–96 CrossRef Medline
- Jansen PR, Dremmen M, van den Berg A, et al. **Incidental findings on brain imaging in the general pediatric population.** *N Engl J Med* 2017;377:1593–95 CrossRef Medline
- Di Pietro NC, Illes J. **Disclosing incidental findings in brain research: the rights of minors in decision-making.** *J Magn Reson Imaging* 2013;38:1009–13 CrossRef Medline
- Zaazoue MA, Manley PE, Kapur K, et al. **Natural history and management of incidentally discovered focal brain lesions indeterminate for tumor in children.** *Clin Neurosurg* 2020;86:357–65 CrossRef Medline
- Ganguli I, Simpkin AL, Lupo C, et al. **Cascades of care after incidental findings in a US national survey of physicians.** *JAMA Netw Open* 2019;2:e1913325 CrossRef Medline
- Davenport MS. **Incidental findings and low-value care.** *AJR Am J Roentgenol* 2023;221:117–23 CrossRef
- Kozyrev DA, Soleman J, Tsering D, et al. **Pediatric thalamic incidentalomas: an international retrospective multicenter study.** *J Neurosurg Pediatr* 2022;29:141–49 CrossRef Medline
- Boelens Keun JT, van Heese EM, Laansma MA, et al. **Structural assessment of thalamus morphology in brain disorders: a review and recommendation of thalamic nucleus segmentation and shape analysis.** *Neurosci Biobehav Rev* 2021;131:466–78 CrossRef Medline
- Gur RE, Kaltman D, Melhem ER, et al. **Incidental findings in youths volunteering for brain MRI research.** *AJNR Am J Neuroradiol* 2013;34:2021–25 CrossRef Medline
- Tuttle C, Boto J, Martin S, et al. **Neuroimaging of acute and chronic unilateral and bilateral thalamic lesions.** *Insights Imaging* 2019;10:24 CrossRef Medline
- Piccirilli M, Lenzi J, Delfinis C, et al. **Spontaneous regression of optic pathways gliomas in three patients with neurofibromatosis type I and critical review of the literature.** *Childs Nerv Syst* 2006;22:1332–37 CrossRef Medline
- Perilongo G, Moras P, Carollo C, et al. **Spontaneous partial regression of low-grade glioma in children with neurofibromatosis-1: a real possibility.** *J Child Neurol* 1999;14:352–56 CrossRef Medline
- Renard D, Castelnovo G, Campello C, et al. **Thalamic lesions: a radiological review.** *Behav Neurol* 2014;2014:154631 CrossRef Medline
- Katramados AM, Burdette D, Patel SC, et al. **Periictal diffusion abnormalities of the thalamus in partial status epilepticus.** *Epilepsia* 2009;50:265–75 CrossRef Medline
- Tschampa HJ, Greschus S, Sassen R, et al. **Thalamus lesions in chronic and acute seizure disorders.** *Neuroradiology* 2011;53:245–54 CrossRef Medline
- Kaneko T, Kawakami R, Fujinaga Y, et al. **Degenerative thalamic hamartoma: CT and MR imaging features.** *AJNR Am J Neuroradiol* 2004;25:766–68

# A Prospective Multi-Institutional Study Comparing the Brain Development in the Third Trimester between Opioid-Exposed and Nonexposed Fetuses Using Advanced Fetal MR Imaging Techniques

 Hyuk Jin Yun,  Usha D. Nagaraj,  P. Ellen Grant,  Stephanie L. Merhar,  Xiawei Ou,  Weili Lin,  Ashley Acheson, Karen Grewen,  Beth M. Kline-Fath, and  Kiho Im

## ABSTRACT

**BACKGROUND AND PURPOSE:** While the adverse neurodevelopmental effects of prenatal opioid exposure on infants and children in the United States are well described, the underlying causative mechanisms have yet to be fully understood. This study aims to compare quantitative volumetric and surface-based features of the fetal brain between opioid-exposed fetuses and unexposed controls by using advanced MR imaging processing techniques.

**MATERIALS AND METHODS:** This is a multi-institutional IRB-approved study in which pregnant women with and without opioid use during the current pregnancy were prospectively recruited to undergo fetal MR imaging. A total of 14 opioid-exposed ( $31.4 \pm 2.3$  weeks of gestation) and 15 unexposed ( $31.4 \pm 2.4$  weeks) fetuses were included. Whole brain volume, cortical plate volume, surface area, sulcal depth, mean curvature, and gyrification index were computed as quantitative features by using our fetal brain MR imaging processing pipeline.

**RESULTS:** After correcting for gestational age, fetal sex, maternal education, polysubstance use, high blood pressure, and MR imaging acquisition site, all of the global morphologic features were significantly lower in the opioid-exposed fetuses compared with the unexposed fetuses, including brain volume, cortical volume, cortical surface area, sulcal depth, cortical mean curvature, and gyrification index. In regional analysis, the opioid-exposed fetuses showed significantly decreased surface area and sulcal depth in the bilateral Sylvian fissures, central sulci, parieto-occipital fissures, temporal cortices, and frontal cortices.

**CONCLUSIONS:** In this small cohort, prenatal opioid exposure was associated with altered fetal brain development in the third trimester. This adds to the growing body of literature demonstrating that prenatal opioid exposure affects the developing brain.

**ABBREVIATIONS:** CP = cortical plate; FDR = false discovery rate; GA = gestational age; GI = gyrification index; OE = opioid-exposed; UE = unexposed

Prenatal opioid exposure is a known public health crisis in the United States today. The use of opioids during pregnancy is very common and is likely underreported, resulting in substantial associated morbidity and hospital costs.<sup>1–6</sup> Opioid-exposed infants have lower birth weights, smaller head circumferences, and neuro-behavioral differences in the first weeks after birth, resulting in longer hospital stays compared with unexposed infants.<sup>7–10</sup> Long-term studies in children with prenatal opioid exposure reveal lower cognitive scores and poorer school performance in childhood and

adolescence.<sup>11,12</sup> Despite the scope of this problem, the underlying causative biology of these poor outcomes has yet to be adequately explored. Brain MR imaging studies of opioid-exposed infants and children have revealed smaller regional brain volumes in multiple areas despite no difference in overall brain volume, increased white matter injury, and altered functional networks on resting-state functional connectivity MR imaging compared with unexposed controls.<sup>13–15</sup> There are descriptions of potential underlying causes, including alterations in cerebral blood flow, neurogenesis, neuronal differentiation, and neuronal activity as a result of the opioid

Received September 14, 2023; accepted after revision November 7.

From the Division of Newborn Medicine (H.J.Y., P.E.G., K.I.) and Department of Radiology (P.E.G.), Boston Children's Hospital, Boston, Massachusetts; Harvard Medical School (H.J.Y., P.E.G., K.I.), Boston, Massachusetts; Department of Radiology and Medical Imaging (U.D.N., B.M.K.-F.) and Division of Neonatology, Perinatal Institute (S.L.M.), Cincinnati Children's Hospital Medical Center, Cincinnati, Ohio; University of Cincinnati College of Medicine (U.D.N., S.L.M., B.M.K.-F.), Cincinnati, Ohio; Departments of Radiology and Pediatrics (X.O.) and Psychiatry and Behavioral Sciences (A.A.), University of Arkansas for Medical Sciences, Little Rock, Arkansas; and Departments of Neurology (W.L.) and Psychiatry (K.G.), University of North Carolina, Chapel Hill, North Carolina.

H.J. Yun and U.D. Nagaraj contributed equally to this work.

This work was supported by Schubert Research Clinic Clinical Research Feasibility Fund, National Institutes of Health Planning Grant Program (Cincinnati Children's Hospital Medical Center R34-DA050268, ACRI R34-DA050261, University of North Carolina R34-DA050262), R01NS114087, R01HD100009, and R01EB032708.

Please address correspondence to Usha D. Nagaraj, MD, Department of Radiology and Medical Imaging, Cincinnati Children's Hospital Medical Center, 3333 Burnet Ave, Cincinnati, OH 45229-3026; e-mail: usha.nagaraj@cchmc.org

<http://dx.doi.org/10.3174/ajnr.A8101>

exposure through the placenta in utero.<sup>16</sup> However, postnatal brain imaging, even in the first few weeks after birth, is likely affected by other factors, such as neonatal treatment for opioid withdrawal and breastfeeding. We recently examined fetal brain MRIs in opioid-exposed (OE) and nonexposed fetuses by means of manually measured 2D biometrics that are used in routine clinical practice, which demonstrated multiple smaller brain measurements in the opioid-exposed fetuses compatible with smaller brains.<sup>17</sup> More detailed and precise information regarding differences in brain volume and cortical folding between OE and unexposed (UE) fetuses can be detected with advanced fetal MR image processing techniques to extract morphologic features of the brain such as tissue volume, surface area, sulcal depth, mean curvature, and gyrification index (GI). These metrics have the potential to provide a better understanding of the underlying causative mechanisms.

This study aims to compare morphologic features of the fetal brain between opioid-exposed fetuses and unexposed controls by using advanced processing MR imaging techniques.

## **MATERIALS AND METHODS**

### **Study Design and Patients**

This is a prospective multi-institutional study that was HIPAA-compliant and approved by the Institutional Review Board at each institution. Participants were recruited from 3 US academic medical centers: Cincinnati Children's Hospital Medical Center, Arkansas Children's Hospital, and the University of North Carolina at Chapel Hill, from July 1, 2020 through December 31, 2021. Patients in the third trimester of pregnancy were recruited to undergo a fetal MR imaging examination for investigational purposes. We recruited women with opioid use during pregnancy from clinics treating women with substance use disorders at each site. Control subjects were recruited from the general public. Substance use, or the lack thereof, was confirmed by questionnaires at the time of the study visit and/or review of maternal charts. Inclusion criteria included age of at least 18 years, singleton pregnancy, and gestational age (GA) of at least 26 weeks. Exclusion criteria assessed by phone interview by a study coordinator included: inability to supply the name of at least 1 additional person to contact in the event that the participant was unable to be reached, fetal abnormality identified on prenatal sonography or known fetal genetic disorder, nonviable fetus, contraindication to MR imaging, and inability to enter the magnet bore due to body habitus. Written informed consent was obtained from all study participants.

Study patients underwent in person detailed questioning at the time of examination by a research coordinator. Substantial opioid use was defined as daily reported opioid use during most of the pregnancy to date, with most enrolled patients on a daily opioid-use disorder maintenance medication, such as buprenorphine or methadone. Polysubstance use was defined as the mother reporting other illicit drugs and/or nicotine during the current pregnancy. Household income was recorded on a 10-point scale based on reported annual income. Maternal education was categorized for each patient as less than 10th grade education level, high school diploma, college enrollment, college

degree, and graduate degree. High blood pressure was documented in those that reported pregnancy-related high blood pressure when queried.

### **MR Imaging Acquisition**

Fetal MR imaging examinations were performed by using a 3T Ingenia scanner (Philips Healthcare) at Cincinnati Children's Hospital, and by using a 3T Prisma scanner (Siemens) at Arkansas Children's Hospital and University of North Carolina at Chapel Hill. All 3 sites used a phased-array abdominal imaging coil. Patients were not sedated during the examinations and were positioned in the left-side-down decubitus position, unless reporting feeling more comfortable in the supine position. Examinations included T2-weighted single-shot fast/turbo spin-echo sequences (Siemens: TR=1600 ms, TE=101 ms; Philips: TR=5720 ms, TE=101 ms) of the fetal brain in the axial, sagittal, and coronal planes with 2-mm interleaved contiguous slices. Each plane of acquisition was performed at minimum of 1 time each and was repeated as needed to the radiologist's satisfaction or as allotted study time allowed. Acquisition parameters were standardized across the 3 participating sites. All images were sent to Boston Children's Hospital for analysis.

### **MR Imaging Processing and Reconstruction of Cortical Plate Surface**

For extracting inner cortical surfaces from MR imaging, we used our pipeline for fetal brain MR imaging processing.<sup>18,19</sup> Fetal brains were extracted from raw MR imaging stacks and then intensity inhomogeneity of the brain regions was corrected by N4 bias field correction.<sup>20</sup> A motion-corrected 3D volume with 0.75 mm isotropic resolution was created by combining bias field corrected MR imaging stacks by using a section to volume registration technique.<sup>21</sup> On the motion-corrected volume, the cortical plate (CP) was segmented by using our deep learning-based approach.<sup>22</sup> Using the marching-cube algorithm in CIVET-2.1.0 software package (<https://www.bic.mni.mcgill.ca/ServicesSoftware/CIVET/>), we extracted the inner CP surfaces.<sup>23</sup> Initial meshes were tessellated by fitting the boundary between the CP and its inner part, and then resampled to the standard format surfaces containing 81,920 triangles and 40,962 vertices.<sup>24</sup> To eliminate small geometrical noise, we applied the Taubin smoothing approach to the inner CP surfaces.<sup>25</sup> The smoothed surfaces were registered to a template surface by using a 2D sphere-to-sphere warping method that enables vertex-wise analysis.<sup>26</sup> By searching optimal correspondences of vertices by using folding similarity between 2 surfaces, the nonrigid warping method finds vertex correspondence between individual and template surfaces. In this study, a 29 GA template surface was selected as a registration target that was created from similarly reconstructed T2 MR imaging volumes in a different 2D fetal cohort.<sup>27</sup>

### **Brain Volume and Surface Measures**

Traditional whole brain measures, such as whole brain volume, CP volume, surface area, sulcal depth, absolute mean curvature, and GI, were calculated to examine the difference between 2 groups. Whole brain volume and hemispheric CP volumes were obtained from the segmentation. Surface area was computed by a summation of Voronoi region area at each vertex of the surfaces.<sup>28</sup> For sulcal depth, we used the adaptive distance transform

that measures the distance of the shortest path from the surface to its convex hull following sulcal geometry.<sup>29</sup> Mean curvature was defined as the angular deviation from a vertex patch.<sup>28</sup> The sign of mean curvature indicates inwardly folded (negative) or outwardly folded (positive) regions. The absolute mean curvature is taken to ensure the complexity of the brain. To eliminate their noise, we applied spatial smoothing with 10 mm full width at half maximum Gaussian kernel to surface area, sulcal depth, and absolute mean curvature on the surface. As a global feature representing the magnitude of cortical convolution, GI was calculated by the area ratio between the surface and the convex hull.<sup>30</sup>

### Statistical Analysis

To assess group differences in each measure, we employed a linear regression model. In the model, each morphologic feature (whole brain volume, CP volume, surface area, sulcal depth, mean curvature, and GI) was used as a dependent variable while controlling for GA, fetal sex, maternal education, polysubstance use, high blood pressure, and MR imaging acquisition site. For global analysis, we obtained summation of surface area, average sulcal depth, and absolute mean curvature across the vertices. We also employed the Cohen *d* statistic to assess the difference in measures between 2 groups. Surface area and sulcal depth were independently analyzed as regional analysis, and false discovery rate (FDR) *q* values were obtained to correct multiple comparisons problems. We set the significance level of FDR *q* value to 0.05.

## RESULTS

### Description of Patient Sample

A total of 63 patients completed the MR imaging: 34 from Cincinnati Children's Hospital Medical Center (OE/UE: 16/18), 16 from University of North Carolina (8/8), and 13 from University of Arkansas for Medical Sciences (4/9). Of these scans, 34 patients were excluded due poor image quality typically related to motion artifact and low SNR that results in poor

reconstruction quality. The remaining 29 patients were successfully reconstructed to high-quality 3D volume and included in this analysis: 14 opioid-exposed fetuses (GA:  $31.4 \pm 2.3$  weeks) and 15 unexposed control fetuses (GA:  $31.4 \pm 2.4$  weeks). These and other demographic data are summarized in Table 1.

### Volumetric and Morphologic Measures

All the morphologic measures were significantly lower in opioid-exposed fetuses compared with unexposed control fetuses (Table 2): whole brain volume: Cohen *d* effect size (*P* value) = 0.3555 (*P* < .001), CP volume: 0.2818 (*P* < .001), cortical surface area: 0.4373 (*P* < .001), sulcal depth: 0.4739 (*P* < .001), cortical mean curvature: 0.3120 (*P* < .001), and GI: 0.4801 (*P* < .001).

The results of the regional analysis of surface area and sulcal depth between the groups were examined. Opioid-exposed fetuses showed significantly smaller surface area (FDR *q* < 0.05) compared with unexposed controls in multiple cortical regions, most pronounced in the bilateral Sylvian fissures, central sulci, parieto-occipital fissures, temporal cortices, and prefrontal cortices (Fig 1). Significantly lower sulcal depth in opioid-exposed fetuses was also found in the bilateral Sylvian fissures, central sulci, parieto-occipital fissures, superior frontal sulci, and temporal sulci (Fig 2).

## DISCUSSION

This prospective, multi-institutional study is one of the first reports of volumetric and morphometric brain parameters on MR imaging of opioid-exposed fetuses. We demonstrate statistically significant lower total brain volumes, CP volumes, and surface areas in the brains of OE fetuses compared with UE controls, even after correcting for potentially confounding variables. We also demonstrate statistically significant decreased mean sulcal depth, cortical mean curvature, and GI in OE fetuses compared with UE controls. Finally, we observed regional predominance of differences in surface area and sulcal depth between the 2 groups in multiple areas of the developing cortex, most notably involving the bilateral perisylvian cortices, perirolandic cortices, and cortices along the parieto-occipital fissures.

Decreased head circumference in infants with prenatal opioid exposure has been well described in the literature, presumed to be a secondary finding of decreased brain volumes.<sup>8,31-33</sup> There is

**Table 1: Description of cohort**

	OE Fetuses (n = 14)	UE Control Fetuses (n = 15)	P Value
Maternal age (yr)	28.5 ± 5.3	28.6 ± 6.5	.93
Gestational age (wk)	31.43 ± 2.34	31.39 ± 2.35	.96
Sex (% male)	62% (9/14)	67% (10/15)	.9
Nicotine exposure	50% (7/14)	6.7% (1/15)	<.01
Other illicit drug exposure <sup>a</sup>	50% (7/14)	6.7% (1/15)	<.01
Site (A/C/N) <sup>b</sup>	4/7/3	5/8/2	NA

<sup>a</sup> Illicit drug exposure inquiries included: marijuana, cocaine, amphetamine or methamphetamine, barbiturates, and benzodiazepines.

<sup>b</sup> A: University of Arkansas for Medical Sciences; C: Cincinnati Children's Hospital Medical Center; N: University of North Carolina at Chapel Hill.

**Table 2: Statistical comparisons of whole brain volume and surface measures between OE and UE control fetuses**

Measures	UE (mean ± SD)	OE (mean ± SD)	t	P Value	Cohen d Effect Size
Brain volume (mm <sup>3</sup> )	196,083 ± 46,338	180,496 ± 41,002	5.22	<.001	0.3555
CP volume (mm <sup>3</sup> )	62,081 ± 20,426	56,797 ± 16,756	4.24	<.001	0.2818
Surface area (mm <sup>2</sup> )	306,930 ± 8147	27,313 ± 7255	5.25	<.001	0.4373
Sulcal depth (mm)	2.152 ± 0.571	1.893 ± 0.517	4.96	<.001	0.4739
Mean curvature	0.145 ± 0.031	0.135 ± 0.031	4.83	<.001	0.3120
GI	1.404 ± 0.160	1.331 ± 0.145	4.41	<.001	0.4801

**Note:**— Positive t: UE > OE.

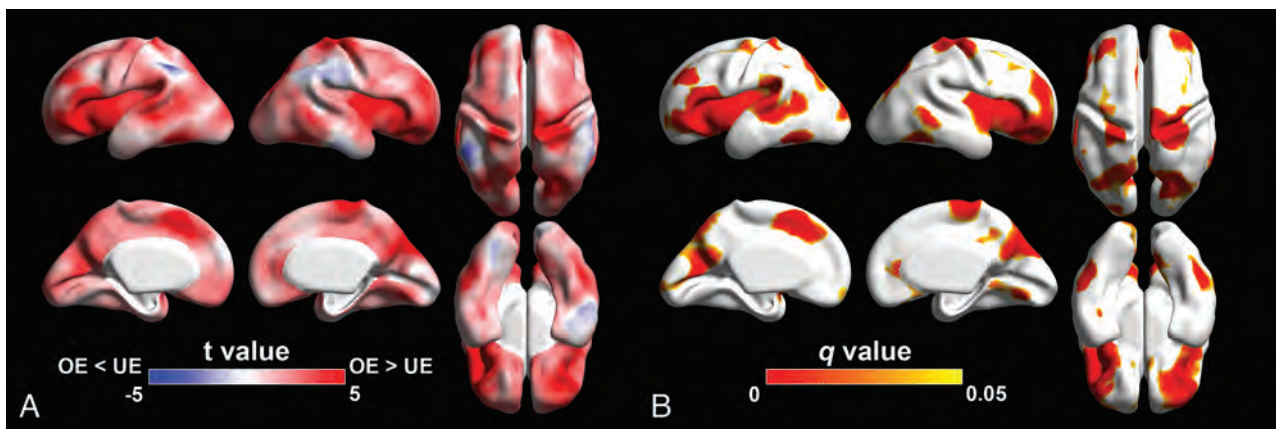


**FIG 1.** Statistical results of the regional analysis of surface area between OE and UE fetuses. *A*, Statistical *t*-map. Red indicates that surface area in OE is smaller than UE fetuses. Blue indicates that surface area in OE is larger than UE fetuses. *B*, FDR *q*-map. Red-yellow indicates regions showing statistically different surface area ( $q < 0.05$ ).

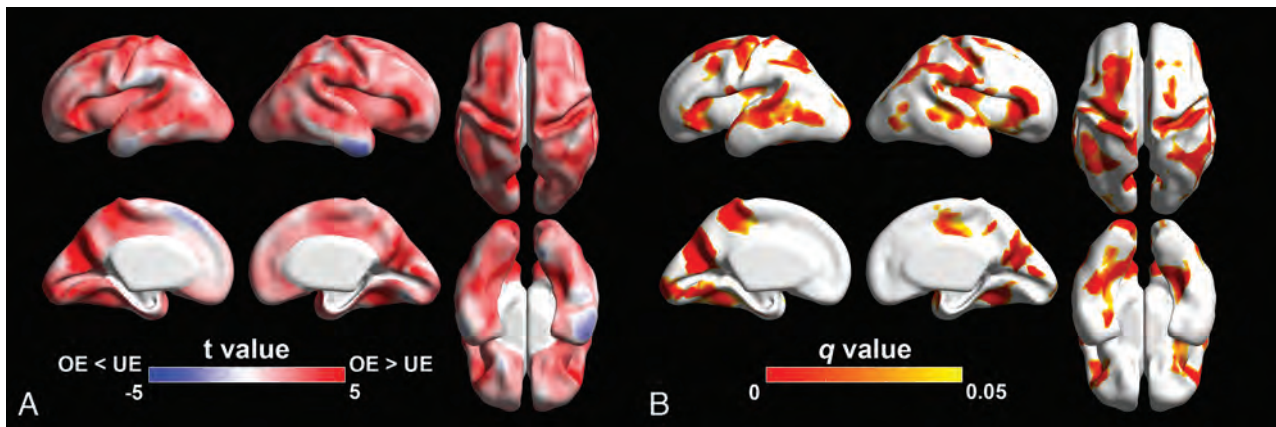


**FIG 2.** Statistical results of the regional analysis of sulcal depth between OE and UE. *A*, Statistical *t*-map. Red indicates that sulcal depth in OE is shallower than UE fetuses. Blue surface area in OE is deeper than UE fetuses. *B*, FDR *q*-map. Red-yellow indicates regions showing statistically different sulcal depth ( $q < 0.05$ ).

also evidence of decreased regional brain volumes on MR imaging in infants with prenatal opioid exposure, particularly involving the deep gray structures.<sup>13,34</sup> Studies extending into the prenatal period are more sparse. In a previous study including this group of patients, we compared multiple 2D measurements of the fetal brains in opioid-exposed fetuses with unexposed controls and found multiple parameters that were lower in the opioid-exposed group.<sup>17</sup> The current study expands on these previous findings by employing advanced MR processing techniques, indicating that 2D measurements used in clinical practice are indeed concordant with volumetric analyses. In addition, the current study adds morphometric data to include lower CP volume and surface area in opioid-exposed fetuses, which has not been previously described. Decreased brain size is a manifestation of a decreased number of neurons, which is presumed to be related at least in part to an abnormality of neuronal proliferation.<sup>35</sup> There is literature demonstrating evidence of impaired neurogenesis, proinflammatory changes, and increased apoptosis in rat models with prenatal opioid exposure, which would in part explain our findings.<sup>36-39</sup>

Our study also adds information on prenatal gyration of the opioid-exposed fetus, which appears to be delayed compared

with unexposed fetuses. The reason for this is less well understood; however, it is believed that the formation of gyri and sulci in the brain is in part a response to the dramatic increase in brain size that occurs during development, the folding of the brain allowing it to fit within the confines of a cranial vault that is small enough to accommodate the birthing process.<sup>40</sup> As such, the impairment in neuronal proliferation may be at least part of the cause of the altered cerebral organization. There is also literature describing evidence of chronic opioid use causing desensitization of opioid receptors in the placenta, which play key roles in modulating neuronal migration and differentiation in the fetus, which may also in part explain differences in gyration.<sup>16</sup> We also observed regional differences in surface area and sulcal depth in multiple functionally critical areas of the developing brain with a predominance in the primary fissures (Sylvian and parieto-occipital) and sulci (central, temporal, and superior frontal), which are some of the first areas of cortical folding we visualize in clinical practice, indicating that structural effects of opioid exposure have already begun early in the second trimester and likely have ongoing or downstream effects on the remaining steps of brain development.<sup>41</sup> The cerebral white

matter microstructure also appears to be altered in infants and children with prenatal opioid exposure, as illustrated in studies examining differences in DTI parameters.<sup>42-45</sup> Because cortical folding is driven in part by regional specialization and developing corticocortical connections, altered folding may be related to differences in DTI metrics observed in neonates. There is even early evidence to suggest that these white matter structural alterations begin in utero when examining fetal DTI parameters.<sup>46</sup> Finally, there are also a number of papers describing alterations in functional connectivity in opioid-exposed infants on resting-state fMRI compared with unexposed infants, which may also be guiding cortical organization.<sup>47-50</sup>

As a result of its multi-institutional nature, we contribute one of the largest cohorts of opioid-exposed fetuses to the existing MR imaging literature. This allowed us to control for multiple potentially confounding variables, including nicotine exposure, fetal sex, high blood pressure, and maternal education. Smaller brain volumes have been documented in fetuses with prenatal nicotine exposure, making it an important confounding variable to control for in this population.<sup>51,52</sup> Differences in brain volumes and growth patterns have also been described on fetal MR imaging between male and female fetuses, making this another important confounding variable to account for.<sup>53,54</sup> Although the existing literature is limited, we also chose to control for patients who reported high blood pressure during pregnancy because there is evidence of neurologic alterations in children born to pre-eclamptic and hypertensive mothers.<sup>55</sup> Finally, we chose to control for maternal education because this has been linked to differences in fetal brain volumes and is associated with other factors affecting fetal brain development including maternal occupation, household income, and material resources.<sup>56</sup>

Our study has a number of limitations. One of the major limitations of this study is that, despite its multi-institutional nature, the overall sample size is relatively small. Another limitation commonly encountered in fetal MR imaging are imaging artifacts, particularly those related to fetal motion. Field inhomogeneity, aliasing, and dielectric effect are other artifacts that compromise image quality. Despite implementation of advanced motion correction techniques, more than one-half of the patients examined had to be excluded for excessive fetal motion in this study. Finally, one of the main limitations of this study relates to the factors potentially associated with both opioid exposure and brain development. Although we controlled for nicotine and polysubstance exposure in our analysis, there may have been other unmeasured factors associated with both opioid exposure and brain development, such as maternal nutrition, stress, and other environmental factors. This highlights the need for future studies in larger patient populations to better isolate these variables and better understand these early findings.

## CONCLUSIONS

This study demonstrates decreased volumes and gyration of the developing fetal brain in fetuses with prenatal opioid exposure compared with unexposed controls by using advanced fetal MR imaging processing techniques. These findings may be related at

least in part to opioids causing impaired neurogenesis in the developing brain; however, given the complexity of human brain development, there are likely multiple underlying mechanisms affected. Fetal MR imaging may prove to be a valuable tool in identifying the effects of opioid exposure in utero and potentially disentangling the impact of postnatal confounding factors. Further studies in larger populations are critical to better understanding these findings.

Disclosure forms provided by the authors are available with the full text and PDF of this article at [www.ajnr.org](http://www.ajnr.org).

## REFERENCES

- Ko JY, D'Angelo DV, Haight SC, et al. **Vital signs: prescription opioid pain reliever use during pregnancy — 34 U.S. Jurisdictions, 2019.** *MMWR Morb Mortal Wkly Rep* 2020;69:897–903 CrossRef Medline
- Desai RJ, Hernandez-Diaz S, Bateman BT, et al. **Increase in prescription opioid use during pregnancy among Medicaid-enrolled women.** *Obstet Gynecol* 2014;123:997–1002 CrossRef Medline
- Bateman BT, Hernandez-Diaz S, Rathmell JP, et al. **Patterns of opioid utilization in pregnancy in a large cohort of commercial insurance beneficiaries in the United States.** *Anesthesiology* 2014;120:1216–24 CrossRef Medline
- Winkelman TN, Villapiano N, Kozhimannil KB, et al. **Incidence and costs of neonatal abstinence syndrome among infants with Medicaid: 2004–2014.** *Pediatrics* 2018;141:e20173520
- Vasan V, Kitase Y, Newville J, et al. **Neonatal opioid exposure: public health crisis and novel neuroinflammatory disease.** *Neural Regen Res* 2021;16:430–32 CrossRef Medline
- Wachman EM, Schiff DM, Silverstein M. **Neonatal abstinence syndrome advances in diagnosis and treatment.** *JAMA* 2018;319:1362–74 CrossRef Medline
- Patrick SW, Dudley J, Martin PR, et al. **Prescription opioid epidemic and infant outcomes.** *Pediatrics* 2015;135:842–50 CrossRef Medline
- Towers CV, Hyatt BW, Visconti KC, et al. **Neonatal head circumference in newborns with neonatal abstinence syndrome.** *Pediatrics* 2019;143:e20180541 CrossRef
- Conradt E, Flannery T, Aschner JL, et al. **Prenatal opioid exposure: neurodevelopmental consequences and future research priorities.** *Pediatrics* 2019;143:e20190128
- Yen E, Davis JM. **The immediate and long-term effects of prenatal opioid exposure.** *Front Pediatr* 2022;10:1039055 CrossRef Medline
- Oei JL, Melhuish E, Uebel H, et al. **Neonatal abstinence syndrome and high school performance.** *Pediatrics* 2017;139:e20162651
- Yeoh SL, Eastwood J, Wright IM, et al. **Cognitive and motor outcomes of children with prenatal opioid exposure: a systematic review and meta-analysis.** *JAMA Netw Open* 2019;2:e197025 CrossRef Medline
- Merhar SL, Kline JE, Braimah A, et al. **Prenatal opioid exposure is associated with smaller brain volumes in multiple regions.** *Pediatr Res* 2021;90:397–402 CrossRef Medline
- Merhar SL, Parikh NA, Braimah A, et al. **White matter injury and structural anomalies in infants with prenatal opioid exposure.** *AJNR Am J Neuroradiol* 2019;40:2161–65 CrossRef Medline
- Merhar SL, Jiang W, Parikh NA, et al. **Effects of prenatal opioid exposure on functional networks in infancy.** *Dev Cogn Neurosci* 2021;51:100996 CrossRef Medline
- Humphries A, Simcox K, Howell B. **A review of the literature: how does prenatal opioid exposure impact placental health and fetal brain development?** *Dev Psychobiol* 2023;65:e22378 CrossRef Medline
- Nagaraj UD, Kline-Fath BM, Zhang B, et al. **MRI findings in third-trimester opioid-exposed fetuses with focus on brain measurements: a prospective multicenter case-control study.** *AJNR Am J Roentgenol* 2022;220:418–27 CrossRef
- Yun HJ, Lee HJ, Lee JY, et al. **Quantification of sulcal emergence timing and its variability in early fetal life: hemispheric asymmetry and sex difference.** *Neuroimage* 2022;263:119629 CrossRef Medline

19. Im K, Guimaraes A, Kim Y, et al. **Quantitative folding pattern analysis of early primary sulci in human fetuses with brain abnormalities.** *AJNR Am J Neuroradiol* 2017;38:1449–55 CrossRef Medline
20. Hong J, Yun HJ, Park G, et al. **Optimal method for fetal brain age prediction using multiplanar slices from structural magnetic resonance imaging.** *Front Neurosci* 2021;15:714252 CrossRef Medline
21. Kuklisova-Murgasova M, Quaghebeur G, Rutherford MA, et al. **Reconstruction of fetal brain MRI with intensity matching and complete outlier removal.** *Med Image Anal* 2012;16:1550–64 CrossRef Medline
22. Hong J, Yun HJ, Park G, et al. **Fetal cortical plate segmentation using fully convolutional networks with multiple plane aggregation.** *Front Neurosci* 2020;14:591683 CrossRef Medline
23. Lepage C, Wagstyl K, Jung B, et al. **CIVET-Macaque: an automated pipeline for MRI-based cortical surface generation and cortical thickness in macaques.** *Neuroimage* 2021;227:117622 CrossRef Medline
24. Liu M, Lepage C, Kim SY, et al. **Robust cortical thickness morphometry of neonatal brain and systematic evaluation using multi-site MRI datasets.** *Front Neurosci* 2021;15:650082 CrossRef Medline
25. Taubin G. Curve and surface smoothing without shrinkage. *Institute of Electrical and Electronics Engineers*. 1995;825–57
26. Boucher M, Whitesides S, Evans A. **Depth potential function for folding pattern representation, registration and analysis.** *Med Image Anal* 2009;13:203–14 CrossRef Medline
27. Yun HJ, Chung AW, Vasung L, et al. **Automatic labeling of cortical sulci for the human fetal brain based on spatio-temporal information of gyrification.** *Neuroimage* 2019;188:473–82 CrossRef Medline
28. Meyer M, Desbrun M, Schröder P, et al. **Discrete differential-geometry operators for triangulated 2-manifolds.** In: Hege HC, Palthier K, eds. *Mathematics and Visualization*. 3rd ed. New York: Springer-Verlag 2003;35–57
29. Yun HJ, Im K, Yang JJ, et al. **Automated sulcal depth measurement on cortical surface reflecting geometrical properties of sulci.** *PLoS One* 2013;8:e55977 CrossRef Medline
30. Zilles K, Armstrong E, Schleicher A, et al. **The human pattern of gyrification in the cerebral cortex.** *Anat Embryol (Berl)* 1988;179:173–79 CrossRef Medline
31. Bier JB, Finger AS, Bier BA, et al. **Growth and developmental outcome of infants with in-utero exposure to methadone vs buprenorphine.** *J Perinatol* 2015;35:656–59 CrossRef Medline
32. Bailey BA, Shah DS, Boynewicz KL, et al. **Impact of in utero opioid exposure on newborn outcomes: beyond neonatal opioid withdrawal syndrome.** *J Matern Fetal Neonatal Med* 2022;35:9383–9390
33. Hudak ML, Makker K. **Fetal opioid exposure and smaller birth head circumference: cause for concern?** *Pediatrics* 2019;143:1–3 CrossRef
34. Sirnes E, Olteidal L, Bartsch H, et al. **Brain morphology in school-aged children with prenatal opioid exposure: a structural MRI study.** *Early Hum Dev* 2017;106:33–39 CrossRef Medline
35. Mochida GH, Walsh CA. **Genetic basis of developmental malformations of the cerebral cortex.** *Arch Neurol* 2004;61:637–40 CrossRef Medline
36. Nasiraei-Moghadam S, Kazeminezhad B, Dargahi L, et al. **Maternal oral consumption of morphine increases Bax/Bcl-2 ratio and caspase 3 activity during early neural system development in rat embryos.** *J Mol Neurosci* 2010;41:156–64 CrossRef Medline
37. Wu PL, Suen JL, Yang CH, et al. **Enhanced H3K4 trimethylation in TNF- $\alpha$  promoter gene locus with cell apoptosis in the ventral-medial striatum following opioid withdrawal of neonatal rat offspring from morphine-addicted mothers.** *Mediators Inflamm* 2021;2021:9828995 CrossRef Medline
38. Mohamed HM, Mahmoud AM. **Chronic exposure to the opioid tramadol induces oxidative damage, inflammation and apoptosis, and alters cerebral monoamine neurotransmitters in rats.** *Biomed Pharmacother* 2019;110:239–47 CrossRef Medline
39. Wu G, Zhao X, Wang F, et al. **Short term exposure to oxycodone alters the survival, proliferation and differentiation of rat embryonic neural stem cell in vitro.** *Brain Res Bull* 2018;143:66–72 CrossRef Medline
40. Stiles J, Jernigan TL. **The basics of brain development.** *Neuropsychol Rev* 2010;20:327–48 CrossRef Medline
41. Nishikuni K, Ribas GC. **Study of fetal and postnatal morphological development of the brain sulci: laboratory investigation.** *J Neurosurg Pediatr* 2013;11:1–11 CrossRef Medline
42. Walhovd KB, Watts R, Amlien I, et al. **Neural tract development of infants born to methadone-maintained mothers.** *Pediatr Neurol* 2012;47:1–6 CrossRef Medline
43. Walhovd KB, Westlye LT, Moe V, et al. **White matter characteristics and cognition in prenatally opiate- and polysubstance-exposed children: a diffusion tensor imaging study.** *AJNR Am J Neuroradiol* 2010;31:894–900 CrossRef Medline
44. Monnelly VJ, Anlagan D, Quigley A, et al. **Prenatal methadone exposure is associated with altered neonatal brain development.** *Neuroimage Clin* 2017;18:9–14 CrossRef Medline
45. Chin EM, Kitase Y, Madurai NK, et al. **In utero methadone exposure permanently alters anatomical and functional connectivity: a pre-clinical evaluation.** *Front Pediatr* 2023;11:1139378 CrossRef Medline
46. Dudley JA, Nagaraj UD, Merhar S, et al. **DTI of opioid-exposed fetuses using ComBat harmonization: a bi-institutional study.** *AJNR Am J Neuroradiol* 2023;44:1084–89 CrossRef Medline
47. Vishnubhotla RV, Zhao Y, Wen Q, et al. **Brain structural connectome in neonates with prenatal opioid exposure.** *Front Neurosci* 2022;16:952322 CrossRef Medline
48. Radhakrishnan R, Vishnubhotla RV, Guckien Z, et al. **Thalamocortical functional connectivity in infants with prenatal opioid exposure correlates with severity of neonatal opioid withdrawal syndrome.** *Neuroradiology* 2022;64:1649–59 CrossRef Medline
49. Radhakrishnan R, Vishnubhotla RV, Zhao Y, et al. **Global brain functional network connectivity in infants with prenatal opioid exposure.** *Front Pediatr* 2022;10:847037 CrossRef Medline
50. Radhakrishnan R, Elsaid NM, Sadhasivam S, et al. **Resting state functional MRI in infants with prenatal opioid exposure: a pilot study.** *Neuroradiology* 2021;63:585–91 CrossRef Medline
51. Anlagan D, Jones NW, Costigan C, et al. **Maternal smoking during pregnancy and fetal organ growth: a magnetic resonance imaging study.** *PLoS One* 2013;8:e67223 CrossRef Medline
52. Roza SJ, Verburg BO, Jaddoe VW, et al. **Effects of maternal smoking in pregnancy on prenatal brain development: the generation R study.** *Eur J Neurosci* 2007;25:611–17 CrossRef Medline
53. Machado-Rivas F, Gandhi J, Choi JJ, et al. **Normal growth, sexual dimorphism, and lateral asymmetries at fetal brain MRI.** *Radiology* 2022;303:162–70 CrossRef Medline
54. Griffiths PD, Jarvis D, Mooney C, et al. **Sex differences in fetal intracranial volumes assessed by in utero MR imaging.** *Biol Sex Differ* 2023;14:13 CrossRef Medline
55. Figueiró-Filho EA, Mak LE, Reynolds JN, et al. **Neurological function in children born to preeclamptic and hypertensive mothers: a systematic review.** *Pregnancy Hypertens* 2017;10:1–6 CrossRef Medline
56. Lu YC, Kapse K, Andersen N, et al. **Association between socioeconomic status and in utero fetal brain development.** *JAMA Netw Open* 2021;4:e213526 CrossRef Medline

# White Matter Injury on Early-versus-Term-Equivalent Age Brain MRI in Infants Born Preterm

 Sriya Roychaudhuri,  Gabriel Côté-Corriveau,  Carmina Erdei, and Terrie E. Inder

## ABSTRACT

**BACKGROUND AND PURPOSE:** White matter injury in infants born preterm is associated with adverse neurodevelopmental outcomes, depending on the extent and location. White matter injury can be visualized with MR imaging in the initial weeks following preterm birth but is more commonly defined at term-equivalent-age MR imaging. Our aim was to see how white matter injury detection in MR imaging compares between the 2 time points.

**MATERIALS AND METHODS:** This study compared white matter injury on early brain MR imaging (30–34 weeks' postmenstrual age) with white matter injury assessment at term-equivalent (37–42 weeks) MR imaging, using 2 previously published and standardized scoring systems, in a cohort of 30 preterm infants born at <33 weeks' gestational age.

**RESULTS:** There was a strong association between the systematic assessments of white matter injury at the 2 time points ( $P = .007$ ) and the global injury severity ( $P < .001$ ).

**CONCLUSIONS:** Although the optimal timing to undertake neuroimaging in the preterm infant remains to be determined, both early (30–34 weeks) and term-equivalent MR imaging provide valuable information on white matter injury and the risk of associated sequelae.

**ABBREVIATIONS:** CUS = cranial ultrasound; IVH = intraventricular hemorrhage; NICU = neonatal intensive care unit; PMA = postmenstrual age; TEA = term-equivalent age; WMI = white matter injury

White matter injury (WMI) in the preterm infant is common and associated with adverse neurodevelopmental outcomes.<sup>1,2</sup> It remains the most prevalent form of brain injury in the vulnerable, developing brain, with the highest risk for those infants born between 23 and 32 weeks' gestational age.<sup>3</sup> While severe cystic WMI is seen in <5% of infants born at <32 weeks' gestational age, focal necroses appearing as punctate white matter lesions in MR imaging are seen in 15%–25% of infants born at <28 weeks, and up to one-half of them may have diffuse lesions with gliosis, which results in subsequent white matter volume loss.<sup>3</sup> Cranial sonography (CUS) is the most widely used and readily available neuroimaging technique in the neonatal intensive care unit (NICU). It is particularly useful and sensitive for

the detection of intraventricular hemorrhage and its short-term sequelae such as ventriculomegaly. CUS is also able to detect more severe white matter lesions such as cystic periventricular leukomalacia. However, it has limited sensitivity to detect focal, punctate WMI, or diffuse WMI.<sup>4</sup> Term-equivalent age (TEA) (37–42 weeks) MR imaging has been shown to have greater sensitivity than CUS for diffuse WMI and punctate white matter lesions or their sequelae such as white matter volume loss.<sup>4–6</sup> Early MR imaging, often performed between 30 and 34 weeks' postmenstrual age (PMA), appears to be most sensitive for the direct visualization of the extent and nature of WMI.<sup>7</sup> These early lesions are subsequently replaced by microglia and astroglia and evolve into cystic spaces or glial tissue, often becoming less conspicuous with time.<sup>6,7</sup> WMI may result in white matter volume loss with a secondary dysmaturational impact leading to reductions in deep and cortical gray matter volume.<sup>3</sup> These secondary dysmaturational impacts of WMI may be best visualized at TEA.<sup>8,9</sup>

Systematic MR imaging scoring methods to assess the extent of WMI have been proposed for both early and TEA times.<sup>5,7</sup> Although there are similar elements in both scoring systems, early MR imaging interpretation focuses primarily on characterization of the lesions of WMI,<sup>7</sup> whereas TEA scores capture WMI

Received September 7, 2023; accepted after revision November 15.

From the Department of Pediatrics (S.R., G.C.-C., C.E., T.E.I.), Brigham and Women's Hospital, Boston, Massachusetts; Department of Pediatrics (G.C.-C.), Sainte-Justine University Hospital Center, Montreal, Quebec, Canada; Harvard Medical School (C.E., T.E.I.), Boston, Massachusetts; and Division of Neonatology (T.E.I.), Department of Pediatrics, Children's Hospital of Orange County, University of California, Irvine, Irvine, California.

Please address correspondence to Terrie E. Inder MB, ChB, MD, Children's Hospital of Orange County, University of California, Irvine, 1201 W. La Veta Ave, Orange, CA 92868; e-mail: terrie.inder@choc.org; @SriyaRC\_twtr

<http://dx.doi.org/10.3174/ajnr.A8105>

sequelae such as cystic lesions, signal abnormalities, delayed myelination, and white matter volume loss.<sup>5</sup> There is no current consensus on the best timing and use of MR imaging in the preterm population, but there is growing evidence that neonatal brain MR imaging offers information that most clearly delineates brain injury with implications for rehabilitation.<sup>10</sup> Thus, the aim of this study was to examine early and TEA brain MRIs in the same cohort of infants born at <33 weeks' gestational age using 2 standardized scoring systems and to assess how WMI and overall scores compared between the 2 time points.

## MATERIALS AND METHODS

### Study Population

Participants of the study were enrolled from Brigham and Women's Hospital, a 66-bed level 3 NICU within a single academic institution in Boston, Massachusetts. From September 2020 to October 2022, we recruited preterm infants born at <33 weeks' gestational age with no congenital anomaly and no congenital infections. The study was approved by the Mass General Brigham Institutional Review Board, and parents of each participant provided written informed consent.

### Brain MR Imaging Acquisition and Scoring

Brain MR imaging was performed at an early time point (30–34 weeks' PMA), and at TEA (37–42 weeks PMA)<sup>5</sup> for all study participants. Infants were imaged after feeding and swaddling, without any sedation. The MR imaging performed at both time points was clearly interpretable with minimal or no artifacts, including those due to motion.

Early MR images were obtained in a 1T in-NICU Embrace MRI system (Aspect). Our team previously described the feasibility of obtaining imaging in hospitalized infants using an in-NICU scanner<sup>11</sup> in our setting. MR imaging included anatomic T1- and T2-weighted imaging and diffusion-weighted sequences. The acquisition parameters for the sequences in this system were T1-weighted fast spin-echo (section thickness = 3–4 mm, TR = 600 ms, TE = 12 ms), T1-weighted 3D gradient-echo (TR = 20 ms, TE = 3.5 ms, section thickness = 1 mm), T2-weighted fast spin-echo (TR = 10–13 seconds, TE = 130–150 ms, section thickness = 3–4 mm), and diffusion-weighted TSE imaging (TR = 14 seconds, TE = 125 ms, section thickness = 3–4 mm, diffusion b-value = 1000). The TEA MR images were acquired using a 3T scanner (Siemens). Sequences included T1-weighted sequences (isotropic voxel size = 1 mm<sup>3</sup>, TR = 2540 ms, TE = 3.4 ms, TI = 1450 ms), T2-weighted (isotropic voxel = 1 mm<sup>3</sup>, TR = 16 seconds, TE = 136 ms), and diffusion-weighted sequences (isotropic voxel size = 2 mm<sup>3</sup>, 104 diffusion directions [10, 30, and 64 directions at b=500, 1000, and 2500 s/mm<sup>2</sup>, respectively], TE = 71 ms, TR = 3.5 seconds).

Because previous studies have reported reassuring developmental outcomes in infants with normal-mild WMI,<sup>6</sup> we aimed to assess the consistency of 2 broad categories of normal-mild and moderate-severe WMI (and global brain injury) as assessed by scoring systems applied to early and TEA MRIs. The scoring system elaborated by Miller et al<sup>7</sup> was used for categorization of WMI as well as global brain injury on early MR imaging. This score has been shown to have robust interrater reliability along with prognostic utility on follow-up.<sup>7</sup> The severity of WMI is

classified as normal (no white matter lesions), minimal ( $\leq 3$  areas of T1 signal abnormality, each measuring  $< 2$  mm), moderate ( $> 3$  areas of T1 signal abnormality or these areas measuring  $> 2$  mm, but  $< 5\%$  of the hemisphere involved), or severe ( $> 5\%$  of the hemisphere involved). To define 5% of a hemisphere, the image in which the echogenicity is most clearly appreciated is selected and the ipsilateral hemisphere is divided into 5 equal pie-like segments. A  $> 5\%$  involvement would entail an echogenicity size of more than one-fourth of a single segment. An overall severity score considers the presence and degree of intraventricular hemorrhage (IVH) and ventriculomegaly in addition to WMI. The global moderate-to-severe category includes moderate-or-severe white matter injury, any ventriculomegaly (defined as a ventricular diameter of  $> 8$  mm), or severe IVH (grade  $\geq 3$  per the Papile classification).<sup>12</sup> The rest were considered normal or having mild degrees of injury. Cerebellar hemorrhage is not formally included in the score; however, we documented its presence.

TEA MRIs were interpreted using the score of Kidokoro et al.<sup>5</sup> As our objective was to examine how early detection of WMI was related to a systematic assessment of its sequelae at TEA, we considered the WMI score as well as the global assessment score. WMI is categorized into 4 grades defined as no WMI, mild, moderate, or severe WMI. Five variables are assessed to assign a score for WMI: 1) cystic degeneration, 2) focal signal abnormalities, 3) delayed myelination, 4) dilated lateral ventricles (a ventricular diameter of  $> 7.5$  mm is considered relevant, and  $> 10$  mm, severe), and 5) reduction of WM volume. Other than WM, scores are assigned for regional injury pertaining to cortical gray matter, deep gray matter, and the cerebellum. A global score of brain injury is assigned by summing all the regional subscores. Four categories of injury are possible: normal, mild, moderate, and severe.

MRIs were interpreted and reported by board-certified neuro-radiologists and scored by research clinicians (S.R., G.C.-C.) proficient in neonatal brain MRIs and the use of the 2 scores. Any divergence was discussed with the experts (T.E.I., C.E.) on the project. CUS, performed routinely during NICU stay, and the "worst result" sonography from day 7 to 1-month PMA were noted.

### Clinical Data Collection

Demographic and clinical characteristics of all participants were collected from the electronic medical record. Data from CUS, which was performed routinely during the NICU stay, were also gathered to document the highest grades of IVH, WMI, and cerebellar hemorrhage.

### Data Analysis

We reported descriptive statistics as means (SD), medians (range), and proportions. We first compared early and TEA MR imaging scores using contingency tables to perform  $\chi^2$  tests. Because some categories included very small numbers, we dichotomized the severity categories (normal-to-mild versus moderate-to-severe) and performed Fisher exact tests to assess the relationship between early and TEA classifications. We further examined the evolution of the 4 WMI severity categories from early to TEA MRIs graphically. All analyses were performed in SPSS Statistics, Version 28.0 (IBM), and *P* values  $< .05$  were considered statistically significant.

## RESULTS

The cohort consisted of 30 infants, 16 males (53.3%) (Table 1) with a mean gestational age of 28.7 weeks and a median birth-weight of 1220 g. All participants were assessed by CUS as per unit protocol, and all participants had satisfactory MR imaging findings at both early and TEA time points. The early MRIs were performed at an average of 33.0 (SD, 1.4) weeks, and the TEA MRIs, at 38.6 (SD, 1.4) weeks' PMA.

Routine clinical CUS identified 5 cases of IVH with dilation (16.7%), 3 infants with cerebellar hemorrhages (10.0%), and 5 with WMI (16.7%). Overall, CUS identified 7 cases with moderate-to-severe injury on global assessment, while early MR imaging identified 11 such infants. MR imaging detected more WMI than CUS (8 versus 5 cases with moderate-severe degrees). Comparison of systematic assessments of early and term MR imaging is shown in Tables 2 and 3. On early MR imaging, 8 infants had moderate-to-severe WMI (26.6%), and 11 met the criteria for moderate-to-severe injury on global assessment (36.7%). By TEA, there were 10 infants with moderate-to-severe WMI (33.3%) and 11 with moderate-to-severe scores for global assessment (36.7%). There was a strong association between the early and TEA WMI severity classifications ( $P = .007$ ); 81.8% of infants with normal-to-minimal WMI on early MR imaging had a normal-to-mild WMI score at TEA, while 75.0% of infants with early moderate-to-severe WMI remained in the moderate-to-severe WMI risk category at TEA. The relationship between the 2 assessment time points was even stronger when considering the global severity score ( $P < .001$ ); 94.7% of infants remained in the normal-to-mild overall risk category from early to TEA assessments, and 90.1% remained in the moderate-to-severe overall risk category.

When we further examined the sequential assessments of WMI, it appeared that the early WMI scoring predominantly focused on delineating WM lesions themselves, whereas the TEA WMI scoring accounted for the consequences of WMI, even

when WM lesions may have themselves become less appreciable (Fig 1). The DWI sequences showed restricted diffusion in 2 cases (of the 30) in the early-acquired MR imaging. Because diffusion restriction is expected in only the acute stages of injury, subsequent imaging at TEA showed normalization of diffusion as an expected evolution. There was no instance of newly detected WMI or increased lesion severity noted on TEA compared with early MR imaging.

The detailed categorization of WMI severity remained overall stable from early-to-TEA MRIs (Fig 2). Most of the 21 infants with no identified WMI on early MR imaging remained in the normal category at TEA (61.9%), and none were diagnosed with severe WMI. Of these 21 infants, 8 were, however, diagnosed with mild (19.0%) or moderate (19.0%) WMI at TEA. Similarly, most of the 7 infants with early severe WMI remained in the severe category at TEA (71.4%), and none had a normal score. Two infants fell in the remaining severity categories, with some overlap.

## DISCUSSION

The application of MR imaging in the preterm infant to evaluate brain injury using systematic scoring systems enables clinicians to analyze images in a systematic manner. A comparison between the 2 commonly used scoring systems for WMI in the preterm infant that are used at differing time points has not been undertaken. In our cohort of 30 preterm infants, early MR imaging detected WMI effectively and correlated highly with the scoring system at TEA that included the sequelae of WMI (Fig 2). The exceptions, those who had TEA scores of higher WMI severity than their corresponding early severity categories, had high grades of IVH, which accounted for the higher TEA score, but no visualized WMI on their early scans. Moreover, the excellent correlation between the global assessment of injury at the 2 time points suggests that MR imaging performed either early or at TEA has prognostic relevance. Individual units may choose to decide the optimal time of imaging according to the availability of resources and the clinical course of the infant. While early imaging may be crucial to inform the next steps, TEA MR imaging exemplifies consequences and evolution of injury in the developing brain. Several mechanisms resulting in dysmaturity of WM with reduced brain

**Table 1: Characteristics of the study participants**

Study Participants (n = 30)	
Gestational age (mean) (SD) (wk)	28.7 (2.8)
Male sex (No.) (%)	16 (53.3)
Twin birth (No.) (%)	6 (20.0)
Cesarean delivery (No.) (%)	16 (53.3)
Birth weight (median) (range) (g)	1220 (515–1930)
Birth weight z score (mean) (SD)	0.23 (0.98)
Head circumference at birth (median) (range) (cm)	26 (20–31)
Head circumference z score at birth (mean) (SD)	0.07 (1.06)

**Table 2: WMI on early-versus-TEA MR imaging**

		WMI Severity on TEA MR Imaging	
		Normal-Mild (n = 20)	Moderate-Severe (n = 10)
WMI severity on early MR imaging	Normal-Minimal (n = 22)	18	4
	Moderate-Severe (n = 8)	2	6

**Table 3: Global assessments on early-versus-TEA MR imaging**

		Global Severity on TEA MR Imaging	
		Normal-Mild (n = 19)	Moderate-Severe (n = 11)
Global severity on early MR imaging	Normal-Mild (n = 19)	18	1
	Moderate-Severe (n = 11)	1	10

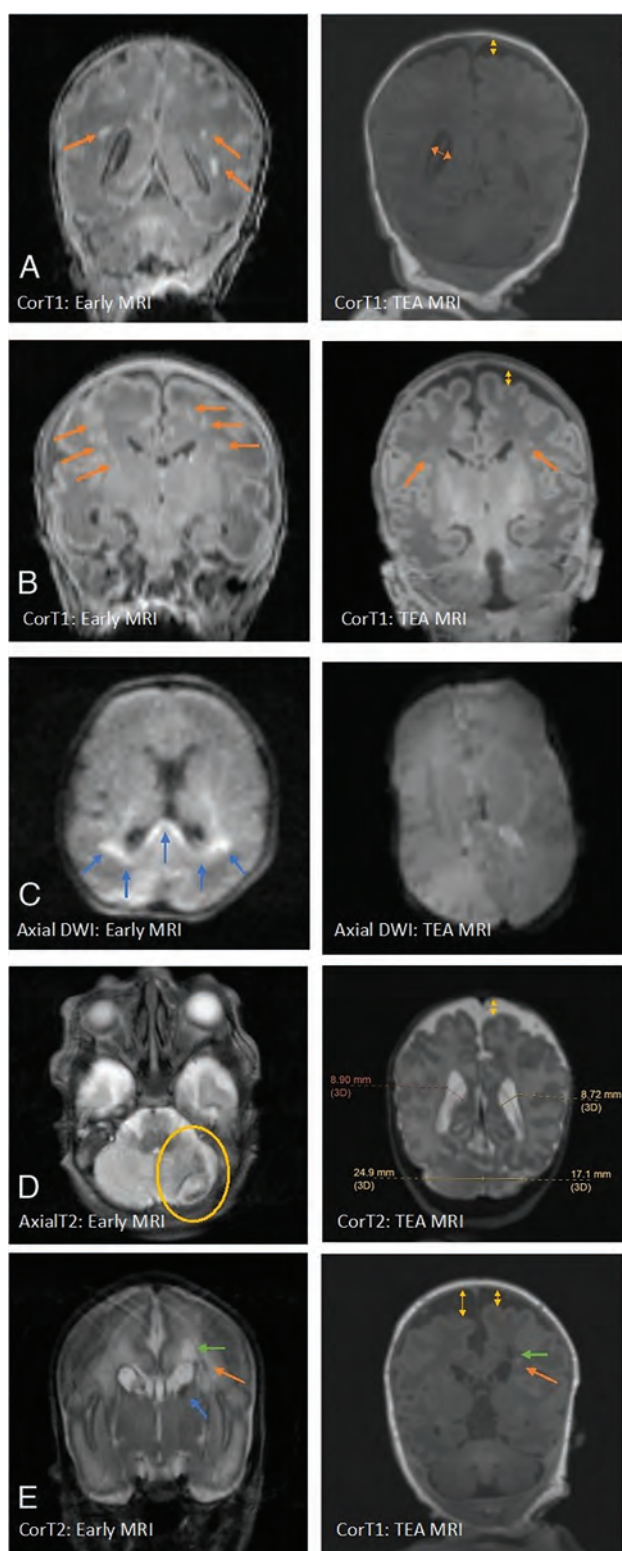


**FIG 1.** WMI as appreciated in early (IT scanner) versus TEA MR imaging (3T scanner) in different cases. **A**, The image on the left shows an early MR imaging and the extent of WMI (orange arrows) and its evolution at TEA (image on the right) in which there is an absence of visible WM lesions. WMI sequelae can be appreciated as volume loss, with arrows indicating a dilated ventricle and enlarged subarachnoid space (yellow arrow). **B**, Early T1 images show severe WMI (orange arrows) with reduced conspicuity at TEA but with some volume loss. **C**, Early MR imaging at day 3 of life shows diffusion restriction in WM

volumes, reflected in TEA MR imaging, as a sequela to IVH have been described in the literature.<sup>3,8</sup> The global severity scores, which considered IVH and posthemorrhagic ventricular dilation, were highly correlated. Two infants differed in their severity categories between the early and TEA assessments, one of whom had an isolated, severe cerebellar hemorrhage, which categorized the infant as having moderate injury in the TEA score, but not according to the early score because cerebellar hemorrhage is not included in the scoring system of Miller et al.<sup>7</sup>

A single infant in our cohort had parenchymal echogenicity detected by sonography, which was not appreciated in the early MR imaging. The gestational age at birth for this infant was 25 weeks 6 days and the echogenicity in the CUS persisted up to the third week of life. The early MR imaging performed at 32 weeks' PMA (7 weeks of life) detected sequelae of IVH but not WMI. The TEA WMI score suggested moderate injury. Thus, an MR imaging at 30–34 weeks might not be early enough when considering infants of extremely low gestational ages who have sustained WMI early. The ideal definition of “early” in terms of PMA remains to be determined, with consideration for the feasibility of early imaging at low gestational ages when very preterm infants are likely to experience considerable clinical instability, and families, increased stress. Especially considering research involving early imaging, parents need some additional time to be approached for discussions.

It is also useful to consider that the timing around which the pre-oligodendrocytes are most vulnerable to injury is around 28 weeks' gestation, resulting in the peak of WMI.<sup>3</sup> Imaging in the first 2 weeks after birth may thus appear to be a reasonable goal in terms of balancing clinical stability and capturing early injury.<sup>13</sup> Repeat imaging may be considered if there are concerns of subsequent WMI due to the NICU course. Early detection of injury would offer an opportunity for higher-intensity and targeted developmental interventions for the high-risk preterm infants and would give essential information regarding evolving neuropathology and research.<sup>14</sup>

The limitations of this study must be considered, including a small sample size and a low number of cases, particularly in the higher severity categories. The cohort, however, is temporally close and from the same NICU; thus, there is homogeneity in extraneous and possibly confounding factors affecting brain growth and maturation, like nutritional management<sup>15</sup> and other aspects of the NICU environment.<sup>16</sup> All infants received developmental support available in the NICU from parents, nurses, and allied health professionals, including occupational and physiotherapy.

The scoring systems used at both time points, though providing systematic approaches that have been used in clinical and research settings, are not validated across large populations and with long-term outcomes. The MRIs at the 2 time points have been obtained using different MR imaging systems (1T versus 3T

(blue arrows), which has resolved at TEA. **D**, Isolated unilateral cerebellar hemorrhage (encircled in yellow) with eventual disparity in cerebellar hemispheric sizes and bilateral cerebral WM volume loss at TEA. **E**, Early IVH (blue arrow) with dilation resulting in periventricular WMI (orange arrows) with cyst formation (green arrows) and volume loss (yellow arrows) at TEA.



**FIG 2.** Evolution of WMI severity categories from early to TEA MRI. The thickness of arrows is proportional to the number of cases.

systems). Our team routinely uses the 1T in-NICU MR imaging system for clinical and research scans. The 1T system is equipped for standard sequence acquisition, including T1- and T2-weighted imaging and diffusion-weighted imaging but not for spectroscopy, vascular, and tensor imaging. Although appreciation of subtle structural abnormalities may be different in a system with a weaker magnet, our data show that >90% of MRIs performed in the 1T system do not require follow-up imaging in a 3T unit for this purpose.<sup>11</sup> In our study, the lesions visualized in the early scans acquired with the 1T system were less appreciated at TEA due to expected temporal evolution of the lesions.<sup>7</sup> Most important, there did not appear to be lesions that were missed on the 1T system.

## CONCLUSIONS

Brain MR imaging in infants born preterm can accurately define brain injury, particularly WMI. Although the optimal timing to image the neonate brain remains to be determined, both early (30–34 weeks) and TEA MR imaging appear independently sensitive for WMI and especially for global assessment of injury when analyzed with systematic assessment tools. Early MR imaging should be considered in this vulnerable cohort, and performing imaging in the first 2 weeks of life may be a reasonable goal, depending on the gestational age at birth, clinical stability, and family circumstances. While earlier imaging may capture WM lesions that later resolve yet remain of clinical relevance, TEA MR imaging may offer insight into the consequences of WMI on the developing brain. How information from each time point may be best used and may potentially guide implementation of early intervention measures should be further studied.

Disclosure forms provided by the authors are available with the full text and PDF of this article at [www.ajnr.org](http://www.ajnr.org).

## REFERENCES

1. Rees P, Callan C, Chadda KR, et al. **Preterm brain injury and neurodevelopmental outcomes: a meta-analysis.** *Pediatrics* 2022;150:e2022057442 CrossRef Medline
2. Novak I, Morgan C, Adde L, et al. **Early, accurate diagnosis and early intervention in cerebral palsy: advances in diagnosis and treatment.** *JAMA Pediatr* 2017;171:897–907 CrossRef Medline
3. Inder TE, Volpe JJ, Anderson PJ. **Defining the neurologic consequences of preterm birth.** *N Engl J Med* 2023;389:441–53 CrossRef Medline
4. de Bruïne FT, van Wezel-Meijler G. **Radiological assessment of white matter injury in very preterm infants.** *Imaging Med* 2012;4:541–50 CrossRef
5. Kidokoro H, Neil JJ, Inder TE. **New MR imaging assessment tool to define brain abnormalities in very preterm infants at term.** *AJNR Am J Neuroradiol* 2013;34:2208–14 CrossRef Medline
6. Woodward LJ, Anderson PJ, Austin NC, et al. **Neonatal MRI to predict neurodevelopmental outcomes in preterm infants.** *N Engl J Med* 2006;355:685–94 CrossRef Medline
7. Miller SP, Ferriero DM, Leonard C, et al. **Early brain injury in premature newborns detected with magnetic resonance imaging is associated with adverse early neurodevelopmental outcome.** *J Pediatr* 2005;147:609–16 CrossRef Medline
8. Ballabh P, de Vries LS. **White matter injury in infants with intraventricular haemorrhage: mechanisms and therapies.** *Nat Rev Neurol* 2021;17:199–214 CrossRef Medline
9. Kidokoro H, Anderson PJ, Doyle LW, et al. **Brain injury and altered brain growth in preterm infants: predictors and prognosis.** *Pediatrics* 2014;134:e444–53 CrossRef Medline
10. Inder TE, de Vries LS, Ferriero DM, et al. **Neuroimaging of the preterm brain: review and recommendations.** *J Pediatr* 2021;237:276–87.e4 CrossRef Medline
11. Thiim KR, Singh E, Mukundan S, et al. **Clinical experience with an in-NICU magnetic resonance imaging system.** *J Perinatol* 2022;42:873–79 CrossRef Medline
12. Papile LA, Burstein J, Burstein R, et al. **Incidence and evolution of subependymal and intraventricular hemorrhage: a study of infants with birth weights less than 1,500 gm.** *J Pediatr* 1978;92:529–34 CrossRef Medline
13. Plaisier A, Govaert P, Lequin MH, et al. **Optimal timing of cerebral MRI in preterm infants to predict long-term neurodevelopmental outcome: a systematic review.** *AJNR Am J Neuroradiol* 2014;35:841–47 CrossRef Medline
14. Pineda R, Smith J, Roussin J, et al. **Randomized clinical trial investigating the effect of consistent, developmentally-appropriate, and evidence-based multisensory exposures in the NICU.** *J Perinatol* 2021;41:2449–62 CrossRef Medline
15. Bell KA, Cherkerzian S, Drouin K, et al. **Associations of macronutrient intake determined by point-of-care human milk analysis with brain development among very preterm infants.** *Children (Basel)* 2022;9:969 CrossRef Medline
16. Pineda RG, Neil J, Dierker D, et al. **Alterations in brain structure and neurodevelopmental outcome in preterm infants hospitalized in different neonatal intensive care unit environments.** *J Pediatr* 2014;164:52–60.e2 CrossRef Medline

# Clinical and Imaging Findings in Children with Myelin Oligodendrocyte Glycoprotein Antibody Associated Disease (MOGAD): From Presentation to Relapse

Elizabeth George, Jeffrey B. Russ, Alexandria Validighi, Heather Early, Mark D. Mamlouk, Orit A. Glenn, Carla M. Francisco, Emmanuelle Waubant, Camilla Lindan, and Yi Li



## ABSTRACT

**BACKGROUND AND PURPOSE:** Myelin oligodendrocyte glycoprotein-antibody associated disease (MOGAD) is an increasingly recognized cause of demyelinating disease in children. The purpose of this study is to characterize the CNS imaging manifestations of pediatric MOGAD and identify clinical and imaging variables associated with relapse.

**MATERIALS AND METHODS:** We retrospectively identified children with serum antibody-positive MOGAD evaluated at our institution between 1997 and 2020. Clinical and demographic data were collected. MRIs of the brain, orbit, and spine at presentation and relapse were reviewed for location and pattern of abnormality.

**RESULTS:** Among 61 cases (34 girls), mean age at presentation was 7 years (IQR 4–11). At presentation, there was imaging involvement of the brain in 78.6% (44/56), optic pathway in 55.4% (31/56), and spine in 19.6% (11/56). Brain involvement was commonly in the frontal (70.5%, 31/44) and subcortical (75%, 33/44) white matter, with involvement of the thalamus and pons in 47.7% each (21/44). Optic neuritis (ON) was commonly bilateral (80.6%, 25/31) involving intraorbital segments (77.4%, 24/31). Spinal cord lesions were typically cervical (72.7%, 8/11) and multifocal (72.7%, 8/11).

The imaging patterns were age-dependent; children  $\leq 9$  years more commonly demonstrated ADEM-like imaging pattern at presentation (39.4%, 13/33) and first relapse (8/23, 34.8%), while children  $> 9$  years more commonly had ON at presentation (34.8%, 8/23,  $P = .001$ ) and FLAIR-hyperintense lesions in anti-MOG-associated encephalitis with seizures at first relapse (5/18, 27.8%,  $P = .008$ ).

**CONCLUSIONS:** We describe the CNS imaging findings in pediatric MOGAD. The imaging pattern is age-dependent at presentation and first relapse. Younger age at presentation is associated with longer time to relapse.

**ABBREVIATIONS:** ADEM = acute disseminated encephalomyelitis; DGN = deep gray nuclei; FLAMES = FLAIR-hyperintense lesions in anti-MOG-associated encephalitis with seizures; MOG = myelin oligodendrocyte glycoprotein; MOGAD = MOG-antibody associated disease; NMOSD = neuromyelitis optica spectrum disorder; ON = optic neuritis

Since myelin oligodendrocyte glycoprotein (MOG) was identified as a target antigen in acute disseminated encephalomyelitis (ADEM),<sup>1</sup> MOG-antibody associated disease (MOGAD) is increasingly recognized as a major cause of demyelinating disease in children and adults.<sup>2–4</sup> MOGAD has a distinct clinical course and management<sup>5,6</sup>

compared with other demyelinating diseases, such as multiple sclerosis and neuromyelitis spectrum disorders (NMOSD), and the ability to prospectively suspect MOGAD based on initial clinical manifestations and imaging phenotype<sup>7,8</sup> would allow for targeted antibody testing and prompt treatment.

While MOGAD has an overall better clinical course compared with NMOSD, a certain proportion of patients will develop relapsing disease (28%–62%)<sup>4,7,9–11</sup> with long-term neurologic sequelae.<sup>12</sup>

Additionally, pediatric patients manifest differently compared with adult patients,<sup>13</sup> and the spectrum of MOGAD is still being defined in the pediatric population, with only a few prior small studies<sup>11,13–17</sup> and recently proposed diagnostic criteria.<sup>18</sup> There is currently limited imaging description at the time of diagnosis and relapse.

The purpose of this study is to comprehensively characterize the brain, orbit, and spine imaging manifestations of pediatric

Received June 29, 2023; accepted after revision November 7.

From the Departments of Radiology and Biomedical Imaging (E.G., O.A.G., C.L., Y.L.), and Neurology (C.M.F., E.W.), Division of Child Neurology (A.V.), University of California San Francisco, San Francisco, California; Department of Pediatrics (J.B.R.), Division of Neurology, Duke University, Durham, North Carolina; Department of Radiology (H.E.), University of Texas Southwestern, Dallas, Texas; and Permanente Medical Group (M.D.M.), Kaiser Permanente Medical Center Santa Clara, Santa Clara, California.

Please address correspondence to Elizabeth George, MBBS, Department of Radiology and Biomedical Imaging, University of California San Francisco, 505 Parnassus Ave, San Francisco, CA 94143; e-mail: Elizabeth.george@ucsf.edu; @LizzRad



Indicates article with online supplemental data.

<http://dx.doi.org/10.3174/ajnr.A8089>

MOGAD at presentation and relapse in a large institutional cohort of seropositive MOGAD, and to identify clinical and imaging variables associated with a relapsing phenotype.

## MATERIALS AND METHODS

Patients were identified retrospectively from the University of California San Francisco pediatric neuroimmunology clinic database, which includes all patients seen between 1997 and 2020. Patients were eligible for inclusion if they had clinical evidence of a noninfectious neuroinflammatory syndrome, at least 1 serologic anti-MOG titer of 1:20 or greater by using a cell-based assay (Mayo Clinic) either while acutely symptomatic or on a banked study serum sample (particularly for patients included in the cohort before routine anti-MOG antibody testing), had clinical exclusion of reasonable alternative diagnoses, and MR imaging available at presentation or at any of the first 2 relapses (Online Supplemental Data). This study was conducted with approval by the Institutional Review Board and in compliance with all policies on the responsible conduct of human research. The need for informed consent was waived. Some of the clinical and CSF analysis of this cohort has been reported previously.<sup>19</sup>

### Clinical and Laboratory Data

Clinical data were collected via retrospective chart review and included clinical features that were documented by a pediatric neurologist who either directly cared for the patient during the initial presentation or who subsequently followed the patient on an outpatient basis. In nearly all cases, relapse was defined as a distinct recurrence of symptomatology following a period of symptom resolution for an interval of at least 2 weeks, which was also confirmed radiographically. In a minority of cases, episodes were still felt to qualify as clinical relapse if based on high clinical suspicion by a trained neuroimmunologist or pediatric neurologist, even in the absence of radiographic confirmation. We collected clinical data from the initial presentation and up to 2 relapses, including age, time to relapse, clinical symptoms, and serum anti-MOG and anti-AQP4 titers either at presentation or on a banked specimen. MOG-IgG testing with a cell-based assay (Mayo Clinic) was done on clinical samples after 2017 when the test became commercially available and on banked research samples for samples collected before 2017. The total number of clinical relapses, up to 10, and total length of follow-up were documented.

### Imaging

All clinical MRIs of the brain, orbit, and spine within 3 months of initial presentation and relapse available in our institutional PACS were reviewed, including those performed at outside institutions.

The MRIs were reviewed by 3 pediatric neuroradiologists with 7–32 years' experience. At the initiation of the study, 10 randomly selected MRIs were reviewed by all reviewers separately and then together by consensus to achieve consistency in scoring. Interreader reliability was assessed on overall imaging pattern in these 10 cases. Given strong interreader reliability (see Results), each subsequent study was reviewed by 1 reviewer and reviewers met periodically thereafter to maintain uniformity in scoring. Detailed imaging review included the assessment of location, symmetry, size, and characterization of abnormalities of the brain,

optic nerves, and the spine (Online Supplemental Data). Locations of involvement were chosen based on prior descriptions in the literature.<sup>15,17,20</sup> Supratentorial locations were characterized as cortex, deep gray nuclei (DGN; caudate, putamen, globus pallidus, thalamus), and white matter (subcortical, deep, periventricular, internal capsule, corpus callosum). The white matter involvement was classified based on lobes involved (frontal, parietal, temporal, and occipital lobes and the insula). The infratentorial regions involved were categorized as midbrain, pons, medulla, brachium pontis, cerebellum, or other. The parenchymal involvement was assessed for size (small, intermediate, or large; Online Supplemental Data). Noncortical involvement was assessed for margin characteristics (well-defined, ill-defined, or mixed) and degree of confluence (discrete, beginning confluence, or confluent). Other imaging features assessed were presence and pattern of enhancement (cortical, leptomeningeal, solid/nodular, peripheral ring, or incomplete ring), presence of reduced diffusion on DWI, and abnormal susceptibility on SWI/gradient echo. Orbital images were evaluated for unilateral versus bilateral involvement, segments of optic nerve abnormality, optic nerve enhancement, perineural enhancement, and presence of reduced diffusion. When dedicated orbital imaging was not available, the orbits were assessed on whole-brain sequences if deemed to be of sufficient quality by the reviewers. Spine involvement was characterized as long (spanning  $\geq 3$  vertebral bodies) or short segment (spanning  $< 3$  vertebral bodies), unifocal or multifocal, region of involvement (cervical, thoracic, conus, or cauda equina), cross-sectional pattern (central, peripheral, holocord, or gray matter only), presence of cord expansion, and pattern of enhancement (none, intramedullary, or leptomeningeal). When spine DWI was available, the presence of reduced diffusion was assessed.

The overall imaging pattern was characterized as ADEM-like, optic neuritis (ON), myelitis (any cord signal abnormality), FLAIR-hyperintense lesions in anti-MOG-associated encephalitis with seizures (FLAMES), or any combination of the above. ADEM-like pattern was defined as multifocal supratentorial or infratentorial white or gray matter T2/T2-FLAIR hyperintense lesions with or without enhancement (Fig 1). When FLAMES occurred in combination with other patterns (ADEM-like, ON, or myelitis), the overall pattern was assigned as FLAMES (Fig 2).

### Statistical Analysis

Interreader reliability was assessed using the Cohen kappa coefficient. The association of age ( $\leq 9$  years versus  $> 9$  years established based on prior literature)<sup>5</sup> and anti-MOG titer with imaging pattern at presentation, presence of clinical relapse, and time to clinical relapse were assessed using the Student *t* test and Wilcoxon rank sum test, as appropriate. The association of imaging pattern with patient age and occurrence of relapse was assessed by using the Fischer exact test. The threshold for significance for all tests was set at  $P < .05$ . All statistical tests used Stata 14.0 (College Station, TX).

## RESULTS

Sixty-one patients were included in the study. The median age at presentation was 7 years (IQR: 4–11). The study population was 55.7% (34/61) female.

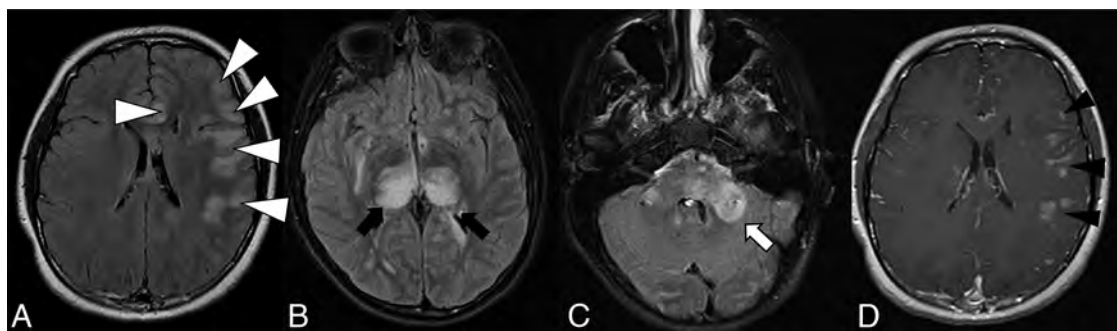


**FIG 1.** Thirteen-year-old adolescent boy who presented with encephalopathy after a viral prodrome, found to have papilledema and opening pressure >39, subsequently found to have serum positivity for anti-MOG antibody. Brain MR imaging demonstrates features of ADEM-like pattern of pediatric MOGAD. A-C, FLAIR hyperintensity involving the left frontal subcortical white matter with ill-defined borders and beginning confluence (white arrowheads), bilateral thalami (black arrows), pons and brachium pontis (white arrow). D, Solid nodular enhancement associated with the left frontal white matter lesions.

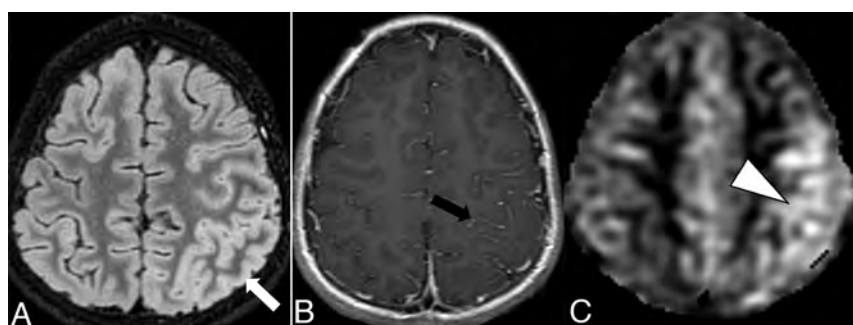


**FIG 2.** Ten-year-old boy with rapid-onset altered mental status and seizures. A, Cortical FLAIR hyperintensity (white arrow) involving the left parietal lobe. B, Associated leptomeningeal enhancement (black arrow). C, Concurrently acquired arterial spin labeling image demonstrates hyperperfusion of the left parietal cortex (white arrowhead), reflective of associated seizure activity.

### Clinical Relapse

The median follow-up time was 6 years (IQR: 3–13 years). Of the study cohort, 73.7% (45/61) had at least 1 relapse and 52% (32/61) had at least 2 relapses. The median time to first relapse was 5 months (IQR: 2–13), and median time between first and second relapse was 8 months (IQR: 2–25.25). Age at presentation was not associated with the presence of relapse (8.7 years without relapse versus 7.8 years with relapse,  $P = .45$ ). The mean follow-up time was longer among those  $\leq 9$  years (10.1 years) compared with those  $> 9$  years (5.6 years,  $P = .003$ ). Older age ( $> 9$  years) at presentation was associated with shorter time to first relapse (4.6 versus 18.8 months,  $P = .04$ ).

### Clinical and Laboratory Data

The most common clinical syndrome at presentation was ON (50.8%, 31/61), followed by ADEM (23%, 14/61) and myelitis (19.7%, 12/61, Table 1). The baseline anti-MOG titer was not significantly different between those with and without relapse (1:100 versus 1:100,  $P = .84$ ). None of the cases had a positive anti-AQP4 titer.

### Imaging Findings

A total of 239 MRIs in 61 patients were reviewed, including 125 brain, 52 orbit, and 62 spine MRIs. MRIs were scanned at 1.5T in

156/239 (65.2%), 3T in 78/239 (32.6%), 1T in 3/239 (1.3%), and unknown in 2/239 (0.8%).

**Presentation.** MR imaging at presentation was available in 91.8% (56/61) of patients, including 56 brain, 18 orbit, and 29 spine MR images.

The imaging characteristics are summarized in Tables 2 and 3. At presentation, there was intracranial involvement in 78.6% (44/56), orbital in 55.4% (31/56), and spinal in 19.6% (11/56). Among those with intracranial abnormalities, the frontal lobe white matter was the most commonly involved (31/44, 70.5%), with the sub-

cortical location being most common (33/44, 75%). The thalamus was the most commonly affected DGN (21/44, 47.8%), and the pons was most commonly affected infratentorial structure (21/44, 47.7%). The lesions commonly had ill-defined margins (32/42, 76.2%) and were beginning to demonstrate confluence (18/42, 42.9%). A range of enhancement patterns was noted, most commonly solid/nodular (17/44, 38.6%) or linear (10/44, 22.7%). The presence of reduced diffusion was rare (4.5%, 2/44), and no cases (0/36) had abnormal magnetic susceptibility.

Orbital involvement was more commonly bilateral (25/31, 80.6%) and more commonly involved the intraorbital segments of the optic nerve (24/31, 77.4%). Most cases with orbital involvement demonstrated optic nerve (86.2%, 25/29) and perineural (68%, 17/25) enhancement.

Spinal cord involvement was more commonly short segment (6/11, 54.5%), multifocal (8/11, 72.7%), with frequent involvement of the cervical cord (8/11, 72.7%). There was a spectrum of involvement of the cross-section of the cord (Table 3), and cord enhancement was uncommon (3/11, 27.3%).

The most common imaging pattern at presentation was ADEM-like (14/56, 25%), followed by ADEM-like with ON (13/56, 23.2%, Fig 3). There was strong interreader reliability in the assessment of overall imaging pattern ( $\kappa = 0.84$ ).

**Relapse.** MR imaging was available in 91.1% (41/45) of patients at the first relapse. MR imaging was available in 87.5% (28/32) of patients with a second relapse.

**Table 1: Demographics and clinical data at time of diagnosis in cohort of pediatric patients with MOGAD**

	<i>n</i> = 61
Age, median (IQR), years	7 (4–11)
Female (%)	34 (55.7)
Race (%)	
African American	6 (9.8)
Hispanic	13 (21.3)
White	22 (36.1)
Other	14 (23.0)
Unknown	6 (9.8)
Initial clinical presentation	
Syndrome	
ADEM	14 (23.0)
ON	31 (50.8)
Myelitis	12 (19.7)
Symptom	
Headache	19 (31.1)
Altered mental status	12 (19.7)
Ataxia	7 (11.5)
Fever	11 (18.0)
Seizure	2 (3.3)
Anti-MOG titer, median (IQR) <sup>a</sup>	1:100 (1:80–1:1000)
Relapsing disease	45 (73.8)
Total episodes up to 10, median (IQR)	3 (1–4)
Time to first relapse, median (IQR), months	5 (2–13)

<sup>a</sup>Titer while acutely symptomatic during initial presentation was not available for 45 patients.

**Table 2: Brain MR imaging features at presentation for serum antibody-positive MOGAD**

Brain Involvement	<i>n</i> = 44		<i>n</i> = 44
Supratentorial	41/44 (93.2)	Margins <sup>a</sup>	
Cortex	9/44 (20.5)	Well-defined	3/42 (7.1)
Deep gray <sup>b</sup>	26/44 (59.1)	Ill-defined	32/42 (76.2)
Caudate	9/44 (20.5)	Mixed	7/42 (16.7)
Putamen	9/44 (20.5)	Confluence <sup>a</sup>	
Globus pallidus	6/44 (13.6)	Discrete	16/42 (38.1)
Thalamus	21/44 (47.7)	Beginning confluence	18/42 (42.9)
White matter <sup>b</sup>		Confluent	8/42 (19)
Frontal lobe	31/44 (70.5)	Mass effect	19/44 (43.2)
Parietal lobe	28/44 (63.6)	Enhancement <sup>b</sup>	
Temporal lobe	22/44 (50)	Solid/nodular	17/44 (38.6)
Occipital lobe	19/44 (43.2)	Peripheral ring	0
Insula	21/44 (47.7)	Incomplete ring	1/44 (2.3)
White matter <sup>b</sup>		Ill-defined	9/44 (20.5)
Subcortical	33/44 (75)	Linear	10/44 (22.7)
Deep	17/44 (38.6)	Leptomeningeal	4/44 (9.1)
Periventricular	14/44 (31.8)	Cortical	0/44
Internal capsule	9/44 (20.5)	None	17/44 (2.3)
Corpus callosum	8/44 (18.2)	>1 enhancement characteristic	10/44 (22.7)
Infratentorial <sup>b</sup>	31/44 (70.5)	Low diffusivity <sup>c</sup>	2/43 (4.7)
Midbrain	15/44 (34.1)	Susceptibility <sup>d</sup>	0/36
Pons	21/44 (47.7)		
Medulla	9/44 (20.5)		
Brachium pontis	12/44 (27.3)		
Cerebellum	15/44 (34.1)		
Other	5/44 (11.4)		

<sup>a</sup>Not applicable in 2 cases of cortical only involvement.

<sup>b</sup>Percentages do not add up to 100% as many cases had multiple combinations of features.

<sup>c</sup>Unknown in 1 patient due to lack of DWI sequence.

<sup>d</sup>Unknown in 8 patients due to lack of SWI/gradiant echo sequence.

The imaging patterns were significantly different at relapse time points, with the combination of ADEM-like and ON (10/41, 24.4%) being the most common pattern at first relapse, and ADEM-like alone (11/29, 37.9%) being the most common pattern at second relapse ( $P = .01$ , Fig 3; Online Supplemental Data). There was a change in imaging pattern between presentation and first relapse in 69.4% (25/36) and between first and second relapse in 65.3% (17/26).

### Association of Clinical Variables and Imaging Findings

At presentation, ADEM-like (13/33, 39.4%) was the most common imaging pattern in younger children (age  $\leq 9$  years) whereas ON (8/23, 34.8%) was most common in older children ( $> 9$  years of age,  $P = .001$ , Table 4). At first relapse, the imaging pattern also differed by age ( $P = .008$ ); ADEM-like (8/23, 34.8%) was most common among those  $\leq 9$  years, while FLAMES (5/18, 27.8%) was most common in older children at first relapse. The imaging patterns were not significantly associated with age at second relapse ( $P = .21$ ). The imaging pattern at presentation was not significantly associated with occurrence of future relapse ( $P = .24$ ).

### DISCUSSION

Our study provides detailed characterization of imaging patterns of CNS involvement in a large cohort of children with MOGAD. We demonstrate an age-dependent imaging phenotype, which persists into first relapse. Furthermore, we demonstrate that imaging phenotypes often differ at relapse compared with presentation. Older age at presentation is associated with shorter time to relapse.

MOGAD is increasingly recognized as a major cause (21%–

75%) of pediatric acquired demyelinating disease.<sup>2–4</sup> Proposed diagnostic criteria<sup>18</sup> and spectrum of imaging manifestations of MOGAD are being defined. Much of the previous literature on imaging manifestations of MOGAD include pediatric and adult populations<sup>8,21–23</sup> and do not provide systematic, detailed radiologic descriptions. In our detailed radiologic study of pediatric MOGAD, lesions at presentation involved predominantly the frontal subcortical white matter and DGN in the supratentorial brain and pons in the infratentorial brain. The lesions were often ill-defined and beginning to confluence, with solid/nodular enhancement, but without reduced diffusion or magnetic susceptibility. This is in agreement with limited previous studies with 10–69 patients which demonstrate predominantly poorly demarcated brain lesions involving the subcortical white matter and DGN in pediatric MOGAD.<sup>11,13–17</sup> The involvement of subcortical white matter as well as pontine involvement is a distinction from NMOSD, which

more commonly affects periventricular white matter and area postrema,<sup>24</sup> in addition to the presence of T1 hypointensity and lack of cortical involvement in NMOSD.<sup>14</sup> MOGAD lesions rarely involve the corpus callosum and are distinct from the small well-defined lesions seen in MS.<sup>10,11,14</sup> Incomplete ring pattern of enhancement, characteristic of MS, was seen in only 1 subject in our study. No cases in our cohort had signal abnormality on SWI;

thus, the presence of SWI abnormality suggests an alternative diagnosis.

Similar to prior studies, optic nerve involvement in our study was commonly bilateral and displayed anterior predominance compared with posterior predominance in NMOSD,<sup>13</sup> with a high prevalence of perineural enhancement (68%) similar to previous reports of 41%–52%.<sup>25,26</sup>

Reports of spine involvement in MOGAD are variable. Many of our cases had short segment, multifocal spinal cord involvement, with the cervical cord most affected. While initial reports of MOGAD favored a lower cord/conus predominance,<sup>20,27,28</sup> later studies in pediatric cohorts suggest cervicothoracic predominance.<sup>13,15</sup> Most prior studies report a predominantly longitudinally extensive myelitis (63%–93%) in MOGAD,<sup>14–17,20</sup> while Xu et al<sup>13</sup> report short segment involvement in 50%, similar to our findings. There are also mixed data on cross-sectional involvement of the cord, with our study demonstrating central cord involvement in slightly more than one-half of the cases and central gray matter involvement in 36%. The central gray matter involvement is described in pediatric MOGAD in ~50%.<sup>20,29</sup> These differences in previous reports might be due

**Table 3: Orbit and spine MR imaging features at presentation for serum antibody-positive MOGAD**

Orbital Involvement	n = 31	Spine Involvement	n = 11
Unilateral	6/31 (19.4)	Long segment	4/11 (36.4)
Bilateral	25/31 (80.6)	Short segment	6/11 (54.5)
Segments involved		Cauda equina enhancement	1/11 (9.1)
Orbital	24/31 (77.4)	Focality	
Intracranial	20/31 (64.5)	Unifocal	3/11 (27.3)
Prechiasmatic	17/31 (54.8)	Multifocal	8/11 (72.7)
Optic chiasm	5/31 (16.1)	Location	
Optic tract	4/31 (12.9)	Cervical	8/11 (72.7)
Optic nerve enhancement <sup>a</sup>	25/29 (86.2)	Thoracic	6/11 (54.5)
Perineural enhancement <sup>b</sup>	17/25 (68)	Conus	5/11 (45.4)
Optic nerve low diffusivity <sup>c</sup>	10/15 (66.7)	Cauda equina	1/11 (9)
		Pattern	
		Central	6/11 (54.5)
		Peripheral	4/11 (36.4)
		Entire cross-section	3/11 (27.3)
		Central gray only	4/11 (36.4)
		Enhancement	
		None	7/11 (63.6)
		Intramedullary	3/11 (27.3)
		Leptomeningeal	1/11 (9)
		Cord expansion	5/11 (45.4)

<sup>a</sup>Unknown in 2 patients due to absence of contrast.

<sup>b</sup>Unknown in 6 patients due to absence of contrast and/or fat saturation.

<sup>c</sup>Unknown in 16 patients due to missing DWI sequence.

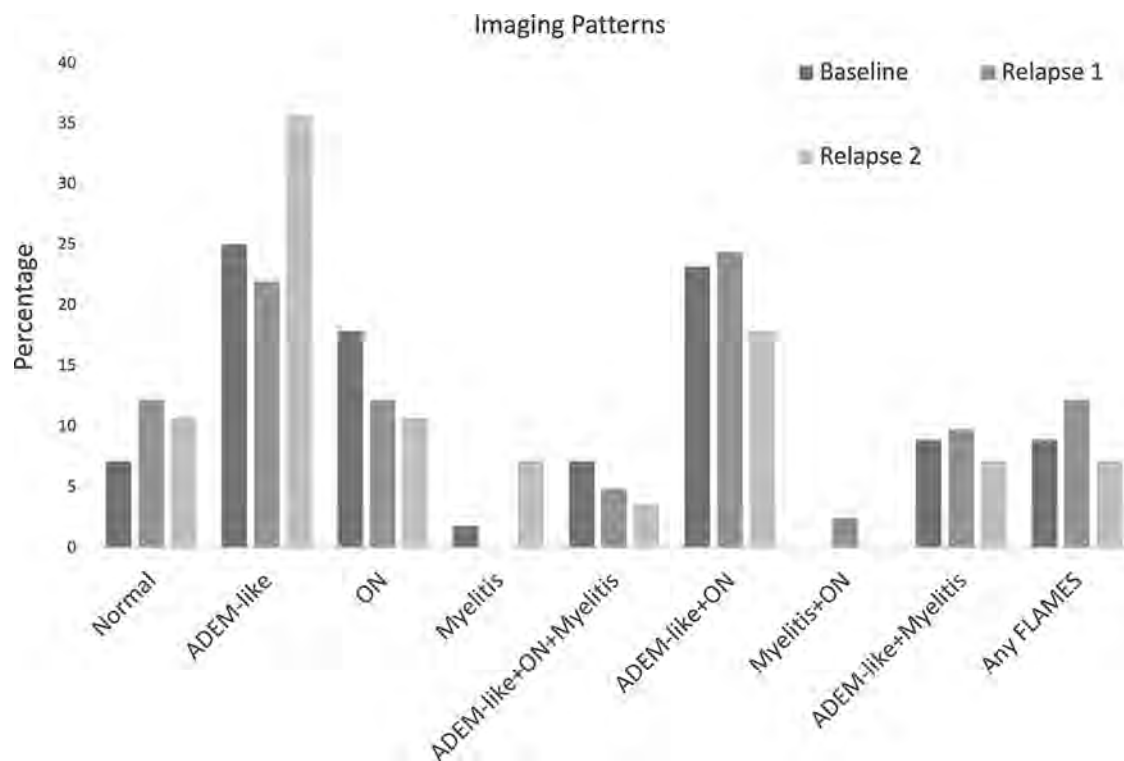


**FIG 3.** Imaging patterns at presentation and relapses.

**Table 4: Variation of imaging patterns at relapse stratified by age greater or less than 9 years**

	Relapse 1			Relapse 2		
	Age ≤9 (n = 23)	Age >9 (n = 18)	P Value	Age ≤9 (n = 13)	Age >9 (n = 15)	P Value
Normal	1/23 (4.3)	4/18 (22.2)	.008	1/13 (7.7)	2/15 (13.3)	.211
ADEM-like	8/23 (34.8)	1/18 (5.6)		8/13 (61.5)	2/15 (13.3)	
ON	3/23 (13.0)	2/18 (11.1)		1/13 (7.7)	2/15 (13.3)	
Myelitis				0	2/15 (13.3)	
ADEM-like + ON + myelitis	2/23 (8.7)	0		0	1/15 (6.7)	
ADEM-like + ON	7/23 (30.4)	3/18 (16.7)		2/13 (15.4)	3/15 (20)	
Myelitis + ON	0	1/18 (5.6)				
ADEM-like + myelitis	2/23 (8.7)	2/18 (11.1)		1/13 (7.7)	1/15 (6.7)	
Any FLAMES	0	5/18 (27.8)		0	2/15 (13.3)	

to small sample size and relatively low prevalence of myelitis in pediatric MOGAD (45%–68%).<sup>15–17</sup>

Our findings are concordant with previous reports of age-related changes in imaging phenotype at presentation with predominantly ADEM-like presentation in younger children and ON in older children.<sup>2,5,10</sup> There are varying rates of relapse reported in pediatric MOGAD from 28% to 62%,<sup>4,7,9–11</sup> with our study on the higher end at 73.8%. This may partly be reflective of referral bias to our tertiary care center; however, this is an advantage of our study, as the higher relapse rates enable us to assess imaging and clinical factors associated with relapse. Clinical manifestations in relapsing pediatric MOGAD suggest varied phenotypes with some predominance of ON and myelitis<sup>7,9,23,30,31</sup> and change in phenotype between episodes in >50%.<sup>9</sup> There is limited published literature on imaging phenotypes at relapse, and our work adds to the literature in this respect. In our cohort, ON was present on imaging in 33%–45% at relapse and ADEM-like appearance on imaging in 60%–63%, which was more frequent at younger age of relapse. These age-dependent variations did not persist at second relapse, but this is difficult to interpret, given the small cohort of patients with second relapse and imaging.

There are mixed data on association of anti-MOG titer and risk of relapse.<sup>4,19</sup> We did not find an association between baseline anti-MOG titer and polyphasic disease. Previous reports indicate higher rate of recurrence among those with persistently high titers.<sup>4,9,31</sup> While older age has been associated with relapsing phenotype in prior studies,<sup>4,31</sup> in our study, older children had a shorter time to first relapse, which may be related to higher rates of persistent seropositivity in older children.<sup>31</sup>

Our study has several limitations. Given the retrospective study design, there is heterogeneity in available clinical, laboratory, and imaging data. The study included patients seen over 20 years, during which imaging techniques and MOGAD diagnosis and treatment have changed, further contributing to the data heterogeneity. All available MRIs corresponding to the first 3 clinical episodes were included in this study, including those performed at other institutions before referral and, hence, were of varying image quality and technique. However, only <2% were deemed to have poor subjective image quality by reviewers. Despite the relatively large sample size, the number of patients with spine involvement was low, limiting comprehensive

assessment of patterns of spine involvement. The use of immunosuppressants and disease-modifying therapy, which may affect the rate,<sup>5</sup> timing, and pattern of relapse, could not be adjusted for given variability in treatment, some of which occurred at other institutions.

## CONCLUSIONS

We describe the detailed imaging manifestations of pediatric MOGAD at presentation and at first 2 relapses. There are age-dependent variations in imaging phenotype at presentation and first relapse. Imaging phenotype at relapse

often differed from phenotype at presentation. Furthermore, older children tend to relapse sooner than younger children.

**Disclosure forms** provided by the authors are available with the full text and PDF of this article at [www.ajnr.org](http://www.ajnr.org).

## REFERENCES

- O'Connor KC, McLaughlin KA, De Jager PL, et al. **Self-antigen tetramers discriminate between myelin autoantibodies to native or denatured protein.** *Nat Med* 2007;13:211–17 CrossRef Medline
- Reindl M, Waters P. **Myelin oligodendrocyte glycoprotein antibodies in neurological disease.** *Nat Rev Neurol* 2019;15:89–102 CrossRef Medline
- de Mol CL, Wong YY, van Pelt ED, et al. **Incidence and outcome of acquired demyelinating syndromes in Dutch children: update of a nationwide and prospective study.** *J Neurol* 2018;265:1310–19 CrossRef Medline
- Hennes EM, Baumann M, Schanda K, BIOMARKER Study Group, et al. **Prognostic relevance of MOG antibodies in children with an acquired demyelinating syndrome.** *Neurology* 2017;89:900–08 CrossRef Medline
- Hacohen Y, Wong YY, Lechner C, et al. **Disease course and treatment responses in children with relapsing myelin oligodendrocyte glycoprotein antibody-associated disease.** *JAMA Neurol* 2018;75:478–87 CrossRef Medline
- Hacohen Y, Banwell B. **Treatment approaches for MOG-Ab-associated demyelination in children.** *Curr Treat Options Neurol* 2019;21:2 CrossRef Medline
- Lopez-Chiriboga AS, Majed M, Fryer J, et al. **Association of MOG-IgG serostatus with relapse after acute disseminated encephalomyelitis and proposed diagnostic criteria for MOG-IgG-associated disorders.** *JAMA Neurol* 2018;75:1355–63 CrossRef Medline
- Jarius S, Ruprecht K, Kleiter I, Neuromyelitis Optica Study Group (NEMOS), et al. **MOG-IgG in NMO and related disorders: a multicenter study of 50 patients. 1. Frequency, syndrome specificity, influence of disease activity, long-term course, association with AQP4-IgG, and origin.** *J Neuroinflammation* 2016;13:279 CrossRef Medline
- Armangue T, Olive-Cirera G, Martinez-Hernandez E, Spanish Pediatric anti-MOG Study Group, et al. **Associations of paediatric demyelinating and encephalitic syndromes with myelin oligodendrocyte glycoprotein antibodies: a multicentre observational study.** *Lancet Neurol* 2020;19:234–46 CrossRef Medline
- Fernandez-Carbonell C, Vargas-Lowy D, Musallam A, et al. **Clinical and MRI phenotype of children with MOG antibodies.** *Mult Scler* 2016;22:174–84 CrossRef Medline
- Wegener-Panzer A, Cleaveland R, Wendel EM, et al. **Clinical and imaging features of children with autoimmune encephalitis and**

- MOG antibodies.** *Neurol Neuroimmunol Neuroinflamm* 2020;7:e731 CrossRef
12. Hennes EM, Baumann M, Lechner C, et al. **MOG spectrum disorders and role of MOG-antibodies in clinical practice.** *Neuropediatrics* 2018;49:3–11 CrossRef Medline
  13. Xu J, Liu L, Xiong J, et al. **The clinical, radiologic, and prognostic differences between pediatric and adult patients with myelin oligodendrocyte glycoprotein antibody-associated encephalomyelitis.** *Front Neurol* 2021;12:679430 CrossRef Medline
  14. Baumann M, Bartels F, Finke C, E.U. Paediatric MOG Consortium, et al. **E.U. Paediatric MOG Consortium Consensus: 2. Neuroimaging features of paediatric myelin oligodendrocyte glycoprotein antibody-associated disorders.** *Eur J Paediatr Neurol* 2020;29:14–21 CrossRef Medline
  15. Baumann M, Grams A, Djurdjevic T, et al. **MRI of the first event in pediatric acquired demyelinating syndromes with antibodies to myelin oligodendrocyte glycoprotein.** *J Neurol* 2018;265:845–55 CrossRef Medline
  16. Baumann M, Sahin K, Lechner C, et al. **Clinical and neuroradiological differences of paediatric acute disseminating encephalomyelitis with and without antibodies to the myelin oligodendrocyte glycoprotein.** *J Neurol Neurosurg Psychiatry* 2015;86:265–72 CrossRef Medline
  17. Konuskan B, Yildirim M, Gocmen R, et al. **Retrospective analysis of children with myelin oligodendrocyte glycoprotein antibody-related disorders.** *Mult Scler Relat Disord* 2018;26:1–7 CrossRef Medline
  18. Banwell B, Bennett JL, Marignier R, et al. **Diagnosis of myelin oligodendrocyte glycoprotein antibody-associated disease: International MOGAD Panel proposed criteria.** *Lancet Neurol* 2023;22:268–82 CrossRef Medline
  19. Lui A, Chong J, Flanagan E, et al. **High titers of myelin oligodendrocyte glycoprotein antibody are only observed close to clinical events in pediatrics.** *Mult Scler Relat Disord* 2021;56:103253 CrossRef Medline
  20. Tantsis EM, Prelog K, Alper G, Paediatric Myelitis MRI Study Group, et al. **Magnetic resonance imaging in enterovirus-71, myelin oligodendrocyte glycoprotein antibody, aquaporin-4 antibody, and multiple sclerosis-associated myelitis in children.** *Dev Med Child Neurol* 2019;61:1108–16 CrossRef Medline
  21. Salama S, Khan M, Levy M, et al. **Radiological characteristics of myelin oligodendrocyte glycoprotein antibody disease.** *Mult Scler Relat Disord* 2019;29:15–22 CrossRef Medline
  22. Dubey D, Pittock SJ, Krecke KN, et al. **Clinical, radiologic, and prognostic features of myelitis associated with myelin oligodendrocyte glycoprotein autoantibody.** *JAMA Neurol* 2019;76:301–09 CrossRef Medline
  23. Cobo-Calvo A, Ruiz A, D'Indy H, et al. **MOG antibody-related disorders: common features and uncommon presentations.** *J Neurol* 2017;264:1945–55 CrossRef Medline
  24. Garbugio Dutra B, da Rocha AJ, Hoffmann Nunes R, et al. **Neuromyelitis optica spectrum disorders: spectrum of MR imaging findings and their differential diagnosis.** *Radiographics* 2018;38:169–193 CrossRef Medline
  25. Song H, Zhou H, Yang M, et al. **Clinical characteristics and outcomes of myelin oligodendrocyte glycoprotein antibody-seropositive optic neuritis in varying age groups: a cohort study in China.** *J Neurol Sci* 2019;400:83–89 CrossRef Medline
  26. Wendel EM, Baumann M, Barisic N, et al. **High association of MOG-IgG antibodies in children with bilateral optic neuritis.** *Eur J Paediatr Neurol* 2020;27:86–93 CrossRef Medline
  27. Sato DK, Callegaro D, Lana-Peixoto MA, et al. **Distinction between MOG antibody-positive and AQP4 antibody-positive NMO spectrum disorders.** *Neurology* 2014;82:474–81 CrossRef Medline
  28. Kitley J, Waters P, Woodhall M, et al. **Neuromyelitis optica spectrum disorders with aquaporin-4 and myelin-oligodendrocyte glycoprotein antibodies: a comparative study.** *JAMA Neurol* 2014;71:276–83 CrossRef Medline
  29. Wang C, Narayan R, Greenberg B. **Anti-myelin oligodendrocyte glycoprotein antibody associated with gray matter predominant transverse myelitis mimicking acute flaccid myelitis: a presentation of two cases.** *Pediatr Neurol* 2018;86:42–45 CrossRef Medline
  30. Ramanathan S, Mohammad S, Tantsis E, Australasian and New Zealand MOG Study Group, et al. **Clinical course, therapeutic responses and outcomes in relapsing MOG antibody-associated demyelination.** *J Neurol Neurosurg Psychiatry* 2018;89:127–37 CrossRef Medline
  31. Waters P, Fadda G, Woodhall M, Canadian Pediatric Demyelinating Disease Network, et al. **Serial anti-myelin oligodendrocyte glycoprotein antibody analyses and outcomes in children with demyelinating syndromes.** *JAMA Neurol* 2020;77:82–93 CrossRef Medline

# A Radiomic “Warning Sign” of Progression on Brain MRI in Individuals with MS

 Brendan S. Kelly, Prateek Mathur, Gerard McGuinness, Henry Dillon,  Edward H. Lee,  Kristen W. Yeom, Aonghus Lawlor, and Ronan P. Killeen



## ABSTRACT

**BACKGROUND AND PURPOSE:** MS is a chronic progressive, idiopathic, demyelinating disorder whose diagnosis is contingent on the interpretation of MR imaging. New MR imaging lesions are an early biomarker of disease progression. We aimed to evaluate a machine learning model based on radiomics features in predicting progression on MR imaging of the brain in individuals with MS.

**MATERIALS AND METHODS:** This retrospective cohort study with external validation on open-access data obtained full ethics approval. Longitudinal MR imaging data for patients with MS were collected and processed for machine learning. Radiomics features were extracted at the future location of a new lesion in the patients' prior MR imaging (“prelesion”). Additionally, “control” samples were obtained from the normal-appearing white matter for each participant. Machine learning models for binary classification were trained and tested and then evaluated the external data of the model.

**RESULTS:** The total number of participants was 167. Of the 147 in the training/test set, 102 were women and 45 were men. The average age was 42 (range, 21–74 years). The best-performing radiomics-based model was XGBoost, with accuracy, precision, recall, and F1-score of 0.91, 0.91, 0.91, and 0.91 on the test set, and 0.74, 0.74, 0.74, and 0.70 on the external validation set. The 5 most important radiomics features to the XGBoost model were associated with the overall heterogeneity and low gray-level emphasis of the segmented regions. Probability maps were produced to illustrate potential future clinical applications.

**CONCLUSIONS:** Our machine learning model based on radiomics features successfully differentiated prelesions from normal-appearing white matter. This outcome suggests that radiomics features from normal-appearing white matter could serve as an imaging biomarker for progression of MS on MR imaging.

**ABBREVIATIONS:** AI = artificial intelligence; MSSEG2 = MS SEGmentation Challenge 2; NAWM = normal-appearing white matter

MS is a chronic, progressive, idiopathic, demyelinating disorder of the CNS.<sup>1</sup> Diagnosis is contingent on timely and precise application of the McDonald criteria, which rely on the interpretation of MR imaging.<sup>2</sup> It is unusual among many chronic conditions in that imaging features can often predate clinical manifestations of disease. Imaging remains a prominent tool in the diagnosis, progress-monitoring, and evaluation of treatment efficacy.<sup>1,2</sup> New MS lesions are an important imaging biomarker because they can signify both disease progression

and the efficacy of disease-modifying drugs.<sup>3</sup> Indeed, the absence of new T2-FLAIR lesions in the CNS is used as the solitary metric of disease-modifying drug effectiveness.<sup>4</sup> However, the monitoring of lesions can be a tedious or repetitive task for neuroradiologists,<sup>5</sup> and that issue, compounded by supply-demand issues in radiology,<sup>6</sup> has prompted research into automated lesion identification.<sup>7</sup>


Computer-assisted segmentation methodologies have been an important topic for scientific exploration for the past 2 decades.<sup>8</sup> More recently, a substantial increase in the incorporation of artificial intelligence (AI) into these methodologies has been observed.<sup>9</sup> Current research trends are shifting away from the simple identification of MS lesions on T2-FLAIR to comparing images captured


Received August 2, 2023; accepted after revision November 8.

From the Department of Radiology (B.S.K., G.M., H.D., R.P.K.), St. Vincent's University Hospital, Dublin, Ireland; Insight Centre for Data Analytics (B.S.K., P.M., A.L.), and School of Medicine (B.S.K.), University College Dublin, Dublin, Ireland; Wellcome Trust and Health Research Board (B.S.K.), Irish Clinical Academic Training, Dublin, Ireland; and Lucille Packard Children's Hospital at Stanford (E.H.L., K.W.Y.), Stanford, California.

This work was performed within the Irish Clinical Academic Training Program, supported by the Wellcome Trust and the Health Research Board (grant No. 203930/B/16/Z); the Health Service Executive National Doctors Training and Planning and the Health and Social Care, Research and Development Division, Northern Ireland; the Faculty of Radiologists, Royal College of Surgeons in Ireland; and the Science Foundation Ireland (SFI) under grant No. SFI/12/RC/2289\_P2.

Please address correspondence to Brendan S. Kelly, MB, Department of Radiology, St Vincent's University Hospital, Dublin, Ireland; e-mail: brendanskelly@me.com; @BSKRad

 Indicates open access to non-subscribers at [www.ajnr.org](http://www.ajnr.org)

 Indicates article with online supplemental data.

<http://dx.doi.org/10.3174/ajnr.A8104>

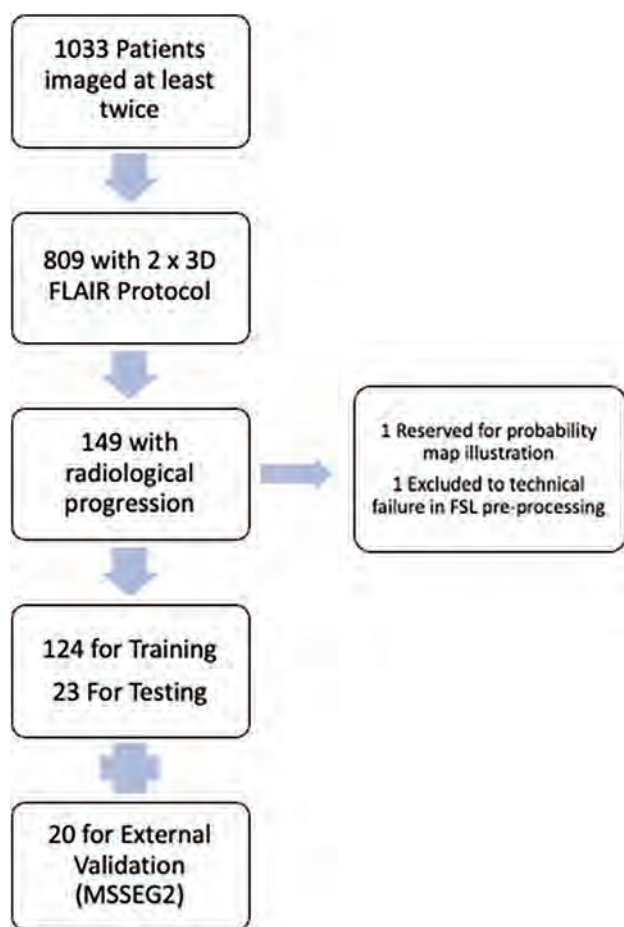


**FIG 1.** Flow chart of included patients.

at distinct time intervals.<sup>7</sup> In response to this escalating interest, the Medical Image Computing and Computer Assisted Interventions society initiated a challenge concentrating on the detection of new lesions (MS SEGmentation Challenge 2 [MSSEG2]), further galvanizing research interest in this domain.<sup>3</sup>

Predictive models in MS have also been the subject of research; however, their methods and external generalizability vary.<sup>10</sup> Many of these models use “systems biology” approaches (Omics data) to predict various disease markers and outcomes.<sup>11</sup> Recent imaging research into predictive modeling for MS includes applications in cognitive decline<sup>12</sup> and deep learning approaches to disease progression.<sup>13</sup> Radiomics is a field of research in which higher-order image features such as texture or intensity distribution are investigated (often using AI and machine learning models to glean deeper information from radiologic images).<sup>14,15</sup> The methodology is widely used in medical imaging research, including applications in MS.<sup>16–19</sup> By transforming simple images into mineable high-dimensional data, it allows in-depth characterization of MS lesions. Thus, radiomics has this potential to augment diagnostic accuracy and individualize patient management.<sup>7</sup>

While previously radiology AI research was focused on a narrow range-of-use cases<sup>6</sup> aligned to the above advances, there has been a significant increase in interest in the concept of temporality in the field.<sup>20</sup> The interpretation of medical images is not a static process, and recent research has shown the importance

both of incorporating prior imaging<sup>21</sup> into the pipeline and also considering medical images as part of a time-series and in making predictions.<sup>22,23</sup>

In this study, we aimed to evaluate the potential of radiomics features in predicting progression on MR imaging of the brain in individuals with MS. In our approach, we propose using a machine learning model and radiomics features to differentiate a “prelesion” from a control sample in the normal-appearing white matter (NAWM).

## MATERIALS AND METHODS

This retrospective study with external validation was designed according to both the Radiological Society of North America and the European Society of Radiology published principles,<sup>24,25</sup> with patient expert involvement.<sup>26</sup> We obtained independent statistical advice. The article was prepared using the Checklist for Artificial Intelligence in Medical Imaging<sup>27</sup> and conforms to the Assessment of Radiomic rEsearch (ARISE) guideline.<sup>28</sup> It received full institutional review board approval (St. Vincent’s University Hospital), and the requirement for prospective consent was waived. This research constitutes Level 5A evidence (data quality and AI model development with external testing) because it represents 1 retrospective study with internal and external data used for final performance reporting.<sup>29</sup>

### Participants and Data

Consecutive patients who had at least 2 MR imaging brain studies for MS at our institution between January 2019 and December 2022 were reviewed (Fig 1). Those with a new lesion on follow-up imaging were included in this study. There is no overlap of the internal cohort with prior studies. The external cohort is publicly available and has been previously described.<sup>3</sup>

Images were acquired on a 1.5T system (Magnetom Avanto syngo MR B19; Siemens). Imaging sequences included a 3D T2-FLAIR sequence using the following parameters: acquired voxel size,  $1.1 \times 1.1 \times 1.1$  mm; TR, 6000 ms; TE, 413 ms; TI, 2030 ms; acquisition time, 6 minutes 44 seconds; orientation, sagittal. All scans were defaced using the FSL Brain Extraction Tool 10 (<https://fsl.fmrib.ox.ac.uk/fsl/fslwiki/BET/UserGuide>) to preserve participant anonymity.<sup>30</sup> All images were coregistered to the first time point also using FSL (<http://www.fmrib.ox.ac.uk/fsl>).

A baseline automated segmentation of MS lesions was generated using DeepMedic (<https://github.com/deepmedic/deepmedic>).<sup>31</sup> These baseline segmentations were then manually corrected by 1 of 2 certified radiologists in their first year post-board examination using ITK-Snap Version 3.8.0 ([www.itksnap.org](http://www.itksnap.org)).<sup>32</sup> Radiologic progression (new or enlarging lesions) was defined according to the Magnetic Resonance Imaging in MS (MAGNIMS) consensus guidelines (<https://www.magnims.eu/>).<sup>33</sup> Cases with progression were initially identified from the radiologic report and confirmed at a dedicated research re-read. In the case of enlarging lesions, subtractions of coregistered intensity-normalized images were used to confirm that the lesion had unequivocally enlarged. Only the newly segmented area (ie, the area that changed) was included. Cases with progression were first segmented and manually corrected as detailed above and then additionally verified by a third radiologist who is a subspecialist neuroradiologist with >10 years postfellowship experience.

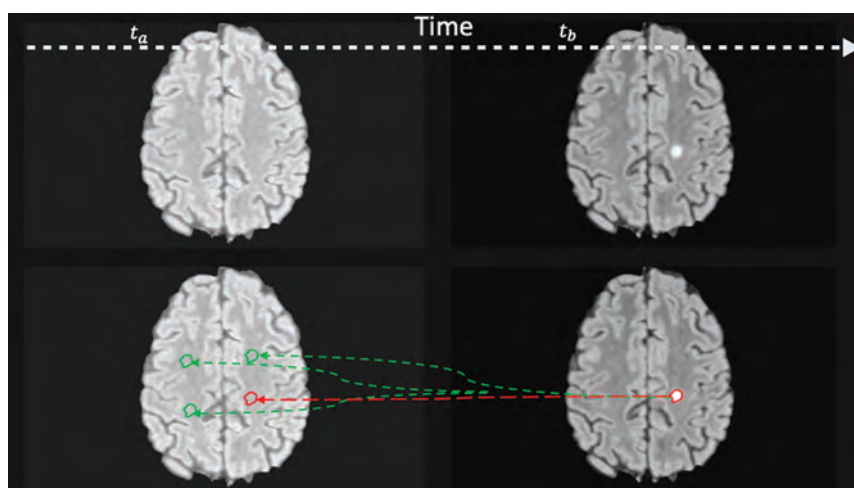


**FIG 2.** Prelesion and control masks. Expert segmentation mask at time  $b$  ( $t_b$ ) is projected backward to time  $a$  ( $t_a$ ) to the location where a lesion will occur (prelesion, red) and the other random areas in the NAWM (control, green). Note that this 2D representation is for illustrative purposes only, and for the experiments, the random translation was in 3D.

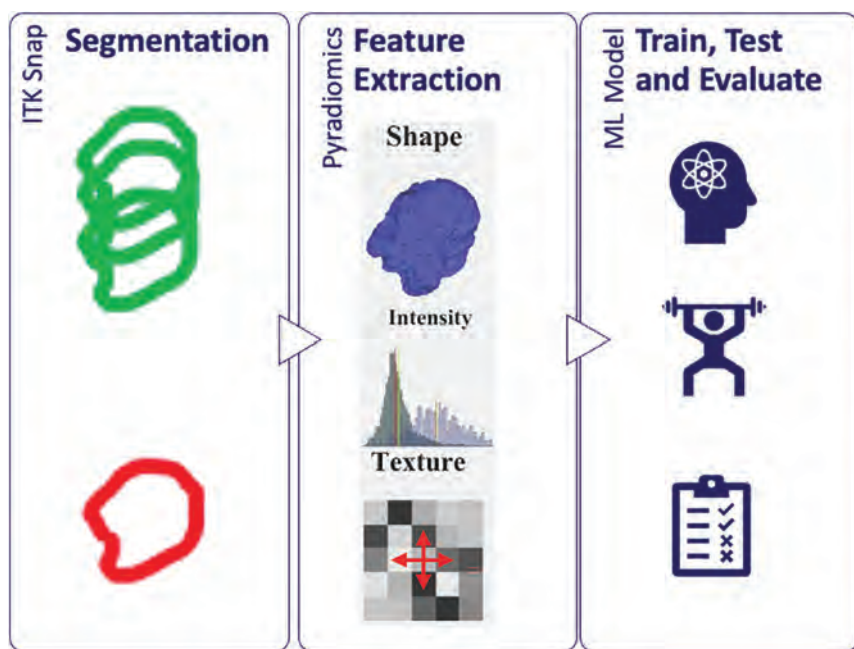


**FIG 3.** Radiomics workflow in which features are extracted from the segmented regions and passed to the machine learning models.

New lesion segmentations were projected backward in time to the same location (dubbed the prelesion) on the prior MR imaging study. This same segmentation was then randomly translated 3 times to other locations within the NAWM to produce 3 control segmentations (Fig 2). The NAWM mask was obtained by subtracting the lesion mask from the white matter mask generated by FSL. By means of PyRadiomics (Version 3.01; <https://pypi.org/project/pyradiomics/>),<sup>34</sup> high-order image features were extracted from the prelesion and control segmentations (Fig 3). The 3 control features were averaged to gain a fairer representation of the NAWM. Because the shapes of the control segmentations were dependent on the original lesion segmentations, shape-related radiomic features were excluded.

## Model, Training, and Evaluation

A baseline model using just the mean intensity value of the segmented regions was first tested to ensure that there was justification to proceed to use higher-order features;<sup>28</sup> control and prelesion regions were compared on both internal and external data.

Several machine learning models were trained and tested (eXtreme Gradient Boosting [XGBoost; <https://xgboost.readthedocs.io/en/stable/>], Support Vector Classifier, K Nearest Neighbor, and logistic regression). Hyperparameter optimization was performed using a grid search. Because the classes were balanced 50:50 in a binary prediction problem, we chose overall prediction accuracy as our primary evaluation metric.<sup>35</sup> Feature importance was extracted from the best-performing model. This was used for feature selection and to give a level of explainability. The optimal number of features is a trade-off between model complexity and performance. The number of features that yields the best performance across the different classification models would be chosen as the optimal number of features. Failure analysis was performed on incorrectly classified cases.<sup>27</sup>

To demonstrate the potential clinical usefulness of our approach,<sup>27,28</sup> we produced a probability map using a previously unseen case. A section with a new lesion was selected, and the image was divided into patches. Radiomics features were extracted from each patch and passed to the best-performing model to predict whether that patch was a prelesion. The absolute and relative probabilities given by the model were calculated and used in a data visualization to illustrate a potential future clinical application.

The code necessary to reproduce these experiments is available here (<https://github.com/insight-ucd/insightmri/tree/main/MSOmic>).

## RESULTS

The total number of participants in the training, test, and external validation sets was 167 (124, 23 and 20); 1 additional participant was randomly chosen for production of the probability map only. Failure of FSL registration and brain extraction led to the exclusion of 1 patient (Fig 1). Of the 147 participants in the training/test set, 102 were women and 45 were men. Overall, the average age was 42 years (range, 21–74 years) (Table 1). Two hundred ninety-four volumetric MR imaging FLAIR images were used in the process of training

and internal testing, with 40 heterogeneous FLAIR acquisitions for external validation.

Results of different models for testing and validation are displayed in Tables 2 and 3. The preliminary model based on first-order image metrics (mean pixel intensity) had modest performance on internal data (accuracy, precision, recall, and F1-score of 0.77, 0.76, 0.77, and 0.75). There was a statistically significant difference in the overall mean pixel intensity between the prelesion samples and controls on internal data with a paired *t* test (*P* < .05). However, this method did not generalize to external data (accuracy, precision, recall, and F1-score of 0.5, 0.25, 0.5, and 0.33), justifying the use of higher-order features.

The best-performing radiomics-based model was XGBoost, with accuracy, precision, recall, and F1-score of 0.91, 0.91, 0.91,

and 0.91 on the test set, and 0.74, 0.74, 0.74, and 0.70 on the external validation set. The 5 most important radiomics features (Fig 4) to the XGBoost model were associated with the overall heterogeneity (RunEntropy, Variance, and GrayLevelNonUniformityNormalized) and low gray-level emphasis (LowGrayLevelEmphasis and LongRunLowGrayLevelEmphasis) of the segmented regions. Complete feature importance of the best-performing model is given in the Online Supplemental Data. The Online Supplemental Data show the performance for a model trained on only 14 features (including only 1 feature for each 10 participants<sup>28</sup>), which was inferior to the chosen model.

Probability maps were produced for illustrative purposes of potential future clinical application and are shown in Fig 5A, -B. These show the probability of a new lesion in absolute terms (A) and relative to the overall risk (B). The relative probability is defined in Equations 1 and 2.

1) 
$$P(x, y) = P(N) \times (NLV / WMV).$$

*P*(*x*, *y*) represents the general probability of a lesion at location coordinates *x*, *y*, where *P*(*N*) represents the probability of a new lesion anywhere. NLV represents the average new lesion volume. WMV represents the NAWM volume.

2) 
$$RP(\bar{x}, \bar{y}) = P(x, y) / P'(\bar{x}, \bar{y}).$$

The relative probability of a new lesion in a specific location (*x̄*, *ȳ*) is represented by *RP* (*x̄*, *ȳ*), where the predicted probability of a lesion by the model in the specific location *x̄*, *ȳ* is *P'*(*x̄*, *ȳ*), and *P*(*x*, *y*) represents the baseline probability of a lesion in any location.

For our data, *P*(*x*, *y*) = 0.5(0.02) = 0.01  
and *RP*(*x̄*, *ȳ*) = 0.01/*P'*(*x̄*, *ȳ*).

Our sample probability map demonstrated 1 true-positive and 1 false-positive using a cutoff of relative increased probability of a new white matter lesion of 4 compared with background (Fig 5).

Failure analysis on external validation showed that in many instances, a potential cause for misclassified cases was misregistration of images rather than the machine learning model. For example, of the 3 false-negatives, 2 were likely related to misregistration (Fig 6).

DISCUSSION

In this study, we have demonstrated the potential of radiomics features in predicting progression on MR imaging of

Table 1: Patient demographics

Demographics	
Total participants	147
Average age (yr)	42.19
Min	21
Max	74
Sex	
Male	45
Female	102

Note:—Max indicates maximum; Min, minimum.

Table 2: Internal test cohort results

Model	Precision	Recall	F1-Score	Accuracy	Best Parameters
XGBoost	0.91	0.91	0.91	0.91	{'classifier__colsample_bylevel': 0.8, 'classifier__gamma': 0, 'classifier__learning_rate': 0.2, 'classifier__max_depth': 4, 'classifier__min_child_weight': 1, 'classifier__n_estimators': 100, 'classifier__subsample': 0.5}
SVC	0.90	0.89	0.89	0.89	{'classifier__C': 10, 'classifier__kernel': 'rbf'}
Logistic regression	0.81	0.78	0.78	0.78	{'classifier__C': 1, 'classifier__penalty': 'l1', 'classifier__solver': 'liblinear'}
KNN	0.83	0.78	0.78	0.78	{'classifier__n_neighbors': 7}
Intensity baseline	0.76	0.77	0.75	0.77	NA

Note:—SVC indicates support vector classifier; KNN, K nearest neighbor; NA, not applicable.

Table 3: External validation cohort results

Model	Precision	Recall	F1-Score	Accuracy	Best Parameters
XGBoost	0.74	0.74	0.70	0.74	{'classifier__colsample_bylevel': 0.8, 'classifier__gamma': 0, 'classifier__learning_rate': 0.2, 'classifier__max_depth': 4, 'classifier__min_child_weight': 1, 'classifier__n_estimators': 100, 'classifier__subsample': 0.5}
SVC	0.69	0.71	0.68	0.71	{'classifier__C': 10, 'classifier__kernel': 'rbf'}
Logistic regression	0.62	0.55	0.56	0.55	{'classifier__C': 1, 'classifier__penalty': 'l1', 'classifier__solver': 'liblinear'}
KNN	0.51	0.42	0.43	0.42	{'classifier__n_neighbors': 7}
Intensity baseline	0.25	0.50	0.33	0.50	NA

Note:—SVC indicates support vector classifier; KNN, K nearest neighbor; NA, not applicable.

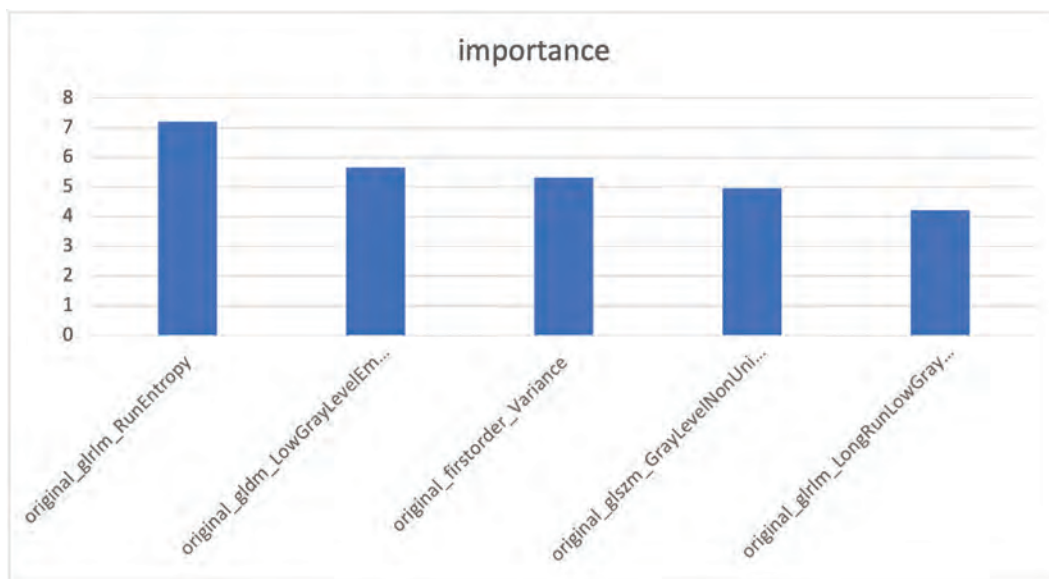


**FIG 4.** Top 5 radiomic features identified by the top performing XGBoost model.

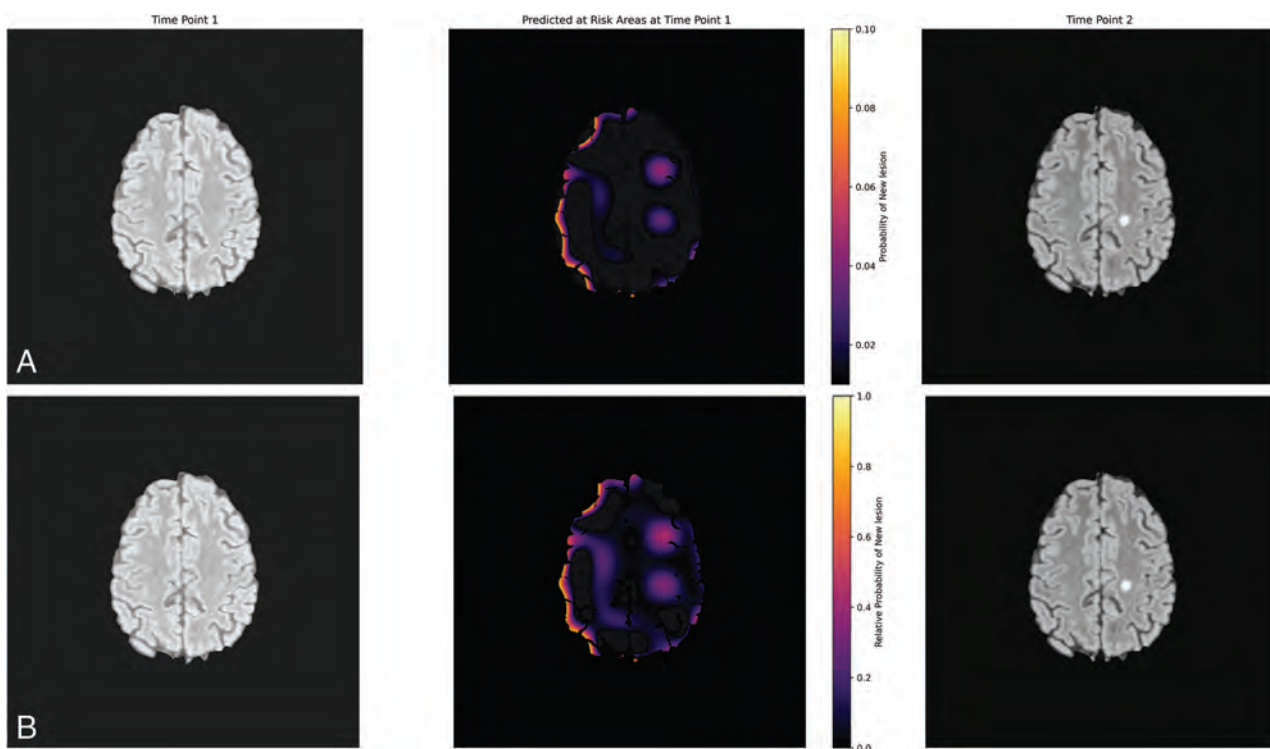


**FIG 5.** Illustrative probability maps showing the absolute (A, Upper row) and relative (B, Lower row) probability of a new lesion occurring in each patch.

the brain in individuals with MS. We used a machine learning model and the extracted features at the location of future progression to predict the occurrence of a new lesion.

AI is revolutionizing the field of MS imaging research, promising to improve diagnostic accuracy, reduce the time taken for image interpretation, and facilitate personalized patient management.<sup>7</sup> Radiomics, the extraction of high-order features from radiologic images using data-characterization algorithms, plays

an increasingly important role in MS research.<sup>16-19</sup> Building on this body of evidence and understanding that the white matter of individuals with MS is quantifiably different from that of healthy controls,<sup>9,36</sup> our hypothesis was that radiomics features could potentially reveal subtle alterations before they become visually discernible on MR imaging. As in previous studies,<sup>37,38</sup> interpretation of the radiomics features that were most important to our final model showed that more homogeneous and lower gray-level

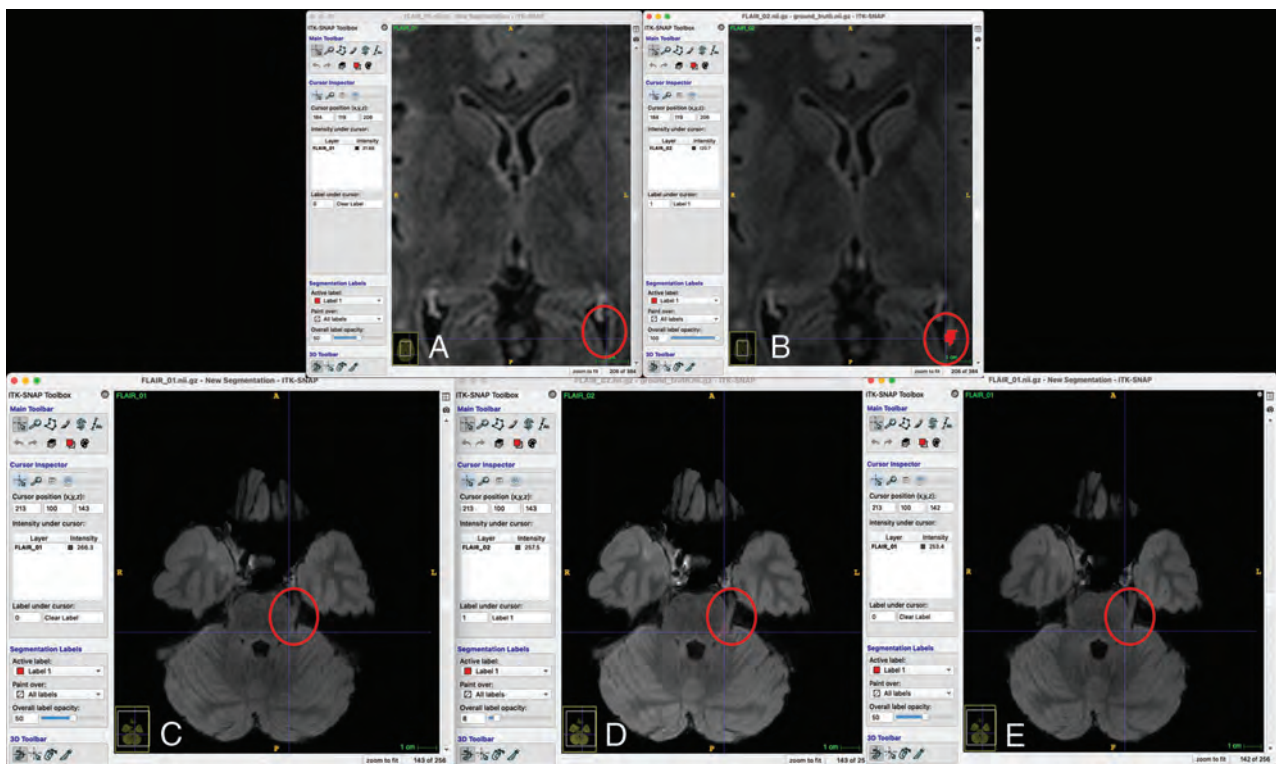


**FIG 6.** False-negative analysis (A and B, Upper row, C–E, Lower row). Two of the 3 false-negative cases in the external validation set are shown. A and B, The new lesion map falls within the ventricle on the prior image, making a negative prediction more likely because the low gray levels were associated with negative predictions (Fig 4). C, D, and E, The orientation of the proximal left trigeminal nerve is different so that the segmentation is cast onto the normal brainstem instead.

regions were more likely to be classified as “control,” yielding a level of intuition about model behavior and suggesting that the model performed as expected.

Temporality or the consideration of time-based changes is increasingly recognized as a critical component in radiology AI research.<sup>21</sup> It allows longitudinal analysis of imaging data, potentially enabling the AI to capture disease progression and treatment responses and even predict future outcomes.<sup>22,23,39</sup> Integrating temporality into AI models enhances their capacity to detect subtle, time-dependent changes in patient imaging data, which may remain undetected by conventional image analysis.<sup>23</sup> We aimed to build on this research because in conditions such as MS, in which the temporal evolution of lesions is a critical aspect of disease-monitoring and management, they could lead to earlier intervention and better patient outcomes.<sup>40,41</sup> The MSSEG2 was a clear recognition of the importance of temporality in research. We demonstrate generalizability through external validation of our results on MSSEG2. While there was a drop in performance at external validation, it was in keeping with what was expected from the literature.<sup>42</sup> Furthermore, the MSSEG2 data are known to be very heterogeneous, including several different institutions, 15 scanners, and scanning protocols with a mix of 1.5T and 3T, meaning that MSSEG2 was a robust test of performance.<sup>3</sup> Diagnostic accuracy results from MSSEG2 have been modest overall, putting our performance in context. Even the best-performing published models from the challenge demonstrate only modest accuracy for new-lesion detection, indicating both the robust challenge represented

by the data set and the potential for improvement in the field.<sup>3</sup> Furthermore, false-negative analysis also shows that some of the misclassifications were technical (Fig 6).

A relative probability map was produced on an unseen case to demonstrate a possible future clinical application. There are some artifacts in the cortical gray matter on the right of the image and lower-level increased probability in a band of subcortical white matter on the right. These could be removed with anatomic filtering or further thresholding, but we chose to present the map “as is” rather than overly “tuning it.” One false-positive was seen, even with thresholding, but this was at the site of a lesion that regressed, so there was a change at this location, albeit in the opposite direction. Furthermore, the purpose of the map is to illustrate a potential clinical application for future work rather than it being directly related to the research question of this study. Prospective analysis would be needed before the relative probability map could be implemented clinically.

### Limitations

The retrospective study design limits the level of evidence. Furthermore, because our experiments only involved those patients with progression, there was a strong selection bias. While this is a common issue in clinical radiology research,<sup>43</sup> it remains a clear limitation. The purpose of the study, to examine the potential for radiomics markers to predict new lesion occurrence, informed our research design; however, this purpose would need to be addressed prospectively before any implementation. Our sample size was modest, but having >120 pairs with change for

training compares favorably with MSSEG2,<sup>3</sup> which comprised only 100 pairs of patients in total, of whom one-half were stable.

### Future Directions and Implications for Practice

Our findings indicate that radiomics features have the potential to serve as an imaging biomarker for predicting radiologic progression of MS. The extracted features could be used to develop a probability map for future lesion occurrence. This map and the relative probabilities of progression have many potential clinical applications. These include making personalized decisions around the timing for follow-up imaging or even interventions. The use of imaging biomarkers in this way is a topic of prospective evaluation in cancer imaging.<sup>44</sup> Furthermore, stratification of patients based on imaging biomarkers to identify individuals suited for preventive intervention is highlighted as a key role of medical imaging in personalized medicine by the European Society of Radiology.<sup>45</sup> Another possible application would be to highlight ROIs during radiologist interpretation<sup>46</sup> or to direct attention<sup>47</sup> in a lesion-detection algorithm.

### CONCLUSIONS

Our machine learning model based on radiomics features successfully differentiated prelesions from NAWM. This result suggests that radiomics features from NAWM could serve as an imaging biomarker for progression of MS on MR imaging.

Disclosure forms provided by the authors are available with the full text and PDF of this article at [www.ajnr.org](http://www.ajnr.org).

### REFERENCES

- McNamara C, Sugrue G, Murray B, et al. **Current and emerging therapies in multiple sclerosis: implications for the radiologist, Part 1: mechanisms, efficacy, and safety.** *AJNR Am J Neuroradiol* 2017;38:1664–71 CrossRef Medline
- McNamara C, Sugrue G, Murray B, et al. **Current and emerging therapies in multiple sclerosis: implications for the radiologist, Part 2: surveillance for treatment complications and disease progression.** *AJNR Am J Neuroradiol* 2017;38:1672–80 CrossRef Medline
- Commowick O, Cervenansky F, Cotton F, et al. **MSSEG-2 challenge proceedings: multiple sclerosis new lesions segmentation challenge using a data management and processing infrastructure.** In: *International Conference on Medical Image Computing and Computer Assisted Intervention*. September 27 to October 1, 2021; Virtual
- Yang J, Hamade M, Wu Q, et al. **Current and future biomarkers in multiple sclerosis.** *Int J Mol Sci* 2022;23:5877 CrossRef Medline
- Martin D, Tong E, Kelly B, et al. **Current perspectives of artificial intelligence in pediatric neuroradiology: an overview.** *Front Radiol* 2021;1:713681 CrossRef Medline
- Kelly BS, Judge C, Bollard SM, et al. **Radiology artificial intelligence: a systematic review and evaluation of methods (RAISE).** *Eur Radiol* 2022;32:8054 CrossRef Medline
- Diaz-Hurtado M, Martínez-Heras E, Solana E, et al. **Recent advances in the longitudinal segmentation of multiple sclerosis lesions on magnetic resonance imaging: a review.** *Neuroradiology* 2022;64:2103–17 CrossRef Medline
- Lladó X, Ganiler O, Oliver A, et al. **Automated detection of multiple sclerosis lesions in serial brain MRI.** *Neuroradiology* 2012;54:787–807 CrossRef Medline
- Filippi M, Preziosa P, Arnold DL, et al. **Present and future of the diagnostic work-up of multiple sclerosis: the imaging perspective.** *J Neurol* 2023;270:1286–99 CrossRef Medline
- Havas J, Leray E, Rollet F, et al. **Predictive medicine in multiple sclerosis: a systematic review.** *Mult Scler Relat Disord* 2020;40:101928 CrossRef Medline
- Lorefice L, Pitzalis M, Murgia F, et al. **Omics approaches to understanding the efficacy and safety of disease-modifying treatments in multiple sclerosis.** *Front Genet* 2023;14:1076421 CrossRef Medline
- Brummer T, Muthuraman M, Steffen F, et al. **Improved prediction of early cognitive impairment in multiple sclerosis combining blood and imaging biomarkers.** *Brain Commun* 2022;4:fcac153 CrossRef Medline
- Storelli L, Azzimonti M, Gueye M, et al. **A deep learning approach to predicting disease progression in multiple sclerosis using magnetic resonance imaging.** *Invest Radiol* 2022;57:423–32 CrossRef Medline
- Santos DP, dos Dietzel M, Baessler B. **A decade of radiomics research: are images really data or just patterns in the noise?** *Eur Radiol* 2021;31:1–4 CrossRef Medline
- Huang EP, O'Connor JP, McShane LM, et al. **Criteria for the translation of radiomics into clinically useful tests.** *Nat Rev Clin Oncol* 2023;20:69–82 CrossRef Medline
- Liu Y, Dong D, Zhang L, et al. **Radiomics in multiple sclerosis and neuromyelitis optica spectrum disorder.** *Eur Radiol* 2019;29:4670–77 CrossRef Medline
- Peng Y, Zheng Y, Tan Z, et al. **Prediction of unenhanced lesion evolution in multiple sclerosis using radiomics-based models: a machine learning approach.** *Mult Scler Relat Disord* 2021;53:102989 CrossRef Medline
- Luo X, Piao S, Li H, et al. **Multi-lesion radiomics model for discrimination of relapsing-remitting multiple sclerosis and neuropsychiatric systemic lupus erythematosus.** *Eur Radiol* 2022;32:5700–10 CrossRef Medline
- Pontillo G, Tommasin S, Cuocolo R, et al. **A combined radiomics and machine learning approach to overcome the clinoradiologic paradox in multiple sclerosis.** *AJNR Am J Neuroradiol* 2021;42:1927–33 CrossRef Medline
- Rajpurkar P, Lungren MP. **The current and future state of AI interpretation of medical images.** *N Engl J Med* 2023;388:1981–90 CrossRef Medline
- Acosta JN, Falcone GJ, Rajpurkar P. **The need for medical artificial intelligence that incorporates prior images.** *Radiology* 2022;304:283–88 CrossRef Medline
- Sushentsev N, Rundo L, Abrego L, et al. **Time series radiomics for the prediction of prostate cancer progression in patients on active surveillance.** *Eur Radiol* 2023;33:3792–800 CrossRef Medline
- Kelly BS, Mathur P, Plesniar J, et al. **Using deep learning-derived image features in radiologic time series to make personalised predictions: proof of concept in colonic transit data.** *Eur Radiol* 2023;33:8376–86 CrossRef Medline
- Moskowitz CS, Welch ML, Jacobs MA, et al. **Radiomic analysis: study design, statistical analysis, and other bias mitigation strategies.** *Radiology* 2022;304:265–73 CrossRef Medline
- Kocak B, Baessler B, Bakas S, et al. **CheckList for Evaluation of Radiomics research (CLEAR): a step-by-step reporting guideline for authors and reviewers endorsed by ESR and EuSoMRI.** *Insights Imaging* 2023;14:75 CrossRef Medline
- Kelly B, Kirwan A, Quinn M, et al. **The ethical matrix as a method for involving people living with disease and the wider public (PPI) in near-term artificial intelligence research.** *Radiography (Lond)* 2023;29(Suppl 1):S103–11 CrossRef Medline
- Mongan J, Moy L, Kahn CE. **Checklist for Artificial Intelligence in Medical Imaging (CLAIM): a guide for authors and reviewers.** *Radiol Artif Intell* 2020;2:e200029 CrossRef Medline
- Kocak B, Chepelev LL, Chu LC, et al. **Assessment of RadiomICS Research (ARISE): a brief guide for authors, reviewers, and readers from the Scientific Editorial Board of European Radiology.** *Eur Radiol* 2023;33:7556–60 CrossRef Medline
- Pham N, Hill V, Rauschecker A, et al. **Critical appraisal of artificial intelligence-enabled imaging tools using the levels of evidence system.** *AJNR Am J Neuroradiol* 2023;44:E21–28 CrossRef Medline

30. Jenkinson M, Beckmann CF, Behrens TEJ, et al. **FSL**. *Neuroimage* 2012;62:782–90 CrossRef Medline
31. Kamnitsas K, Ferrante E, Parisot S, et al. **Brainlesion: glioma, multiple sclerosis, stroke and traumatic brain injuries**. In: *Second International Workshop, BrainLes 2016, with the Challenges on BRATS, ISLES and mTOP 2016, Held in Conjunction with MICCAI 2016*. Athens, Greece. October 17, 2016
32. Yushkevich PA, Gao Y, Gerig G, et al. **ITK-SNAP: an interactive tool for semi-automatic segmentation of multi-modality biomedical images**. *Annu Int Conf IEEE Eng Med Biol Soc* 2016;2016:3342–45 CrossRef Medline
33. Rovira À, Wattjes MP, Tintoré M, et al; MAGNIMS study group. **MAGNIMS consensus guidelines on the use of MRI in multiple sclerosis: clinical implementation in the diagnostic process**. *Nat Rev Neurol* 2015;11:471–82 CrossRef Medline
34. Griethuysen JJM, van Fedorov A, Parmar C, et al. **Computational radiomics system to decode the radiographic phenotype**. *Cancer Res* 2017;77:e104–07 CrossRef Medline
35. Maier-Hein L, Reinke A, Christodoulou E, et al. **Metrics reloaded: pitfalls and recommendations for image analysis validation**. *ArXiv* 2023. <https://arxiv.org/abs/2206.01653v1>. Accessed November 1, 2023
36. Filippi M, Preziosa P, Rocca MA. **Brain mapping in multiple sclerosis: lessons learned about the human brain**. *Neuroimage* 2019;190:32–45 CrossRef Medline
37. Wang L, Kelly B, Lee EH, et al. **Multi-classifier-based identification of COVID-19 from chest computed tomography using generalizable and interpretable radiomics features**. *Eur J Radiol* 2021;136:109552 CrossRef Medline
38. Ardakani AA, Bureau NJ, Ciaccio EJ, et al. **Interpretation of radiomics features: a pictorial review**. *Comput Methods Programs Biomed* 2022;215:106609 CrossRef Medline
39. Kelly B, Martinez M, Do H, et al. **DEEP MOVEMENT: deep learning of movie files for management of endovascular thrombectomy**. *Eur Radiol* 2023;33:5728–39 CrossRef Medline
40. Brex PA, Ciccarelli O, O'Riordan JI, et al. **A longitudinal study of abnormalities on MRI and disability from multiple sclerosis**. *N Engl J Med* 2002;346:158–64 CrossRef Medline
41. Todea AR, Melie-Garcia L, Barakovic M, et al; Swiss MS Cohort Study. **A multicenter longitudinal MRI study assessing LeMan-PV Software accuracy in the detection of white matter lesions in multiple sclerosis patients**. *J Magn Reson Imaging* 2023;58:864–76 CrossRef Medline
42. Yu AC, Mohajer B, Eng J. **External validation of deep learning algorithms for radiologic diagnosis: a systematic review**. *Radiol Artif Intell* 2022;4:e210064 CrossRef Medline
43. Sica GT. **Bias in research studies**. *Radiology* 2006;238:780–89 CrossRef Medline
44. Martí-Bonmatí L, Alberich-Bayarri Á, Ladenstein R, et al. **PRIMAGE project: predictive in silico multiscale analytics to support childhood cancer personalised evaluation empowered by imaging biomarkers**. *Eur Radiol Exp* 2020;4:22 CrossRef Medline
45. European Society of Radiology (ESR). **Medical imaging in personalised medicine: a white paper of the research committee of the European Society of Radiology (ESR)**. *Insights Imaging* 2015;6:141–55 CrossRef Medline
46. Yap MH, Goyal M, Osman F, et al. **Breast ultrasound region of interest detection and lesion localisation**. *Artif Intell Med* 2020;107:101880 CrossRef Medline
47. Akinci D'Antonoli T, Stanzione A, Bluethgen C, et al. **Large language models in radiology: fundamentals, applications, ethical considerations, risks, and future directions**. *Diagn Interv Radiol* 2023 October 3. [Epub ahead of print] CrossRef Medline

# AI-Assisted Summarization of Radiologic Reports: Evaluating GPT3davinci, BARTcnn, LongT5booksum, LEDbooksum, LEDlegal, and LEDclinical

 Aichi Chien,  Hubert Tang,  Bhavita Jagessar, Kai-wei Chang, Nanyun Peng,  Kambiz Nael, and  Noriko Salamon



## ABSTRACT

**BACKGROUND AND PURPOSE:** The review of clinical reports is an essential part of monitoring disease progression. Synthesizing multiple imaging reports is also important for clinical decisions. It is critical to aggregate information quickly and accurately. Machine learning natural language processing (NLP) models hold promise to address an unmet need for report summarization.

**MATERIALS AND METHODS:** We evaluated NLP methods to summarize longitudinal aneurysm reports. A total of 137 clinical reports and 100 PubMed case reports were used in this study. Models were 1) compared against expert-generated summary using longitudinal imaging notes collected in our institute and 2) compared using publicly accessible PubMed case reports. Five AI models were used to summarize the clinical reports, and a sixth model, the online GPT3davinci NLP large language model (LLM), was added for the summarization of PubMed case reports. We assessed the summary quality through comparison with expert summaries using quantitative metrics and quality reviews by experts.

**RESULTS:** In clinical summarization, BARTcnn had the best performance (BERTscore = 0.8371), followed by LongT5Booksum and LEDlegal. In the analysis using PubMed case reports, GPT3davinci demonstrated the best performance, followed by models BARTcnn and then LEDbooksum (BERTscore = 0.894, 0.872, and 0.867, respectively).

**CONCLUSIONS:** AI NLP summarization models demonstrated great potential in summarizing longitudinal aneurysm reports, though none yet reached the level of quality for clinical usage. We found the online GPT LLM outperformed the others; however, the BARTcnn model is potentially more useful because it can be implemented on-site. Future work to improve summarization, address other types of neuroimaging reports, and develop structured reports may allow NLP models to ease clinical workflow.

**ABBREVIATIONS:** BART = bidirectional and auto-regressive transformer; BERT = bidirectional encoder representations from transformer; LED = long-former-encoder-decoder; LLM = large language model; NLP = natural language processing; ROUGE = recall-oriented understudy for gisting evaluation

ChatGPT and other large language models (LLMs) have raised interest in using natural language processing (NLP) for clinical research (eg, to collect clinical outcome data).<sup>1-3</sup> We sought to utilize AI technology to improve brain aneurysm research and clinical workflow by summarizing radiology imaging reports.<sup>4</sup> Imaging reports are written by radiologists to describe findings of

clinical imaging for disease diagnosis, treatment, and follow-up. As additional imaging is performed and follow-up duration increases, additional time is required to review reports and make the diagnosis in a follow-up visit.<sup>4-6</sup> Longitudinal imaging which captures aneurysm changes over the course of 3–5 years is common.<sup>7,8</sup> This study specifically evaluated AI language models' summarization of a longitudinal series of aneurysm imaging reports. We tested the capability and quality of different NLP models, including a GPT text model. We present methodology that can be used to evaluate NLP models. We aim to promote a systematic approach using quantitative evaluation to understand the performance of NLP models so that clinical researchers can objectively understand the strength and weakness of these new technologies and further harness the benefits they may provide to medical research.

In our analysis using real longitudinal brain aneurysm imaging reports, we first locally implemented 5 state-of-the-art summarization models: BARTcnn (Meta [previously Facebook] Menlo


Received June 28, 2023; accepted after revision November 9.

From the Department of Radiological Science (A.C., H.T., B.J., K.N., N.S.), David Geffen School of Medicine at UCLA, Los Angeles, California; and Department of Computer Science (K.C., N.P.), University of California, Los Angeles, Los Angeles, California.

This work was supported in part by National Institutes of Health R01HL152270.

Please address correspondence to Aichi Chien, PhD, Department of Radiology, David Geffen School of Medicine at UCLA, 10833 LeConte Ave, Box 951721, Los Angeles, CA 90095; e-mail: aichi@ucla.edu; @Chienlab\_UCLA; @RadiologyUcla

 Indicates open access to non-subscribers at [www.ajnr.org](http://www.ajnr.org)

 Indicates article with online supplemental data.

<http://dx.doi.org/10.3174/ajnr.A8102>

Park, California),<sup>9</sup> LongT5booksum (Google, Mountain View, California),<sup>10</sup> LEDbooksum, LEDlegal, and LEDclinical (Allen Institute for AI, Seattle, Washington) and compared the performance using expert-generated summaries (ground truth) within the hospital firewall. These are all machine learning models for NLP tasks. These models were developed and shared by Meta, Google, and the Allen Institute for AI, and further improved by individual users for NLP research. For example, BART (bidirectional and auto-regressive transformer [BART]-large-cnn by Meta) was trained on the CNN/DailyMail data set, with >300,000 news articles and their respective summaries from CNN and Daily Mail articles. GPT3davinci (OpenAI, San Francisco), a massive LLM, can only be accessed online and is therefore not a HIPAA-compliant application. But to compare it with the other 5 models, we used 100 publicly accessible English case reports related to brain aneurysms from PubMed.<sup>5</sup> This evaluation allowed us to fairly understand the strengths of all the models in the tasks to generate aneurysm follow-up summarization reports.

## MATERIALS AND METHODS

### Clinical Collection

This study was approved by the Institutional Review Board. We anonymized and analyzed clinical imaging reports from 52 patients (64 aneurysms) from 2005 to 2022 undergoing monitoring for intracranial aneurysm progression. There were 44 females and 8 males. A total of 137 clinical imaging reports were used for this study. The average interval between the first and second visits, and second and third visits was 15.35 and 12.36 months, respectively. Typically, our center recommends aneurysm follow-up every 12 months. Sometimes patients return later than the recommended length of time. Usually, after the second visit, they will adhere closer to the schedule for the third visit. The aneurysm imaging reports include 3 modalities: MR angiography, CT angiography, and DSA. Online Supplemental Data show the patient demographic and imaging report information.

### Case Report Analysis

We also performed comparative analysis and evaluated the NLP summary models using a data set derived from PubMed. A total of 100 publicly accessible English case reports on neurovascular disease (brain aneurysms, neuroangiography, vascular malformations) were collected through PubMed search, and their body texts were used for this part of the analysis. Expert-generated summaries based on these case reports as well as compiled figure captions were used as reference comparisons.

### Reference Standards Preparation

H.T., B.J., and A.C., who trained in neuroradiology and brain aneurysm disease clinical reports, performed the following roles: wrote the summaries and graded the PubMed case reports and clinical imaging reports that were used in this research.<sup>11-13</sup> K.N. and N.S., 2 board-certified neuroradiologists, reviewed and revised the summaries and grading. For each patient, summaries were generated from the first visit, first 2 visits, and first 3 visits. Patient information, aneurysm features, imaging technique, and treatment were essential information in the summary.

## Summarization Models

We used 6 state-of-the-art NLP summarization models that have been trained with different source data sets and shown strength in faithful summary: BARTcnn—BART model trained on the CNN/DailyMail news data set;<sup>9</sup> LongT5booksum—T5 trained on the booksum data set, a collection of human written summaries of various literature;<sup>10</sup> LEDbooksum—Longformer Encoder-Decoder (LED) model trained on the booksum data set;<sup>14</sup> LEDlegal—LED model trained on sec-litigation-releases data set containing more than 2700 litigation releases and complaints;<sup>14</sup> LEDclinical—LED model trained on references extracted from revised references in the MIMIC-III data set, a database of public health—related data;<sup>15</sup> GPT3davinci—GPT3 davinci-003 LLM utilizing 1.75 billion parameters to generate summaries and only accessible from an API provided by OpenAI.<sup>16</sup> Except for GPT3davinci, models were implemented locally in Python (<http://www.python.org>). Online Supplemental Data aggregate information about each model and information to access the source code.

## Quantitative Evaluation

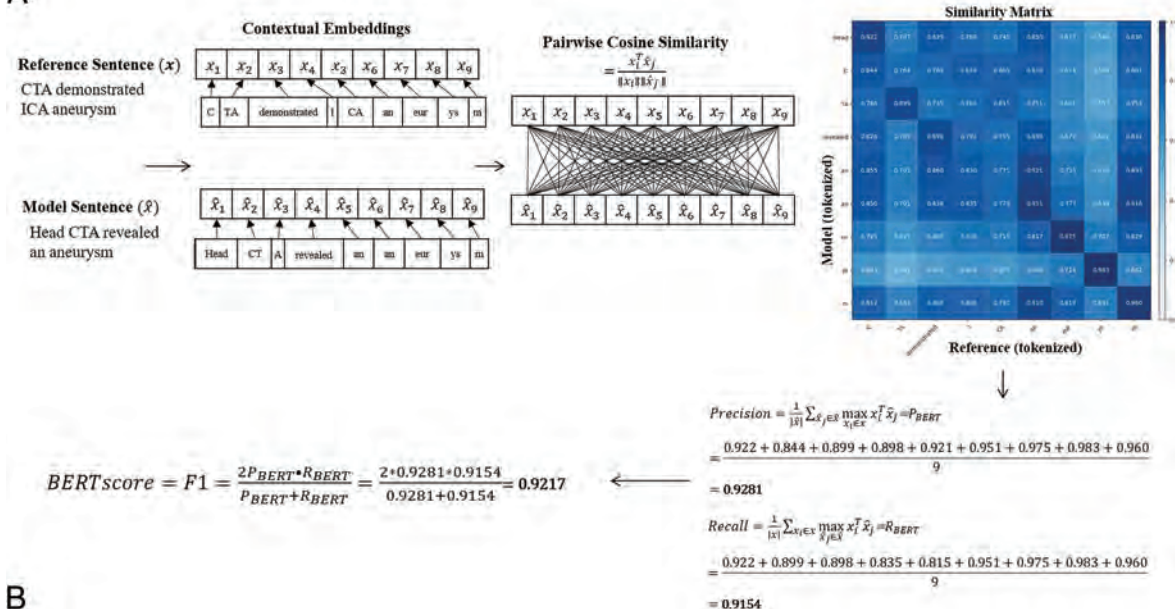
We compared model-outputted summaries (model summary) to expert generated summaries (ground truth summary) through evaluation of recall-oriented understudy for gisting evaluation (ROUGE)-1, ROUGE-2, ROUGE-L score, and BERTscore. ROUGE-1, ROUGE-2, ROUGE-L, and bidirectional encoder representations from transformer (BERT) score are the standard matrix using computational approaches to assess the quality of NLP models.<sup>17,18</sup> We also calculated text reduction: the ratio of the length of the summary with the length of the original text. Online Supplemental Data show the list of equations. Specifically, a unit of text, *grams*, was used in ROUGE-1, ROUGE-2, and ROUGE-L score. (For example, a unigram refers to a single word.) BERTScore evaluates words in the reference summary and model summary by finding the cosine similarity and implements greedy matching techniques to define the score. For each metric, the F1-score, a statistical calculation to estimate the accuracy for each score type, was used to compare the performance of the models. The Figure illustrates the NLP parameters and the processes for calculating these scores.

## Expert Evaluation

The expert evaluation was performed by 4 experts (H.T., B.J., K.N., N.S.) based on assessed *readability*, *accuracy of information*, *comprehensiveness*, and *redundancy* following the approach proposed by Goldstein et al.<sup>13,19-21</sup> Online Supplemental Data show the evaluation matrix for each category and how the score was evaluated. Specifically, we evaluate each summary by comparing the model-generated summary against the expert generated summary (ground truth) for *readability*—refers to grammatical correctness of each summary, *accuracy*—refers to correctness of information in each summary, *comprehensiveness*—refers to amount of aneurysm information in each summary, and *redundancy*—measures length and amount of redundant information present in each summary. Each summary was evaluated and given a numeric score of 1 to 5 (5 being best) in the categories

	Sentence	ROUGE-1 (Unigram)	ROUGE-2 (Bigram)	ROUGE-L (LCS)
REFERENCE sentence	..at 2 months follow-up, patient recovered completely..	{at, 2, months, follow-up, patient, recovered, completely}	{at 2, 2 months, months follow-up, follow-up patient, patient recovered, recovered completely}	
MODEL sentence	..the patient made a full recovery at 2 months follow-up..	{the, patient, made, a, full, recovery, at, 2, months, follow-up}	{the patient, patient made, made a, a full, full recovery, recovery at, at 2, 2 months, months follow-up}	{at, 2, months, follow-up}
Score		$P = \frac{\# \text{ unigrams in REFERENCE and MODEL}}{\# \text{ unigrams in MODEL}} = \frac{5}{10}$ $R = \frac{\# \text{ unigrams in REFERENCE and MODEL}}{\# \text{ unigrams in REFERENCE}} = \frac{5}{7}$ $F1 = 2 \frac{PR}{P+R} = \frac{2 * \frac{5}{10} * \frac{5}{7}}{\frac{5}{10} + \frac{5}{7}} = 0.588$	$P = \frac{\# \text{ bigrams in REFERENCE and MODEL}}{\# \text{ bigrams in MODEL}} = \frac{3}{9}$ $R = \frac{\# \text{ bigrams in REFERENCE and MODEL}}{\# \text{ bigrams in REFERENCE}} = \frac{3}{6}$ $F1 = 2 \frac{PR}{P+R} = \frac{2 * \frac{3}{9} * \frac{3}{6}}{\frac{3}{9} + \frac{3}{6}} = 0.400$	$P = \frac{\# \text{ unigrams in LCS}}{\# \text{ unigrams in MODEL}} = \frac{4}{10}$ $R = \frac{\# \text{ unigrams in LCS}}{\# \text{ unigrams in REFERENCE}} = \frac{4}{7}$ $F1 = 2 \frac{PR}{P+R} = \frac{2 * \frac{4}{10} * \frac{4}{7}}{\frac{4}{10} + \frac{4}{7}} = 0.471$

A



B

**FIGURE.** Visualization of quantitative evaluation with examples. The example gives expert generated reference sentence and model-generated sentences. A, Different ROUGE scores are calculated based on defining unigrams, bigrams, and longest common subsequences. Matching between the reference and candidate sentences are highlighted in red. ROUGE-1, ROUGE-2, and ROUGE-L are computed as F1 scores using P (precision) and R (recall) values. B, BERTScore was calculated by 1) first converting text into tokens, 2) calculating pair-wise cosine similarity between every reference and model token, and 3) identifying the tokens in the other sentence with the highest similarity value, and using the highest similarity values to calculate F1.

independently by H.T. and B.J. The average score was then approved by K.N. and N.S. to be the final score. In the case of discrepancies with a score difference of  $>3$  (medium score), the summary was rescored until consensus was reached and the score was approved.

## RESULTS

Our analysis using patient data showed that BARTcnn performed the best overall for single and longitudinal visit reports when both quantitative and expert evaluation was considered (Online Supplemental Data). LEDbooksum ranked second for 1 imaging report, followed by LongT5Booksum. For more than 2 imaging reports, BARTcnn held the best performance followed by LongT5Booksum and LEDlegal. Comparing the reduction of the text, experts were able to reduce report text to an average of 16.29%, 13.14%, and 9.86% for 1, 2, and 3 visit reports, respectively. LEDlegal and LongT5Booksum showed better text reduction but were low in comprehensiveness. BARTcnn provided the next best reduction and maintained reasonable comprehensiveness.

Our comparative study of model performance with GPT3davinci (Online Supplemental Data) found that GPT3davinci demonstrated superior performance in case report summarization, scoring highest in all categories. It was followed by BARTcnn and LEDbooksum. Based on the expert quality analysis, GPT3davinci and BARTcnn had the closest readability, accuracy, and redundancy. BARTcnn, which had the second-best overall performance, could produce comparable output to GPT3davinci while using local workstations (Online Supplemental Data).

## DISCUSSION

Given the sophistication of the models and large training sets, we expected GPT3 and BARTcnn to be among the best models for summarization. Although there is room for improvement, these 2 characteristics appear to have been the most important determinants of summarization performance. LEDclinical was trained based on a critical care database (MIMIC-III), yet the performance was relatively poor.<sup>22</sup> This may be because the radiology reports we summarized are more limited in scope than the broad assortment of clinical notes used to train LEDclinical against

discharge reports, and thus do not benefit from its reference revision approach.<sup>15</sup> Additionally, the radiology reports may not be sufficiently long for the Longformer network model underlying the LED models (LEDclinical, LEDbooksum, LEDlegal) to have an advantage over the other models.<sup>14</sup> The performance of LongT5booksum, LEDbooksum, and LEDlegal on average fell between BARTcnn and LEDclinical. This likely reflects the purpose of the original models (book summarization, and legal document summarization) being more restricted, while GPT3 and BARTcnn were trained on a wider range of topics. However, in some limited contexts (eg, LEDbooksum, single clinical visit quantitative metrics), they were able to surpass BARTcnn. In the expert assessment of redundancy, the BARTcnn model did have a tendency to repeat sentences, but this did not have a large impact on the human readers' ability to parse the summaries. (For example: *Patient will have follow-up MRA in 12 months. Patient will have follow-up MRA in 12 months.*)

Summarization of longitudinal clinical imaging reports is a relatively new area of research. However, in the past, work has focused on both NLP processing of neuroradiology reports<sup>23-25</sup> and extracting temporal relations from clinical reports.<sup>26,27</sup> Processing of neuroradiology reports includes different objectives, such as generating diagnoses or summarization. Recently, neural network NLP models have become the focus, in particular variations of BERT-based models.<sup>28</sup> Models such as ClinicalBERT predict 30-day hospital readmission based on discharge summaries and various intensive care clinical notes, including radiology reports.<sup>29</sup> Recently, a variety of BERT derivatives, collectively referred to as RadBERT, were trained with a broad set of Veterans Affairs' radiology reports and tested on tasks including summarization.<sup>30</sup> The testing methodology differed from that presented here. Summaries generated by experts were not used, and the data set, likewise, was not focused on a specific disease or longitudinal data. Their results therefore are not directly comparable with ours, and their reported ROUGE scores were uniformly lower than our results. The BARTcnn model we tested extends BERT with an autoregressive decoder, effectively adding a key feature of GPT to BERT.<sup>9</sup> The model design, along with initial training set, is a large part of why BARTcnn was able to outperform other local models in our study.

Defining temporal relations in clinical reports is essential to follow the course of disease and treatment. Previous research has largely focused on encoding the sequence of events with a structure digestible by software for further analysis. Based on a few forms of cancer, the clinical data sets (THYME/THYME2) have been carefully annotated.<sup>31</sup> Other diseases and longitudinal series of radiology reports have both not been a focus. Direct summarization via deep learning models, as we present here, has only recently become viable and bypasses the explicit extraction of temporal relationships. This approach shares the pros and cons with many other machine learning solutions. The model is largely a black box that is simple to use and very effective, but because it does not explicitly give structure to the data, modifying the form of the output into, for example, a chart or table may require another model focused on temporal relation extraction.

The models we evaluated showed great potential to help clinical workflow and follow-up management. These models were not designed for clinical imaging reports, and with the exception of LEDclinical, not trained on clinical data sets. Based on our qualitative (expert) evaluation, we identified some common limitations. Online Supplemental Data provide examples and critiques of the output from the different models. Many models had qualitative deductions in readability, including spelling and grammatical errors, as well as a lack of comprehensiveness (Online Supplemental Data). This lack of comprehensiveness often concerned the end of the text, leaving out important information that occurred at the end (eg, patient outcomes or treatment). This limitation means that these existing models are not immediately ready for clinical usage. In the future, better focusing the models on the characteristics of the data set can further improve the models. Future steps to improve summarization can be first to tune the models, adjusting input/output length and other parameters, followed by transfer learning on the longitudinal aneurysm imaging report data set we have now created. Currently, we are researching other related topics as well, including the combination of CNN image-processing with NLP text to process complete imaging reports.<sup>32</sup>

Based on this study, we found that the type of data missing (eg, aneurysm locations) varies between different models. In the current state, the models can only reliably provide information, such as general patient history and sometimes miss critical diagnostic information. However, NLP models continue to rapidly improve. Our intention was to compare these models in a relevant way, so that as new models are developed, we can objectively assess model performance. Comparing different models with expert evaluation can also help computer scientists identify future areas to be addressed and facilitate further developing better AI-generated summaries that can be sufficient for a clinical review.

## ACKNOWLEDGMENTS

Due to the sensitive nature of the aneurysm clinical reports collected for this study and to protect patient privacy, requests to access the data by researchers trained in human subject research may be sent to the corresponding author or NIH NHLBI BioLINCC Biologic Specimen and Data Repositories Information Coordinating Center following NIH public access policy reference to project R01HL152270. To access the source code for the models described in this study, links are provided in Online Supplemental Data.

## CONCLUSIONS

The AI NLP models showed great potential to generate clinical summaries. Although these models were not created for clinical imaging reports, the summaries were able to capture critical information, albeit not yet at a level suitable for clinical usage. While the GPT model had superior performance, a local BARTcnn model provided comparable quality results. This work showed a new pipeline to evaluate AI NLP models for future neuroimaging report applications. Future steps to improve summarization will be to tune the models with transfer learning on different clinical longitudinal imaging report data sets.

## REFERENCES

- Shen Y, Heacock L, Elias J, et al. **ChatGPT and other large language models are double-edged swords.** *Radiology* 2023;307:e230163 CrossRef Medline
- Akinci D'Antonoli T, Stanzione A, Bluethgen C, et al. **Large language models in radiology: fundamentals, applications, ethical considerations, risks, and future directions.** *Diagn Interv Radiol* 2023 Oct 3. [Epub ahead of print] CrossRef Medline
- Tipparedy C, Jiang S, Bera K, et al. **Radiology reading room for the future: harnessing the power of large language models like ChatGPT.** *Curr Probl Diagn Radiol* 2023 Aug 30. [Epub ahead of print] CrossRef Medline
- Moharasan G, Ho TB. **Extraction of temporal information from clinical narratives.** *J Healthc Inform Res* 2019;3:220–44 CrossRef Medline
- Mishra R, Bian J, Fiszman M, et al. **Text summarization in the biomedical domain: a systematic review of recent research.** *J Biomed Inform* 2014;52:457–67 CrossRef Medline
- Sarzynski E, Hashmi H, Subramanian J, et al. **Opportunities to improve clinical summaries for patients at hospital discharge.** *BMJ Qual Saf* 2017;26:372–80 Medline
- Chien A, Callender RA, Yokota H, et al. **Unruptured intracranial aneurysm growth trajectory: occurrence and rate of enlargement in 520 longitudinally followed cases.** *J Neurosurg* 2019;132:1077–87 CrossRef Medline
- Eskey CJ, Meyers PM, Nguyen TN, American Heart Association Council on Cardiovascular Radiology and Intervention and Stroke Council, et al. **Indications for the performance of intracranial endovascular neurointerventional procedures: a scientific statement from the American Heart Association.** *Circulation* 2018;137:e661–89 CrossRef Medline
- Lewis M, Liu Y, Goyal N, et al. **BART: denoising sequence-to-sequence pre-training for natural language generation, translation, and comprehension.** *Proceedings of the 58th Annual Meeting of the Association for Computational Linguistics*. 2020 CrossRef
- Guo M, Ainslie J, Uthus D, et al. **Longt5: efficient text-to-text transformer for long sequences.** *Findings of the Association for Computational Linguistics: NAACL 2022*. 2022 CrossRef
- Alfattni G, Peek N, Nenadic G. **Extraction of temporal relations from clinical free text: a systematic review of current approaches.** *J Biomed Inform* 2020;108:103488 CrossRef Medline
- Bhandari M, Gour PN, Ashfaq A, et al. **Re-evaluating evaluation in text summarization.** *Proceedings of the 2020 Conference on Empirical Methods in Natural Language Processing (EMNLP)*. 2020 CrossRef
- Goldstein A, Shahar Y. **An automated knowledge-based textual summarization system for longitudinal, multivariate clinical data.** *J Biomed Inform* 2016;61:159–75 CrossRef Medline
- Beltagy I, Peters ME, Cohan A. **Longformer: the long-document transformer.** *arXiv* 2020;2004.05150
- Adams G, Shing HC, Sun Q, et al. **Learning to revise references for faithful summarization.** *arXiv* 2022;2204.10290
- Goyal T, Jessy Li J, Durrett G. **News summarization and evaluation in the era of gpt-3.** *arXiv* 2022;2209.12356
- Lin CY. **Rouge: a package for automatic evaluation of summaries.** *Text Summarization Branches Out* 2004;74–81
- Zhang T, Kishore V, Wu F, et al. **Bertscore: evaluating text generation with Bert.** *arXiv* 2019;1904.09675
- Hirsch JS, Tanenbaum JS, Lipsky Gorman S, et al. **Harvest, a longitudinal patient record summarizer.** *J Am Med Inform Assoc* 2015;22:263–74 CrossRef Medline
- Percha B. **Modern clinical text mining: a guide and review.** *Annu Rev Biomed Data Sci* 2021;4:165–87 CrossRef Medline
- Sun W, Cai Z, Li Y, et al. **Data processing and text mining technologies on electronic medical records: a review.** *J Healthc Eng* 2018;2018:4302425 CrossRef Medline
- Johnson AE, Pollard TJ, Shen L, et al. **Mimic-III, a freely accessible critical care database.** *Sci Data* 2016;3:160035 CrossRef Medline
- Fu S, Leung LY, Wang Y, et al. **Natural language processing for the identification of silent brain infarcts from neuroimaging reports.** *JMIR Med Inform* 2019;7:e12109 CrossRef Medline
- Kim C, Zhu V, Obeid J, et al. **Natural language processing and machine learning algorithm to identify brain MRI reports with acute ischemic stroke.** *PLoS One* 2019;14:e0212778 CrossRef Medline
- Wheater E, Mair G, Sudlow C, et al. **A validated natural language processing algorithm for brain imaging phenotypes from radiology reports in UK electronic health records.** *BMC Med Inform Decis Mak* 2019;19:184 CrossRef Medline
- Sun W, Rumshisky A, Uzuner O. **Evaluating temporal relations in clinical text: 2012 i2b2 challenge.** *J Am Med Inform Assoc* 2013;20:806–13 CrossRef Medline
- Moskovitch R, Shahar Y, Wang F, et al. **Temporal biomedical data analytics.** *J Biomed Inform* 2019;90:103092 CrossRef Medline
- Devlin J, Chang MW, Lee K, et al. **Bert: pre-training of deep bidirectional transformers for language understanding.** *arXiv* 2019;1810.04805
- Huang K, Altosaar J, Ranganath R. **Clinicalbert: modeling clinical notes and predicting hospital readmission.** *arXiv* 2020;1904.05342
- Yan A, McAuley J, Lu X, et al. **Radbert: adapting transformer-based language models to radiology.** *Radiol Artif Intell* 2022;4:e210258 CrossRef Medline
- Styler IW, Bethard S, Finan S, et al. **Temporal annotation in the clinical domain.** *TACL* 2014;2:143–54 CrossRef Medline
- Monajatipoor M, Rouhsedaghat M, Li LH, et al. **Berthop: an effective vision-and-language model for chest x-ray disease diagnosis.** *Med Image Comput Comput Assist Interv* 2022;13435:725–34 CrossRef Medline

## Setting the Bar: The Japanese College of Radiology's Perspective on Safeguarding Quality in the Interpretation of Cross-Sectional Studies per Day

**W**e read with keen interest the recent article titled “Realistic Productivity in Academic Neuroradiology: A National Survey of Neuroradiology Division Chiefs.”<sup>1</sup> Many studies have reported on the correlation between diagnostic errors and an increase in workload volume, prompting claims for guidelines that define a range of cross-sectional studies that can be safely interpreted in a typical workday.<sup>2,3</sup>

The Japanese College of Radiology (JCR), a bastion of two-thirds of the board-certified radiologists in Japan, was established in 1973. The JCR is an organization including diagnostic radiologists, interventional radiologists, nuclear medicine physicians, and radiation oncologists as members. Owing to the world's leading concentration of CT and MR imaging scanners alongside one of the lowest ratios of radiologists per capita based on the data of the Organization for Economic Co-operation and Development (OECD), the workload of Japanese radiologists exceeds the OECD average by 4-fold.<sup>4</sup> Consequently, Japanese radiologists have been required to work at very intense paces, even at academic/educational institutions. In this context, the JCR released a position statement on the appropriate workload for radiologists in 2022. This position statement reads, “To maintain the quality of radiology services, the number of radiologists' reports should ideally be limited to less than four cross-sectional studies per hour of uninterrupted reading time (ie, protected time excluding activities such as scheduling, conferences, and consultations).” This document can be found on our web page ([https://jcr.or.jp/site/wp-content/uploads/2023/09/JCR\\_statement\\_on\\_appropriate\\_workload\\_of\\_radiologists\\_Updated\\_on\\_March\\_242022\\_en.pdf](https://jcr.or.jp/site/wp-content/uploads/2023/09/JCR_statement_on_appropriate_workload_of_radiologists_Updated_on_March_242022_en.pdf)).

Our statement may resonate very well with the “median of 32 cross-sectional studies as a reasonable and safe threshold for interpretation during a standard clinical day” stated in the article by Wintermark et al.<sup>1</sup> There are minor differences between this survey and the statement by the JCR. Our recommendation of 4 cases per hour includes the interpretation of CT, MR imaging, and PET/CT across the entire body. This number is based on the optimal interpretation durations for various representative imaging studies and their ratio in average high-volume Japanese


institutions. This number should be further reduced in teaching institutions, aligning with that in the survey reported in the article discussed in this letter.<sup>1</sup>


Our work goes beyond image interpretations. We radiologists have to make decisions regarding choosing the appropriate imaging modalities, managing the optimal protocols, and giving instructions to technologists. In addition, prompt and effective communication with referring physicians is vital for patient safety. All of these activities are time-consuming. It is, therefore, necessary to establish international guidelines for a safe number of interpreted cross-sectional studies per day to maintain the quality of our radiology services worldwide.

Disclosure forms provided by the authors are available with the full text and PDF of this article at [www.ajnr.org](http://www.ajnr.org).

### REFERENCES

1. Wintermark M, Gupta V, Hess C, et al. **Realistic productivity in academic neuroradiology: A national survey of neuroradiology division chiefs.** *AJNR Am J Neuroradiol* 2023;44:759–61 CrossRef Medline
2. Patel SH, Stanton CL, Miller SG, et al. **Risk factors for perceptual-verus-interpretative errors in diagnostic neuroradiology.** *AJNR Am J Neuroradiol* 2019;40:1252–56 CrossRef Medline
3. Ivanovic V, Paydar A, Chang YM, et al. **Impact of shift volume on neuroradiology diagnostic errors at a large tertiary academic center.** *Acad Radiol* 2023;30:1584–88 CrossRef Medline
4. Kumamaru KK, Machitori A, Koba R, et al. **Global and Japanese regional variations in radiologist potential workload for computed tomography and magnetic resonance imaging examinations.** *Jpn J Radiol* 2018;36:273–81 CrossRef Medline

 **Satoru Takahashi**  
Imaging Research Center  
Takatsuki General Hospital  
Osaka, Japan

 **Kei Yamada**  
Department of Radiology  
Kyoto Prefectural University of Medicine  
Kyoto, Japan

Board members of Japanese College of Radiology